Roksana Maria Pirzgalska

Master's degree in Engineering, Biotechnology

Neuro-immune interactions in obesity.

Thesis submitted for the degree of Doctor of Philosophy

in Bioengineering (MIT)

Orientadora:	Doutora Ana Isabel Dias Neto Domingos, Investigadora Principal, Instituto Gulbenkian de Ciência
Co-orientador:	Doutor Manuel Luís de Magalhães Nunes da Ponte, Professor Catedrático, Faculdade de Ciências e Tecnologia da Universidade NOVA de Lisboa

Júry

Presidente:	Professor Doutor Fernando José Pires Santana
Arguentes:	Professor Doutor Jorge Lira Ruas
	Professor Doutor Miguel António López Pérez
Vogais:	Professor Doutor Pedro Miguel Ribeiro Viana Baptista
	Investigatora Doutora Ana Isabel Dias Neto Domingos
	Investigator Doutor Colin Adrain

FACULDADE DE CIÊNCIAS E TECNOLOGIA
UNIVERSIDADE NOVA DE LISBOA

February 2018

NOVA University of Lisbon

Faculty of Sciences and Technology

Neuro-immune interactions in obesity.

Roksana Maria Pirzgalska

supervised by

Supervisor: Ana Isabel Dias Neto Domingos, PhD, Instituto Gulbenkian de Ciência

Co-supervisor: Manuel Luís de Magalhães Nunes da Ponte, PhD, FCT-UNL

February 2018

Neuro-immune interactions in obesity.

Obesity in prehistoric art.

Venus of Hohle Fels (left), Germany, 60 millimeters in height, dated to between 35,000 and 40,000 years ago and Venus of Willendorf (right), Austria, 105 millimeters in height, dated to 28,000 years ago.

Image credits: H.Jensen[1] and J.Royan[2].

[1] Venus of Hohle Fels: http://www.nytimes.com/2009/05/14/science/14venus.html
[2] Venus of Willendorf: http://obesitytimebomb.blogspot.pt/2016/02/100-fat-activists-venus-of-willendorf.html

Acknowledgements

To my supervisor Ana Domingos for introducing me to the obesity research and giving me the opportunity to develop my work.

To the institutions that financially supported my work: Fundação para a Ciência e a Tecnologia (FCT; SFRH/BD/88454/2012), European Molecular Biology Organization (EMBO), Instituto Gulbenkian de Ciência (IGC), Professor Francisco Pulido Valente Foundation.

To the Instituto Gulbenkian de Ciência (IGC) for creating a great place and atmosphere to do science and to Èlio Sucena for his help even though I was an "external" student.

To Colin Adrain and Rui Oliveira for being helpful and always ready to arrange the thesis committee meetings.

Special thanks to all the people from the Obesity Lab:
Especially to Elsa, who was absolutely crucial to this work: for help, support and the many hours we spent on trying to get at least 1, 000 cells...
To the ones that joined the lab very early on: Elsa, Nadiya, Mafalda, Ines, Andreia and Imogen.
And to the ones that joined more recently: Noelia, Vitka, Bernardo, Raquel, Chelsea, Miguel and Francesco.
It was really great to work with you! Our cosy space at -1 will be always remembered!

To our collaborator Chris Glass for giving me the opportunity to work and learn with his group. Special thanks to Jason and Verena, who were crucial to the RNA-seq part in this work.

To Rita Gusmão for being extremely helpful in dealing with any administrative tasks.

To the numerous people from the IGC facilities:
Advanced Imaging Unit: Gaby, Nuno, Ania and Hugo.
Flow Cytometry Unit: Marta, Mariana, Rui, Claudia x2.
Electron Microscopy Facility: Ana and Erin.
Histopathology Unit: Joana, Marta, Pedro.
Antibody Service: Ana.
And to all the people from the Animal House Facility.

To the great amount of people from the IGC that made the whole journey more pleasant and fun!

Finally, to my family and friends:

Uli i Jarkowi za pokazanie mi, że środowisko akademickie nie jest wcale takie złe :)

A Julia e o João pelo apoio.

Ani i Paulinie za przyjaźń na odleglość!

Jankowi i Maćkowi - Więcbork górą!

Magdzie i Patrykowi - rodzeństwo górą!

Rodzicom – Ewie i Waldkowi za bezwarunkową pomoc, wspieranie moich decyzji i za to, że zawsze we mnie wierzyliście!

Moving on to "sports, rock&roll, beautiful substances and stuff":

To my Paulo – for being my journey, my home and my love!

Thank you! Dziękuję! Obrigada!

List of publications

This thesis was based on the following publications:

Zeng, W.*, **Pirzgalska, R.M.***, Pereira, M.M.A., Kubasova, N., Barateiro, A., Seixas, E., Lu, Y.-H., Kozlova, A., Voss, H., Martins, G.G., Friedman, J.M., Domingos, A.I. (2015). Sympathetic Neuro-adipose Connections Mediate Leptin-Driven Lipolysis. Cell 163, 84–94. *co-first authors

Pirzgalska, R.M.*, Seixas, E.*, Seidman, J.S., Link, V.M., Sanchez, N.M., Mahu, I., Mendes, R., Gres, V., Kubasova, N., Morris, I., Arús B.A., Larabee, C.M., Vasques, M., Tortosa, F., Sousa, A.L., Anandan, S., Tranfield, E., Hahn, M.K., Iannacone, M., Spann, N.J., Glass, C.K., Domingos, A.I. (2017). Sympathetic neuron-associated macrophages contribute to obesity by importing and metabolizing norepinephrine. Nat. Med. 23, 1309–1318. *co-first authors

Original versions of the articles can be found in **Annex 1**.

Resumo

Nas últimas décadas, a obesidade tem-se vindo a revelar como uma das principais doenças complexas a afetar as populações humanas. Apesar de vários avanços na melhoria de algumas das complicações associadas a esta doença, ainda não existem terapias efetivas contra a obesidade.

Para compreender a obesidade é fundamental compreender a regulação do tecido adiposo (TA), tanto em saúde como em condições patológicas. Nos últimos anos, o nosso conhecimento sobre a biologia do TA tem crescido significativamente. Tal conhecimento resultou numa visão mais precisa de como a obesidade afeta o TA. Nesse sentido, decidimos focar o nosso trabalho num aspecto particularmente importante da biologia do TA: a sua regulação neuro-imune. Mais especificamente, o nosso trabalho centra-se no estudo de como a massa adiposa é modulada por sinais provenientes do sistema nervoso simpático (SNS), assim como da integração de tais sinais ao nível imunológico.

Os nossos resultados mostram que feixes nervosos simpáticos inervam o TA branco (TAB) subcutâneo. De um ponto de vista funcional, demonstramos que esses axónios simpáticos no TA mediam a resposta lipolítica à leptina. Mais especificamente, a ablação local do SNS no TA resultou numa diminuição da ação da leptina e, consequentemente, numa redução dos níveis de lipólise no tecido. Por outro lado, a utilização de técnicas de optogenética para ativar seletivamente os feixes simpáticos no TA, levou a uma libertação localizada do neurotransmissor norepinefrina (NE) e uma subsequente perda de massa adiposa. Desta forma, os nossos dados suportam o conceito que os feixes nervosos simpáticos do TA branco são necessários e suficientes para promover, neste mesmo tecido, a lipólise mediada por leptina.

A associação entre obesidade e inflamação de baixo grau, quer em tecidos periféricos quer no sistema nervoso central, é um dado bem estabelecido na literatura. Os nossos resultados permitiram expandir esta associação. Mais especificamente, observámos que a inflamação de baixo grau associada à obesidade também ocorre no SNS. A utilização de microscopia multi-fotão permitiu-nos demonstrar que os axónios simpáticos no TAB albergam uma população discreta de macrófagos com características celulares distintas das dos macrófagos no TA circundante. Estes macrófagos associados aos neurónios simpáticos (SAMs) possuem uma profusão de prolongamentos celulares dendritiformes, que se estendem e retraem de uma forma dinâmica ao longo do tempo. Pelo contrário, os macrófagos do TA (ATMs) são menores, redondos e possuem um mobilidade totalmente distinta. Os nossos resultados sugerem que a inflamação no TA induzida pela obesidade afeta preferencialmente as fibras nervosas simpáticas que inervam o

TAB, traduzindo-se numa acumulação de SAMs neste interface. Adicionalmente, a obesidade promove a aquisição de um perfil pró-inflamatório tanto nos SAMs como nos ATMs.

O nosso estudo sugere um possível mecanismo de regulação do neurotransmissor NE diretamente no TA através da ação dos macrófagos associados aos neurónios simpáticos. Neste âmbito, os nossos dados sugerem que os SAMs possuem a maquinaria molecular para incorporar e catabolizar NE (via o transportador SLC6A2 e a enzima Monoamina Oxidase-A, respetivamente). É de notar que esta maquinaria não foi detetada em nenhuma outra população de macrófagos estudada. Numa perspetiva funcional, a deleção de SLC6A2 no compartimento hematopoiético (por transplante de medula óssea de ratinhos SLC6A2-KO para ratinhos obesos *ob/ob*), resultou numa melhoria das capacidades termogénicas e de oxidação de gordura nos animais obesos. Para concluir, os nossos resultados ilustram a importância funcional do interface neuro-imune na regulação do tecido adiposo em casos de obesidade

Palavras-chave: obesidade, tecido adiposo, regulação neuro-imune do tecido adiposo, sistema nervoso simpático, macrófagos

Abstract

For the past few decades, obesity has emerged as one of the major complex diseases affecting human populations. Despite recent breakthroughs in ameliorating some of the complications associated with this disease, there are still no effective therapies against obesity

To understand obesity one must know how the adipose tissue (AT) is regulated in normal and affected conditions. Our knowledge on AT biology has grown significantly in the last few years. This knowledge has resulted in a clearer picture of how obesity shapes the AT. In this regard, we have decided to focus our work on one important aspect of AT biology: its neuro-immune regulation. More specifically, we set out to understand if signals originating from the sympathetic nervous system (SNS) can modulate the adipose mass, and if such signaling may be regulated at the immunological level.

Here we show that sympathetic nerve bundles target the subcutaneous white AT (WAT). Furthermore, we demonstrate that the sympathetic axons in the WAT mediate the lipolytic response to leptin. Importantly, local ablation of the SNS in WAT resulted in decreased leptin activity and blunted lipolysis. Conversely, by using optogenetics to selectively activate these sympathetic bundles, we observed a local release of the neurotransmitter norepinephrine (NE) and subsequent fat loss. Our data provide evidence supporting that sympathetic axons in the AT are both necessary and sufficient for leptin-driven lipolysis in WAT.

Obesity has long been associated with low-grade inflammation in peripheral tissues and in the central nervous system (CNS). We have observed that obesity-associated low-grade inflammation also occurs in the SNS. By using multiphoton microscopy tools, we demonstrate that sympathetic axons in WAT are populated by a discrete population of macrophages with cellular characteristics different from those of the macrophages in the surrounding AT. Such Sympathetic-neuron Associated Macrophages (SAM) exhibit profuse dendritiform processes, which dynamically extend and retract over time. On the other hand, AT macrophages (ATMs) were smaller, round and had a substantially different cellular displacement. Our study demonstrates that obesity-induced inflammation of the AT preferentially affects the sympathetic nerve fibers targeting the WAT and is closely associated with the accumulation of SAMs. Furthermore, we also observed that obesity drove the up-regulation of pro-inflammatory profiles in both SAMs and ATMs.

We provide some insight into the possible mechanism that may link macrophages in the AT to the

neurotransmitter NE. Our results suggest that SAMs possess the machinery to incorporate NE (via the Norepinephrine Transporter SLC6A2) and to catabolize it (via the enzyme Monoamine Oxidase-A). Of note, this machinery was not present in any other macrophage population we studied. In this regard, the deletion of SLC6A2 in the hematopoietic compartment (by bone marrow transfer from SLC6A2-KO mice into genetically obese *ob/ob* mice), improved thermogenic capacities and fat oxidation in this mouse model of obesity. Overall, our results demonstrate the functional significance of the neuro-immune interface for the regulation of the adipose tissue during obesity.

Key-words: obesity, adipose tissue, neuro-immune regulation of the adipose tissue, sympathetic nervous system, macrophages

List of Abbreviations

ACh Acetylcholine

AT Adipose tissue

ATGL Adipose triglyceride lipase

AT1-ILCs Adipose type 1 innate lymphoid cells

Agrp Agouti-related peptide

ATM Adipose tissue macrophages

BABB Benzyl Alcohol:Benzyl Benzoate

Adrb2 β2 adrenergic receptor

BAT Brown adipose tissue

CART Cocaine- and amphetamine-regulated transcript

CCR2 C-C motif chemokine receptor–2

JNK C-Jun NH2-terminal kinase

CNS Central nervous system

ChR2 Channelrhodopsin 2

CCK Cholecystokinin

cAMP Cyclic adenosine monophosphate

DIO Diet-induced obesity

DTR Diphtheria toxin receptor

DBH Dopamine β-hyroxylase

DRG Dorsal root ganglia

ER Endoplasmic reticulum

FFAs Free fatty acids

GLP-1 Glucagon-like peptide 1

GeRPs Glucan encapsulated RNAi particles

HFD High fat diet

HSL Hormone-sensitive lipase

ARH Hypothalamic arcuate nucleus

IKKβ Inhibitor of nuclear factor-kβ kinase

IL Interleukin

KO Knockout

MAGL Monoacylglycerol lipase

MAOA Monoamine oxidase A

MCP-1 Monocyte chemoattractant protein–1

NPY Neuropeptide Y

NO Nitric oxide

NE Norepinephrine

NF Nuclear factor

OPT Optical projection tomography

NPY Orexigenic neuropeptide Y

PACT Passive Clarity Technique

PYY Peptide YY

PARS Perfusion-assisted Agent Release in Situ

PLIN Perilipin

PPAR-γ Peroxisome proliferator-activated receptor-γ

PCA Principle component analysis

POMC Pro-opiomelanocortin

PKA Protein kinase A

RPKM Reads Per Kilobase of transcript per Million mapped reads

RT Room temperature

SGC Satellite glial cells

sATM Subcutaneous adipose tissue macrophages

SCG Superior cervical ganglia

SLC6A2 Solute carrier family 6 member 2

SpM Spleen macrophages

SNS Sympathetic nervous system

SAMs Sympathetic neuron–associated macrophages

TLR Toll-like receptor

TGF Transforming growth factor

TRPV Transient receptor potencial vaniloid

TNF Tumour necrosis factor

TH Tyrosine hydroxylase

Tub-3 β3-tubulin

UCP1 Uncoupling protein-1

vATMs Visceral adipose tissue macrophages

WAT White adipose tissue

WT Wild-type

WHO World Health Organization

List of Figures

Contents

1 | GENERAL INTRODUCTION

Roksana M Pirzgalska[1]

[1]Obesity Laboratory, Instituto Gulbenkian de Ciência, Oeiras, 2780-156, Portugal

Hippocrates wrote that "the obese should eat only once a day and take no baths and sleep on a hard bed and walk naked as long as possible."
Progress in this area will require that we move beyond this 2,000-year-old prescription and instead develop strategies that are based on twenty-first-century science.

Jeffrey Friedman, "Modern science versus the stigma of obesity", 2004

1.1 SYNOPSIS.

According to the World Health Organization (WHO), obesity is defined by a body mass index[1] of 30 or more (WHO guidelines on obesity, 2017). In Europe, nearly one in six adults is obese (Eurostat European Health Interview Survey, 2016). Obesity results from the excessive accumulation of adipose tissue (AT). For the past few decades, obesity has emerged as one of the major complex diseases affecting human populations (Ghosh and Bouchard, 2017; Haslam and James, 2005). Such situation can be attributed to a societal environment that provides favorable conditions for the epidemic of obesity. Indeed, a sedentary lifestyle and easy access to processed, highly caloric foods are commonplace in contemporary societies. Not surprisingly, obesity and its closely associated comorbidities (depression, type 2 diabetes, cardiovascular disease and certain cancers), have created a tremendous clinical and economic burden across the world (Hruby and Hu, 2015).

[1]A person's weight divided by the square of his or her height.

The increased prevalence of obesity has led to an intensified search for its causal factors (Ghosh and Bouchard, 2017). In the past few years, our knowledge on AT biology has grown exponentially (Rosen and Spiegelman, 2014), resulting in a clearer picture of how the AT is regulated during the onset of obesity. Such understanding is a pivotal aspect in the development of therapeutic approaches to this complex disease. The following sub-chapters will summarize the major advances in the field of AT biology, particularly at the level of the neuro-immune control of AT during obesity.

1.2 LESSONS FROM THE OBESE: LEPTIN AS A MASTER REGULATOR OF LIPID HOMEOSTASIS.

"Obesity is not a personal failing. In trying to lose weight, the obese are fighting a difficult battle. It is a battle against biology, a battle that only the intrepid take on and one in which only a few prevail."

Jeffrey Friedman, "A War on Obesity, Not the Obese", 2003

Obesity has been a subject of interest since the prehistoric era (Bray, 2011). However, the complications associated with excessive accumulation of fat were, for a long time, greatly underappreciated. Advances in medicine and biology allowed a better understanding of the severe impact of obesity on the balance between health and disease. Essential contributions came from animal studies that were pivotal in establishing different models of obesity. For example, brain lesions in the hypothalamic nuclei (ventromedial, paraventricular and dorsomedial) were identified as causal factors of hyperphagia and obesity in rats (Brobeck et al., 1943; Hetherington and Ranson, 1940). In 1950, the first murine genetic model of obesity was established at the Jackson Laboratory (Ingalls et al., 1950). The single gene mutation was named *obese* and the responsible gene was designated by the symbol *ob* (Ingalls et al., 1950). Several years later another single gene mutation, *diabetes*(*db*), was reported to cause severe obesity and metabolic complications resembling *diabetes mellitus* (Hummel et al., 1966).

Both *ob* and *db* homozygous mice (*ob/ob* and *db/db*, respectively) were obese, hyperglycemic and infertile (Hummel et al., 1966; Ingalls et al., 1950). Furthermore, parabiosis studies in which only one of the partners was genetically obese (*ob/ob* or *db/db*) suggested that the *ob/ob* mice did not produce a satiety factor whereas the *db/db* mice were able to do so but did not respond to it (Figure 1.1, Coleman, 1973; Coleman and Hummel, 1969). These observations were put into a mechanistic perspective upon the discovery of the *ob* and *db* gene products – leptin and its receptor (Bahary et al., 1990; Zhang et al., 1994).

The discovery of leptin (a 167-amino acid hormone produced by adipocytes) by Jeffrey Friedman was a major breakthrough in obesity research. This discovery proved, for the first time, that adiposity and

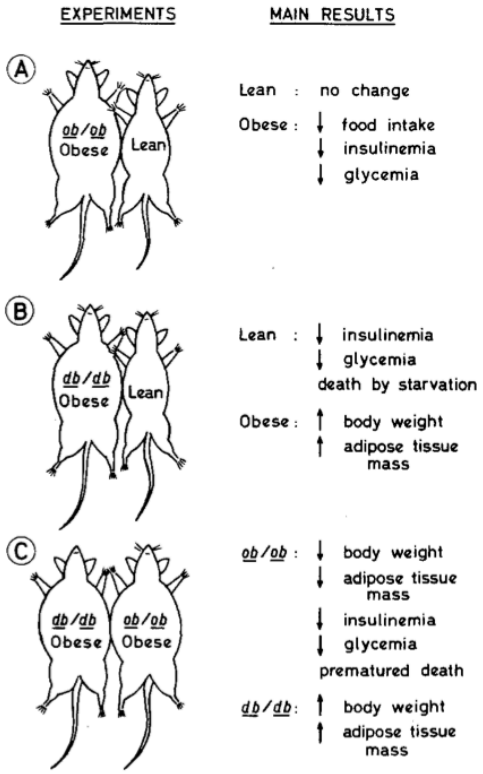

Figure 1.1. Schematic representation of experiments suggesting a role for the hypothalamus in the hyperphagia of spontaneously obese mice.

Obese hyperglycemic mice of the *ob/ob* and *db/db* type and lean mice are parabiosed as indicated. Based upon the following studies: Coleman, 1973; Coleman and Hummel, 1969. Adapted from Assimacopoulos-Jeannet and Jeanrenaud, 1976.

food intake were under molecular control (Zhang et al., 1994). It was later demonstrated that AT mass is homeostatically controlled by an endocrine loop in which leptin is produced in the AT in proportion to its mass and acts on neural circuits in the hypothalamus (and elsewhere in the brain) to regulate food intake and peripheral metabolism (Friedman and Halaas, 1998). Leptin administration reduced food intake and stimulated fat mass depletion in both wild type (*WT*) and leptin-deficient *ob/ob* animals (Halaas et al., 1995, 1997; Montez et al., 2005). Moreover, the reduction of fat mass due to leptin treatment differed from that observed during food restriction: leptin spared lean body mass and stimulated glucose metabolism, while starvation led to the loss of lean body mass and was associated with insulin resistance (Awad et al., 2009; Elia et al., 1999; Koffler and Kisch, 1996). *Ob/ob* mice pair-fed to leptin-treated *ob/ob* mice lost substantially less weight, thus confirming that the weight loss caused by leptin went beyond reduced food intake (Rafael and Herling, 2000). Moreover, leptin was shown to up-regulate the energy expenditure and the sympathetic efferent signal to brown adipose tissue (BAT) (Figure 1.2, Rezai-Zadeh and Münzberg, 2013; Scarpace and Matheny, 1998). These actions of leptin also differed from the ones

triggered by food restriction, which suppressed the activity of the sympathetic nervous system (SNS) (Young and Landsberg, 1997).

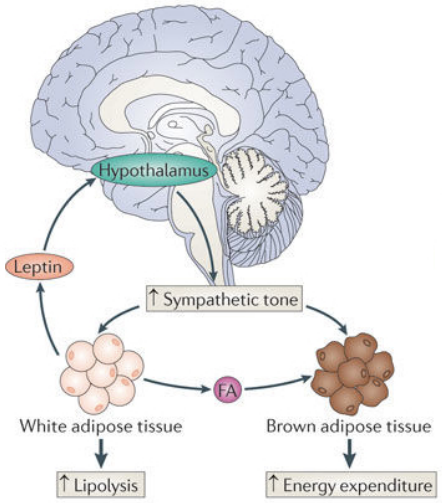

Figure 1.2. The adipocyte-derived hormone leptin increases energy expenditure by acting on hypothalamic centres that increase sympathetic outflow.
Increased sympathetic tone stimulates lipolysis and the release of fatty acids (FAs) from WAT stores. Circulating FAs are taken up and oxidized by BAT. Adapted from Altarejos and Montminy, 2011.

In light of the aforementioned properties of leptin, it was initially thought that administration of recombinant leptin would be a potent anti-obesity treatment. Yet, it was soon realized that leptin therapy served just for a relatively small number of obese patients: the ones who were leptin-deficient. In such cases, leptin replacement was extremely robust and effective in reducing body weight in a sustained manner (Farooqi et al., 1999). However, most obese individuals are characterized by high leptin levels in circulation (Heymsfield et al., 1999). Therefore, administration of recombinant leptin in such cases is of limited clinical value. Indeed, in most endocrine disorders, it is easier to treat hormonal deficiencies than the excess of hormones. This observation is equally true in the context of leptin resistance.

Several theories were put forward to explain the mechanisms behind the obesity-induced leptin resistance. These could be broadly ascribed to three overlapping fields: 1) decreased leptin transport to the hypothalamic centers, 2) reduced leptin signaling in target neurons and 3) compromised signaling in descending circuits or in target cells (Caro et al., 1996; Coppari and Bjørbæk, 2012; Jung and Kim, 2013; Ramírez and Claret, 2015). Some of these concepts will be discussed in greater detail in the subchapters **1.4 The Central and Peripheral Nervous System in obesity** and **1.10 Neuro-immune interactions during obesity**.

Although the discovery of leptin did not provide a general solution to the problem of obesity, it certainly paved the way to our understanding of this disease. Importantly, it provided a well-grounded alternative to the explanation that obesity always results from the lack of willpower.

1.3 LIPOLYSIS: THE MECHANISMS BEHIND FAT LOSS.

The survival of all living organisms is determined by energy. To meet energy demands in times of reduced caloric intake, eukaryotes have developed systems allowing the efficient storage of calories in the form of lipid droplets (Ottaviani et al., 2011). In higher organisms such as mammals, these lipid-rich organelles can form depots that accumulate in a specific cell type: the adipocyte. Adipocytes organize into AT, serving as a major energy reservoir. Historically, adipocytes have been divided into unilocular white adipocytes and multilocular brown adipocytes. The first are organized into white AT (WAT), the latter into brown AT (BAT) (Rosen and Spiegelman, 2014). While the WAT is responsible for the storage of fat, BAT has developed additional mechanisms to convert accumulated chemical energy into heat (Cannon and Nedergaard, 2004). In a simplified model for energy storage and mobilization, WAT synthesizes and stores energy-rich triglycerides in adipocytes during times of abundance. These are, in turn, mobilized when energy availability is low, as part of an adaptive response to energy shortage.

Lipolysis, the process of hydrolyzing stored triglycerides in adipocytes, is controlled by the activity of three key enzymes: adipose triglyceride lipase (ATGL), hormone-sensitive lipase (HSL), and monoacylglycerol lipase (MAGL) (Haemmerle et al., 2002; Taschler et al., 2011; Zechner et al., 2012). The combined activity of these enzymes converts triglycerides into glycerol and free fatty acids (FFAs) in three consecutive steps (Figure 1.3).

The process of lipolysis can be regulated by different hormones and neurotransmitters through either anti-lipolytic (ex: insulin) or lipolytic (ex: epinephrine, norepinephrine, adrenocorticotropic hormone) signalling (Chernick et al., 1986; Froesch, 1967). G-protein-coupled receptors (including β-adrenergic receptors), stimulate lipolysis by increasing intracellular cyclic adenosine monophosphate (cAMP) levels and by activating protein kinase A (PKA) (Figure 1.3, (Blad et al., 2012)). PKA also phosphorylates several key target proteins, including lipid-droplet-associated protein perilipin (PLIN), hormone-sensitive lipase (HSL), and a set of esterases that collectively promote the hydrolysis of triglycerides into glycerol and FFAs. These molecules are subsequently released into the circulating plasma to meet the energy demands of other tissues. In this regard, the turnover of triglycerides can serve as proxy for the state of lipid homeostasis.

Obesity is linked to increased levels of basal lipolysis (Reynisdottir et al., 1995) and to a reduced response of adipocytes to lipolytic signals such as catecholamines (Large et al., 1999). The impairment in β-adrenergic-dependent signaling in adipocytes of obese subjects has been attributed to disturbances in HSL (Large et al., 1999). Therefore, the modulation of HSL activity may circumvent the defective lipid homeostasis characteristic of obesity

In addition, tumour necrosis factor (TNF)-α, a pro-inflammatory molecule up-regulated in AT from obese and insulin-resistant subjects (Hotamisligil et al., 1993), was also associated with abnormal lipol-

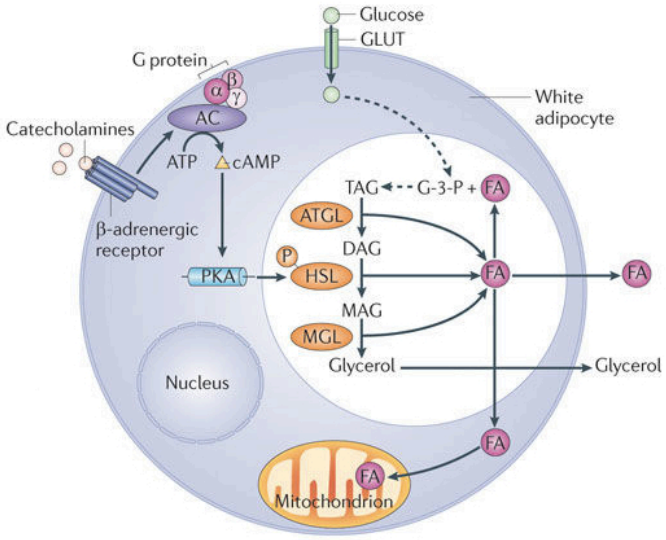

Figure 1.3. Lipolysis step by step.

In white adipocytes, catecholamines bind to β-adrenergic receptors and subsequently stimulate adenylyl cyclase (AC) and cyclic AMP production. Increased cellular cAMP levels stimulate protein kinase A (PKA), which phosphorylates and activates hormone-sensitive lipase (HSL). During lipolysis, triacylglycerol (TAG) is hydrolysed by adipocyte triglyceride lipase (ATGL). The resultant diacylglycerol (DAG) is subsequently hydrolysed to monoacylglycerol (MAG) by HSL. MAG is further hydrolysed by MAG lipase (MGL) to generate glycerol, which enters the circulation. The FAs generated during the lipolysis of TAG may also enter the circulation. Alternatively, the FAs may undergo β-oxidation or may be re-esterified to TAG. Glycerol-3-phosphate (G-3-P) is utilized as the backbone for TAG synthesis and is generated from glucose, which is transported into the adipocyte via glucose transporters (GLUTs). Adapted from Altarejos and Montminy, 2011.

ysis in obesity (Ryden et al., 2002). Accordingly, human adipocytes incubated with TNF- α exhibited enhanced basal lipolysis, which was accompanied by decreased expression of PLIN (Rydén et al., 2004). Furthermore, these effects were reversible upon treatment with the MAPK inhibitors specific for p44/42 and c-Jun NH2-terminal kinase (JNK), indicating that TNF-alpha-linked down-regulation of PLIN occurs via p44/42 and JNK pathway (Rydén et al., 2004).

1.4 THE CENTRAL AND THE PERIPHERAL NERVOUS SYSTEM IN OBESITY.

Energy homeostasis requires integration of a variety of signals to the nervous system. Long-term signals in the central nervous system (CNS) include leptin produced by adipocytes or insulin produced by pancreatic beta-cells. On the other hand, short-term CNS signals are mainly gut-derived (such as glucagon-like peptide 1, peptide YY, cholecystokinin or ghrelin) (Figure 1.4, Cummings and Schwartz, 2003). This tightly controlled framework maintains the energy balance under constant vigilance. However, prolonged environmental disturbances, such as exposure to high-fat diet (HFD), may override these homeostatic mechanisms and contribute to obesity and leptin resistance (Morris and Rui, 2009). Diminished transport of leptin to the CNS was thought to be one of the causes of central leptin resistance. This hypothesis was supported by the observation that mice which were peripherally resistant to leptin (due to prolonged HFD feeding), exhibited a robust response to centrally-administered leptin (Van Heek et al., 1997). However, it is also known that while central overexpression of leptin is effective in preventing diet-induced obesity in rats, it fails to improve leptin sensitivity in already obese, leptin-resistant cases. These observations suggest that the lack of response to leptin in obese subjects may be modulated by additional factors (Dube et al., 2002; Wilsey et al., 2003).

One of the first demonstrations that the peripheral nervous system (PNS) was directly involved in fat mobilization was made in 1937 (Beznák and Hasch, 1937). In this study, the site-specific removal of abdominal sympathetic ganglia in cats was shown to be associated with substantial fat accumulation on the sympathectomized side (Beznák and Hasch, 1937). The causality behind this observation was, however, only established decades later. More specifically, in 1963 it was shown that the production of FFAs in AT was increased by the *in vitro* electrical stimulation of dissected nerve fibers (Figure 1.5, Correll, 1963). This experiment supported the hypothesis that neural stimulation leads to lipolysis. Indeed, many *in vitro* studies have provided further evidence suggesting that catecholamines can stimulate lipolysis in adipocytes (Morimoto et al., 1997; Rosen and Spiegelman, 2014; Vaughan, 1967). Nevertheless, the formal validation of this hypothesis *in vivo* has remained elusive.

The molecular identity of AT innervation was established in 1967, when Wirsén and Hamberger demonstrated a dense network of delicate catecholaminergic fibers within BAT (Wirsén and Hamberger, 1967). Two years later, the vasculature-associated adrenergic innervation of WAT was also demonstrated (Daniel and Derry, 1969). However, the neural inputs to WAT were difficult to be distinguished from *en passant* axons with terminals on other cell types, such as those in vasculature (Bartness and Song, 2007; Bartness et al., 2005; Giordano et al., 1996; Youngstrom and Bartness, 1995). Indeed, some reports have suggested that the only innervation of WAT is perivascular, and that white adipocytes themselves are not directly innervated (Giordano et al., 2005).

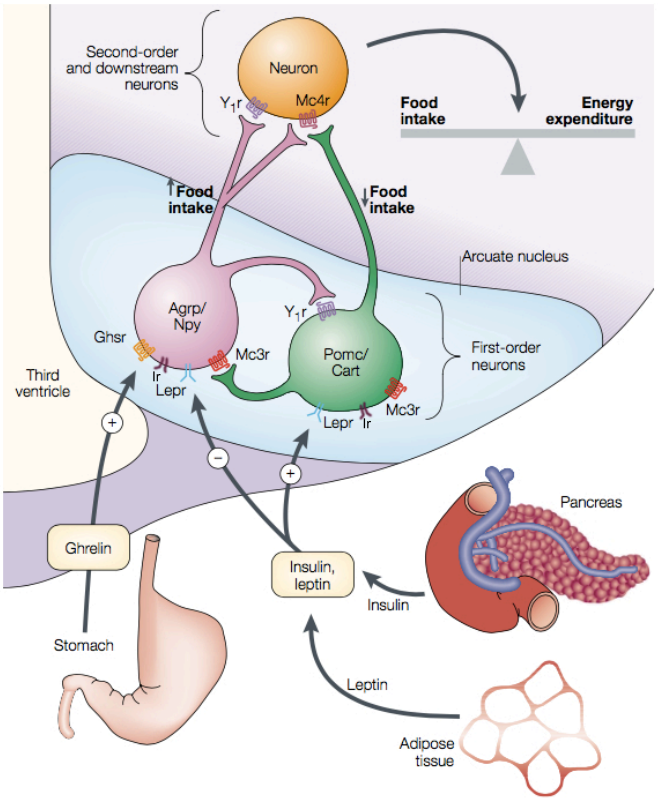

Figure 1.4. Control of energy homeostasis by arcuate nucleus neurons.
There are two sets of neurons in the arcuate nucleus — Agrp/Npy and Pomc/Cart neurons — that are regulated by circulating hormones. Agrp (agouti-related protein) and Npy (neuropeptide Y) are neuropeptides that stimulate food intake and decrease energy expenditure, whereas α-melanocyte stimulating hormone (a post-translational derivative of proopiomelanocortin, Pomc) and Cart (cocaine- and amphetamine-regulated transcript) are neuropeptides that inhibit food intake and increase energy expenditure. Insulin and leptin are hormones that circulate in proportion to body adipose stores; they inhibit Agrp/Npy neurons and stimulate adjacent Pomc/Cart neurons. Lower insulin and leptin levels are therefore predicted to activate Agrp/Npy neurons, while inhibiting Pomc/Cart neurons. Ghrelin is a circulating peptide secreted from the stomach that can activate Agrp/Npy neurons, thereby stimulating food intake; this provides a potential molecular mechanism for integrating long-term energy balance signals with short-term meal pattern signals. Ghsr, growth hormone secretagogue receptor; Lepr, leptin receptor; Ir, insulin receptor; Mc3r/Mc4r, melanocortin 3/4 receptor; Y1r, neuropeptide Y1 receptor. Adapted from Barsh and Schwartz, 2002.

Given the lipolytic effects of catecholamines, the relationship between the activity of the SNS and obesity has been a topic of debate. Genetically obese *ob/ob* mice were reported to have decreased norepinephrine (NE) turnover in BAT when compared to lean mice (Knehans and Romsos, 1982). Ventromedial hypothalamic lesions, which essentially lead to obesity by increasing food intake and downregulating the SNS activity in rats (Vander Tuig et al., 1982), further indicated a negative correlation between the activity of the SNS in AT and obesity. These observations also extended to humans as the NE spillover in AT was shown to be substantially decreased in obese woman (Coppack et al., 1998).

However, one can find in the literature studies claiming the exact opposite. Several reports on human

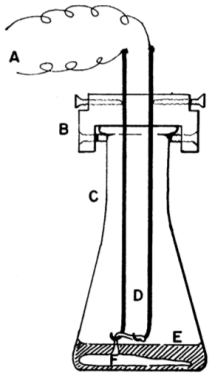

Figure 1.5. Schematic representation of the experiment demonstrating that *in vitro* stimulation of neurons results in increased production of FFAs.

Plastic unit (B) carrying chlorided bipolar silver electrodes (D) mounted on a 25 mL erlenmeyer flask (C), is shown in contact with pedicle containing nerves to isolated adipose tissue (F), immersed in medium (E). Wire leads (A) carry electrical stimulus. Adapted from Correll, 1963.

abdominal obesity have shown increased sympathetic activity in the muscle and kidneys of obese patients (as measured by up-regulated urinary NE excretion) (Grassi et al., 1995, 2004; Troisi et al., 1991). In agreement with these studies, others report the up-regulation of sympathetic activity in obesity-related hypertension (Esler et al., 2006; Lip and Hall, 2007). In this context, the elevated renal sympathetic activation of obese individuals was not only associated with altered arterial pressure but also positively correlated with obesity-linked hypertension (Esler et al., 2006; Lohmeier and Iliescu, 2013; Rumantir et al., 1999; Vaz et al., 1997). Moreover, these effects seemed to be dependent on the sympathetic output to peripheral tissues, as adrenal epinephrine production was not significantly altered between lean and obese individuals (Vaz et al., 1997).

These findings challenge the classic view that the SNS is controlled in an unified manner (Cannon, 1920). On one hand, the decreased levels of NE in the AT of obese individuals suggest a down-regulation of neuronal input in the fat organs. On the other, sympathetic activity is up-regulated in the muscle and kidneys of obese individuals. To solve this conundrum, one can posit that the SNS output to one organ does not reflect the global activity of all outputs (Morrison, 2001). An alternative explanation would be that the SNS is indeed controlled in a whole-body manner, but the transmission of the signal is tissue-dependent. Understanding the exact mechanisms linking SNS activity to obesity remains an area of clear clinical interest.

1.5 BROWN, BEIGE AND WHITE: THE UNITED COLOURS OF FAT.

Thermoregulatory properties of BAT have long been appreciated in rodents, small mammals (Golozoubova et al., 2006) and human infants. From a mechanistic perspective, uncoupling protein-1 (UCP1) is highly expressed in BAT mitochondria and works as a long-chain fatty acid/H+ transporter. Such activity allows it to perform mitochondrial "uncoupling" – that is the production of heat rather than ATP (Fedorenko et al., 2012). Recently, functional BAT has also been detected in human adults (Enerbäck, 2010). Such observation was a serendipitous finding from the routine medical examination of oncological patients. More specifically, it was noted that areas in the supraclavicular paracervical region and along the thoracic chain could take up a glucose tracer. Further studies in healthy human subjects showed that cold exposure up-regulates glucose uptake in the above-mentioned regions nearly 15-fold, confirming their thermogenic capacities (Virtanen et al., 2009). Functional human BAT and the possibility of harnessing its glucose- and lipid-lowering properties have opened entirely new avenues in the study of obesity.

In rodents, cold exposure was known to trigger the appearance of brown-like cells within the WAT, however, for a long time this cell population was either ignored or classified as brown adipocytes (Cousin et al., 1993). Different adipose depots can show a variable abundance of these inducible, brown-like cells. In particular, inguinal and retroperitoneal adipose tissues are characterised by higher numbers of multilocular adipocytes upon cold exposure. On the other hand, much lower numbers of these cells are detected in visceral fat (Rosen and Spiegelman, 2014). These observations correlate with the beneficial metabolic effects of transplanting either inguinal adipose tissue or BAT to visceral AT (Tran and Kahn, 2010). The importance of AT location in organismal homeostasis is further highlighted by the classic observation that increased abdominal adiposity associates with higher predisposition to diabetes and other diseases (Vague, 1956).

A key study from Bruce Spiegelman's lab showed that brown adipocytes are derived from the same progenitors as muscle cells (Myf+ lineage) (Seale et al., 2008). This raised the hypothesis that the brown-like adipocytes within the WAT originated from the same lineage. The hypothesis was only disproved in 2012, when it was shown that brown-like cells within the subcutaneous white depots do not share the same origin as classical brown adipocytes. Instead, these cells derive from the same progenitors as white adipocytes (Wu et al., 2012). Thus, multilocular cells in WAT were defined as beige adipocytes, and the possibility of inducing the thermogenic potential of white fat holds promise for improving the energy balance of obese patients. In this context, some molecules do seem to emerge as clinically-relevant targets. PRDM16, a transcriptional regulator involved in muscle vs. brown fat fate, is one of them (Cohen et al., 2014). PRDM16 expression in adipocytes is crucial to induce the white to beige adipocyte switch, and its ablation leads to an increased propensity to obesity and insulin resistance when mice are challenged with high fat diet (HFD) (Cohen et al., 2014). It remains to be established whether the pharmacological

activation of the PRDM16 in fat can circumvent some of the obesity-related complications in humans.

It has been estimated that BAT thermogenesis accounts for around 5% of the basal metabolic rate in humans. Thus, fully activated BAT could contribute to roughly 4 kg of WAT loss per year (van Marken Lichtenbelt and Schrauwen, 2011; Virtanen et al., 2009). Additionally, since short-term cold exposure was shown to influence the metabolism of triglyceride-rich lipoproteins in mice, stimulating the BAT could also serve as a triglyceride-clearing approach (Bartelt et al., 2011). The aforementioned features of BAT are particularly important from the clinical point of view, as activating BAT or inducing beige adipocytes could not only correct obesity-linked excessive body-weight, but also hyperlipidemia (Bartelt et al., 2011).

1.6 SEEING IS BELIEVING: LOOK AT MY FAT.

Given the central role of the AT in energy balance and nutritional homeostasis, both the quantification of the adipose mass and the description of the anatomical organization of the different fat organs are areas of interest among the research community (Borkan et al., 1982; Hu et al., 2013; Thomas et al., 1998).

Computer tomography (CT) has made it possible to differentiate between subcutaneous and internal fat stores. Although the imaging is done at relatively fast acquisition rates, the exposure to ionising radiation makes this technique less suited to routine measurements, either at the clinical or research levels (Klopfenstein et al., 2012). Magnetic resonance imaging (MRI), on the other hand, does not require the use of radiation and gives a fast and unbiased measurement of AT volume (Thomas et al., 1998). At a macroscopic spatial scale, methods such as MRI or CT are well suited for the measurement of whole-body fat distribution. However, both methods lack the spatial resolution that is required to visualize detailed structures within an organ that is fairly uncharacterized from an anatomical perspective.

The anatomy of the adipose organs has been mostly studied with classical histology methods (requiring serial slicing) or electron microscopy (Cinti, 2014). Both are suitable for analysis at the 2-D scale but require complex, labor-intensive adaptations to provide a 3-D perspective of the organ and its cellular compartments. With the development of confocal microscopy, the optical sectioning of fluorescently labelled specimens into several focal planes became a conventional technique. Furthermore, two-photon imaging has profoundly changed light microscopy by allowing the increase of imaging depth to hundreds of micrometres (Helmchen and Denk, 2005). Nevertheless, none of these methods is suitable for imaging entire tissues or organs. A common procedure to circumvent this issue is one adapted from conventional histology: the mechanical slicing of tissues. Thin sections can be labelled by immunofluorescence and imaged using confocal or two-photon microscopy. This common work-around, however, also has its limitations at the level of 3-D reconstruction. More specifically, high-resolution reconstruction is time-consuming and limited to small volumes of tissue.

Optical Projection Tomography (OPT) further revolutionised the imaging field. OPT is a technique with physical principles similar to X-ray CT/gamma radiation, which uses visible light instead of radiation (Sharpe, 2004). Cleared specimens minimise scattering of the light passing through the tissues. A full series of projections of the whole sample are acquired from multiple angles (typically 800 to 1600), and from this series of projections a stack of axial slices is reconstructed through back-projection reconstruction. The slice reconstruction assumes perfect parallel projection (Quintana and Sharpe, 2011). Unlike most methods currently available, OPT coupled to tissue clearing is suitable for imaging whole-mount samples within a spatial scale in the order of centimetres.

Given the demand for techniques that increase tissue transparency, several tissue and organ clearing

methods have emerged. Optical sectioning of bleached perfusion-fixed mouse brains by hydrogen peroxide and subsequent immunohistochemical staining allowed to detect GFP-labelled neurons (Dodt et al., 2007). Mouse brain sections (60 μm thick) were also successfully rendered transparent by using *Scale*, an urea-based solution for tissue fixation and clearing (Hama et al., 2011). It is important to mention that urea causes partial denaturation and protein loss. Thus, samples after *Scale* treatment are very challenging to handle and susceptible to deformation. This problem was overcome by using *See-DB*, a water-based clearing agent, that, combined with two-photon microscopy, allows the imaging of fixed mouse brains at a millimetre-scale depth (Ke et al., 2013). Although the aforementioned clearing approaches are effective, they are not suitable for detailed molecular phenotyping. To deal with this limitation, the CLARITY platform has been developed. CLARITY chemically transforms biological tissues into a hydrogel-tissue hybrid that allows analysis with both light and macromolecular labels (Tomer et al., 2014). Through whole-body clearing, CLARITY allowed single-cell phenotyping (Yang et al., 2014), at the level of not only brain, but also spinal cord, kidney, heart, and lung. This can be achieved by passive tissue clearing coupled to immunostaining using either Passive Clarity Technique (PACT) or Perfusion-assisted Agent Release in Situ (PARS) method. In the latter method, the vasculature of the animal is used to infuse the hydrogel monomer, the clearing solutions, and the labelling antibodies. However, CLARITY is a resource-intensive technique with associated high costs.

An alternative technique allows the visualization of intact structures within large-size organs without immunohistochemical labelling. This technique is based on a Benzyl Alcohol:Benzyl Benzoate clearing method coupled to OPT. This method is feasible since OPT works with both fluorescent and non-fluorescent contrasts. Clearing is typically performed by dehydration followed by the transferring of the sample to a Benzyl Alcohol: Benzyl Benzoate solution (Sharpe, 2003). This technique has been proven well suited for the imaging of large samples, such as whole embryos and mouse organs (Quintana and Sharpe, 2011). Depending on tissue size and density, the clearing protocol takes from 1 to 2 weeks. Given that some of the aforementioned clearing protocols can take up to 1.5 months (Yang et al., 2014), this reduced preparation time is a significant advantage. To further visualize molecularly-labelled structures within entire organs, Tessier-Lavigne and colleagues developed a method called iDISCO (Renier et al., 2014). iDISCO constitutes a promising and affordable tool for immunolabeling large biological samples within 8 to 18 days (Renier et al., 2014). Multiple antibodies have been validated as compatible with the iDISCO protocol, and the list of tested applications in constantly growing (https://idisco.info/).

In conclusion, recent advances in whole organ imaging techniques provide new opportunities to characterize the AT at an unprecedented degree of detail. Immunolabeling of cleared, intact adipose organs might unravel new aspects of the cellular networks within fat depots.

1.7 INVASION! LOW-GRADE INFLAMMATION OF THE ADIPOSE TISSUE DURING OBESITY.

It was observed, more than twenty years ago, that TNF-α is overexpressed in the adipose organ of obese mice (Hotamisligil et al., 1993). This observation suggested a link between obesity, diabetes, and inflammation. Indeed, increased levels of TNF-α in the AT were also reported to promote insulin resistance through serine phosphorylation of insulin receptor substrate 1 (Hotamisligil et al., 1996). Yet, it took several years to finally associate TNF-α cytokine up-regulation to the accumulation of macrophages in the AT of obese mice (Weisberg et al., 2003). Furthermore, an increasing amount of evidence indicates that besides macrophages, other immune cells such as mast cells, recruited neutrophils, monocytes, and multiple lymphoid cell types also play a role at the onset of obesity (Caspar-Bauguil et al., 2005; Elgazar-Carmon et al., 2008; Kintscher et al., 2008; Liu et al., 2009; Mathis, 2013; Rausch et al., 2008; Rocha et al., 2008; Wu et al., 2007).

AT mast cell numbers were reported to be positively correlated with WAT growth and angiogenesis (Liu et al., 2009). Interestingly, these effects were reversed in mice deficient in a proto-oncogene receptor tyrosine kinase *Kit*. Such mice lacked mast cells and displayed a lower diet-induced body weight gain and improved glucose tolerance (Liu et al., 2009). More recently, hematopoietic *Kit* deficiency has been proposed as the origin of this phenotype. Indeed, a *Kit*-independent $Cpa3^{Cre/+}$ mast-cell-deficient mouse strain was not protected both from diet-induced obesity and insulin resistance (Gutierrez et al., 2015).

The recruitment of neutrophils to the AT has been shown to occur transiently at an early stage of the HFD regimen (3 to 7 days). This observation places neutrophils among the potential initiators of the inflammatory processes in the AT (Elgazar-Carmon et al., 2008). Nevertheless, neutrophils constitute a very small fraction of the AT immune compartment (less than 2% of all immune cells in the visceral AT from obese mouse). Therefore, efforts were shifted to more abundant populations, such as macrophages or T cells (Ferrante, 2013; Mathis, 2013).

At more advanced stages of obesity, macrophages constitute the most abudant immune population in the AT (Kraakman et al., 2014). Murine macrophages are thought to play a central role in the disfunction of the AT in obesity (Mathis, 2013). Furthermore, growing evidence indicates that macrophage cell numbers in the subcutaneous and visceral ATs are higher in overweight than in lean individuals (Cancello et al., 2006; Curat et al., 2004, 2006). The functional significance of these observations has remained largely unexplored.

T-cell infiltration to the AT has been positively correlated with obesity (Rausch et al., 2008; Wu et al., 2007). Since the appearance of CD8+ T cells in the visceral fat has been shown to occur as early as after five weeks of the HFD feeding, it was suggested that their recruitment preceded the accumulation of macrophages (Kintscher et al., 2008). However, more detailed studies are required to understand the

timings and the contribution of each immune cell type to this disease.

Contrasting with the increased abundance of several types of immune cells in the AT of obese mice, it has been observed that the number of T regulatory (Tregs) cells decreases during the progression of obesity (Feuerer et al., 2009). This lower number of Tregs could facilitate macrophage infiltration and the onset of inflammation. Likewise, a group of innate lymphoid cells called adipose type 1 innate lymphoid cells (AT1-ILCs) was also reported to be diminished upon prolonged HFD feeding (Boulenouar et al., 2017). At steady state AT1-ILCs exhibit cytotoxic properties towards AT macrophages (ATMs). Indeed, the increased accumulation of ATMs during the development of obesity is associated with substantially diminished numbers of AT1-ILCs (Boulenouar et al., 2017).

1.8 MACROPHAGES IN FAT: WHERE DO THEY COME FROM?

In 1968, Ralph van Furth and Zanvil Cohn demonstrated that macrophages originate from the pool of circulating bone marrow-derived monocytes (van Furth and Cohn, 1968). Further studies expanded this concept and established the framework for the mononuclear phagocyte system, in which all macrophages originate from blood monocytes (van Furth et al., 1972). Yet, some observations did challenge this view by highlighting tissue-resident macrophage proliferation (Sawyer et al., 1982) and the presence of macrophages in the embryo before the onset of primitive hematopoiesis (Naito et al., 1996). Nevertheless, at that time there were no adequate tools to thoroughly refute the mononuclear phagocyte model. Only later, with the development of fate mapping techniques, it became clear that not all tissue-resident macrophages originate from monocytes (Gautier and Yvan-Charvet, 2014; Gomez Perdiguero et al., 2015; Schulz et al., 2012).

All of the above studies characterized macrophage origin at the steady state, yet they did not address what happens during inflammation. Acute inflammation was previously reported to drive the replacement of tissue-resident phagocytes with monocytes from the circulation (Epelman et al., 2014). In obesity, chronic low-grade inflammation of the AT underlies cellular dysfunction, to which macrophage accumulation is thought to play a central role (Mathis, 2013; Weisberg et al., 2003). Initial attempts to ameliorate some of the consequences of obesity were focused on the reduction of the monocyte recruitment to the AT. The C-C motif chemokine receptor–2 (CCR2) regulates monocyte and macrophage chemotaxis. It plays, therefore, an essential role in macrophage recruitment during obesity (Weisberg et al., 2006). Mice lacking CCR2 were protected from diet-induced obesity and displayed improved insulin sensitivity (Weisberg et al., 2006). Furthermore, depletion of monocyte chemoattractant protein–1 (MCP-1) surpassed insulin resistance and reduced macrophage infiltration to the AT of mice fed with HFD (Kanda et al., 2006). Another line of research showed that clodronate liposome-mediated deletion of macrophages in obese mice improved systemic glucose and insulin maintenance (Feng et al., 2011). Finally, in 2014 Myriam Aouadi and colleagues demonstrated that the local proliferation of macrophages within the AT was considerably up-regulated during obesity (Amano et al., 2014). This result proved that monocyte recruitment, despite substantially contributing to the increased number of ATMs, was not the only factor regulating macrophage balance in obesity.

The origin of the AT-resident macrophages remains vastly unexplored and further studies are necessary to elucidate the origin of these cells. For instance, fate-mapping experiments revealed that tissue-resident macrophages derive from the yolk-sac erythro-myeloid progenitors (Gomez Perdiguero et al., 2015). Is that also the case for the AT macrophages? If so, what happens to that population as obesity progresses?

1.9 INFLAMMATORY PROFILES OF MACROPHAGES IN OBESITY.

AT from lean mice is predominantly populated by M2-like macrophages. These are characterised by the expression of CD11b, F4/80, CD301 and CD206. M2-like macrophages contribute to AT homeostasis and insulin sensitivity (Odegaard et al., 2007; Olefsky and Glass, 2010). In this regard, interleukin (IL)-4 is highly expressed in the AT of lean mice and mediates the alternative activation state of ATMs (Wu et al., 2011). Furthermore, IL-4 stimulates macrophage expression of the peroxisome proliferator-activated receptor-γ (PPAR-γ), a ligand-dependent nuclear receptor involved in fatty acid storage, adipocyte-differentiation and glucose-homeostasis (Huang et al., 1999; Lehmann et al., 1995; Tontonoz et al., 1994). Macrophage-specific disruption of PPAR-γ was shown to blunt the alternative activation of macrophages and contribute to glucose intolerance (Hevener et al., 2007; Odegaard et al., 2007). Such results highlight the importance of lipid metabolism in macrophage activation.

However, AT from obese mice is predominantly populated by M1-like macrophages. These mainly secrete pro-inflammatory factors, such as TNF-α, IL-6, and nitric oxide (NO) (Lumeng et al., 2007a). In this regard, Osborn and Olefsky proposed a model in which M1-like or classical activation of macrophages is triggered by lipids released from adipocytes at the onset of obesity (Osborn and Olefsky, 2012). However, this model has been challenged by evidence suggesting that ATMs buffer lipid excess in a manner independent from classical polarisation (Xu et al., 2013). In this regard, the tissue-specific alterations ATMs are subjected to during obesity is an area in need of clarification. Nevertheless, several lines of evidence support the view that the classical or M1-like activation of macrophages plays a role in the onset of obesity. In addition to the studies described above, it was shown that ATMs from obese mice express CD11c and produce high levels of pro-inflammatory cytokines that contribute to the development of insulin resistance (Patsouris et al., 2008). Moreover, CD11c-positive ATMs were reported as hallmarks of inflammation and insulin resistance in human obesity (Wentworth et al., 2010). Conversely, conditional ablation of CD11c-positive cells reduced local and systemic levels of pro-inflammatory markers and normalised insulin sensitivity in obese mice (Patsouris et al., 2008). Additional insight into this topic has been generated by the study of the c-Jun NH2-terminal kinase 1 (JNK1). JNK1 is a coordinator of inflammatory responses that is activated upon increased serum FFA levels (Jaeschke and Davis, 2007). JNK1 was shown to be up-regulated (both mRNA and protein) in mouse macrophages upon HFD feeding (Han et al., 2013). Macrophage-specific ablation of JNK1 resulted in reduced obesity-linked infiltration of ATMs and protected mice from insulin resistance (Han et al., 2013). These results further highlighted the significance of the macrophage-mediated inflammatory response in the context of obesity.

It is well established that overnutrition triggers inflammatory responses in the AT and also in other metabolic tissues such as muscle or liver (Figure 1.6, Schenk et al., 2008). Indeed, chronic overnutrition

results in AT expansion and increased production of inflammatory molecules such as TNF-alpha, IL-6, transforming growth factor (TGF)- b1 and monocyte chemotactic protein (MCP)-1. Some of these pro-inflammatory molecules are involved in the development of obesity-linked insulin resistance (Fried et al., 1998; Hotamisligil et al., 1993; Perreault and Marette, 2001; Samad et al., 1997; Sartipy and Loskutoff, 2003). Importantly, many of these molecules are mainly produced by the ATMs (Weisberg et al., 2003; Xu et al., 2003). As obesity progresses, the absence of *de novo* angiogenesis in the AT causes hypoxia and affects adipokine production by inducing adipocyte endoplasmic reticulum (ER) stress (Hosogai et al., 2007). In parallel, pro-inflammatory programs are propagated within metabolic tissues and in most cases result in cell-autonomous insulin resistance (Ye, 2009). Furthermore, altered fatty acid metabolism in liver and muscle also contributes to the development of insulin resistance (Sears and Perry, 2015). Given the number of factors involved in the development of obesity-linked insulin resistance, it is difficult to determine to what extent the obesity-associated inflammatory signalling in the ATMs plays a role in the whole-body metabolism. In this context, clodronate liposome-mediated deletion of macrophages was shown to reduce the numbers of ATMs in the visceral fat and improved metabolic profile of obese mice (Feng et al., 2011). Authors attributed this beneficial phenotype to depletion of the ATMs (Feng et al., 2011). However, clodronate liposomes can also access the liver and other metabolically active tissues (Feng et al., 2011; Stienstra et al., 2010).

To date, the most robust study addressing the role of ATMs in whole-body metabolism and insulin resistance, was a gene silencing approach using glucan encapsulated RNAi particles (GeRPs) (Aouadi et al., 2013). GeRPs allow *in vivo* macrophage-specific RNAi delivery and subsequent gene silencing (Aouadi et al., 2009; Tesz et al., 2011). By using this approach to reduce the production of inflammatory molecules (TNF-α or osteopontin) specifically in ATMs, it was shown that glucose tolerance could be systemically improved. This result highlighted a direct connection between insulin resistance and cytokines produced by macrophages in the visceral AT (Aouadi et al., 2013). The application of the same method to reduce the production of the nuclear factor (NF)-ϰB (a master regulator of inflammation) in Kupffer cells (liver macrophages) also resulted in improved glucose sensitivity in genetically obese mice (Tencerova et al., 2015). Collectively, these results highlight the fact that the metabolic deregulation of obese patients results from the disruption of multiple pathways in different organs.

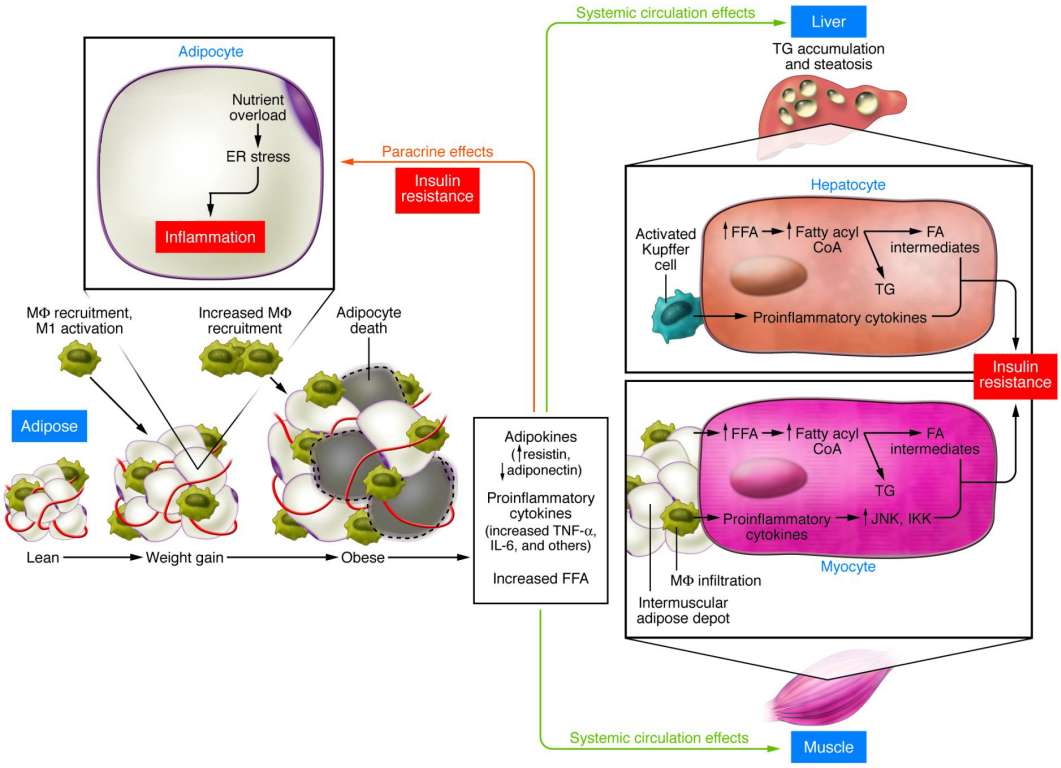

Figure 1.6. Obesity, tissue inflammation, and insulin resistance.

With adipose tissue expansion, total FFA release into the circulation is increased and oxygen delivery to the adipocyte is decreased. The combination of microhypoxia and nutrient excess leads to ER stress within the adipocyte. In parallel, the inflammatory response includes increased production and release of proinflammatory cytokines/chemokines. This results in cell autonomous insulin resistance in adipocyte, liver, exacerbation of the inflammatory state, and systemic insulin resistance. With these inflammation-related changes, alterations in fatty acid metabolism can lead to the accumulation of fatty acid intermediates within the liver and skeletal muscle, which can also lead to insulin resistance. Adapted from Schenk et al., 2008.

1.10 NEURO-IMMUNE INTERACTIONS DURING OBESITY.

Metabolic challenges are known to activate two of the main body sensory interfaces: the nervous and the immune systems. Collectively, these two interfaces perceive, incorporate and respond to environmental stimuli (Veiga-Fernandes and Mucida, 2016). The interplay between the two systems is driven not only by cell-to-cell contact but also by communication molecules such as cytokines, chemokines, neuropeptides or other neurotransmitters (Gabanyi et al., 2016; Ordovas-Montanes et al., 2015). Not surprisingly, the chronic activation of either system poses a clear obstacle to their regulatory role. In the AT, chronic low-grade inflammation leads to macrophage accumulation and obesity (Hotamisligil et al., 1993; Weisberg et al., 2003; Xu et al., 2003). Although the cellular and molecular mechanisms underlying AT inflammation have recently started to be addressed (Lumeng et al., 2007b, 2007a; Shoelson et al., 2006; Suganami et al., 2005), the neuro-immune regulation of the fat organ remains largely unknown.

A mounting body of evidence suggests that obesity is associated to the onset of two different types of inflammatory responses. The first develops in peripheral tissues over weeks of HFD feeding, while the second occurs considerably faster in the CNS. Indeed, it was shown that just one to three days of HFD feeding resulted in the up-regulation of pro-inflammatory markers in the hypothalamic arcuate nucleus (ARH) (Thaler et al., 2012). Of note, neurocircuits located in the ARH area (and their projections to other brain centres) are essential to maintain normal energy homeostasis. In this regard, there are at least two ARH subpopulations involved in the regulation of whole-body energy levels: the anorexigenic Pro-opiomelanocortin (POMC)/cocaine- and amphetamine-regulated transcript neurons, and the orexigenic neuropeptide Y/agouti-related peptide neurons (Aponte et al., 2011; Schwartz et al., 2000; Zhan et al., 2013). The former are leptin-excited, the latter leptin-inhibited.

Prolonged exposure to HFD results in elevated hypothalamic autophagy, which is a common readout for neuronal stress/injury (Chu, 2006; Thaler et al., 2012; Wong and Cuervo, 2010). This response is predominantly localized to the POMC neurons, which are responsible for orchestrating feeding behaviors and stimulating thermogenesis in BAT (Fenselau et al., 2017). In this context, the ablation of the POMC neurons was previously shown to cause hyperphagia and obesity in mice (Gropp et al., 2005). Therefore, HFD-driven injury in POMC neurons could explain the increased energy intake observed during diet-induced obesity (Lin et al., 2000). Furthermore, this could also explain the lack of leptin action on this neuronal population after prolonged HFD feeding.

Since obesity is known to up-regulate several pro-inflammatory molecules in the ARH, it was hypothesized that inflammation could be involved in the disruption of central energy balance and, ultimately, lead to leptin-resistance. In this context, microglia are important mediators of the hypothalamic inflammation observed during diet-induced obesity. Hypothalamic microglia were shown to act as sensors of saturated fat and orchestrators of local inflammatory responses (Valdearcos et al., 2014). Early inflammatory state and accumulation of microglia are neuroprotective (Graeber, 2010; Paolicelli et al., 2011). However,

chronic exposure to HFD sustains increased numbers of ARH microglia and their pro-inflammatory activation (Gao et al., 2014). Consistent with this, microglia-targeted disruption of a transcription factor that mediates pro-inflammatory responses, namely NF-κB, reduced accumulation of the ARH microglia, lowered food intake and body weight of mice fed HFD (Valdearcos et al., 2017). The aforementioned results validate that a pro-inflammatory activation of microglia contributes to diet-induced obesity.

Collectively, these observations bring an essential question of whether the microglial activation during HFD is causal or secondary to the hypothalamic neuronal injury and what are the exact timings of these events. More in-depth understanding of the neuro-immune interactions and how they alter during obesity may result in more effective treatments to mitigate the obesity epidemic and circumvent or ameliorate central leptin resistance.

In the next chapters I will address how the AT is directly regulated from both a neuronal and immunological perspective.

REFERENCES

Altarejos, J.Y., and Montminy, M. (2011). CREB and the CRTC co-activators: sensors for hormonal and metabolic signals. Nat. Rev. Mol. Cell Biol. 12, 141.

Amano, S.U., Cohen, J.L., Vangala, P., Tencerova, M., Nicoloro, S.M., Yawe, J.C., Shen, Y., Czech, M.P., and Aouadi, M. (2014). Local Proliferation of Macrophages Contributes to Obesity-Associated Adipose Tissue Inflammation. Cell Metab. 19, 162–171.

Aouadi, M., Tesz, G.J., Nicoloro, S.M., Wang, M., Chouinard, M., Soto, E., Ostroff, G.R., and Czech, M.P. (2009). Orally delivered siRNA targeting macrophage Map4k4 suppresses systemic inflammation. Nature 458, 1180.

Aouadi, M., Tencerova, M., Vangala, P., Yawe, J.C., Nicoloro, S.M., Amano, S.U., Cohen, J.L., and Czech, M.P. (2013). Gene silencing in adipose tissue macrophages regulates whole-body metabolism in obese mice. Proc. Natl. Acad. Sci. 110, 8278–8283.

Aponte, Y., Atasoy, D., and Sternson, S.M. (2011). AGRP neurons are sufficient to orchestrate feeding behavior rapidly and without training. Nat. Neurosci. 14, 351.

Assimacopoulos-Jeannet, F., and Jeanrenaud, B. (1976). The hormonal and metabolic basis of experimental obesity. Clin. Endocrinol. Metab. 5, 337–365.

Awad, S., Constantin-Teodosiu, D., Macdonald, I.A., and Lobo, D.N. (2009). Short-term starvation and mitochondrial dysfunction - a possible mechanism leading to postoperative insulin resistance. Clin. Nutr. Edinb. Scotl. 28, 497–509.

Bahary, N., Leibel, R.L., Joseph, L., and Friedman, J.M. (1990). Molecular mapping of the mouse db mutation. Proc. Natl. Acad. Sci. U. S. A. 87, 8642–8646.

Barsh, G.S., and Schwartz, M.W. (2002). Genetic approaches to studying energy balance: perception and integration. Nat. Rev. Genet. 3, 589–600.

Bartelt, A., Bruns, O.T., Reimer, R., Hohenberg, H., Ittrich, H., Peldschus, K., Kaul, M.G., Tromsdorf, U.I., Weller, H., Waurisch, C., et al. (2011). Brown adipose tissue activity controls triglyceride clearance. Nat. Med. 17, 200–205.

Bartness, T.J., and Song, C.K. (2007). Thematic review series: adipocyte biology. Sympathetic and sensory innervation of white adipose tissue. J. Lipid Res. 48, 1655–1672.

Bartness, T.J., Kay Song, C., Shi, H., Bowers, R.R., and Foster, M.T. (2005). Brain-adipose tissue cross talk.

Proc. Nutr. Soc. 64, 53–64.

Beznák, A.B.L., and Hasch, Z. (1937). The Effect of Sympathectomy on the Fatty Deposit in Connective Tissue. Q. J. Exp. Physiol. 27, 1–15.

Blad, C.C., Tang, C., and Offermanns, S. (2012). G protein-coupled receptors for energy metabolites as new therapeutic targets. Nat. Rev. Drug Discov. 11, nrd3777.

Borkan, G.A., Gerzof, S.G., Robbins, A.H., Hults, D.E., Silbert, C.K., and Silbert, J.E. (1982). Assessment of abdominal fat content by computed tomography. Am. J. Clin. Nutr. 36, 172–177.

Boulenouar, S., Michelet, X., Duquette, D., Alvarez, D., Hogan, A.E., Dold, C., O'Connor, D., Stutte, S., Tavakkoli, A., Winters, D., et al. (2017). Adipose Type One Innate Lymphoid Cells Regulate Macrophage Homeostasis through Targeted Cytotoxicity. Immunity 46, 273–286.

Bray, G.A. (2011). A Guide to Obesity and the Metabolic Syndrome: Origins and Treatment (CRC Press).

Brobeck, J.R., Tepperman, J., and Long, C.N.H. (1943). Experimental Hypothalamic Hyperphagia in the Albino Rat. Yale J. Biol. Med. 15, 831–853.

Cancello, R., Tordjman, J., Poitou, C., Guilhem, G., Bouillot, J.L., Hugol, D., Coussieu, C., Basdevant, A., Bar Hen, A., Bedossa, P., et al. (2006). Increased infiltration of macrophages in omental adipose tissue is associated with marked hepatic lesions in morbid human obesity. Diabetes 55, 1554–1561.

Cannon, W.B. (1920). Bodily Changes In Pain Hunger Fear And Rage (D.Appleton And Company.).

Cannon, B., and Nedergaard, J. (2004). Brown adipose tissue: function and physiological significance. Physiol. Rev. 84, 277–359.

Caro, J.F., Kolaczynski, J.W., Nyce, M.R., Ohannesian, J.P., Opentanova, I., Goldman, W.H., Lynn, R.B., Zhang, P.L., Sinha, M.K., and Considine, R.V. (1996). Decreased cerebrospinal-fluid/serum leptin ratio in obesity: a possible mechanism for leptin resistance. Lancet Lond. Engl. 348, 159–161.

Caspar-Bauguil, S., Cousin, B., Galinier, A., Segafredo, C., Nibbelink, M., André, M., Casteilla, L., and Pénicaud, L. (2005). Adipose tissues as an ancestral immune organ: site-specific change in obesity. FEBS Lett. 579, 3487–3492.

Chernick, S.S., Spooner, P.M., Garrison, M.M., and Scow, R.O. (1986). Effect of epinephrine and other lipolytic agents on intracellular lipolysis and lipoprotein lipase activity in 3T3-L1 adipocytes. J. Lipid Res. 27, 286–294.

Chu, C.T. (2006). Autophagic Stress in Neuronal Injury and Disease. J. Neuropathol. Exp. Neurol. 65, 423–432.

Cinti, P.S. (2014). Anatomy of the adipose organ. Eat. Weight Disord. - Stud. Anorex. Bulim. Obes. 5, 132–142.

Cohen, P., Levy, J.D., Zhang, Y., Frontini, A., Kolodin, D.P., Svensson, K.J., Lo, J.C., Zeng, X., Ye, L., Khandekar, M.J., et al. (2014). Ablation of PRDM16 and Beige Adipose Causes Metabolic Dysfunction and a Subcutaneous to Visceral Fat Switch. Cell 156, 304–316.

Coleman, D.L. (1973). Effects of parabiosis of obese with diabetes and normal mice. Diabetologia 9, 294–298.

Coleman, D.L., and Hummel, K.P. (1969). Effects of parabiosis of normal with genetically diabetic mice. Am. J. Physiol. 217, 1298–1304.

Coppack, S.W., Horowitz, J.F., Paramore, D.S., Cryer, P.E., Royal, H.D., and Klein, S. (1998). Whole body, adipose tissue, and forearm norepinephrine kinetics in lean and obese women. Am. J. Physiol. 275, E830-834.

Coppari, R., and Bjørbæk, C. (2012). Leptin revisited: its mechanism of action and potential for treating diabetes. Nat. Rev. Drug Discov. 11, 692–708.

Correll, J.W. (1963). Adipose Tissue: Ability to Respond to Nerve Stimulation in vitro. Science 140, 387–388.

Cousin, B., Casteilla, L., Dani, C., Muzzin, P., Revelli, J.P., and Penicaud, L. (1993). Adipose tissues from various anatomical sites are characterized by different patterns of gene expression and regulation. Biochem. J. 292 (Pt 3), 873–876.

Cummings, D.E., and Schwartz, M.W. (2003). Genetics and pathophysiology of human obesity. Annu. Rev. Med. 54, 453–471.

Curat, C.A., Miranville, A., Sengenès, C., Diehl, M., Tonus, C., Busse, R., and Bouloumié, A. (2004). From blood monocytes to adipose tissue-resident macrophages: induction of diapedesis by human mature adipocytes. Diabetes 53, 1285–1292.

Curat, C.A., Wegner, V., Sengenès, C., Miranville, A., Tonus, C., Busse, R., and Bouloumié, A. (2006). Macrophages in human visceral adipose tissue: increased accumulation in obesity and a source of resistin and visfatin. Diabetologia 49, 744–747.

Daniel, H., and Derry, D.M. (1969). Criteria for differentiation of brown and white fat in the rat. Can. J. Physiol. Pharmacol. 47, 941–945.

Dodt, H.-U., Leischner, U., Schierloh, A., Jährling, N., Mauch, C.P., Deininger, K., Deussing, J.M., Eder, M., Zieglgänsberger, W., and Becker, K. (2007). Ultramicroscopy: three-dimensional visualization of neuronal networks in the whole mouse brain. Nat. Methods 4, 331–336.

Dube, M.G., Beretta, E., Dhillon, H., Ueno, N., Kalra, P.S., and Kalra, S.P. (2002). Central leptin gene therapy blocks high-fat diet-induced weight gain, hyperleptinemia, and hyperinsulinemia: increase in serum ghrelin levels. Diabetes 51, 1729–1736.

Elgazar-Carmon, V., Rudich, A., Hadad, N., and Levy, R. (2008). Neutrophils transiently infiltrate intra-abdominal fat early in the course of high-fat feeding. J. Lipid Res. 49, 1894–1903.

Elia, M., Stubbs, R.J., and Henry, C.J. (1999). Differences in fat, carbohydrate, and protein metabolism between lean and obese subjects undergoing total starvation. Obes. Res. 7, 597–604.

Enerbäck, S. (2010). Human Brown Adipose Tissue. Cell Metab. 11, 248–252.

Epelman, S., Lavine, K.J., Beaudin, A.E., Sojka, D.K., Carrero, J.A., Calderon, B., Brija, T., Gautier, E.L., Ivanov, S., Satpathy, A.T., et al. (2014). Embryonic and adult-derived resident cardiac macrophages are maintained through distinct mechanisms at steady state and during inflammation. Immunity 40, 91–104.

Esler, M., Straznicky, N., Eikelis, N., Masuo, K., Lambert, G., and Lambert, E. (2006). Mechanisms of sympathetic activation in obesity-related hypertension. Hypertens. Dallas Tex 1979 48, 787–796.

Farooqi, I.S., Jebb, S.A., Langmack, G., Lawrence, E., Cheetham, C.H., Prentice, A.M., Hughes, I.A., McCamish, M.A., and O'Rahilly, S. (1999). Effects of recombinant leptin therapy in a child with congenital leptin deficiency. N. Engl. J. Med. 341, 879–884.

Fedorenko, A., Lishko, P.V., and Kirichok, Y. (2012). Mechanism of Fatty-Acid-Dependent UCP1 Uncoupling in Brown Fat Mitochondria. Cell 151, 400–413.

Feng, B., Jiao, P., Nie, Y., Kim, T., Jun, D., Rooijen, N. van, Yang, Z., and Xu, H. (2011). Clodronate Liposomes Improve Metabolic Profile and Reduce Visceral Adipose Macrophage Content in Diet-Induced Obese Mice. PLOS ONE 6, e24358.

Fenselau, H., Campbell, J.N., Verstegen, A.M.J., Madara, J.C., Xu, J., Shah, B.P., Resch, J.M., Yang, Z., Mandelblat-Cerf, Y., Livneh, Y., et al. (2017). A rapidly acting glutamatergic ARC-PVH satiety circuit postsynaptically regulated by α-MSH. Nat. Neurosci. 20, 42.

Ferrante, A.W. (2013). The Immune Cells in Adipose Tissue. Diabetes Obes. Metab. 15, 34–38.

Feuerer, M., Herrero, L., Cipolletta, D., Naaz, A., Wong, J., Nayer, A., Lee, J., Goldfine, A.B., Benoist, C., Shoelson, S., et al. (2009). Lean, but not obese, fat is enriched for a unique population of regulatory T cells that affect metabolic parameters. Nat. Med. 15, 930.

Fried, S.K., Bunkin, D.A., and Greenberg, A.S. (1998). Omental and subcutaneous adipose tissues of obese

subjects release interleukin-6: depot difference and regulation by glucocorticoid. J. Clin. Endocrinol. Metab. 83, 847–850.

Friedman, J.M. (2003). A War on Obesity, Not the Obese. Science 299, 856–858.

Friedman, J.M. (2004). Modern science versus the stigma of obesity. Nat. Med. 10, 563–569.

Friedman, J.M., and Halaas, J.L. (1998). Leptin and the regulation of body weight in mammals. Nature 395, 763–770.

Froesch, E.R. (1967). The physiology and pharmacology of adipose tissue lipolysis: Its inhibition and implications for the treatment of diabetesPhysiologie et Pharmacologie de la lipolyse du tissu adipeux: son inhibition et ses implications dans le traitement du diabètePhysiologie und Pharmakologie der Lipolyse des Fettgewebes: Ihre Hemmung und Bedeutung bei der Behandlung des Diabetes mellitus. Diabetologia 3, 475–487.

van Furth, R., and Cohn, Z.A. (1968). THE ORIGIN AND KINETICS OF MONONUCLEAR PHAGOCYTES. J. Exp. Med. 128, 415–435.

van Furth, R., Cohn, Z.A., Hirsch, J.G., Humphrey, J.H., Spector, W.G., and Langevoort, H.L. (1972). The mononuclear phagocyte system: a new classification of macrophages, monocytes, and their precursor cells. Bull. World Health Organ. 46, 845–852.

Gabanyi, I., Muller, P.A., Feighery, L., Oliveira, T.Y., Costa-Pinto, F.A., and Mucida, D. (2016). Neuro-immune Interactions Drive Tissue Programming in Intestinal Macrophages. Cell 164, 378–391.

Gao, Y., Ottaway, N., Schriever, S.C., Legutko, B., García-Cáceres, C., de la Fuente, E., Mergen, C., Bour, S., Thaler, J.P., Seeley, R.J., et al. (2014). Hormones and diet, but not body weight, control hypothalamic microglial activity. Glia 62, 17–25.

Gautier, E.L., and Yvan-Charvet, L. (2014). Understanding macrophage diversity at the ontogenic and transcriptomic levels. Immunol. Rev. 262, 85–95.

Ghosh, S., and Bouchard, C. (2017). Convergence between biological, behavioural and genetic determinants of obesity. Nat. Rev. Genet. nrg.2017.72.

Giordano, A., Morroni, M., Santone, G., Marchesi, G.F., and Cinti, S. (1996). Tyrosine hydroxylase, neuropeptide Y, substance P, calcitonin gene-related peptide and vasoactive intestinal peptide in nerves of rat periovarian adipose tissue: an immunohistochemical and ultrastructural investigation. J. Neurocytol. 25, 125–136.

Giordano, A., Frontini, A., Murano, I., Tonello, C., Marino, M.A., Carruba, M.O., Nisoli, E., and Cinti, S. (2005). Regional-dependent increase of sympathetic innervation in rat white adipose tissue during prolonged fasting. J. Histochem. Cytochem. Off. J. Histochem. Soc. 53, 679–687.

Golozoubova, V., Cannon, B., and Nedergaard, J. (2006). UCP1 is essential for adaptive adrenergic nonshivering thermogenesis. Am. J. Physiol. Endocrinol. Metab. 291, E350-357.

Gomez Perdiguero, E., Klapproth, K., Schulz, C., Busch, K., Azzoni, E., Crozet, L., Garner, H., Trouillet, C., de Bruijn, M.F., Geissmann, F., et al. (2015). Tissue-resident macrophages originate from yolk-sac-derived erythro-myeloid progenitors. Nature 518, 547–551.

Graeber, M.B. (2010). Changing face of microglia. Science 330, 783–788.

Grassi, G., Seravalle, G., Cattaneo, B.M., Bolla, G.B., Lanfranchi, A., Colombo, M., Giannattasio, C., Brunani, A., Cavagnini, F., and Mancia, G. (1995). Sympathetic activation in obese normotensive subjects. Hypertens. Dallas Tex 1979 25, 560–563.

Grassi, G., Dell'Oro, R., Facchini, A., Quarti Trevano, F., Bolla, G.B., and Mancia, G. (2004). Effect of central and peripheral body fat distribution on sympathetic and baroreflex function in obese normotensives. J. Hypertens. 22, 2363–2369.

Gropp, E., Shanabrough, M., Borok, E., Xu, A.W., Janoschek, R., Buch, T., Plum, L., Balthasar, N., Hampel, B., Waisman, A., et al. (2005). Agouti-related peptide–expressing neurons are mandatory for feeding. Nat. Neurosci. 8, 1289.

Gutierrez, D.A., Muralidhar, S., Feyerabend, T.B., Herzig, S., and Rodewald, H.-R. (2015). Hematopoietic Kit Deficiency, rather than Lack of Mast Cells, Protects Mice from Obesity and Insulin Resistance. Cell Metab. 21, 678–691.

Haemmerle, G., Zimmermann, R., Strauss, J.G., Kratky, D., Riederer, M., Knipping, G., and Zechner, R. (2002). Hormone-sensitive lipase deficiency in mice changes the plasma lipid profile by affecting the tissue-specific expression pattern of lipoprotein lipase in adipose tissue and muscle. J. Biol. Chem. 277, 12946–12952.

Halaas, J.L., Gajiwala, K.S., Maffei, M., Cohen, S.L., Chait, B.T., Rabinowitz, D., Lallone, R.L., Burley, S.K., and Friedman, J.M. (1995). Weight-reducing effects of the plasma protein encoded by the obese gene. Science 269, 543–546.

Halaas, J.L., Boozer, C., Blair-West, J., Fidahusein, N., Denton, D.A., and Friedman, J.M. (1997). Physiological response to long-term peripheral and central leptin infusion in lean and obese mice. Proc. Natl. Acad. Sci. U. S. A. 94, 8878–8883.

Hama, H., Kurokawa, H., Kawano, H., Ando, R., Shimogori, T., Noda, H., Fukami, K., Sakaue-Sawano, A., and Miyawaki, A. (2011). Scale: a chemical approach for fluorescence imaging and reconstruction of transparent mouse brain. Nat. Neurosci. 14, 1481–1488.

Han, M.S., Jung, D.Y., Morel, C., Lakhani, S.A., Kim, J.K., Flavell, R.A., and Davis, R.J. (2013). JNK expression by macrophages promotes obesity-induced insulin resistance and inflammation. Science 339, 218–222.

Haslam, D.W., and James, W.P.T. (2005). Obesity. The Lancet 366, 1197–1209.

Helmchen, F., and Denk, W. (2005). Deep tissue two-photon microscopy. Nat. Methods 2, 932–940.

Hetherington, A.W., and Ranson, S.W. (1940). Hypothalamic lesions and adiposity in the rat. Anat. Rec. 78, 149–172.

Hevener, A.L., Olefsky, J.M., Reichart, D., Nguyen, M.T.A., Bandyopadyhay, G., Leung, H.-Y., Watt, M.J., Benner, C., Febbraio, M.A., Nguyen, A.-K., et al. (2007). Macrophage PPAR gamma is required for normal skeletal muscle and hepatic insulin sensitivity and full antidiabetic effects of thiazolidinediones. J. Clin. Invest. 117, 1658–1669.

Heymsfield, S.B., Greenberg, A.S., Fujioka, K., Dixon, R.M., Kushner, R., Hunt, T., Lubina, J.A., Patane, J., Self, B., Hunt, P., et al. (1999). Recombinant leptin for weight loss in obese and lean adults: a randomized, controlled, dose-escalation trial. JAMA 282, 1568–1575.

Hosogai, N., Fukuhara, A., Oshima, K., Miyata, Y., Tanaka, S., Segawa, K., Furukawa, S., Tochino, Y., Komuro, R., Matsuda, M., et al. (2007). Adipose tissue hypoxia in obesity and its impact on adipocytokine dysregulation. Diabetes 56, 901–911.

Hotamisligil, G.S., Shargill, N.S., and Spiegelman, B.M. (1993). Adipose expression of tumor necrosis factor-alpha: direct role in obesity-linked insulin resistance. Science 259, 87–91.

Hotamisligil, G.S., Peraldi, P., Budavari, A., Ellis, R., White, M.F., and Spiegelman, B.M. (1996). IRS-1-mediated inhibition of insulin receptor tyrosine kinase activity in TNF-alpha- and obesity-induced insulin resistance. Science 271, 665–668.

Hruby, A., and Hu, F.B. (2015). The Epidemiology of Obesity: A Big Picture. PharmacoEconomics 33, 673–689.

Hu, H.H., Perkins, T.G., Chia, J.M., and Gilsanz, V. (2013). Characterization of Human Brown Adipose Tissue by Chemical-Shift Water-Fat MRI. AJR Am. J. Roentgenol. 200, 177–183.

Huang, J.T., Welch, J.S., Ricote, M., Binder, C.J., Willson, T.M., Kelly, C., Witztum, J.L., Funk, C.D., Conrad, D., and Glass, C.K. (1999). Interleukin-4-dependent production of PPAR-gamma ligands in macrophages by 12/15-lipoxygenase. Nature 400, 378–382.

Hummel, K.P., Dickie, M.M., and Coleman, D.L. (1966). Diabetes, a New Mutafton in the Mouse. Science 153, 1127–1128.

Ingalls, A.M., Dickie, M.M., and Snell, G.D. (1950). Obese, a new mutation in the house mouse. J. Hered. 41, 317–318.

Jaeschke, A., and Davis, R.J. (2007). Metabolic stress signaling mediated by mixed-lineage kinases. Mol. Cell 27, 498–508.

Jung, C.H., and Kim, M.-S. (2013). Molecular mechanisms of central leptin resistance in obesity. Arch. Pharm. Res. 36, 201–207.

Kanda, H., Tateya, S., Tamori, Y., Kotani, K., Hiasa, K., Kitazawa, R., Kitazawa, S., Miyachi, H., Maeda, S., Egashira, K., et al. (2006). MCP-1 contributes to macrophage infiltration into adipose tissue, insulin resistance, and hepatic steatosis in obesity. J. Clin. Invest. 116, 1494–1505.

Ke, M.-T., Fujimoto, S., and Imai, T. (2013). SeeDB: a simple and morphology-preserving optical clearing agent for neuronal circuit reconstruction. Nat. Neurosci. 16, 1154–1161.

Kintscher, U., Hartge, M., Hess, K., Foryst-Ludwig, A., Clemenz, M., Wabitsch, M., Fischer-Posovszky, P., Barth, T.F.E., Dragun, D., Skurk, T., et al. (2008). T-lymphocyte infiltration in visceral adipose tissue: a primary event in adipose tissue inflammation and the development of obesity-mediated insulin resistance. Arterioscler. Thromb. Vasc. Biol. 28, 1304–1310.

Klopfenstein, B.J., Kim, M.S., Krisky, C.M., Szumowski, J., Rooney, W.D., and Purnell, J.Q. (2012). Comparison of 3 T MRI and CT for the measurement of visceral and subcutaneous adipose tissue in humans. Br. J. Radiol. 85, e826–e830.

Knehans, A.W., and Romsos, D.R. (1982). Reduced norepinephrine turnover in brown adipose tissue of ob/ob mice. Am. J. Physiol. - Endocrinol. Metab. 242, E253–E261.

Koffler, M., and Kisch, E.S. (1996). Starvation diet and very-low-calorie diets may induce insulin resistance and overt diabetes mellitus. J. Diabetes Complications 10, 109–112.

Kraakman, M.J., Murphy, A.J., Jandeleit-Dahm, K., and Kammoun, H.L. (2014). Macrophage Polarization in Obesity and Type 2 Diabetes: Weighing Down Our Understanding of Macrophage Function? Front. Immunol. 5.

Large, V., Reynisdottir, S., Langin, D., Fredby, K., Klannemark, M., Holm, C., and Arner, P. (1999). Decreased expression and function of adipocyte hormone-sensitive lipase in subcutaneous fat cells of obese subjects. J. Lipid Res. 40, 2059–2066.

Lehmann, J.M., Moore, L.B., Smith-Oliver, T.A., Wilkison, W.O., Willson, T.M., and Kliewer, S.A. (1995). An antidiabetic thiazolidinedione is a high affinity ligand for peroxisome proliferator-activated receptor gamma

(PPAR gamma). J. Biol. Chem. 270, 12953–12956.

Lin, S., Thomas, T.C., Storlien, L.H., and Huang, X.F. (2000). Development of high fat diet-induced obesity and leptin resistance in C57Bl/6J mice. Int. J. Obes. 24, 639.

Lip, G.Y.H., and Hall, J.E. (2007). Comprehensive Hypertension E-Book (Elsevier Health Sciences).

Liu, J., Divoux, A., Sun, J., Zhang, J., Clément, K., Glickman, J.N., Sukhova, G.K., Wolters, P.J., Du, J., Gorgun, C.Z., et al. (2009). Genetic deficiency and pharmacological stabilization of mast cells reduce diet-induced obesity and diabetes in mice. Nat. Med. 15, 940–945.

Lohmeier, T.E., and Iliescu, R. (2013). The Sympathetic Nervous System in Obesity Hypertension. Curr. Hypertens. Rep. 15, 409–416.

Lumeng, C.N., Bodzin, J.L., and Saltiel, A.R. (2007a). Obesity induces a phenotypic switch in adipose tissue macrophage polarization. J. Clin. Invest. 117, 175–184.

Lumeng, C.N., DeYoung, S.M., Bodzin, J.L., and Saltiel, A.R. (2007b). Increased Inflammatory Properties of Adipose Tissue Macrophages Recruited During Diet-Induced Obesity. Diabetes 56, 16–23.

van Marken Lichtenbelt, W.D., and Schrauwen, P. (2011). Implications of nonshivering thermogenesis for energy balance regulation in humans. Am. J. Physiol. Regul. Integr. Comp. Physiol. 301, R285-296.

Mathis, D. (2013). Immunological Goings-on in Visceral Adipose Tissue. Cell Metab. 17, 851–859.

Montez, J.M., Soukas, A., Asilmaz, E., Fayzikhodjaeva, G., Fantuzzi, G., and Friedman, J.M. (2005). Acute leptin deficiency, leptin resistance, and the physiologic response to leptin withdrawal. Proc. Natl. Acad. Sci. U. S. A. 102, 2537–2542.

Morimoto, C., Tsujita, T., and Okuda, H. (1997). Norepinephrine-induced lipolysis in rat fat cells from visceral and subcutaneous sites: role of hormone-sensitive lipase and lipid droplets. J. Lipid Res. 38, 132–138.

Morris, D.L., and Rui, L. (2009). Recent advances in understanding leptin signaling and leptin resistance. Am. J. Physiol. Endocrinol. Metab. 297, E1247-1259.

Morrison, S.F. (2001). Differential control of sympathetic outflow. Am. J. Physiol. Regul. Integr. Comp. Physiol. 281, R683-698.

Naito, M., Umeda, S., Yamamoto, T., Moriyama, H., Umezu, H., Hasegawa, G., Usuda, H., Shultz, L.D., and Takahashi, K. (1996). Development, differentiation, and phenotypic heterogeneity of murine tissue macrophages. J. Leukoc. Biol. 59, 133–138.

Odegaard, J.I., Ricardo-Gonzalez, R.R., Goforth, M.H., Morel, C.R., Subramanian, V., Mukundan, L., Red Eagle, A., Vats, D., Brombacher, F., Ferrante, A.W., et al. (2007). Macrophage-specific PPARgamma controls alternative activation and improves insulin resistance. Nature 447, 1116–1120.

Olefsky, J.M., and Glass, C.K. (2010). Macrophages, inflammation, and insulin resistance. Annu. Rev. Physiol. 72, 219–246.

Ordovas-Montanes, J., Rakoff-Nahoum, S., Huang, S., Riol-Blanco, L., Barreiro, O., and Andrian, U.H. von (2015). The Regulation of Immunological Processes by Peripheral Neurons in Homeostasis and Disease. Trends Immunol. 36, 578–604.

Osborn, O., and Olefsky, J.M. (2012). The cellular and signaling networks linking the immune system and metabolism in disease. Nat. Med. 18, 363–374.

Ottaviani, E., Malagoli, D., and Franceschi, C. (2011). The evolution of the adipose tissue: A neglected enigma. Gen. Comp. Endocrinol. 174, 1–4.

Paolicelli, R.C., Bolasco, G., Pagani, F., Maggi, L., Scianni, M., Panzanelli, P., Giustetto, M., Ferreira, T.A., Guiducci, E., Dumas, L., et al. (2011). Synaptic pruning by microglia is necessary for normal brain development. Science 333, 1456–1458.

Patsouris, D., Li, P.-P., Thapar, D., Chapman, J., Olefsky, J.M., and Neels, J.G. (2008). Ablation of CD11c-positive cells normalizes insulin sensitivity in obese insulin resistant animals. Cell Metab. 8, 301–309.

Perreault, M., and Marette, A. (2001). Targeted disruption of inducible nitric oxide synthase protects against obesity-linked insulin resistance in muscle. Nat. Med. 7, 1138–1143.

Quintana, L., and Sharpe, J. (2011). Optical Projection Tomography of Vertebrate Embryo Development. Cold Spring Harb. Protoc. 2011, pdb.top116.

Ramírez, S., and Claret, M. (2015). Hypothalamic ER stress: A bridge between leptin resistance and obesity. FEBS Lett. 589, 1678–1687.

Rausch, M.E., Weisberg, S., Vardhana, P., and Tortoriello, D.V. (2008). Obesity in C57BL/6J mice is characterized by adipose tissue hypoxia and cytotoxic T-cell infiltration. Int. J. Obes. 2005 32, 451–463.

Renier, N., Wu, Z., Simon, D.J., Yang, J., Ariel, P., and Tessier-Lavigne, M. (2014). iDISCO: A Simple, Rapid Method to Immunolabel Large Tissue Samples for Volume Imaging. Cell 159, 896–910.

Reynisdottir, S., Langin, D., Carlström, K., Holm, C., Rössner, S., and Arner, P. (1995). Effects of weight reduction on the regulation of lipolysis in adipocytes of women with upper-body obesity. Clin. Sci. Lond. Engl. 1979 89, 421–429.

Rezai-Zadeh, K., and Münzberg, H. (2013). Integration of sensory information via central thermoregulatory leptin targets. Physiol. Behav. 121, 49–55.

Rocha, V.Z., Folco, E.J., Sukhova, G., Shimizu, K., Gotsman, I., Vernon, A.H., and Libby, P. (2008). Interferon-gamma, a Th1 cytokine, regulates fat inflammation: a role for adaptive immunity in obesity. Circ. Res. 103, 467–476.

Rosen, E.D., and Spiegelman, B.M. (2014). What We Talk About When We Talk About Fat. Cell 156, 20–44.

Rumantir, M.S., Vaz, M., Jennings, G.L., Collier, G., Kaye, D.M., Seals, D.R., Wiesner, G.H., Brunner-La Rocca, H.P., and Esler, M.D. (1999). Neural mechanisms in human obesity-related hypertension. J. Hypertens. 17, 1125–1133.

Ryden, M., Dicker, A., van Harmelen, V., Hauner, H., Brunnberg, M., Perbeck, L., Lonnqvist, F., and Arner, P. (2002). Mapping of early signaling events in tumor necrosis factor-alpha -mediated lipolysis in human fat cells. J. Biol. Chem. 277, 1085–1091.

Rydén, M., Arvidsson, E., Blomqvist, L., Perbeck, L., Dicker, A., and Arner, P. (2004). Targets for TNF-alpha-induced lipolysis in human adipocytes. Biochem. Biophys. Res. Commun. 318, 168–175.

Samad, F., Yamamoto, K., Pandey, M., and Loskutoff, D.J. (1997). Elevated expression of transforming growth factor-beta in adipose tissue from obese mice. Mol. Med. Camb. Mass 3, 37–48.

Sartipy, P., and Loskutoff, D.J. (2003). Monocyte chemoattractant protein 1 in obesity and insulin resistance. Proc. Natl. Acad. Sci. U. S. A. 100, 7265–7270.

Sawyer, R.T., Strausbauch, P.H., and Volkman, A. (1982). Resident macrophage proliferation in mice depleted of blood monocytes by strontium-89. Lab. Investig. J. Tech. Methods Pathol. 46, 165–170.

Scarpace, P.J., and Matheny, M. (1998). Leptin induction of UCP1 gene expression is dependent on sympathetic innervation. Am. J. Physiol. 275, E259-264.

Schenk, S., Saberi, M., and Olefsky, J.M. (2008). Insulin sensitivity: modulation by nutrients and inflammation. J. Clin. Invest. 118, 2992–3002.

Schulz, C., Gomez Perdiguero, E., Chorro, L., Szabo-Rogers, H., Cagnard, N., Kierdorf, K., Prinz, M., Wu, B., Jacobsen, S.E.W., Pollard, J.W., et al. (2012). A lineage of myeloid cells independent of Myb and hematopoietic stem cells. Science 336, 86–90.

Schwartz, M.W., Woods, S.C., Jr, D.P., Seeley, R.J., and Baskin, D.G. (2000). Central nervous system control of food intake.

Seale, P., Bjork, B., Yang, W., Kajimura, S., Chin, S., Kuang, S., Scimè, A., Devarakonda, S., Conroe, H.M., Erdjument-Bromage, H., et al. (2008). PRDM16 controls a brown fat/skeletal muscle switch. Nature 454, nature07182.

Sears, B., and Perry, M. (2015). The role of fatty acids in insulin resistance. Lipids Health Dis. 14.

Sharpe, J. (2003). Optical projection tomography as a new tool for studying embryo anatomy. J. Anat. 202, 175–181.

Sharpe, J. (2004). Optical Projection Tomography. Annu. Rev. Biomed. Eng. 6, 209–228.

Shoelson, S.E., Lee, J., and Goldfine, A.B. (2006). Inflammation and insulin resistance. J. Clin. Invest. 116, 1793–1801.

Stienstra, R., Saudale, F., Duval, C., Keshtkar, S., Groener, J.E.M., van Rooijen, N., Staels, B., Kersten, S., and Müller, M. (2010). Kupffer cells promote hepatic steatosis via interleukin-1beta-dependent suppression of peroxisome proliferator-activated receptor alpha activity. Hepatol. Baltim. Md 51, 511–522.

Suganami, T., Nishida, J., and Ogawa, Y. (2005). A Paracrine Loop Between Adipocytes and Macrophages Aggravates Inflammatory Changes Role of Free Fatty Acids and Tumor Necrosis Factor α. Arterioscler. Thromb. Vasc. Biol. 25, 2062–2068.

Taschler, U., Radner, F.P.W., Heier, C., Schreiber, R., Schweiger, M., Schoiswohl, G., Preiss-Landl, K., Jaeger, D., Reiter, B., Koefeler, H.C., et al. (2011). Monoglyceride Lipase Deficiency in Mice Impairs Lipolysis and Attenuates Diet-induced Insulin Resistance. J. Biol. Chem. 286, 17467–17477.

Tencerova, M., Aouadi, M., Vangala, P., Nicoloro, S.M., Yawe, J.C., Cohen, J.L., Shen, Y., Garcia-Menendez, L., Pedersen, D.J., Gallagher-Dorval, K., et al. (2015). Activated Kupffer cells inhibit insulin sensitivity in obese mice. FASEB J. 29, 2959–2969.

Tesz, G.J., Aouadi, M., Prot, M., Nicoloro, S.M., Boutet, E., Amano, S.U., Goller, A., Wang, M., Guo, C.-A., Salomon, W.E., et al. (2011). Glucan particles for selective delivery of siRNA to phagocytic cells in mice. Biochem. J. 436, 351–362.

Thaler, J.P., Yi, C.-X., Schur, E.A., Guyenet, S.J., Hwang, B.H., Dietrich, M.O., Zhao, X., Sarruf, D.A., Izgur, V., Maravilla, K.R., et al. (2012). Obesity is associated with hypothalamic injury in rodents and humans. J. Clin. Invest. 122, 153–162.

Thomas, E.L., Saeed, N., Hajnal, J.V., Brynes, A., Goldstone, A.P., Frost, G., and Bell, J.D. (1998). Magnetic resonance imaging of total body fat. J. Appl. Physiol. 85, 1778–1785.

Tomer, R., Ye, L., Hsueh, B., and Deisseroth, K. (2014). Advanced CLARITY for rapid and high-resolution imaging of intact tissues. Nat. Protoc. 9, 1682–1697.

Tontonoz, P., Hu, E., and Spiegelman, B.M. (1994). Stimulation of adipogenesis in fibroblasts by PPAR gamma 2, a lipid-activated transcription factor. Cell 79, 1147–1156.

Tran, T.T., and Kahn, C.R. (2010). Transplantation of adipose tissue and stem cells: role in metabolism and disease. Nat. Rev. Endocrinol. 6, 195–213.

Troisi, R.J., Weiss, S.T., Parker, D.R., Sparrow, D., Young, J.B., and Landsberg, L. (1991). Relation of obesity and diet to sympathetic nervous system activity. Hypertension 17, 669–677.

Vague, J. (1956). The degree of masculine differentiation of obesities: a factor determining predisposition to diabetes, atherosclerosis, gout, and uric calculous disease. Am. J. Clin. Nutr. 4, 20–34.

Valdearcos, M., Robblee, M.M., Benjamin, D.I., Nomura, D.K., Xu, A.W., and Koliwad, S.K. (2014). Microglia Dictate the Impact of Saturated Fat Consumption on Hypothalamic Inflammation and Neuronal Function. Cell Rep. 9, 2124–2138.

Valdearcos, M., Douglass, J.D., Robblee, M.M., Dorfman, M.D., Stifler, D.R., Bennett, M.L., Gerritse, I., Fasnacht, R., Barres, B.A., Thaler, J.P., et al. (2017). Microglial Inflammatory Signaling Orchestrates the Hypothalamic Immune Response to Dietary Excess and Mediates Obesity Susceptibility. Cell Metab. 26, 185–197.e3.

Van Heek, M., Compton, D.S., France, C.F., Tedesco, R.P., Fawzi, A.B., Graziano, M.P., Sybertz, E.J., Strader, C.D., and Davis, H.R. (1997). Diet-induced obese mice develop peripheral, but not central, resistance to leptin. J. Clin. Invest. 99, 385–390.

Vander Tuig, J.G., Knehans, A.W., and Romsos, D.R. (1982). Reduced sympathetic nervous system activity in rats with ventromedial hypothalamic lesions. Life Sci. 30, 913–920.

Vaughan, M. (1967). The Mechanism of the Lipolytic Action of Catecholamines. Ann. N. Y. Acad. Sci. 139, 841–848.

Vaz, M., Jennings, G., Turner, A., Cox, H., Lambert, G., and Esler, M. (1997). Regional sympathetic nervous activity and oxygen consumption in obese normotensive human subjects. Circulation 96, 3423–3429.

Veiga-Fernandes, H., and Mucida, D. (2016). Neuro-Immune Interactions at Barrier Surfaces. Cell 165, 801–811.

Virtanen, K.A., Lidell, M.E., Orava, J., Heglind, M., Westergren, R., Niemi, T., Taittonen, M., Laine, J., Savisto, N.-J., Enerbäck, S., et al. (2009). Functional Brown Adipose Tissue in Healthy Adults. N. Engl. J. Med.

360, 1518–1525.

Weisberg, S.P., McCann, D., Desai, M., Rosenbaum, M., Leibel, R.L., and Ferrante, A.W. (2003). Obesity is associated with macrophage accumulation in adipose tissue. J. Clin. Invest. 112, 1796–1808.

Weisberg, S.P., Hunter, D., Huber, R., Lemieux, J., Slaymaker, S., Vaddi, K., Charo, I., Leibel, R.L., and Jr, A.W.F. (2006). CCR2 modulates inflammatory and metabolic effects of high-fat feeding. J. Clin. Invest. 116, 115–124.

Wentworth, J.M., Naselli, G., Brown, W.A., Doyle, L., Phipson, B., Smyth, G.K., Wabitsch, M., O'Brien, P.E., and Harrison, L.C. (2010). Pro-Inflammatory CD11c+CD206+ Adipose Tissue Macrophages Are Associated With Insulin Resistance in Human Obesity. Diabetes 59, 1648–1656.

Wilsey, J., Zolotukhin, S., Prima, V., and Scarpace, P.J. (2003). Central leptin gene therapy fails to overcome leptin resistance associated with diet-induced obesity. Am. J. Physiol. Regul. Integr. Comp. Physiol. 285, R1011-1020.

Wirsén, C., and Hamberger, B. (1967). Catecholamines in Brown Fat. Nature 214, 214625a0.

Wong, E., and Cuervo, A.M. (2010). Autophagy gone awry in neurodegenerative diseases. Nat. Neurosci. 13, 805–811.

Wu, D., Molofsky, A.B., Liang, H.-E., Ricardo-Gonzalez, R.R., Jouihan, H.A., Bando, J.K., Chawla, A., and Locksley, R.M. (2011). Eosinophils sustain adipose alternatively activated macrophages associated with glucose homeostasis. Science 332, 243–247.

Wu, H., Ghosh, S., Perrard, X.D., Feng, L., Garcia, G.E., Perrard, J.L., Sweeney, J.F., Peterson, L.E., Chan, L., Smith, C.W., et al. (2007). T-cell accumulation and regulated on activation, normal T cell expressed and secreted upregulation in adipose tissue in obesity. Circulation 115, 1029–1038.

Wu, J., Boström, P., Sparks, L.M., Ye, L., Choi, J.H., Giang, A.-H., Khandekar, M., Virtanen, K.A., Nuutila, P., Schaart, G., et al. (2012). Beige adipocytes are a distinct type of thermogenic fat cell in mouse and human. Cell 150, 366–376.

Xu, H., Barnes, G.T., Yang, Q., Tan, G., Yang, D., Chou, C.J., Sole, J., Nichols, A., Ross, J.S., Tartaglia, L.A., et al. (2003). Chronic inflammation in fat plays a crucial role in the development of obesity-related insulin resistance. J. Clin. Invest. 112, 1821–1830.

Xu, X., Grijalva, A., Skowronski, A., van Eijk, M., Serlie, M.J., and Ferrante, A.W. (2013). Obesity Activates a Program of Lysosomal-Dependent Lipid Metabolism in Adipose Tissue Macrophages Independently of Classic Activation. Cell Metab. 18, 816–830.

Yang, B., Treweek, J.B., Kulkarni, R.P., Deverman, B.E., Chen, C.-K., Lubeck, E., Shah, S., Cai, L., and Gradinaru, V. (2014). Single-Cell Phenotyping within Transparent Intact Tissue through Whole-Body Clearing. Cell 158, 945–958.

Ye, J. (2009). Emerging Role of Adipose Tissue Hypoxia in Obesity and Insulin Resistance. Int. J. Obes. 2005 33, 54–66.

Young, J.B., and Landsberg, L. (1997). Suppression of sympathetic nervous system during fasting. Obes. Res. 5, 646–649.

Youngstrom, T.G., and Bartness, T.J. (1995). Catecholaminergic innervation of white adipose tissue in Siberian hamsters. Am. J. Physiol. 268, R744-751.

Zechner, R., Zimmermann, R., Eichmann, T.O., Kohlwein, S.D., Haemmerle, G., Lass, A., and Madeo, F. (2012). FAT SIGNALS–lipases and lipolysis in lipid metabolism and signaling. Cell Metab. 15, 279–291.

Zhan, C., Zhou, J., Feng, Q., Zhang, J.-E., Lin, S., Bao, J., Wu, P., and Luo, M. (2013). Acute and long-term suppression of feeding behavior by POMC neurons in the brainstem and hypothalamus, respectively. J. Neurosci. Off. J. Soc. Neurosci. 33, 3624–3632.

Zhang, Y., Proenca, R., Maffei, M., Barone, M., Leopold, L., and Friedman, J.M. (1994). Positional cloning of the mouse obese gene and its human homologue. Nature 372, 425–432.

Eurostat European Health Interview Survey, 2016. Retrieved from URL: http://ec.europa.eu/eurostat/documents/2995521/7700898/3-20102016-BP-EN.pdf/.

WHO guidelines on obesity, 2017. Retrieved from URL: http://www.who.int/topics/obesity/en/

2 | SYMPATHETIC NEURO-ADIPOSE CONNECTIONS MEDIATE LEPTIN DRIVEN LIPOLYSIS

Wenwen Zeng[1,7], Roksana M Pirzgalska[2,7], Mafalda M Pereira[2], Nadiya Kubasova[2], Andreia Barateiro[2,3], Elsa Seixas[2], Yi-Hsueh Lu[1], Albina Kozlova[1], Hennig Voss[4], Gabriel G Martins[5], Jeffrey M Friedman[1,6,8], Ana I Domingos[2,6,8].

[1] Laboratory of Molecular Genetics, The Rockefeller University, New York, NY 10021, USA

[2] Obesity Laboratory, Instituto Gulbenkian de Ciência, Oeiras 2780-156, Portugal

[3] Research Institute for Medicines (iMed.ULisboa), Faculty of Pharmacy, Universidade de Lisboa, Avenue Professor Gama Pinto, Lisbon 1649-003, Portugal

[4] Department of Radiology, Weill Cornell Medical College, New York, NY 10021, USA

[5] Advanced Microscopy Unit, Instituto Gulbenkian de Ciência, Oeiras 2780-156, Portugal

[6] Howard Hughes Medical Institute (HHMI), New York, NY, USA

[7] co-first authors

[8] co-senior authors

Author's contribution: R.M.P and A.I.D performed two-photon microscopy. R.M.P performed optogenetics ex vivo. A.I.D and R.M.P performed optogenetics in vivo. W.Z. and Y.H.L. performed western blots. R.M.P performed tissue clearing for the OPT. G.G.M. aquired OPT images. R.M.P and M.M.A.P performed OPT image segmentation. MRI scans were conducted by H.V. Amira segmentation of MRI data was performed by R.M.P. Cell cultures and neuronal explants were developed by A.B. and R.M.P. Whole body fat composition and body weights were performed W.Z., Y.H.L and A.K. E.S, M.M.A.P and R.M.P performed functional studies. Mouse husbandry and genotyping were performed by N.K. and A.K. A.I.D, J.M.F. and R.M.P wrote the manuscript.

ABSTRACT

Leptin is an adipose-derived hormone that acts in the brain to promote fat-breakdown. However, the mechanism underlying the lipolytic effect of leptin has not been established. Here we demonstrate by intra-vital two-photon microscopy that sympathetic nerve fibers can envelop adipocytes. Local optogenetic stimulation of sympathetic inputs was sufficient to induce local lipolytic response with depletion of white adipose mass. Conversely, genetic ablation of sympathetic inputs onto fat pads blocked leptin-stimulated phosphorylation of hormone sensitive lipase and consequent lipolysis, as did knockouts of dopamine β-hydroxylase, an enzyme required for catecholamine synthesis. Here we visualize neuro-adipose junctions and demonstrate that they are both necessary and sufficient for the induction of lipolysis in white adipose tissue, and are an efferent effector of leptin action. Direct activation of sympathetic inputs to adipose tissues could represent a strategy for the induction of fat loss that would circumvent central leptin resistance.

2.1 INTRODUCTION

White adipose tissues (WAT) serve as a storage depot for energy rich triglycerides. In times of privation, this lipid storage can be released as part of an adaptive response to the energy shortage. Lipolysis, the process of hydrolyzing stored triglycerides in adipocytes, is regulated by several G protein-coupled receptors, including adrenergic receptors, all of which activate protein kinase A (PKA) and elevate the intracellular levels of cyclic adenosine monophosphate (cAMP) (Brasaemle, 2007). PKA also phosphorylates several key target proteins, including lipid droplet-associated protein perilipin, HSL, and a set of esterases, that collectively promote the hydrolysis of triglycerides into free fatty-acids (FFA) and glycerol, which are then released into plasma to meet the energy demands of other tissues (Brasaemle, 2007). HSL is a canonical target of PKA in adipocytes and this enzyme catalyzes the conversion of diacylglycerol to monoacyl glycerol (Brasaemle, 2007).

Adipose tissue mass is homeostatically controlled by an endocrine loop in which leptin acts on neural circuits in the hypothalamus and elsewhere in brain to regulate food intake and peripheral metabolism. In wild type (WT) and leptin-deficient ob animals, leptin treatment reduces food intake and leads to a rapid depletion of fat mass (Halaas et al., 1995, 1997; Montez et al., 2005). Of note, the depletion of fat mass after leptin treatment is distinct from that observed after food restriction in a number of respects: leptin treatment spares lean body mass and also potently stimulates glucose metabolism, while starvation results in a loss of lean body mass and causes insulin resistance (Newman and Brodows, 1983; Koffler and Kisch, 1996; Awad et al., 2009; Elia et al., 1999). In addition, leptin deficient *ob/ob* mice pair-fed to leptin-treated ob mice lose only half the weight of those treated with leptin, further implicating a mechanism beyond a reduced food intake (Rafael and Herling, 2000). Because leptin has been shown to increase the sympathetic efferent signal to brown adipose tissues (BAT) (Scarpace and Matheny, 1998; Rezai-Zadeh and Munzberg, 2013), it has been suggested that leptin also activates sympathetic efferents to white adipose tissue to increase lipolysis in WAT. However, this has not been directly shown and the nature of the effector mechanism underlying leptin-stimulated lipolysis in WAT has not been defined. In particular, it has not been established whether the increased lipolysis in white adipose tissue in response to leptin is due to a circulating hormone(s) such as norepinephrine (NE) and/or another mediator that is released either centrally or peripherally (adrenal gland or macrophages), or specific efferent neural inputs to WAT, which mediate central leptin action. However, the effect of leptin on energy balance does not require the presence of intact adrenals suggesting that this organ is unlikely to be the source of the lipolytic signal (Arvaniti et al., 1998).

While numerous previous studies have shown dense neural innervation of BAT both functionally and anatomically, the innervation of WAT has been difficult to visualize. It has thus been suggested that neural inputs to WAT are either very sparse, or difficult to be distinguished from en passant axons with terminals on other cell types, such as those in vasculature (Bartness et al., 2005; Bartness and Song, 2007; Youngstrom and Bartness, 1995; Giordano et al., 1996). Indeed, some reports have suggested that the only innervation of WAT is perivascular, and that white adipocytes themselves are not directly innervated (Giordano et al., 2005). This controversy has heightened the uncertainty as to the relative

roles of sympathetic neural activity to regulate WAT metabolism. Alternatively, macrophages in adipose tissue account for about 10% of the stromal vascular fraction (SVF), hence local catecholamines produced by these cells could also contribute to lipolysis in WAT *in vivo* (Weissberg et al., 2003; Nguyen et al., 2011). Thus, the dramatic decrease of adipose tissue mass observed after leptin treatment could, in principle, be mediated by catecholamines or other mediators that are either locally produced or produced by neurons.

In this study, we use anatomic, optogenetic, biochemical, and genetic approaches to show that the catecholamines released at heretofore unidentified neuro-adipose junctions mediates the lipolytic effect of leptin, thus establishing the effector mechanism underlying depletion of fat mass by leptin, and potentially other stimuli. Our data demonstrate that the local sympathetic activity in WAT is necessary and sufficient for the lipolytic effect of leptin. In addition, genetic evidence shows that the β- but not α-adrenergic receptors partially constitute a signaling pathway that accounts for the lipolytic effect of leptin.

2.2 RESULTS

Phosphorylation of HSL in WAT as a Lipolysis Marker for Leptin Action.

To directly assess the cellular effect of leptin on lipolysis in white adipocytes and provide a marker for leptin action, we searched for biochemical responses in white adipocytes that were specifically activated by leptin treatment. We used a battery of phospho-specific antibodies and found that the phosphorylation of HSL was robustly increased in adipose tissue in response to leptin treatment. Note, our ability to define a biochemical effect of leptin is dependent on the quality of the antibodies and we found that the anti-pHSL antibody was extremely robust. As shown, peripheral administration of leptin led to a significant increase of phosphorylated HSL (p-HSL) in WAT that could be visualized by immunohistochemistry (Figure 2.1 a), and quantified by immunoblot analysis (Figure 2.1 b). We set out to investigate whether the effect of leptin to increase HSL phosphorylation was mediated by neural efferent outputs onto WAT.

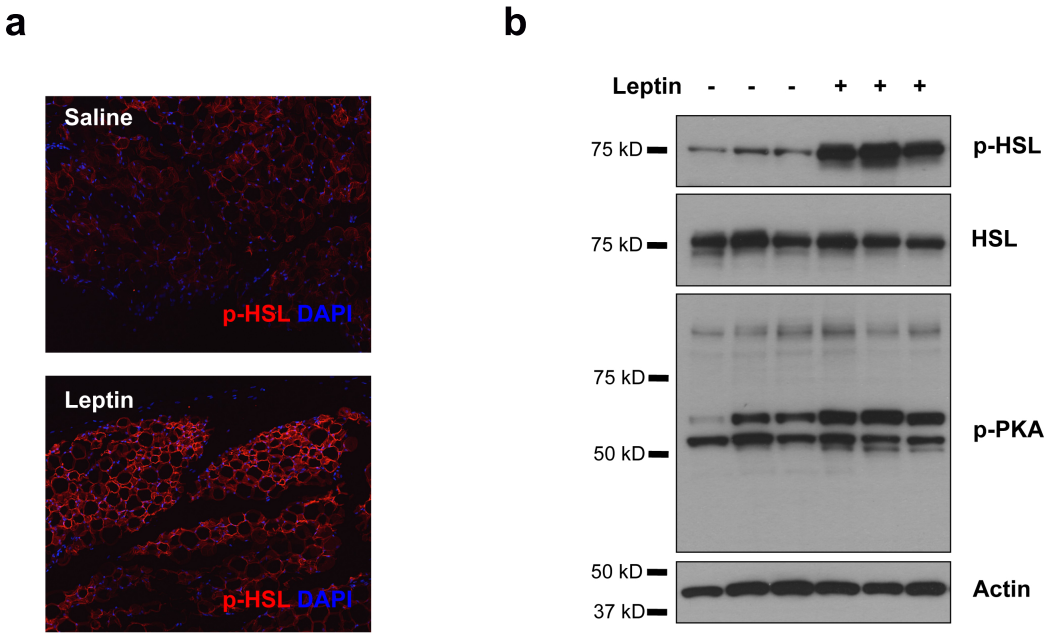

Figure 2.1. Leptin Stimulates HSL Phosphorylation in WAT.
(a) Immunostaining of phosphorylated HSL (red) in paraffin sections of epididymal fat of *C57Bl6/J* mice that were peripherally administrated with 500 ng/h recombinant leptin for 2 days. **(b)** Phosphorylated HSL and phosphorylated PKA substrates in total protein extracts of epididymal fats were examined by immunoblot analysis.

Axonal Bundles Project to WAT and Form Sympathetic Neuro-Adipose Junctions.

We first used tomography methods to determine whether fat pads were innervated. By coupling optical projection tomography (OPT) to a fat clearing method that renders whole organs transparent (Figure 2.S1), we were able to macroscopically visualize and document the nerve bundles that innervate the inguinal fat pad (Figure 2.2 a and Experimental Procedures for details) (Gualda et al., 2013, Quintana and Sharpe, 2011). A full series of projections of the whole organ are acquired from multiple angles, typically 800-1600 angles, and from this series of projections a stack of axial slices can be visualized through back-projection reconstruction (Figure 2.2 b).

From an OPT series of coronal optical sections of inguinal fat organ we performed a 3-D reconstruction, which enabled the visualization of thick axon bundles targeting the fat pad (Figure 2.2 c, d). Axon bundles can be identified based on the grey threshold level and morphological features that distinguish them from the vasculature (Figure 2.2 e). At the same time, we did not find similarly looking nerve bundles within the visceral adipose tissue (Figure 2.S2). These structures within the fat were then segmented using semi-automated software (see Experimental Procedures). By using these tools, we were able to identify thick nerve bundles in the inguinal fat and a niche enriched with globular structures within the visceral fat depot (Figure 2.2 and Figure 2.S2).

The neural bundles were micro-dissected from the subcutaneous fat pads and subjected to immunostaining for tyrosine hydroxylase (TH), a marker of sympathetic neurons, and β3-tubulin (Tub-3), a general marker for the peripheral nervous system (PNS) (Figure 2.3 a). We found that overall 50% of the Tub-3-positive neurons also expressed TH, thus establishing the presence of both catecholaminergic and non-catecholaminergic axons innervating subcutaneous fat pads (Figure 2.3. a). We then used multi-photon microscopy on the intact inguinal WAT of a living mouse to visualize sympathetic neuro-adipose connections (see Experimental Procedures and Figure 2.3 b, c). We labeled adipocytes with LipidTOX, a lipophylic dye, and sympathetic axons by crossing TH Cre-recombinase mice (TH-Cre) with a Tdtomato-reporter line (Rosa26-LSL-Tdtomato) (Figure 2.3 c). We observed Tdtomato-positive axons in fat pads made dense contacts with adipocytes through bouton-like structures that had the anatomic appearance of neuro-adipocyte junctions, resembling synapses (Figure 2.3 c). We quantified these from 8 independent 2-photon micrographs, and determined that $8 \pm 4.6\%$ of adipocytes are in direct contact with sympathetic nerves.

Optogenetic Stimulation of Sympathetic Inputs to WAT Leads to Catecholamine release, HSL Phosphorylation, and Fat Mass Depletion.

We assessed the function of the catecholaminergic fibers by crossing the *TH-Cre* mice to a channelrhodopsin (ChR2) reporter line, *LSL-ChR2-YFP* . ChR2-YFP showed a complete co-localization with the endogenous TH as determined by immunostaining of YFP and TH (Figure 2.4 a). ChR2-YFP-expressing axons that projected onto subcutaneous WAT were then optogenetically activated using a subcutaneously implanted optical fiber targeting the right inguinal fat depot (see Experimental Procedures for surgical

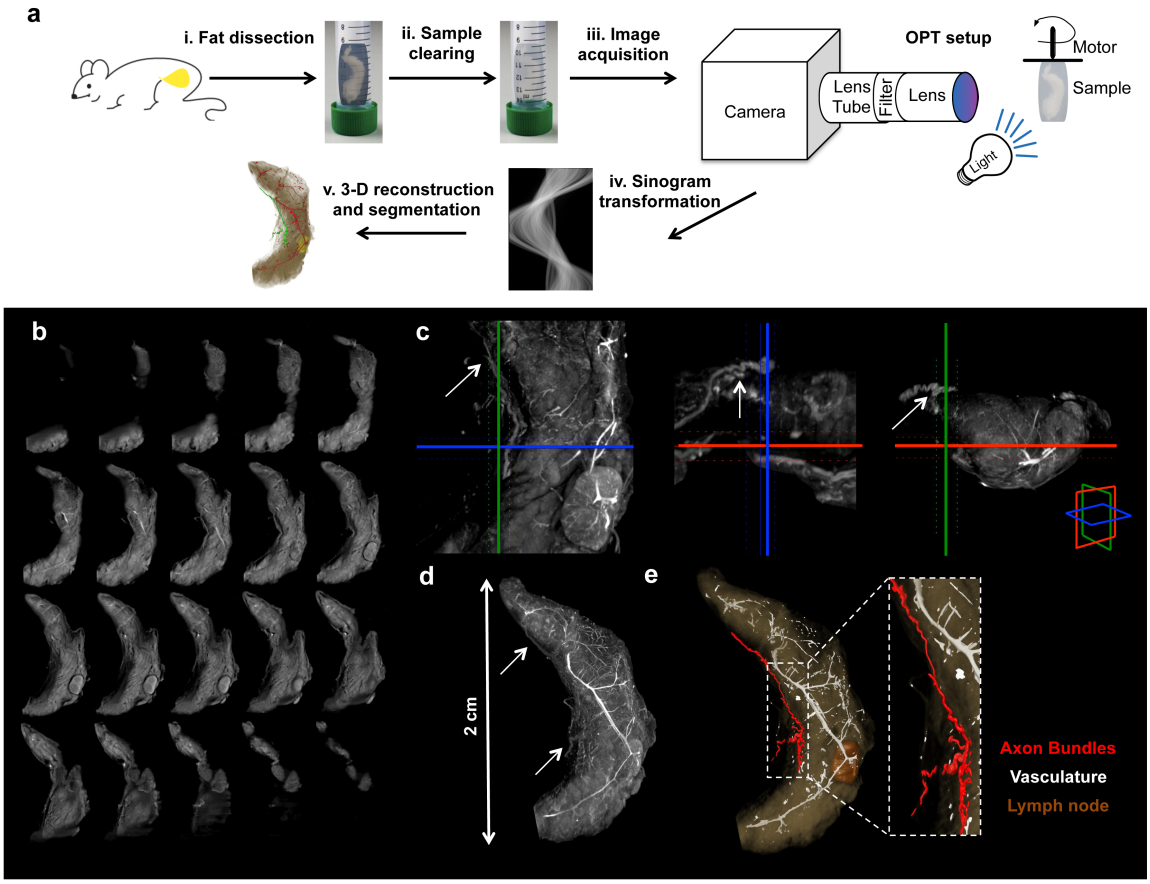

Figure 2.2. Neural Projections in Fat Detected with Optical Projection Tomography.
(a) Schematic representation of the OPT method applied to the subcutaneous inguinal fat: (i) Tissue dissection. (ii) Sample clearing. (iii) Image acquisition. (iv) Sinogram transformation. (v) 3-D reconstruction and segmentation. **(b)** OPT series of coronal sections of inguinal fat organ after 3-D reconstruction. **(c)** Orthogonal 400 µm OPT-slabs of inguinal fat in coronal, axial and sagittal view. Axon budles were identified based on the grey threshold level (arrows). **(c)** Orthogonal 400 µm OPT-slabs of inguinal fat in coronal, axial and sagittal view. Axon budles were identified based on the grey threshold level (arrows). **(d)** 3-D reconstruction in maximal intensity projection of the OPT coronal sections. **(e)** Surface view of segmented structures within inguinal fat.

details).

While optogenetic tools have been widely used in the central nervous system (CNS), it has not been used as frequently to probe the function of peripheral cells including sympathetic neurons. We began by validating the use of optogenetic stimulation of sympathetic neurons in primary cultures of superior cervical ganglia (SCG) of *TH-Cre* X *LSL-ChR2-YFP* mice; SCG can be dissected with less difficulty compared to other sympathetic ganglia (see Supplemental Experimental Procedures for culture details). We found that optogenetic stimulation of cultured sympathetic neurons increased expression of cFos, a marker for neuronal activity, in TH-positive cells and significantly stimulated NE release ex vivo as assayed with ELISA (Figure 2.4. b, c). NE release of ChR2-positive neurons was significantly higher relative to that of ChR2-negative cells (749.6 $\pm$ 170.1 pg/ml vs. 4.8 $\pm$ 1.7 pg/ml, *P $<$ 0.05, Figures 2.4

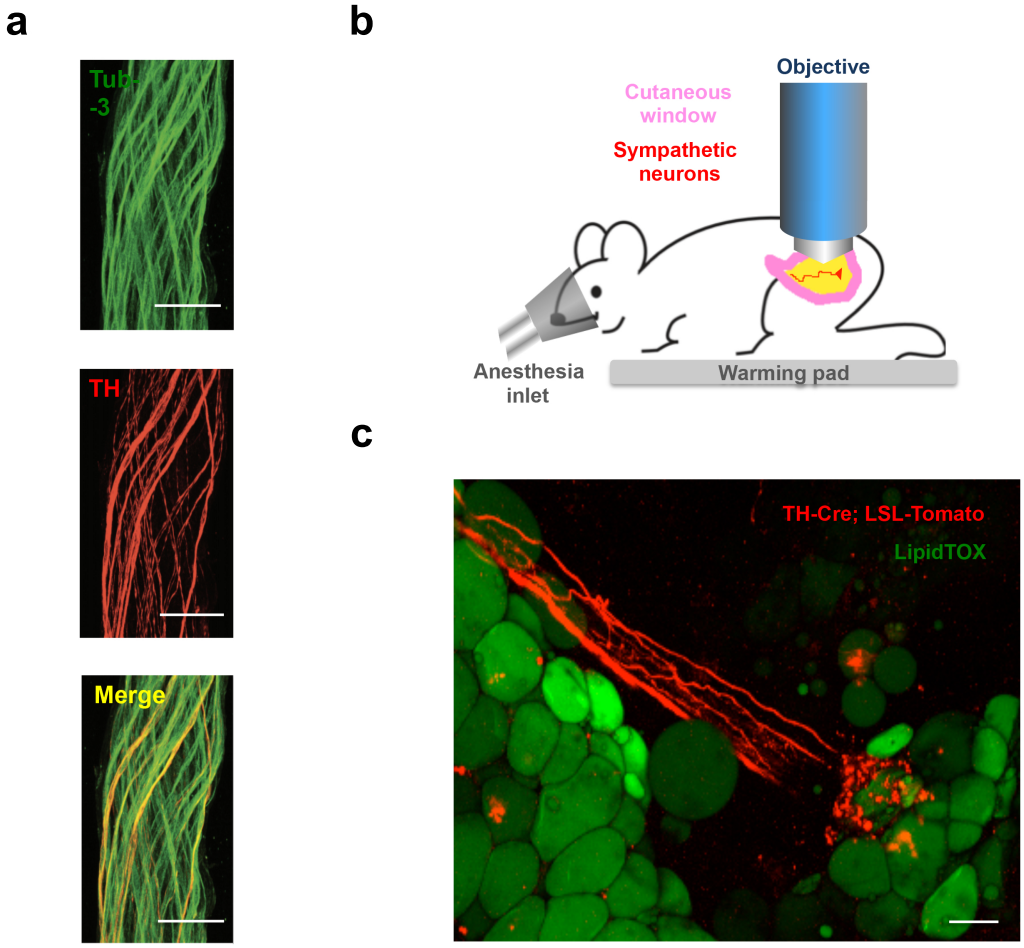

Figure 2.3. Catecholaminergic Neurons Innervating Adipocytes Integrate Nerve Bundles of Mixed Molecular Identity.

(a) Partial co-localization of TH (red), an SNS marker, and Tub-3 (green), a general PNS marker, shown by immunohistochemistry of nerve bundles dissected from the inguinal fat pads of WT mice. Scale bar = 50 μm. **(b)** Schematic representation of the two-photon intra-vital imaging of neurons in the inguinal fat pad. **(c)** Intra-vital two-photon microscopy visualization of a neuro-adipose connection in the inguinal fat pad of a live TH-Cre; LSL-Tomato mouse. LipidTOX (green) labels adipocytes. Scale bar = 100 μm.

b, c - see Experimental Procedures for culture and stimulation details).

We next stimulated ChR2-YFP-expressing axons in vivo unilaterally by placing optical fibers subcutaneously, aiming at inguinal fat pad located in the supra-pelvic flank of *TH-Cre* X *LSL-ChR2-YFP* mice (see Experimental Procedures for stimulation details). Activation of the ChR2-positive axons in subcutaneous WAT led to a significant increase of NE in the stimulated fat pad, relative to the contralateral un-stimulated control side (2.7 ± 0.5 vs. 1.1 ± 0.2, $^*P < 0.05$, Figure 2.4 d). We also observed a significant increase of HSL phosphorylation of fat on the side ipsilateral to the optical fiber, compared to the contralateral un-stimulated side (Figure 2.4 e). These data show that local activation of catecholaminergic inputs to fat could locally mimic the biochemical effect of leptin (Figure 2.4 d, e). We then tested whether a more prolonged (4 weeks) optogenetic stimulation of ChR2-positive neurons in WAT

could deplete fat mass (Figure 2.4 f). The optical stimulation protocol was set to deliver light for every other second at 20 Hz, and the volume of subcutaneous WAT was determined using magnetic resonance imaging (MRI) with 3D reconstruction (Figure 4 f, g - see Experimental Procedures for details). After chronic activation, the size of the optogenetically stimulated ipsilateral fat pads of *TH-Cre*; *LSL-ChR2-YFP* mice was 23 ± 3.4 percent that of the contralateral control side, representing a statistically and biologically significant decrease in fat mass (Figure 2.4 f, g, ****P $<$ 0.0001). This effect depended on ChR2 expression, as the fat pad volume of stimulated fat pads in ChR2-negative mice was unchanged (86 ± 4.3% of the size of contralateral control fat pad) ruling out potential nonspecific effect of laser stimulation (Figure 2.4 g, see Experimental Procedures for details). Together, the results provide anatomical and functional evidence that there are synapse-like sympathetic inputs onto white adipocytes, and that their activation is sufficient to promote local NE release, HSL phosphorylation, and a reduction in the mass of an adipose tissue depot.

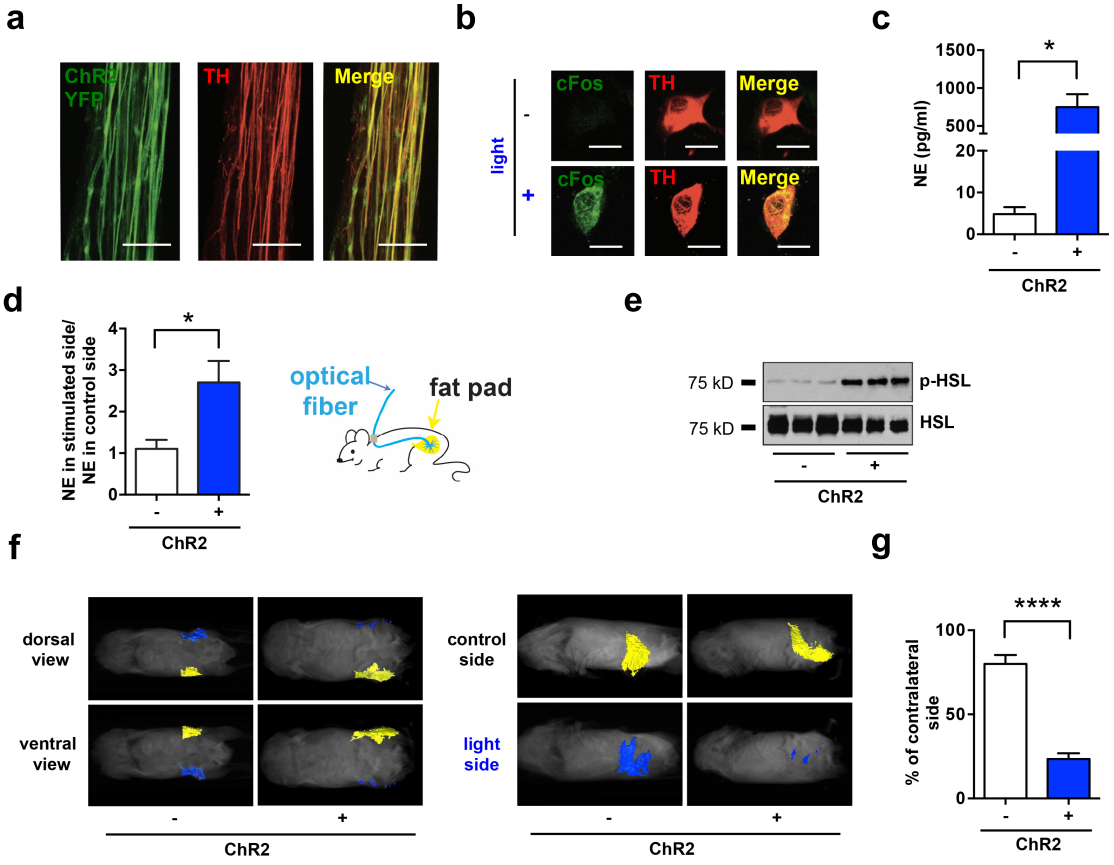

Figure 2.4. Optogenetic Stimulation of SNS Neurons in Fat is Sufficient to Drive Lipolysis. **(a)** Complete co-localization of YFP (green) and TH (red), shown by immunohistochemistry of nerve bundles dissected from the inguinal fat pads of *TH-Cre*; *LSL-ChR2-YFP* . **(b)** C-Fos (green) induction in cultured SNS neurons after optogenetic activation. **(c)** *Ex vivo* NE release upon optogenetic stimulation of sympathetic SCG explants isolated from *TH-Cre*; *LSL-ChR2-YFP* mice and *LSL-ChR2-YFP* control mice (*P $<$ 0.05, n=3-6). **(d)** *In vivo* NE release in subcutaneous fat upon optogenetic stimulation of sympathetic neurons in white adipose tissues of *TH-Cre*; *LSL-ChR2-YFP* and *LSL-ChR2-YFP* control mice that were subcutaneously implanted with optical fibers targeting the inguinal fat pad (*P $<$ 0.05, n=8). **(e)** Immunoblot analysis of phosphorylated HSL in total protein extracts of subcutaneous fats of *TH-Cre*; *LSL-ChR2-YFP* and *LSL-ChR2-YFP* control mice that were subcutaneously implanted with optical fibers targeting the inguinal fat pad and optogenetically stimulated for 2 weeks. **(f)** MRI-guided visualization of fat in *TH-Cre*; *LSL-ChR2-YFP* and *LSL-ChR2-YFP* control mice that were optogenetically stimulated for 4 weeks (yellow is control inguinal fat pat, blue is light-stimulated fat pad; details in Experimental Procedures section). **(g)** Quantification of fat reduction in stimulated side versus the contralateral control side (****P $<$ 0.0001, n=6). Results are shown as mean ± SEM.

Local Sympathetic Inputs are Required for Leptin-stimulated HSL Lipolysis in WAT.

Similarly to optogenetic stimulation of sympathetic innervation in white fat, leptin treatment led to an increase in NE levels in the subcutaneous adipose organ. NE levels in white adipose tissues dissected from leptin treated animals were significantly higher than in controls (78.7 $\pm$ 16.8 pg NE/ ug of protein vs. 30.7 $\pm$ 4.1 pg NE/ ug of protein, *P $<$ 0.05, Figure 2.5 a). Interestingly, leptin treatment did not affect serum NE levels (Figure 2.5 b) indicating that leptin locally increases NE release in white fat, but not systemically.

We next evaluated whether sympathetic activation is necessary for leptin-stimulated lipolysis by disrupting the neural inputs in WAT using pharmacologic blockade or local genetic ablation. First, we observed that administration of hexamethonium, a non-depolarizing anti-cholinergic ganglion blocker, significantly decreased the leptin-stimulated phosphorylation of HSL in adipose tissue (Figure 2.5 c). However, as the action of hexamethonium is systemic and is not cell type specific, affecting all ganglionic transmission, we took a complementary approach by introducing a local neural crush injury to the fibers innervating epididymal fat pads. Because of the anatomy of the fat pad, nerve fibers in the distal portion of the tissues can be efficiently eliminated by a surgical crush of the perivascular axons running parallel to the main vessels (see Experimental Procedures). We carried out physical denervation with a forcep crushing the fibers 2 mm from the distal tip for 30 seconds. Leptin was delivered 3 days post surgery through osmotic pump for 2 days. Consistent with the effect of hexamethonium, after a crush injury to the local nerve, leptin treatment failed to increase HSL phosphorylation on the denervated side compared to the intact contralateral control (Figure 2.5 d). This showed that local neural activation to WAT is required for the biochemical changes associated with leptin treatment.

To confirm that leptin-mediated lipolysis is the result of activation of sympathetic neural outputs to fat, we ablated these neurons by crossing the *TH-Cre* line with the diphtheria toxin receptor (DTR) mice - *LSL-DTR* , and injected diphtheria toxin (DT) locally in subcutaneous inguinal WAT (Buch et al., 2005). Local treatment with DT eliminated only those sympathetic axons in the regions of the injection site, without effects on other local neuronal populations as shown by the sparing TH-negative Tub-3 positive axons at the site of injection (Figure 2.5 e, **P $<$ 0.001, see Experimental Procedures for details). These injections were administered peripherally at low doses (10 ng/g) to ensure that the effect was local and to also spare TH-positive neurons in CNS (Figure S1, Domingos et al., 2013). Genetic ablation of sympathetic input to adipose tissue completely blocked the effect of leptin on HSL phosphorylation on the ipsilateral compared to the contralateral untreated side (Figure 2.5 f). Together, these results demonstrate that activation of sympathetic neurons in fat is necessary for leptin to stimulate HSL phosporylation in adipose tissue.

β-Adrenergic Signaling Influences Leptin-stimulated Lipolysis in WAT.

Consistent with a sympathetic mechanism for the leptin mediated stimulation of lipolysis, systemic administration of the β-adrenergic agonist isoproterenol resulted in the rapid induction of p-HSL. As

previously reported, isoproterenol also increased FFA release from WAT in vitro and in vivo (data not shown). We thus set out to test whether β-adrenergic signaling was required for leptin-stimulated lipolysis.

We first examined the lipolytic response to leptin in mice with a knockout (KO) of dopamine β-hyroxylase (DBH), a key enzyme in the synthesis of NE and epinephrine from dopamine (Figure 2.6.). After peripheral administration of leptin, there was a dramatic increase of HSL phosphorylation in WAT in the *WT* or *DBH+/+* animals, but a markedly diminished response in the *DBH-/-* littermates (Figure 2.6. a). Consistent with this, the total fat composition dramatically decreased in the *WT* mice treated with leptin, while there was only a slight change of fat mass in mice with the DBH deletion (*P $<$ 0.05, Figure 2.6. b). Also consistent with a diminished lipolytic effect of leptin, there was also a lower amount of weight loss in the *DBH-/-* (Figure 2.6. c). After two days of leptin treatment body weight of wild type mice decreased more than 6 percent while the weight loss of DBH-/- was less than 2 percent (*P $<$ 0.05). The data suggests that catecholamines contribute to more than 50 percent of leptin's effect on body weight. Altogether, the results confirm that catecholamines are required for the leptin-stimulated lipolysis and HSL phosphorylation in WAT.

To test whether the action of leptin to drive lipolysis is mediated through β-adrenergic signaling, we crossed the *β1/β2* double KO to *β3* KO to generate animals with a deletion of all three β-adrenergic receptors (Figure 2.7). Animals with a deletion of all the three isoforms of β-adrenergic receptors showed significantly decreased HSL phosphorylation after leptin treatment in comparison to the double KO controls (Figure 2.7 a). However, this decrease was not as marked as that seen in individual depots after local ablation of sympathetic fibers using DT (see Figure 2.5 d). While leptin treatment significantly decreased total fat mass in $\beta1^{-/-}\beta2^{-/-}$ mice, this effect was significantly reduced in $\beta1^{-/-}\beta2^{-/-}\beta3^{-/-}$ triple knockout mice (Figure 6b Paired ANOVA post hoc test *P $<$ 0.01, comparing $\beta1^{-/-}\beta2^{-/-}\beta3^{-/-}$ with $\beta1^{-/-}\beta2^{-/-}\beta3^{+/+}$ mice after leptin treatment). In contrast, α-adrenergic receptors appeared to play only a minor role in the leptin-stimulated loss of fat mass, because α-adrenergic blockers phentolamine (5 mg/kg, IP) and phenoxybenzamine (10 mg/kg IP) failed to diminish the catabolic responses to leptin treatment in $\beta1^{-/-}\beta2^{-/-}\beta3^{+/+}$ control mice or $\beta1^{-/-}\beta2^{-/-}\beta3^{-/-}$ mice (Figure 2.7 c). There was also a small suppression of body weight loss in response to leptin in the $\beta1^{-/-}\beta2^{-/-}\beta3^{-/-}$ mice (Figure 2.7 d). These results showed that the β-adrenergic receptors are only partially necessary for leptin-mediated lipolysis of WAT, but the magnitude of the effect of a loss of β-adrenergic signaling is not as great as that observed by interfering with local neural outputs, thus suggesting that there could also be other neural mediators or interacting receptors on adipocytes (Figure 2.5).

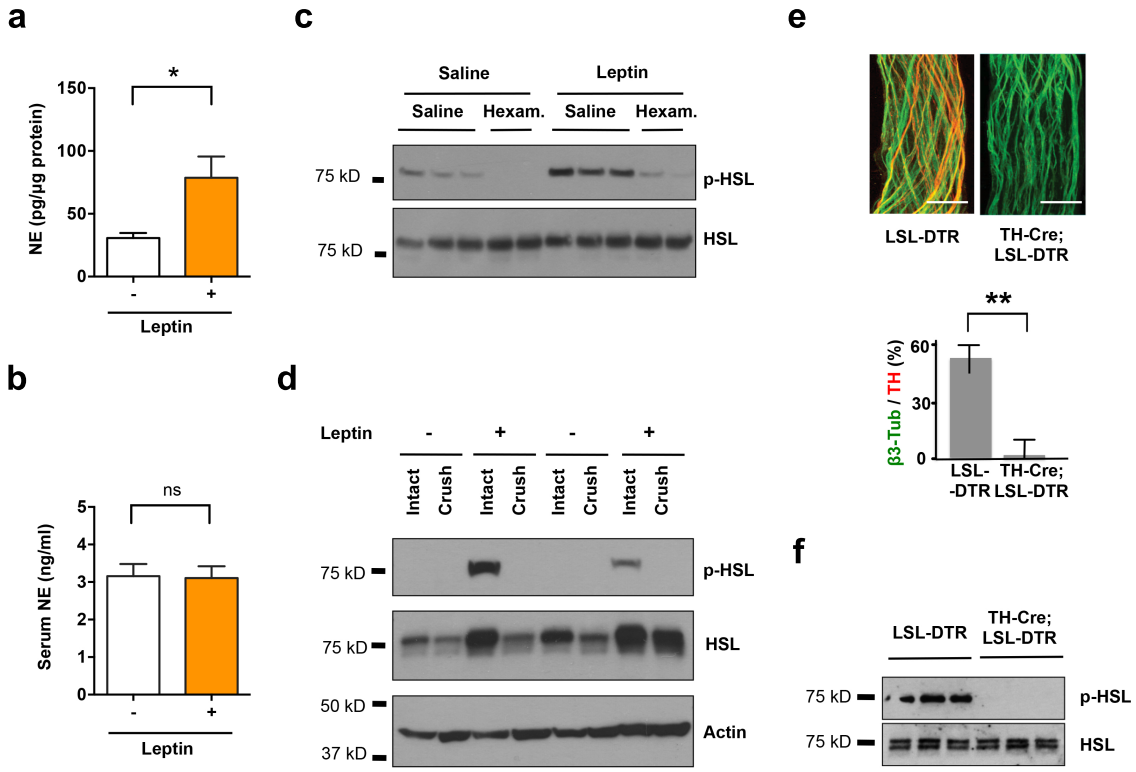

Figure 2.5. Sympathetic Neurons are Locally Required for Leptin induced Lipolysis.
(a-b) *C57BL6/J* mice were peripherally administrated with 500 ng/h recombinant leptin or saline for 2 days. **(a)** NE content in subcutaneous fat pads (*P $<$ 0.05, n=5) and **(b)** NE serum levels were measured by NE ELISA (n=4). Results are shown as mean ± SEM ns, not significant. **(c-d)** *C57BL6/J* mice were peripherally administrated with 500 ng/h recombinant leptin **(c)** in combination with 500 ng/h ganglionic blocker hexamethonium (Hexam.) or **(d)** at 3 days after local crush injury of nerves in fat pads. p-HSL in total protein extracts of epididymal fats were examined by immunoblot analysis. **(e)** Fat pads in *TH-Cre; LSL-DTR* mice were locally treated with DT. Tissue specific ablation of SNS axons confirmed by immunostaining for Tub-3 and TH (**P $<$ 0.001, n=6). Results are shown as mean ± SEM. **(f)** Immunoblot analysis of p-HSL in total protein extracts of subcutaneous fats of *TH-Cre; LSL-DTR* and control mice injected with DT, following leptin treatment (500 ng/h). See also Figure 2.S3.

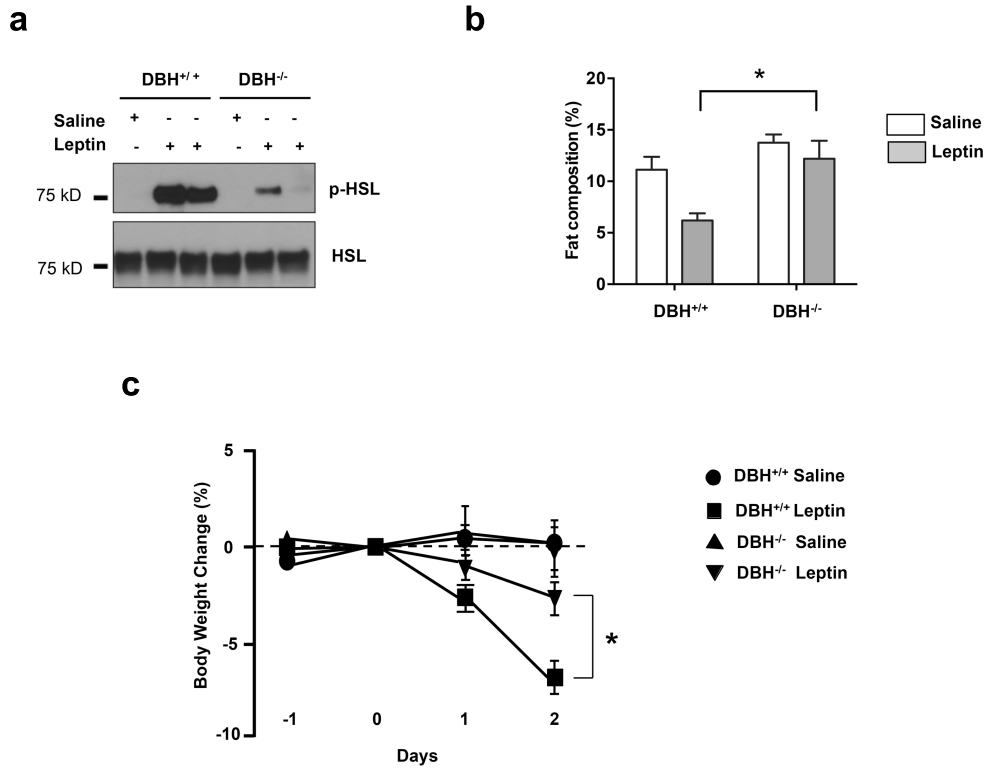

Figure 2.6. Norepinephrine Deficiency Impairs Leptin induced Lipolysis.

(a) Immunoblot analysis of phosphorylated HSL in total protein extracts of fat pads of dopamine β-monoxygenase mutant and control littermates (*DBH-/-* and *DBH+/+* respectively) mice that were treated with 500 ng/h recombinant leptin. **(b)** Whole-body fat composition (*P $<$ 0.05). Results are shown as mean ± SEM (n=4-5). **(c)** Body weight change after leptin treatment (*P $<$ 0.05). Results are shown as mean ± SEM (n=5).

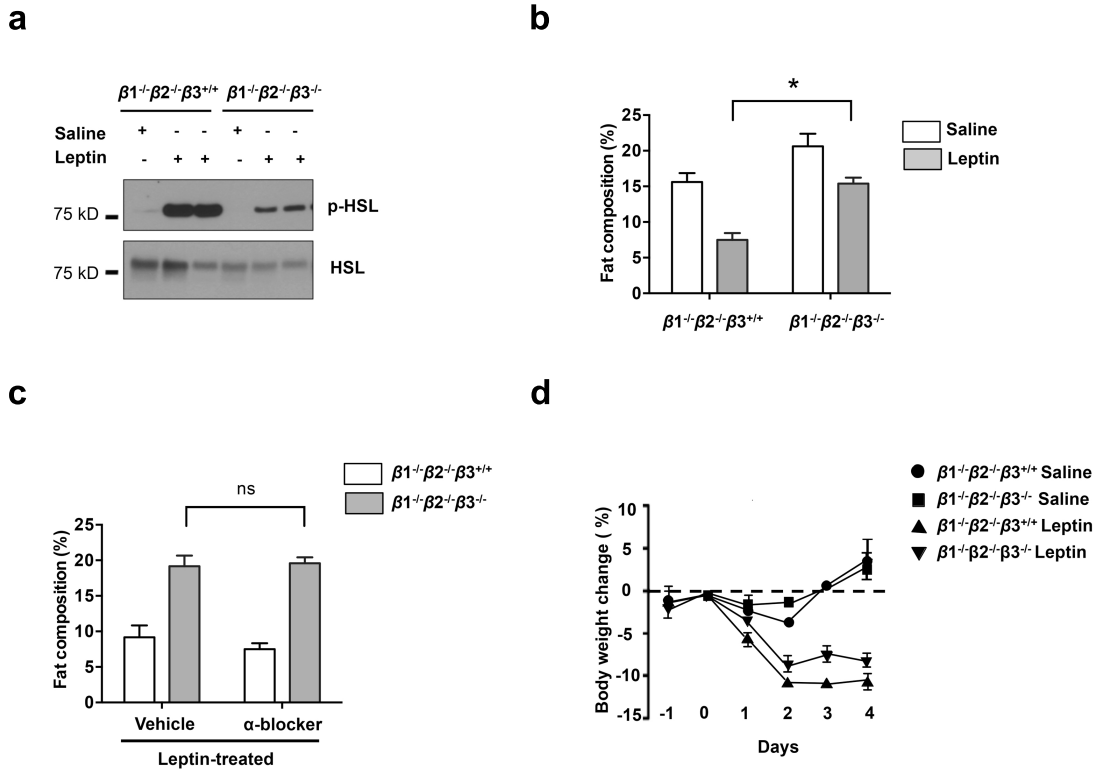

Figure 2.7. Deficiency of all β-adrenergic Receptors Influences Leptin-induced Lipolysis.
(a) IImmunoblot analysis of phosphorylated HSL in total protein extracts of fat pads of $\beta1^{-/-}\beta2^{-/-}\beta3^{+/+}$ and $\beta1^{-/-}\beta2^{-/-}\beta3^{-/-}$ mice that were treated with 500 ng/h recombinant leptin. **(b)** Whole-body fat composition (*P $<$ 0.05, n=4-5). **(c)** α-adrenergic receptors had a minor function in leptin-induced lipolysis (*P $>$ 0.05, n=4-5). **(d)** Whole-body fat composition of mice peripherally treated with recombinant leptin and α-blockers (phentolamine (5 mg/kg, IP) and phenoxybenzamine (10 mg/kg IP) was measured (n=4-5). Results are shown as mean ± SEM.

2.3 DISCUSSION

Leptin is known to stimulate lipolysis and reduce fat mass though the physiologic mechanisms responsible for this have not been fully delineated. In this study, we present data employing functional, anatomic, biochemical and genetic approaches to show that leptin increases lipolysis via the actions of sympathetic neuronal efferents to adipose tissue. These data also provide molecular, cellular and anatomic evidence confirming the existence of neuronal projections onto adipocytes, which have been the subject of conjecture but which have not been directly visualized.

The existence of neuro-adipose junctions in WAT had been inferred based on the fact that a pseudorabies retrograde tracing virus can visualize a set of neural projections in the brain (Bartness and Song, 2007). In addition, immunohistochemistry and immunofluorescence have been used to visualize contacts between sympathetic neurons and adipocytes in sliced tissue (Giordano et al., 1996; Giordano et al., 2005; Thompson, 1986). However, these methods, which require tissue slicing and fixation, do not distinguish en passant neurons from those that directly project onto adipocytes. The visualization of adipocyte-projecting neurons that can completely envelop an adipocyte has not been accomplished so far. We were able to directly visualize neural termini onto adipocytes using intra-vital multiphoton microscopy, which allows deep penetrance onto the live intact tissue, allowing us to visualize deeper structures without the perturbations associated with classical histological methods, which in past studies may have compromised the integrity of the neuro-adipose termini (Helmchen and Denk, 2005).

Confocal or multiphoton microscopy methods are suitable for histological analysis at a microscopic spatial scale, but do not give a 3-dimensional perspective of the organization of the organ as a whole. At a macroscopic spatial scale, methods such as MRI or computed tomography (CT) allow for measurement of whole body fat distribution. However, all of these methods lack the spatial resolution that is required for visualizing structures such as nerve bundles. OPT is a technique with physical principles similar to X-ray CT/gamma radiation, which uses visible light instead of radiation (Gualda et al., 2013.). Scattering of light passing through tissues is minimized by clearing lipids from the whole organ (Quintana and Sharpe, 2011). Unlike most currently available methods, OPT coupled to tissue clearing allows imaging of whole-mount samples with a spatial scale in the order of centimeters.

It has been previously shown that electrical stimulation of WAT nerve bundles can drive lipolysis (Correll, 1963). However, as shown here, nerve bundles in WAT have mixed molecular identity, making it difficult to ascertain the identity of the neurons responsible for this effect. To address this limitation we employed optogenetics, which allows for cell specific stimulation of neurons and in the current studies was used to specifically activate sympathetic neurons in *TH-Cre* mice (Domingos et al., 2011; Domingos et al., 2013). Another advantage of this approach is that it enables the specific activation of axonal projections and, does not require stimulation of neuronal cell bodies (Petreanu et al., 2007; Vrontou et al., 2013). This feature is particularly convenient for autonomic neurons, given the deep localization of their cell bodies along the anterior face of the spinal cord and the intrinsic difficulty of implanting optical fibers in this location. Previous studies using neural tracing have revealed that sympathetic neurons innervating the subcutaneous inguinal fat pads localize to the 13th thoracic ganglia, which localizes at the dorsal

edge of the diaphragm muscle, in the transition between the thorax and the abdomen (Youngstrom and Bartness, 1995). This anatomical location is particularly inaccessible and unsuitable for chronic implants of optical fibers or equivalent devices. However, as we show here, subcutaneous implant of optical fibers for stimulation of nerve terminals is feasible and effective. We used this approach to show that optogenetic gain of function of the catecholaminergic signaling to the neuro-adipose junction can lead to the phosphorylation of HSL and lipolysis of WAT. Similarly, previous loss of function experiments that assessed the effect of sympathetic input on lipolysis also did not allow analysis of the effect of specific cells in the way that optogenetics can. Thus, the use of mechanical denervation, does not distinguish between neurons that directly innervate adipocytes versus those that are passing through. We have not yet profiled the non-TH nerve fibers but it is reasonable to expect that some might be parasympathetic, nociceptive, sensory fibers and/or en passant axons. The function of these fibers could be assessed similarly to those that we report using optogenetics to activate other populations including cholinergic neurons by studying choline acetyltransferase (ChAT)-*Cre* mice and/or neurons expressing other molecular markers. Chemical ablation with capsaicin also has limitations, as this treatment is not specific to sympathetic neurons and affects all transient receptor potencial vaniloid (TRPV)-expressing fibers (Holzer, 1991). Chemical ablation with 6-hydroxydopamine is likely to affect dopaminergic as well as enteric neurons, creating secondary systemic effects (Ding et al., 2004).

To avoid these limitations and gain local control over sympathetic neural activity, we used additional molecular genetic tools that combine tissue-specificity with a localized effect. We show that ablation of the sympathetic neurons by DTR expression in TH-positive neurons followed by local DT injection in WAT abolishes the effect of leptin on HSL phosphorylation. We also noted that the loss of function due to post-synaptic manipulations (i.e. the triple β-adrenergic receptor KO in Figure 2.7) has a lesser effect on the size of adipose tissue depots than that seen after pre-synaptic manipulations such as a loss of DBH, or pharmacologic or mechanical ablation of neural input to fat (Figure 2.6). This suggests that leptin-induced production of NE from sympathetic neurons could act through additional receptors that are not one of the three β-adrenergic receptors that we tested. Alternatively, sympathetic neurons may co-release other neurotransmitters or neuropeptides that signal through non-adrenergic receptors. This could account for the residual leptin-induced weight loss seen in *DBH-/-*, although this effect is not significant when compared to controls. Thus, an in-depth knowledge of the underlying sympathetic neural circuits could provide strategies to pharmacologically activate specific sympathetic neuronal population, thus circumventing leptin resistance, as potential treatment of obesity.

A canonical effect of leptin is to increase sympathetic signaling to BAT thus promoting the thermogenesis (Bachman et al., 2002; Landsberg et al., 1984). However the role of autonomic stimulation of white fat has been less well studied. We now show that the sympathetic activity is also responsible for the leptin-stimulated lipolysis in WAT. While leptin has been assumed to increase lipolysis via activation of sympathetic efferent fibers, this has not been directly shown. Adrenergic agonists have been shown to induce the formation of beige (brite) fat and these data suggest that sympathetic innervation may also stimulate this phenotypic change in adipose tissue (Bachman et al., 2002; Giralt and Villarroya, 2013; Dempersmier et al., 2015). Consistent with this, leptin has also been suggested to increase the formation

of beige fat (Dodd et al., 2015).

Because brown adipocytes have relatively smaller fat storages compared to white adipocytes, while having higher metabolic demand, the continuous thermogenic response of BAT might require the supply of FFA from WAT mobilized in other parts of the body. It is therefore reasonable to speculate that the coordinated sympathetic actions in BAT and WAT in response to leptin could help maximize the hormone's effect on energy expenditure and fat metabolism. Future studies delineating the neural circuits connecting the central action of leptin with the peripheral activation of sympathetic system will be necessary to test this hypothesis. Particularly, it would be of great importance to develop technologies that would allow whole body visualization and mapping of peripheral neuronal circuits using some of the approaches presented here.

In summary, we provide direct evidence that the sympathetic neuro-adipose junction is both necessary and sufficient for leptin to drive lipolysis in WAT.

2.4 EXPERIMENTAL PROCEDURES

Antibodies and drugs

The antibodies were obtained from the following vendors: HSL (Cellsignaling), phospho-HSL (Cellsignaling), phospho-PKA substrate (Cellsignaling), TH (Peel-freez), TH (Aves Lab) and actin (Sigma). Hexomethinium Choloride, phentolamine and phenoxybenzamine were from Sigma. DT was purchased from Merck Millipore. Recombinant mouse leptin was obtained from Amylin Pharmaceuticals (San Diego, CA).

Mice

DBH-/- mice were kindly provided by Steve Thomas in University of Pennsylvania. *Adrβ1*$^{-/-}$*β2*$^{-/-}$ and *Adrβ3*$^{-/-}$ were kindly provided by Bruce Spiegelman at Harvard Medical School. *TH-Cre* , *LSL-ChR2-YFP* (Stock No. 012-569, Daou et al., 2013), *LSL-DTR* and *C57BL/B6J* mice at 6-10 weeks old were purchased from The Jackson Laboratory (JAX). Animal procedures were approved by the ethics committee of Instituto Gulbenkian de Ciência and IACUC of Rockefeller University.

Optical Projection Tomography

6 weeks old *C57BL/B6J* mice were sacrificed with carbon dioxide. The inguinal fat pads were dissected from the mice with Dumont 5 Forceps, fixed in 4% paraformaldehyde (Sigma-Aldrich) for 3 h at room temperature (RT) and subjected to the OPT clearing protocol as described below. Images of the whole fat tissue were acquired using a 1x lens, mounted on an Infinitube tube lens, and projected into an Hamamatsu FlashLT sCMOS camera. A total of 1600 images were acquired for a full rotation (0.25 degree steps). The series of projections were then pre-processed for back-projection using FIJI in order to remove hot pixels, re-align the axis of rotation in relation to the camera-chip, and finally the back-projection reconstruction was done using the Skyscan's NRecon software (Schindelin et al., 2012). The stack of slices was further processed with FIJI, to increase contrast and saved to posterior analysis with the software Amira V5.3. Using this software, 3D reconstructions and image segmentation was performed to identify and reconstruct individual parts of the fat organs. Detailed instructions for setting up an OPT system can be found at https://sites.google.com/site/openspinmicroscopy/home/opt.

Clearing for Optical Projection Tomography

The adipose organ was fixed in 4% paraformaldehyde (Sigma-Aldrich) for 3 h at room temperature (RT) with agitation, followed by 15 min wash step with Phosphate Buffered Saline (PBS) 1X at RT. The wash step was repeated two more times. The sample was placed in 1% low melting agarose (Sigma-Aldrich). The agarose volume was approximately 24.5 cm^3 (height 3.5 cm and diameter 1.5 cm). The inguinal fat pad was immersed in a 10% methanol (VWR) solution at RT (with agitation). Afterwards 10% increasing steps were performed every day until dehydration in 100% methanol was reached (RT with agitation). The replacement of the methanol with 1:2 mixture of benzyl alcohol (BA) (Merck) and benzyl benzoate (BB) (Merck) was performed in 15% increasing steps every day until clarification was reached.

In-vivo 2-photon microscopy

Mice 2 months old were kept anesthetized with 2% isofluorane. During surgery, body temperature was maintained at 37°C with a warming pad. After application of local anesthetics (lidocaine), a sagittal incision of the skin is made above the supra-pelvic flank to expose the subcutaneous inguinal fat pad. An imaging chamber was custom built to minimize fat movement. Warm imaging solution (in mM: 130 NaCl, 3 KCl, 2.5 CaCl2, 0.6 6H2O,MgCl2, 10 HEPES without Na, 1.2 NaHCO3, 10 glucose, pH 7.45 with NaOH) (37°C) mixed with a fat dye (LipidTOX) was applied to label adipocytes, maintain tissue integrity, and to allow the use of immersion objective. Imaging experiments were performed under a two-photon laser-scanning microscope (Ultima, Prairie Instruments Inc.). Live images were acquired at 8–12 frames per second, at depths below the surface ranging from 100 to 250 mm, using an Olympus 20x 0.8 N.A. water immersion objective, with a laser tuned to 860-940 nm wavelength, and emission filters 525/50 nm and 595/50 nm for green and red fluorescence, respectively. Laser power was adjusted to be 20–25 mW at the focal plane (maximally 35 mW), depending on the imaging depth and level of expression of dtTomato and LipidTOX spread. tdTomato fluorescence was used to identify TH-positive fibers until photo-bleaching occurred.

Leptin treatment and lipolysis analysis

To examine the effect of leptin treatment on lipolysis, leptin (delivery rate of 500 ng/h) or saline was delivered through osmotic pumps (Alzet; Palo Alto, CA) subcutaneously for 2 days. Body weight was recorded daily. Body fat composition was measured using EchoMRI body analyzer at end point before subcutaneous or epididymal adipose tissues were collected. HSL phosphorylation was detected by both immunohistochemistry of paraffin sections at 6 μm thickness and/or western blot of subcutaneous or epididymal adipose tissues. NE levels in serum and subcutaneous fad pads were determined with NE ELISA kit (Labor Diagnostika Nord GmbH, Nordhorn, Germany). Tissues were homogenized and sonicated in homogenization buffer (0.01 N HCl, 1 mM EDTA) and cellular debris was pelleted by centrifugation at 13 000 r.p.m. for 15 min at 4°C. All tissue samples were normalized to total tissue protein concentration.

Sympathetic neuronal cultures

Sympathetic neurons of primary cultures of SCG were performed from postnatal day 30 *TH-Cre; LSL-ChR2-YFP* mice. Briefly, after decapitation, both SCG of each animal were removed and cleaned of all visible adipose tissue and surrounding connective tissue before transfer to Hank's Balanced Salt Solution (HBSS). Then, SCG were treated enzymatically in two steps to yield single neurons. First, SCG were subjected to enzymatic dissociation in collagenase solution (2.5 mg/mL) in HBSS, followed by trypsin solution (0.25%) in PBS at 37°C with agitation. The SCG were next mechanically dissociated into a suspension of single cells. Isolated sympathetic cells were plated in a final concentration of 2500 cells per coverslip (6 mm) coated with poly-D-lysine and growth factor-reduced Matrigel, and cultured for 7 days in vitro (DIV) in Neurobasal medium supplemented with 2% B-27, 10% fetal bovine serum, 1% penicillin/streptomycin, nerve growth factor (100 ng/mL) and 5-fluoro-2'-deoxyuridine (5 μM).

Diphtheria toxin injections

General anesthesia was induced and maintained with isofluorane. After application of local anesthetics (lidocaine), a small incision of the skin was made above the supra- pelvic flank. A Hamilton syringe (10 µl) is inserted into the incision aiming at the inguinal WAT. Each DT injection is made slowly, over period of 30 minutes. Posology was 10 ng/g.

Mechanical denervation

The nerve bundle 2 mm distal from the tip of the epididymal fat was physically crushed for 30 seconds and then released using a forcep. Leptin was administrated through osmotic pump 3 days after nerve crush. HSL phosphorylation was detected two days upon leptin treatment.

Hexomethium chloride, isopreterenol and α-blocker treatment

Hexomethium chloride (500 µg/h) was administrated during leptin treatment through separate osmotic pump, and α-blockers, phentolamine (5 mg/kg, IP) and phenoxybenzamine (10 mg/kg IP) were administrated twice a day during the course of leptin treatment (500 ng/h). Isopreterenol (250 µg per mouse) was delivered in saline through jugular vein injection. Blood was drawn through tail bleeding and plasma free fatty acid was measured using NETO kit (Wako). For FFA release upon isopreterenol treatment in vitro, adipose tissue explants were dissected and cultured in Hanks medium and stimulated with isopretenerol at 10 µg/ml for 3 hours. FFA was measured in the medium.

NE measurements after optogenetic stimulation ex vivo

SCG were removed from 28-30 days old *TH-Cre; LSL-ChR2-YFP* mice under a stereomicroscope and placed in Dulbecco's Modified Eagle's medium (DMEM, Invitrogen, Carlsbad, CA, U.S.A.). Ganglia were cleaned from the surrounding tissue capsule and transferred into 8-well Tissue Culture Chambers (Sarstedt, Nümbrecht, Germany) that were previously coated with poly-D-lysine (Sigma/Aldrich, Steinheim, Germany) in accordance to the manufacturer's instructions. Ganglia were then covered with 5 µl of Matrigel (BD Bioscience, San Jose, CA, U.S.A.) and incubated for 7 min at 37°C. DMEM without phenol red (Invitrogen) supplemented with 10 percent fetal bovine serum (Invitrogen), 2 mM L-Glutamine (Biowest, Nuaillé, France) and nerve growth factor (Sigma/Aldrich) was subsequently added. SCG ganglia were cultured for minimum 24 h prior to further manipulation. Depolarization of sympathetic neurons in explant cultures was performed on a Yokogawa CSU-X Spinning Disk confocal using the 488 nm laser line and pointing at the region of interest (ROI) for 200 µs. Stimulation was repeated 5 times using 40 percent of laser intensity. NE in the SCG explant culture medium was determined with NE ELISA kit (Labor Diagnostika Nord GmbH, Nordhorn, Germany). The same procedure was performed for *LSL-ChR2-YFP* control mice.

Surgeries and optogenetic stimulation

General anesthesia was induced and maintained with isofluorane. After application of local anesthetics (lidocaine), a sagittal incision of the skin was made above the neck and supra-pelvic flank. A hemostat was inserted into the incision, and, by opening and closing the jaws of the hemostat, spread the subcutaneous tissue to create a longitudinal pocket for the optical fiber. The pocket was made long enough to allow about 4-6 cm of fiber (Thor

Labs FT200). The tip of the fiber targeted the anatomical location of the inguinal fat pad. The other end of the fiber, the ferrule-connector end, was secured along the skin via sutures and dermal staples. Appropriate local analgesic was used post-surgically. Optogenetical stimulations were performed 48 hours after surgical procedures. Stimulation session in Figure 2.3 d lasted 4-6 h and was done via a one second 20 Hz pulse of blue laser every other second, originating from a 473 nm solid laser source (OEM-BL-473-00100-CWM-SD-05). Laser source had an output power of 100 mW. Ferrule-coupled optical fibers of 200 um diameter (Thorlabs - FT200EMT-CANNULA - TS1031629) were connected to ferrule patch cords (Thorlabs - FT200EMT-FC/PC-ferrule) with mating sleeves (Thorlabs - ADAF1), and the later to the laser source via FC/PC adaptor. NE in subcutaneous fad pads was determined with NE ELISA kit (Labor Diagnostika Nord GmbH, Nordhorn, Germany) as described above. Stimulation protocol in Figure 2.3 e took place every day for two weeks, and solely during the rodent rest period. Longer sessions as in Figure 2.3 f had duration of four weeks. Stimulation sessions lasted 4-6 h and were performed as described above.

MRI fat measurements and fat pad segmentation

Mice were subjected to optogenetic stimulation as stated above, perfused with 4% PFA/PBS, post-fixed over 2-3 days and embedded in Fomblin Oil (Sigma) for scanning. Imaging was performed on a 7.0 Tesla 70/30 Bruker Biospec small animal MRI system with a 12 cm diameter 450 mT/m amplitude and 4500 T/m/s slew rate actively shielded gradient subsystems with integrated shim capability. A linear coil with 7 cm diameter and a length sufficient to cover the whole body of the animal is used for excitation and reception of the magnetic resonance signal. Two image sets were acquired, one with fat suppression and one without. Axial images, covering the whole animal in 75 0.4 mm thick slices without gap were acquired in an interleaved way by using a RARE pulse sequence with RARE factor 2. The fat suppression, added to the second scan, consists of a 90° Gaussian pulse with 2.6067 ms duration and 1051.1 Hz bandwidth. Data was converted into TIF files by FIJI software. The subcutaneous inguinal fat distribution was determined with semi-automated Amira V5.3 software segmentation of scanned images. Amira V5.3 software segmentation relies on automated grouping of pixels with the same index of intensity in the grey-scale. An automatic segmentation based on the grey threshold levels, which decomposes the image domain into subsets, allowed to define the right and the left inguinal fat depots, which were further saved as unique fields. Volume of the right and the left subcutaneous fat pad was defined as the number of voxels times size of a single voxel. The size of stimulated fat pads was determined, and the effect of optogenetic stimulation of neurons on fat mass was calculated in the same animal relative to non-stimulated contralateral side.

Statistical methods

Statistics were performed in GraphPad Prism and involved computation of means, standard errors of the mean, which accompany each figure legends. T-tests and ANOVAs were employed where appropriate and are indicated in the text together with the P values.

2.5 REFERENCES

Arvaniti, K., Deshaies, Y., and Richard, D. (1998). Effect of leptin on energy balance does not require the presence of intact adrenals. Am. J. Physiol. 275, R105-111.

Awad, S., Constantin-Teodosiu, D., Macdonald, I.A., and Lobo, D.N. (2009). Short-term starvation and mitochondrial dysfunction - a possible mechanism leading to postoperative insulin resistance. Clin. Nutr. 28, 497-509.

Bachman, E.S., Dhillon, H., Zhang, C.Y., Cinti, S., Bianco, A.C., Kobilka, B.K., and Lowell, B.B. (2002). betaAR signaling required for diet-induced thermogenesis and obesity resistance. Science 297, 843-845.

Bartness, T.J., Kay Song, C., Shi, H., Bowers, R.R., and Foster, M.T. (2005). Brain-adipose tissue cross talk. Proc. Nutr. Soc. 64, 53-64.

Bartness, T.J., and Song, C.K. (2007). Thematic review series: adipocyte biology. Sympathetic and sensory innervation of white adipose tissue. J. Lipid Res. 48, 1655-1672.

Brasaemle, D.L. (2007). Thematic review series: adipocyte biology. The perilipin family of structural lipid droplet proteins: stabilization of lipid droplets and control of lipolysis. J. Lipid Res. 48, 2547-2559.

Buch, T., Heppner, F.L., Tertilt, C., Heinen, T.J., Kremer, M., Wunderlich, F.T., Jung, S., and Waisman, A. (2005). A Cre-inducible diphtheria toxin receptor mediates cell lineage ablation after toxin administration. Nat. Methods 2, 419-426.

Campfield, L.A., Smith, F.J., Guisez, Y., Devos, R., and Burn, P. (1995). Recombinant mouse OB protein: evidence for a peripheral signal linking adiposity and central neural networks. Science 269, 546-549.

Correll, J.W. (1963). Adipose tissue: ability to respond to nerve stimulation in vitro. Science 140, 387-388.

Daou, I., Tuttle, A.H., Longo, G., Wieskopf, J.S., Bonin, R.P., Ase, A.R., Wood, J.N., Koninck, Y.D., Ribeiro-da-Silva, A., Mogil, J.S., et al. (2013). Remote Optogenetic Activation and Sensitization of Pain Pathways in Freely Moving Mice. J. Neurosci. 33, 18631–18640.

Dempersmier, J., Sambeat, A., Gulyaeva, O., Paul, S.M., Hudak, C.S., Raposo, H.F., Kwan, H.Y., Kang, C., Wong, R.H., and Sul, H.S. (2015). Cold-inducible Zfp516 activates UCP1 transcription to promote browning of white fat and development of brown fat. Mol. Cell 57, 235-246.

Ding, Y.M., Jaumotte, J.D., Signore, A.P., and Zigmond, M.J. (2004). Effects of 6-hydroxydopamine on primary cultures of substantia nigra: specific damage to dopamine neurons and the impact of glial cell line-derived neurotrophic factor. J. Neurochem. 89, 776-787.

Dodd, G.T., Decherf, S., Loh, K., Simonds, S.E., Wiede, F., Balland, E., Merry, T.L., Munzberg, H., Zhang,

Z.Y., Kahn, B.B., et al. (2015). Leptin and insulin act on POMC neurons to promote the browning of white fat. Cell 160, 88-104.

Domingos, A.I., Sordillo, A., Dietrich, M.O., Liu, Z.W., Tellez, L.A., Vaynshteyn, J., Ferreira, J.G., Ekstrand, M.I., Horvath, T.L., de Araujo, I.E., et al. (2013). Hypothalamic melanin concentrating hormone neurons communicate the nutrient value of sugar. Elife 2, e01462.

Domingos, A.I., Vaynshteyn, J., Voss, H.U., Ren, X., Gradinaru, V., Zang, F., Deisseroth, K., de Araujo, I.E., and Friedman, J. (2011). Leptin regulates the reward value of nutrient. Nat. Neurosci. 14, 1562-1568.

Elia, M., Stubbs, R.J., and Henry, C.J. (1999). Differences in fat, carbohydrate, and protein metabolism between lean and obese subjects undergoing total starvation. Obes. Res. 7, 597-604.

Friedman, J.M., and Halaas, J.L. (1998). Leptin and the regulation of body weight in mammals. Nature 395, 763-770.

Giordano, A., Frontini, A., Murano, I., Tonello, C., Marino, M.A., Carruba, M.O., Nisoli, E., and Cinti, S. (2005). Regional-dependent increase of sympathetic innervation in rat white adipose tissue during prolonged fasting. J. Histochem. Cytochem. 53, 679-687.

Giordano, A., Morroni, M., Santone, G., Marchesi, G.F., and Cinti, S. (1996). Tyrosine hydroxylase, neuropeptide Y, substance P, calcitonin gene-related peptide and vasoactive intestinal peptide in nerves of rat periovarian adipose tissue: an immunohistochemical and ultrastructural investigation. J. Neurocytol. 25, 125-136.

Giralt, M., and Villarroya, F. (2013). White, brown, beige/brite: different adipose cells for different functions? Endocrinology 154, 2992-3000.

Gualda, E.J., Vale, T., Almada, P., Feijo, J.A., Martins, G.G., and Moreno, N. (2013). OpenSpinMicroscopy: an open-source integrated microscopy platform. Nat. Methods 10, 599-600.

Halaas, J.L., Boozer, C., Blair-West, J., Fidahusein, N., Denton, D.A., and Friedman, J.M. (1997). Physiological response to long-term peripheral and central leptin infusion in lean and obese mice. Proc. Natl. Acad. Sci. U S A 94, 8878-8883.

Halaas, J.L., Gajiwala, K.S., Maffei, M., Cohen, S.L., Chait, B.T., Rabinowitz, D., Lallone, R.L., Burley, S.K., and Friedman, J.M. (1995). Weight-reducing effects of the plasma protein encoded by the obese gene. Science 269, 543-546.

Helmchen, F., and Denk, W. (2005). Deep tissue two-photon microscopy. Nat. Methods 2, 932-940.

Holzer, P. (1991). Capsaicin: cellular targets, mechanisms of action, and selectivity for thin sensory neurons. Pharmacol. Rev. 43, 143-201.

Landsberg, L., Saville, M.E., and Young, J.B. (1984). Sympathoadrenal system and regulation of thermogenesis. Am. J. Physiol. 247, E181-189.

Montez, J.M., Soukas, A., Asilmaz, E., Fayzikhodjaeva, G., Fantuzzi, G., and Friedman, J.M. (2005). Acute leptin deficiency, leptin resistance, and the physiologic response to leptin withdrawal. Proc. Natl. Acad. Sci. U S A 102, 2537-2542.

Newman, W.P., and Brodows, R.G. (1983). Insulin action during acute starvation: evidence for selective insulin resistance in normal man. Metabolism 32, 590-596.

Nguyen, K.D., Qiu, Y., Cui, X., Goh, Y.P., Mwangi, J., David, T., Mukundan, L., Brombacher, F., Locksley, R.M., and Chawla, A. (2011). Alternatively activated macrophages produce catecholamines to sustain adaptive thermogenesis. Nature 480, 104-108.

Pelleymounter, M.A., Cullen, M.J., Baker, M.B., Hecht, R., Winters, D., Boone, T., and Collins, F. (1995). Effects of the obese gene product on body weight regulation in ob/ob mice. Science 269, 540-543.

Petreanu, L., Huber, D., Sobczyk, A., and Svoboda, K. (2007). Channelrhodopsin-2-assisted circuit mapping of long-range callosal projections. Nat. Neurosci. 10, 663-668.

Quintana, L., and Sharpe, J. (2011). Optical projection tomography of vertebrate embryo development. Cold Spring Harb. Protoc. 2011, 586-594.

Rafael, J., and Herling, A.W. (2000). Leptin effect in ob/ob mice under thermoneutral conditions depends not necessarily on central satiation. Am. J. Physiol. Regul. Integr. Comp. Physiol. 278, R790-795.

Rezai-Zadeh, K., and Munzberg, H. (2013). Integration of sensory information via central thermoregulatory leptin targets. Physiol. Behav. 121, 49-55.

Scarpace, P.J., and Matheny, M. (1998). Leptin induction of UCP1 gene expression is dependent on sympathetic innervation. Am. J. Physiol. 275, E259-264.

Schindelin, J., Arganda-Carreras, I., Frise, E., Kaynig, V., Longair, M., Pietzsch, T., Preibisch, S., Rueden, C., Saalfeld, S., Schmid, B., et al. (2012). Fiji: an open-source platform for biological-image analysis. Nat. Methods 9, 676-682.

Tavernier, G., Jimenez, M., Giacobino, J.P., Hulo, N., Lafontan, M., Muzzin, P., and Langin, D. (2005). Norepinephrine induces lipolysis in beta1/beta2/beta3-adrenoceptor knockout mice. Mol. Pharmacol. 68, 793-799.

Thompson, G.E. (1986). Vascular and lipolytic responses of the inguinal fat pad of the sheep to adrenergic stimulation, and the effects of denervation and autotransplantation. Q. J. Exp. Physiol. 71, 559-567.

Vrontou, S., Wong, A.M., Rau, K.K., Koerber, H.R., and Anderson, D.J. (2013). Genetic identification of C fibres that detect massage-like stroking of hairy skin in vivo. Nature 493, 669-673.

Weisberg, S.P., McCann, D., Desai, M., Rosenbaum, M., Leibel, R.L., and Ferrante, A.W., Jr. (2003). Obesity is associated with macrophage accumulation in adipose tissue. J. Clin. Invest. 112, 1796-1808.

Youngstrom, T.G., and Bartness, T.J. (1995). Catecholaminergic innervation of white adipose tissue in Siberian hamsters. Am. J. Physiol. 268, R744-751.

2.6 SUPPLEMENTARY FIGURES

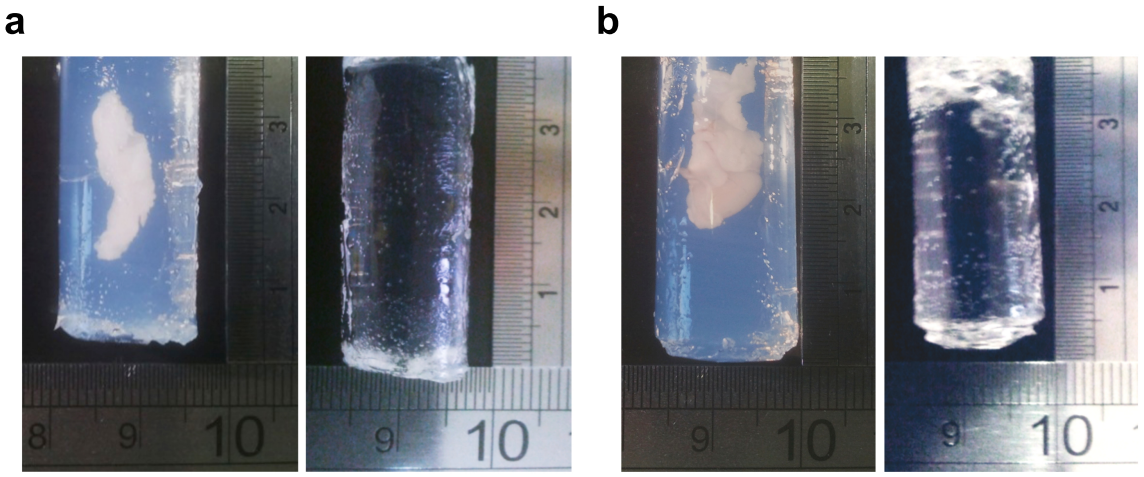

Figure 2.S1. Representative images of adipose tissues embedded in agarose blocks. Adipose tissue are shown before and after the BA:BB clearing procedure

(a) Inguinal and **(b)** visceral adipose tissues embedded in agarose blocks and shown before (left) and after (right) BA:BB clearing.

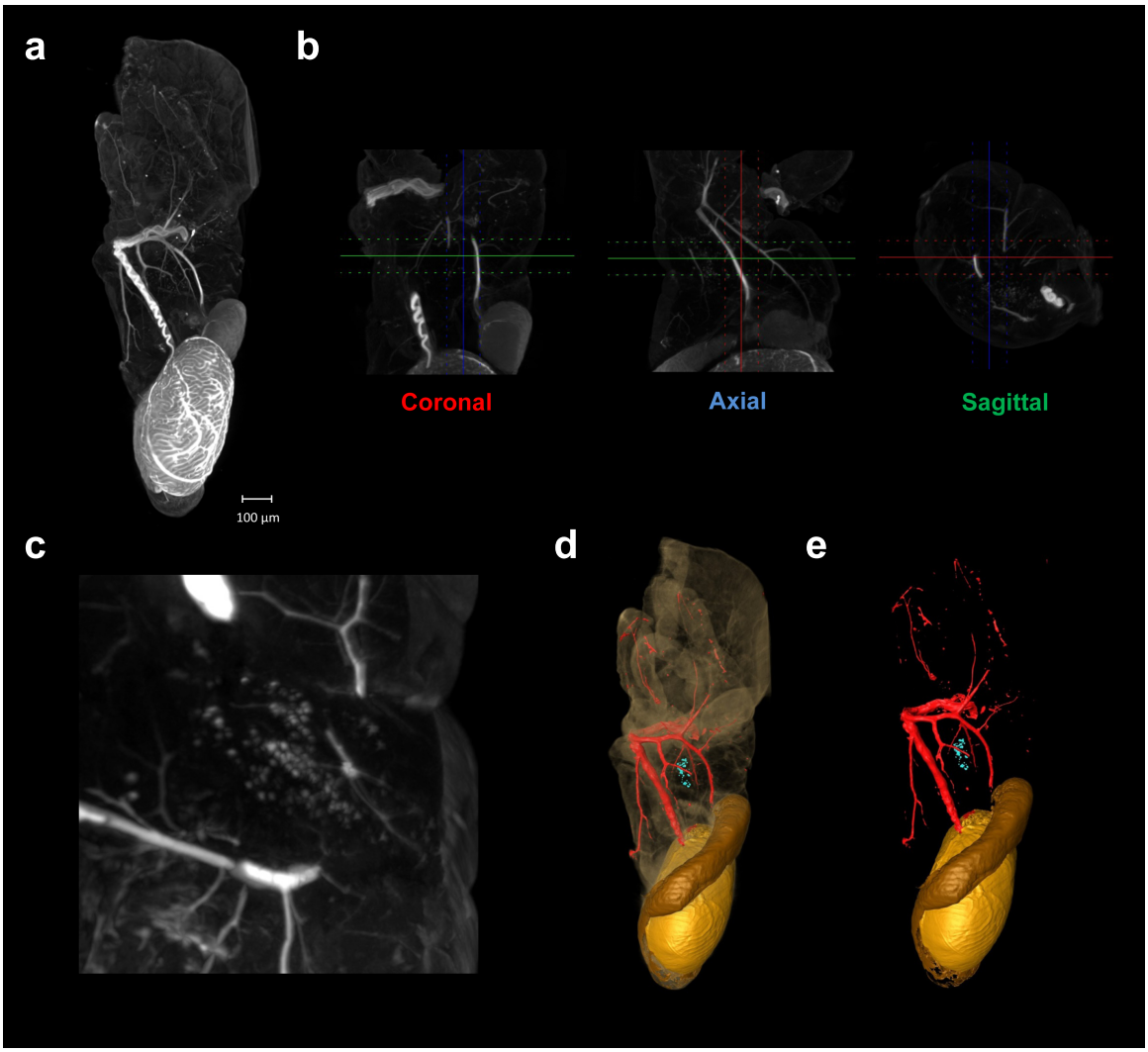

Figure 2.S2. Visceral adipose tissue visualised with the OPT method.
(a) 3-D reconstruction in maximal intensity projection of the OPT coronal sections. Scale bar = 100µm **(b)** Orthogonal 400 µm OPT-slabs of visceral fat in coronal, axial and sagittal view. **(c)** Axial view of the globular structures within visceral fat **(d)** Segmentation of blood vessels (red), testicle (yellow), epididymis (brown) and granular structures (blue) within the visceral fat. **(e)** Surface view of segmented structures within visceral adipose tissue.

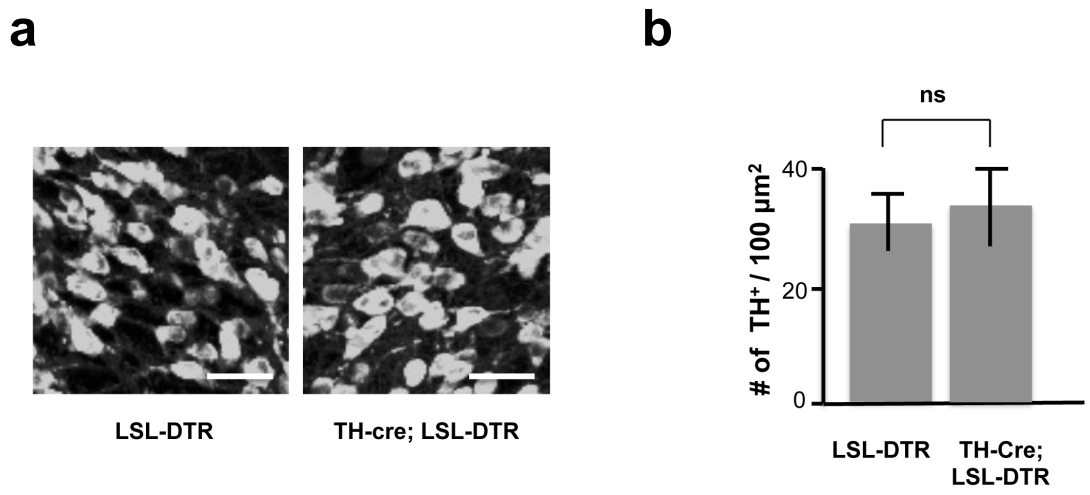

Figure 2.S3. Local injection of DT in inguinal fat preserves TH-positive neurons in the brain. **(a)** Staining of TH positive neurons in brains of *LSL-DTR* (left) and *TH-Cre; LSL-DTR* mice which were locally injected in inguinal fat pads with DT. **(b)** Quantification of TH-positive cell bodies per area of photomicrograph. Results are shown as mean ± SEM.

3 | SYMPATHETIC NEURON--ASSOCIATED MACROPHAGES CONTRIBUTE TO OBESITY

Roksana M Pirzgalska[1, 11], Elsa Seixas[1, 11], Jason S Seidman[2], Verena M Link[2,3], Noelia Matínez Sánchez[1], Ines Mahú[1], Raquel Mendes[1], Vitka Gres[1], Nadiya Kubasova[1], Imogen Morris[1], Bernardo A Arús[1,4], Chelsea M Larabee[1], Miguel Vasques[1,5], Francisco Tortosa[6], Ana L Sousa[7], Sathyavathy Anandan[1], Erin Tranfield[7], Maureen K Hahn[8], Matteo Iannacone[9], Nathaneal J Spann[2], Christopher K Glass[2], Ana I Domingos[1,10]

[1] Obesity Laboratory, Instituto Gulbenkian de Ciência, Oeiras, Portugal

[2] Department of Cellular and Molecular Medicine, University of California, San Diego, La Jolla, California, USA

[2,3] Faculty of Biology, Department II, Ludwig-Maximilians Universität München, Planegg-Martinsried, Germany

[4]Departamento de Bioquímica, Instituto de Ciências Básicas da Saúde, Universidade Federal do Rio Grande do Sul, Porto Alegre, Brazil

[5] Department of Endocrinology, Curry Cabral Hospital, Centro Hospitalar de Lisboa Central, Lisbon, Portugal

[6] Department of Pathology, Centro Hospitalar Lisboa Norte, Hospital de Santa Maria, EPE, Lisbon, Portugal

[7] Electron Microscopy Unit, Instituto Gulbenkian de Ciência, Oeiras, Portugal

[8] Vanderbilt Kennedy Center for Research on Human Development, Vanderbilt University School of Medicine, Nashville, Tennessee, USA

[9] Division of Immunology, Transplantation and Infectious Diseases, Istituto di Ricovero e Cura a Carattere Scientifico (IRCCS) San Raffaele Scientific Institute, Milan, Italy

[10] The Howard Hughes Medical Institute (HHMI), New York, NY, USA

[11] co-first authors

Author's contribution: R.M.P performed two-photon and confocal microscopy. E.S. and R.M.P performed flow cytometry. E.S. and R.M.P performed RT-PCR. J.S.S. and R.M.P performed low-input RNA-seq. V.M.L., J.S.S. and R.M.P analyzed low-input RNA-seq. R.M.P. performed optogenetics. A.L.S. performed electron microscopy. S.A. and R.M.P helped processing samples for electron microscopy. E.S. and R.M.P did bone marrow chimeras and functional tests. M.I. and and E.T. helped developing protocols for electron microscopy. N.K., I. Morris, R.M. and V.G. performed mouse husbandry and genotyping. B.A.A. performed quantification of adipocyte diameter. N.M.S. performed immunohistochemistry for UCP-1. R.M.P performed NE ELISAs. I. Mahú helped with NE ELISAs. F.T. and M.V. processed human ganglia. M.K.H. provided Slc6a2 -/- mice. N.J.S. developed low input RNA-seq protocols. A.I.D, C.K.G. and R.M.P wrote the manuscript. C.M.L helped editing the text. R.M.P prepared figures and legends.

ABSTRACT

The cellular mechanism(s) linking macrophages to norepinephrine (NE)-mediated regulation of thermogenesis have been a topic of debate. Here we identify sympathetic neuron–associated macrophages (SAMs) as a population of cells that mediate clearance of NE via expression of solute carrier family 6 member 2 (SLC6A2), a NE transporter, and monoamine oxidase A (MAOA), a degradation enzyme. Optogenetic activation of the sympathetic nervous system (SNS) upregulates NE uptake by SAMs and shifts the SAM profile to a more proinflammatory state. NE uptake by SAMs is prevented by genetic deletion of Slc6a2 or inhibition of the encoded transporter. We also observed an increased proportion of SAMs in the SNS of two mouse models of obesity. Genetic ablation of Slc6a2 in SAMs increases increases thermogenesis and leads to substantial and sustained weight loss in obese mice. We further show that this pathway is conserved, as human sympathetic ganglia also contain SAMs expressing the analogous molecular machinery for NE clearance, which thus constitutes a potential target for obesity treatment.

3.1 INTRODUCTION

The SNS innervates the adipose tissue to locally promote lipolysis and fat mass reduction via norepinephrine (NE) signaling (Zeng et al., 2015). In obesity, chronic inflammation of adipose tissue underlies adipose tissue dysfunction, in which macrophages are thought to play a central role (Mathis, 2013; Zeng et al., 2015). The mechanism that links macrophages in the adipose tissue (AT) to NE remains controversial. Whereas some groups defend that anti-inflammatory AT macrophages (ATMs) produce NE to sustain thermogenesis and browning, other groups have evidence that ATM do not have the biosynthetic machinery for NE production, thus refuting this model (Fischer et al., 2017; Nguyen et al., 2011; Spadaro et al., 2017).

In this study, we identify a previously undescribed population of sympathetic-associated macrophages (SAM) that uptake NE via a specific molecular machinery that is not present in ATMs. First, we visualize SAMs in vivo with two-photon microscopy, and ultrastructurally, to document their elaborate morphology. Second, we isolate SAMs from dissected nerve bundles in white adipose tissue (WAT) and subject them to transcriptional profiling to reveal a constellation of neural and adrenergic-related genes that are differentially expressed, as compared to neighboring macrophages in fat (ATM), distant macrophages in the spleen, or microglia. Unlike ATMs, SAMs accumulate intracellular NE, despite not expressing tyrosine hydroxylase (TH), a critical enzyme in the pathway for NE biosynthesis. We use optogenetics to demonstrate that SNS activity increases NE content in SAMs, which correlates with a pro-inflammatory state. We functionally demonstrate that SAMs uptake and degrade NE via, respectively, the norepinephrine transporter (Slc6a2) and the enzyme monoamine oxidase (MAOa). This molecular machinery is specific to SAMs, and is not present in nearby ATMs residing in the parenchyma of white adipose tissue, nor in any other hematopoietic population that has insofar been gene profiled. We took advantage of such tissue specificity in the hematopoietic lineage to knockout Slc6a2 from SAMs by transfer of bone marrow from donor *Slc6a2-/-* mice onto genetically obese *ob/ob* recipient mice. Leptin deficient *ob/ob* mice with Slc6a2 loss of function in SAMs lose substantial percent of body weight after a brief normalization of food intake and this loss is stable for at least 8 weeks. These mice have higher thermogenesis and lipid mobilization, which is not due to decreased food intake, but may rather rely on rescue of brown adipose tissue and browning of white fat. Finally, we demonstrate that SAMs are not unique to mice, as they are also present in human sympathetic ganglia, along with the molecular machinery identified in mice. SAMs reconcile the controversy of previous reports, constituting an unforeseen neuroimmunological player in noradrenergic homeostasis, and a potential new target for obesity.

3.2 RESULTS

Specialized morphology and activation of SNS Cx3cr1+ cells.

Our initial aim was to visualize the in vivo morphology of ATMs using two-photon and confocal microscopy in *Cx3cr1*$^{GFP/+}$ mice, in which macrophages are GFP-labeled. ATMs in fat parenchyma had a regular circular shape (Fig. 3.1 a), whereas those located on sympathetic nerve bundles exhibited profuse pseudopodia that extended over greater surface area (Fig. 3.1 b and Fig. 3.S1 a,b). Furthermore, we observed that sympathetic neuron-associated *Cx3cr1*$^{GFP/+}$ cells displayed dynamic extensions and retractions of dendritiform processes over time (Fig. 3.1 c). In contrast, ATMs surrounding adipocytes displayed minimal temporal plasticity or displacement (Fig. 3.1 c). Using correlative light electron microscopy on WAT-derived nerve bundles, we confirmed that *Cx3cr1*$^{GFP/+}$ cells extended thin pseudopodia processes that envelop non-myelinated SNS axons (Fig. 3.1 d,e).

We then investigated whether sympathetic neuron-associated *Cx3cr1*$^{GFP/+}$ cells were present in other SNS compartments, such as paravertebral sympathetic ganglia. Upon imaging superior cervical ganglia (SCG) and thoracic chains, we visualized *Cx3cr1*$^{GFP/+}$ cells that were morphologically similar to those within WAT-derived SNS bundles (Fig. 3.S2). Due to established ex vivo explant potential, we used SCGs along with WAT-derived SNS nerve bundles as model systems for subsequent functional and molecular analyses.

SNS Cx3cr1+ SAMs exhibit hematopoietic characteristics.

Because nearly all *Cx3cr1*$^{GFP/+}$ cells isolated from sympathetic fibers were positive for the immune marker CD45 (Fig. 3.S3) and macrophage marker F4/80 (Fig. 3.S4), we designate these cells sympathetic neuron-associated macrophages (SAMs). Given the specialized morphology and location of SAMs, we next explored how these cells compared to other tissue macrophages and brain microglia. We sorted F4/80+CD45+ double-positive cells from the following tissues: sympathetic ganglia (SAM ganglia), sympathetic nerve fibers from inguinal fat (SAM fibers), neighboring subcutaneous fat (sATM), visceral fat (vATM), spleen (SpM) and brain (BrM) (Fig. 3.2 a; gating details in Fig. 3.S5). The relative abundance of *Cx3cr1*$^{GFP/+}$ (CD45$^{\mathrm{High/Medium}}$) cells was nearly four times higher within nerve fibers (SAMs) than in sWAT (sATMs; Fig. 3.S4b). CD45 is highly expressed in hematopoietic cells but expressed at lower levels in brain macrophages. Flow cytometric analysis revealed that SAMs are CD45$^{\mathrm{Medium/High}}$ (Fig. 3.S3), suggesting a hematopoietic origin of these cells. To this end, we generated bone marrow chimeras from *Cx3cr1*$^{GFP/+}$ (CD45.2) donors into irradiated CD45.1 recipient mice and observed complete repopulation of CD45+ cells derived from *Cx3cr1*$^{GFP/+}$ (CD45.2) donors (Fig. 3.S4 c). Eight weeks post-transplantation, we established that *Cx3cr1*$^{GFP/+}$ (CD45.2) SAMs repopulated sympathetic nerve bundles in WAT, whereas macrophage repopulation in the brain did not occur (Fig. 3.S4 d). This suggests that SAMs in sympathetic fibers have similar origin to other hematopoietic macrophages as opposed to microglial lineage.

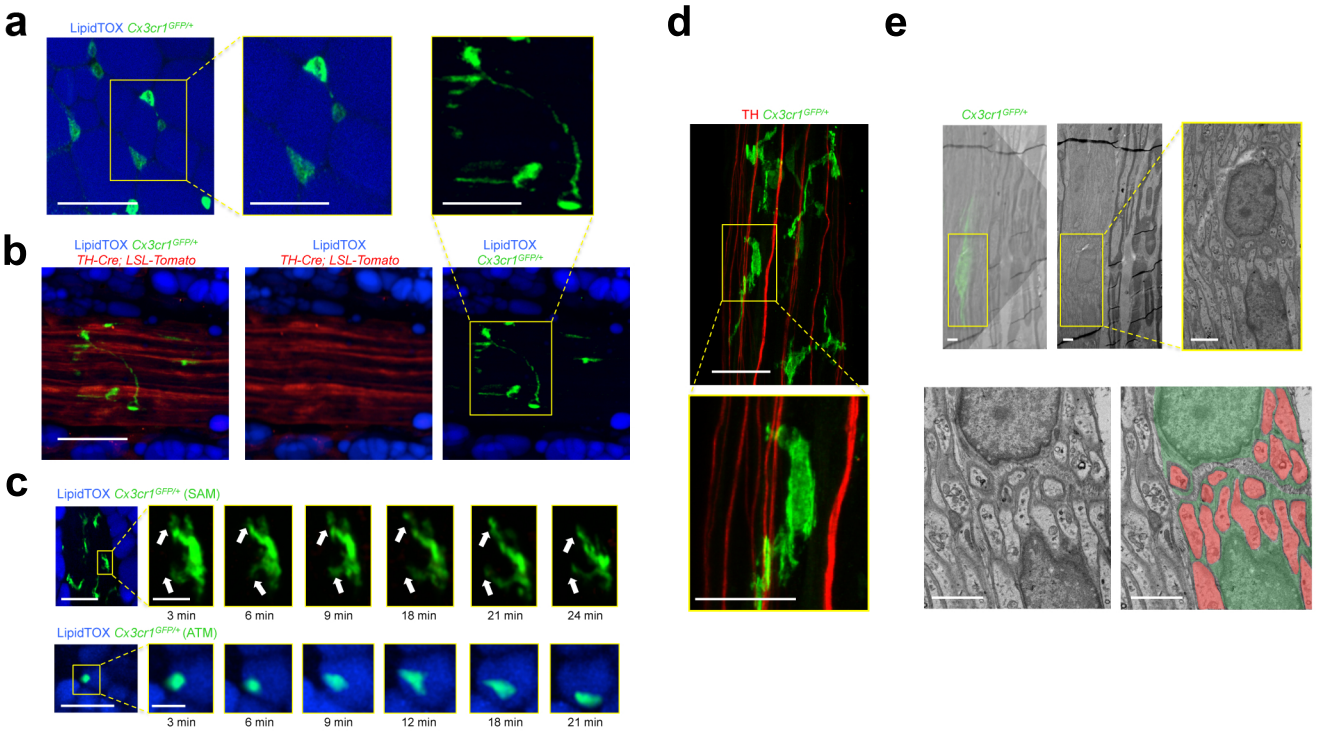

Figure 3.1. Sympathetic neuron-associated *Cx3cr1*$^{GFP/+}$ cells exhibit differentiated morphology for specific association with SNS neurons

(a) Confocal images from white adipose tissue isolated from *Cx3cr1*$^{GFP/+}$ mice and stained using lipid stain LipidTOX (blue) and anti-GFP (green) antibody. Images are representative of 5 similar experiments. **(b)** Confocal images of sympathetic nerve fibers in subcutaneous adipose tissue isolated from a cross of *TH-Cre; LSL-Tomato* (red) and *Cx3cr1*$^{GFP/+}$ (green) mice. Adipocytes were stained using lipid stain LipidTOX (blue). Images are representative of 3 similar experiments. Scale bars in a and b, 50 μm. Boxed regions in a and b represent higher magnification of the main micrographs - scale bars, 25 μm **(c)** Intra-vital multi-photon visualization of a neuro-adipose connection in the inguinal fat pad of a live *Cx3cr1*$^{GFP/+}$ mouse; LipidTOX (blue) labels adipocytes. Images are depicting morphological features and cell dynamics of Cx3cr1$^{GFP/+}$ cells associated with sympathetic nerve fibers (upper panels) and *Cx3cr1*$^{GFP/+}$ cells in the parenchyma of subcutaneous fat (lower panels). Images are representative of 3 similar experiments. Scale bars, 50 μm. Boxed regions represent higher magnification of the main micrograph at time points indicated below micrographs – scale bars, 10 μm. **(d)** Confocal images from sympathetic nerve fibers isolated from inguinal fat pad of *Cx3cr1*$^{GFP/+}$ mice and stained using anti-TH (red) and anti-GFP (green) antibodies. Images are representative of 5 similar experiments. Scale bar, 50 μm. Boxed region represents higher magnification of the main micrograph – scale bar, 25 μm. **(e)** Correlative confocal and transmission electron microscopy of the nerve fibers isolated from subcutaneous fat pad of *Cx3cr1*$^{GFP/+}$ mice. Shown is an overlay of the *Cx3cr1*$^{GFP/+}$ fluorescence (green) with the electron micrograph from the same section, (upper left with the lower left panel being a higher magnification), electron micrograph alone (upper middle with the yellow boxed region in the right panel being a higher magnification), and electron micrograph (lower left) with false color-coding of the same image highlighting *Cx3cr1*$^{GFP/+}$ cells (green) and sympathetic nerves (red) (lower right). Images are representative of 2 similar experiments. Scale bars, 2 μm.

SAM expression profile is more macrophage- than glia-like.

Given their association with neurons, we asked how the gene expression profile of SAMs compared to other resident tissue macrophages (Fig. 3.2). We sorted macrophages from various tissues as described above (F4/80+CD45+ double-positive cells designated as SAM ganglia, SAM fibers, sATMs, vATMs, SpM, and BrM; Fig. 3.2 a) and profiled gene expression by low input RNAseq (Fig. 3.2 b-f). As expected, SAMs highly expressed markers common to both microglia and macrophages, such as Adgre1, Csf1r, Cx3cr1 (Fig. 3.2 b). SAMs expressed macrophage-associated genes that are not present in microglia, such as Fn1 or Ciita (Fig. 3.2 b)(Gosselin et al., 2014). By flow cytometric analysis, additional macrophage-specific markers which are not present in microglia (CD68, Ly6c, MHCII, and CD11b) were also highly expressed in SAMs (Fig. 3.S5 a,b). SAMs do not robustly express microglial- or glial-specific genes relative to peripheral macrophage-specific genes (Fig. 3.2 b and Fig. 3.S5 b)(Anlauf and Derouiche, 2013; Bignami et al., 1972; Chaudhry et al., 1995; Jessen and Mirsky, 2005; Ludwin et al., 1976; Mearow et al., 1989; Raff et al., 1978; Regan et al., 2007; Rusnakova et al., 2013; Sensenbrenner et al., 1997). In addition, Sall1, a key microglia lineage-determining transcription factor, is strikingly absent in SAMs (Buttgereit et al., 2016) (Fig. 3.2 b).

Principle component analysis (PCA) of the RNAseq data shows tight clustering across replicates, indicating low contamination and high reproducibility (Fig. 3.2 d). The absence of tyrosine hydroxylase (Th) expression in SAMs (Fig. 3.S5 d) further excluded the possibility of contaminating cargo from neighboring cells, as Th is highly expressed in adjacent SNS neurons (Fig. 3.1 b,d). PCA analysis indicated that SAMs from fibers and ganglia are closely related, but both are distant from brain macrophages and other macrophage populations (Fig. 3.2 d and Fig. 3.2 e).

We hypothesized that the increased motility of SAMs (Fig. 3.1 c) could indicate an activated state. Therefore, we measured expression of a constellation of pro- and anti-inflammatory markers in SAMs by RNA-seq (Fig. 3.2 c). Relative to other macrophage populations, SAMs highly expressed genes associated with macrophage activation, including Cxcl2, Tnf, Socs3, and Il1a (Fig. 3.2 c), suggesting a constitutively pro-inflammatory steady state.

SAMs exhibit different gene expression landscapes from other macrophages.

Consistent with the PCA analysis (Fig. 3.2 d), Pearson correlation analyses of transcript levels indicated differential expression patterns across SAMs, sATMs, vATMs, SpMs and BrM (Fig. 3.S6 a,b). Adipose tissue macrophages (sATMs and vATMs) showed similar expression landscapes ($R = 0.92$) that were distant from fiber SAMs ($R = 0.63$ for sATM and $R = 0.61$ for vATMs; Fig. 3.S6 b). Brain and spleen macrophages were least correlated with other groups (Fig. 3.S6 b). Gene ontology analyses indicated several biological processes associated with genes enriched in SAMs relative to surrounding sATMs (Fig. 3.S6 c). SAMs preferentially expressed genes involved in synaptic signaling, cell-cell adhesion, and neuron development (Fig. 3.S6 c), suggesting that these cells fulfill an intrinsic role in local neuronal maintenance. Taken together, these data demonstrate divergent gene expression patterns in SAMs and ATMs, further indicating intra-tissue macrophage specialization within the AT.

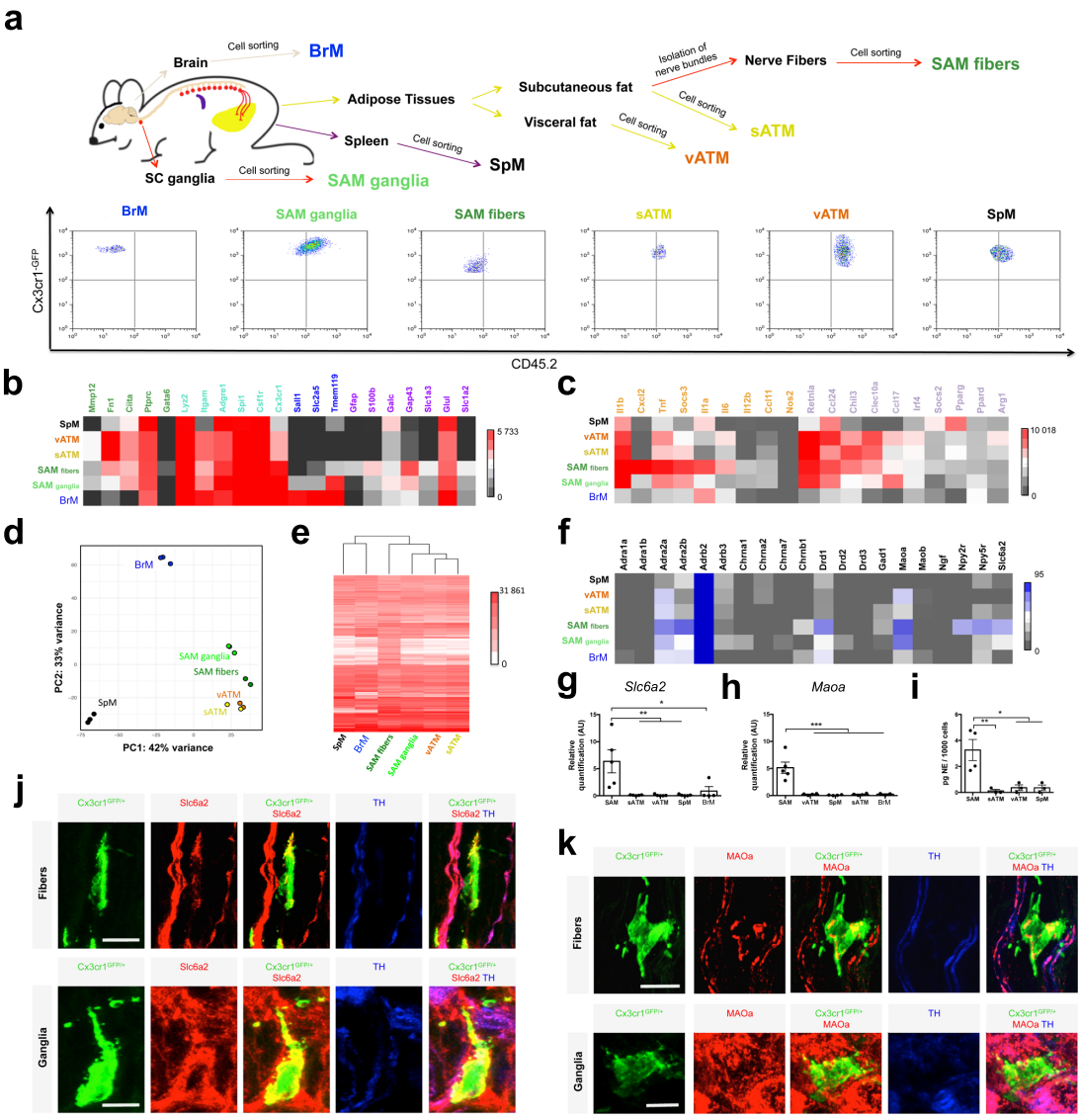

Figure 3.2. SAMs highly express macrophage-associated markers and possess the machinery for uptake and degradation of norepinephrine.

(a) Schematic representation (top) of tissue dissections and processing. Representative flow cytometry dot plots (bottom) indicating the CD45.2 status of macrophages from each tissue analyzed. **(b)** Heat map for genes associated with macrophage (green and cyan), microglia (blue and cyan) and glia (purple) profiles, determined by low-input RNA-seq. Values are Reads Per Kilobase of transcript per Million mapped reads (RPKM). **(c)** Heat map for pro-inflammatory (orange) and anti-inflammatory (purple) genes, determined by low-input RNA-seq. Values are RPKM. **(d)** Principal component (PC) analysis based on the top 500 most variable genes across SAM fibers (green), SAM ganglia (light green), vATM (orange), sATM (yellow), SpM (black) and BrM (blue). Each dot represents an independent experiment. **(e)** Heat map of transcripts (RPKM values) based on the top 5000 genes expressed by SAM fibers, determined by low-input RNA-seq.**(f)** Heat map of genes for neurotransmitter receptors, transporters and catalyzing enzymes. RPKM values are determined by low-input RNA-seq. Values in panels **b-f** represent 3 independent experiments (SpM, BrM and SAM ganglia, n = 3) or 2 independent experiments (vATM, sATM and SAM fibers, n = 2).

(g) Expression of mRNA for Slc6a2 determined by qRT-PCR presented normalized to Gapdh expression. Each data point represents tissues pooled from 10 mice. n = 5 experiments for SAM, SpM, vATM, sATM and n = 4 experiments for brain macrophages (BrM), *P $<$ 0.05, **P $<$ 0.01. **(h)** Expression of mRNA for Maoa determined by qRT-PCR normalized to Gapdh expression. Each data point represents tissues pooled from 10 mice. n = 5 experiments for SAM, n = 4 experiments for SpM, vATM, sATM and n = 3 experiments for BrM, ***P $<$ 0.001. **(i)** NE content in sorted CD45.2-PE, F4/80-Alexa Fluor 647-double-positive cells measured by NE ELISA. Number of cells used in NE assays were as followed: 858 ± 258 for SAMs (n = 4 experiments), and 1000 cells for sATM, vATM and SpM (n = 3 experiments), *P $<$ 0.05, **P $<$ 0.01. **(j,k)** Confocal images from sympathetic nerve fibers (upper panels) and superior cervical ganglia (lower panels) isolated from *Cx3cr1*$^{GFP/+}$ mice and stained using anti-GFP (green), anti-Slc6a2 **(j)** or anti-MAOa **(k)** (red) and anti-TH (blue) antibodies. Images are representative of 2 experiments. Scale bars, 10 μm. Data in **g**, **h** and **i** were analyzed by one-way ANOVA followed by Tukey's multiple comparison test. Data are shown as average ± SEM.

SAMs have the machinery to import and degrade, but not to synthesize, NE.

We next examined the specific transcripts comprising divergent macrophage gene expression landscapes. The aforementioned populations of macrophages were sorted (Fig. 3.2 a) for transcriptome analysis via low-input RNA-seq. Given the gene ontology results (Fig. S.3.6 c) and spatial proximity of SAMs to nerves (Fig. 3.1), we hypothesized differential expression of neurotransmitter receptors, transporters or catalyzing enzymes (Fig. 3.2 f). We detected abundant β2 adrenergic receptor (Adrb2) expression in all macrophage populations (Fig. 3.2 f), which was confirmed by qRT-PCR (Fig. 3.S6 d).

However, SAMs were the only population that expressed Slc6a2, the gene for the NE transporter (Fig. 3.2 f). Similarly, Maoa, the gene responsible for oxidative deamination of amines, was highly expressed in SAMs relative to the other macrophage types (Fig. 3.2 f). Both results were validated by qRT-PCR (Fig. 3.2 g,h). As Slc6a2 imports and MAOa degrades NE, we also tested for and detected NE by ELISA in sorted SAMs (Fig. 3.2 i and Fig. 3.S6 e). Furthermore, we validated Slc6a2 and MAOa protein expression by immunofluorescence in *Cx3cr1*$^{GFP/+}$ SNS nerve fibers and SCG cryo-sections (Fig. 3.2 j,k). Representative photomicrographs depict GFP-containing SAMs were double-positive for membrane-bound Slc6a2 (Fig. 3.2 j) or mitochondrial-bound MAOa (Fig. 3.2 k).

As SAMs, but not other macrophage types assessed, possess the molecular machinery for import (Fig. 3.2 f,g,j) and degradation (Fig. 3.2 f,h,k) of NE, as well as significantly more NE relative to other macrophages (Fig. 3.2 I and Fig. 3.S6 e), we tested the possibility that SAMs synthesize NE. By qRT-PCR of sorted SAMs, we did not detect expression of Th, which encodes an enzyme necessary for NE biosynthesis (Fig. 3.S5 d). Taken together, these results indicate that SAMs possess the molecular machinery for importing and degrading NE, but not for biosynthesis.

To explore the responsiveness of SAMs to NE, we optogenetically stimulated sympathetic neurons in SCG cultures from *TH-Cre; Rosa26-LSL-ChR2-YFP* mice (Zeng et al., 2015), which allowed us to visualize sympathetic neuron-macrophage interactions ex vivo (Fig. 3.3 a,b). After optogenetic stimulation, we measured NE content of sorted CD45+F4/80+ cells. SAMs from ChR2-positive cultures exhibited

significantly higher NE levels (Fig. 3.3 c) that were proportional to NE availability in the culture medium (Fig. 3.3. d). NE release by ChR2-positive neurons was significantly higher relative to ChR2-negative neurons (Fig. 3.3 d). Uptake of NE by SAMs was prevented by pharmacologic blockade of Slc6a2 by the pharmacological inhibitor Nisoxetine, despite significant increase of NE in the culture medium (Fig. 3.3 c,d).

To validate our optogenetic findings with a physiologically relevant stimulus, we activated SNS explants with acetylcholine (ACh), which is pre-synaptically released from spinal cord neurons to innervate SCG. ACh-treated CD45+F4/80+ cells sorted from SCG explants contained significantly higher levels of NE than vehicle controls (Fig. 3.3 e). We validated that blockade of the NE importer Slc6a2 by Nisoxetine prevented NE accumulation in SAMs (Fig. 3.3 e). Co-incubation with ACh and Nisoxetine further abolished NE uptake (Fig. 3.3 e) despite the substantial increase of extracellular NE levels in the culture medium (Fig. 3.3 f). These results, along with the negligible expression levels AChRs in SAMs (Fig. 3.S7 a; also validated by qRT-PCR in Fig. 3.S7 b), ruled out a role for AChRs in mediating NE import.

We further probed whether the availability of NE, which can be manipulated in vivo by optogenetic activation of SNS neurons, changes the inflammatory profile of SAMs. We found that optogenetic stimulation of SCG explants correlated with an increase of pro-inflammatory gene expression as measured by changes in Tnfa and Il1 (Fig. 3.3 g) and decrease of anti-inflammatory gene expression as measured by changes in Il4ra and Arg1 (Fig. 3.3 h).

SAMs are recruited and activated in obesity.

We next utilized two mouse models to characterize the effect of obesity on tissue-specific functions of SAMs. In total, we employed four experimental groups: high-fat diet (HFD)-fed, leptin-deficient (*ob/ob*), normal diet (ND)-fed, and 24-hr fasted ND-fed mice. Flow cytometric analysis demonstrated that both obesity models (HFD and *ob/ob*) exhibited significantly higher percentages of SAMs compared to lean mice (ND) (Fig. 3.4 a and Fig. 3.S8 a). Furthermore, the acute metabolic challenge of fasting did not result in upregulation of SAMs, suggesting an obesity-specific causation of elevated macrophage content in sympathetic fibers (Fig. 3.4 a and Fig. 3.S8 a). Within the F4/80+ SAM fraction in HFD and *ob/ob* mice, we noted a high frequency of CD11c+ cells (Fig. 3.4 b), which are hallmarks of inflammation and insulin resistance in human obesity (Wentworth et al., 2010). In contrast to SAM accumulation in SNS nerve fibers dissected from WAT, SAMs do not accumulate in SCG, which innervates neck structures such as salivary glands (Fig. 3.S8 a b).

The differential distribution of macrophages in states of obesity suggested cytokine levels were also sensitive to obesity. Comparing anti- and pro-inflammatory gene profiles of SAMs, ATMs, and SpMs (Fig. 3.4 c-e) revealed that obesity correlated with higher levels of pro-inflammatory gene expression (i.e., Tnfa or Il1; Fig. 3.4 c,e) and lower levels of anti-inflammatory gene expression (i.e., Arg1 or Il10; Fig. 3.4 d,e).

To determine if local proliferation contributes to SAM accumulation, we measured the proliferation marker Ki67 in SAMs by flow cytometry (Fig. 3.S8 c,d). We observed that obesity (via HFD or *ob/ob*

models) does not significantly increase Ki67+ SAM content, whereas (consistent with previous reports (Amano et al., 2014)) obesity increases Ki67+ ATMs from sWAT (Fig. 3.S8 d).

Slc6a2 deletion in SAMs improves thermogenic capacities of obese mice.

We probed how ablating Slc6a2 in SAMs affected obesity-associated pathology. We considered a Cre-Lox approach, but the established macrophage Cre lines (*Cx3Cr1-Cre* (Gosselin et al., 2017; Wolf et al., 2017) and *LysM-Cre* (Clausen et al., 1999)) would not allow for SAM-specificity. We thus took advantage of the cell type-specificity of Slc6a2 expression, which is high in SAMs and negligible in other macrophage and hematopoietic populations (Fig. 3.2. b,g and ImmGen (Merad et al., 2002)). We validated that, besides SAMs, there did not exist another hematopoietic-derived population that expressed Slc6a2; a rare population of CD45+F4/80- cells were present in SCG (Fig. 3.S9 a) but did not express Slc6a2 (Fig. 3.S9 b). SAM-specific genetic ablation of Slc6a2 was attained by bone marrow transfer from *Slc6a2-/-* mice (Shirey-Rice et al., 2013) into genetically obese *ob/ob* recipients ($ob/ob^{Slc6a2-/-}$) (Fig. 5a). Control chimeras consisted of bone marrow transfer from *B6-CD45.1* mice into *ob/ob* recipients (ob/ob^{Ctrl}). Chimeras recovered for nine weeks post-transplant to allow irradiation-induced inflammation to subside.

As cold temperature is a robust driver of SNS activity, we challenged mice for 2 hr at 4°C and observed that $ob/ob^{Slc6a2-/-}$ chimeras displayed superior capacity for maintaining body temperature compared to control ob/ob^{Ctrl} chimeras (Fig. 3.5 b). These thermogenic effects were accompanied by significant upregulation of NE serum levels (Fig. 3.5 c), rescue of BAT morphology (Fig. 3.5 d), and browning of white fat, as measured by Ucp1 mRNA and protein levels (Fig. 3.5 e-g).

Slc6a2-/- transplant into ob/ob prevented obesity-induced hypertrophy of both BAT and WAT adipocytes (Fig. 3.5 h) but did not affect total body weight (Fig. 3.5 i). To further determine whether a dieting challenge could have a different effect on the ob/ob chimeras, we normalized their daily food intake for 2 weeks (Fig. 3.5 i,j). After a dieting challenge $ob/ob^{Slc6a2-/-}$, relative to control chimeras, lost nearly 30% of body weight (Fig. 3.5 i). $Ob/ob^{Slc6a2-/-}$ mice also exhibited higher lipid mobilization during food restriction (Fig. 3.5 j).

We analyzed wild-type *B6* chimeras reconstituted with control *CD45.1* bone marrow or *Slc6a2-/-* bone marrow (Fig. 3.S9 c). SAMs from $B6^{Slc6a2-/-}$ chimeras did not accumulate NE (Fig. 3.S9 d). Consistent with the results from ob/ob chimeras (Fig. 3.5), $B6^{Slc6a2-/-}$ chimeras also exhibited increased serum NE levels and higher body temperature. Finally, a key enzyme of lipolysis Pnpla2 was up-regulated in WAT from $B6^{Slc6a2-/-}$ chimeras, but the levels of lpl expression were not affected (Fig. 3.S9).

SAMs in BAT.

In light of the enhanced thermogenic capacity of $ob/ob^{Slc6a2-/-}$ chimeras, we questioned whether SAMs are also present in BAT (Fig. 3.S10). BAT did contain $Cx3cr1^{GFP/+}$ cells (consistent with previous reports (Wolf et al., 2017)) that exhibited an intermediate morphology between SAMs (multiple pseudopodia) and ATMs (round) (Fig. 3.S.10 a compared to Fig. 3.1 c). Some of these cells appeared to make close contact with thin TH+ axons (Fig. 3.S.10 a). Because TH+ nerve fibers in BAT are

too delicate for dissection, we sorted macrophages from whole BAT for qRT-PCR analysis. Slc6a2 and MAOa were expressed in BAT macrophages, although at much lower levels relative to SAMs isolated from dissected SNS nerve bundles in sWAT or SCG (Fig. 3.S.10 b, c). BAT macrophages also contained NE, although at lower levels than SAMs (Fig. 3.S.10 d). The lower levels of Slc6a2, MAOa, and NE content may reflect a dilution of BAT-SAMs by BAT-ATMs since mixed (as opposed to isolated) populations were analyzed.

Human sympathetic ganglia also contain NE-degrading SAMs.

Finally, we asked if SAMs exist in humans. We obtained nine human excisional biopsies of SNS or thoracolumbar ganglia that were collected during sympathectomy and/or gangliotomy. We stained tissue sections with H and E (Fig. 3.6 a,b) or an antibody against CD68, a human macrophage marker, identifying the presence of macrophages in SNS tissues (Fig. 3.6 c,d and Fig. 3.S.11).

We next determined whether SAMs in human sympathetic ganglia also contain the machinery for uptake and degradation of NE (Fig. 3.6 e,f and Fig. 3.S.11). The CD68 macrophage marker co-localized with staining for Slc6a2 (Fig. 3.6 e and Fig. 3.S.11 a) and MAOa (Fig. 3.6 f and Fig. 3.S.11 b). Both Slc6a2- and MAOa-positive neurons exist, but the background levels are low relative to control human gut-associated lymphoid tissue (GALT) samples that also contain CD68+ macrophages (3.S.11 c, d).

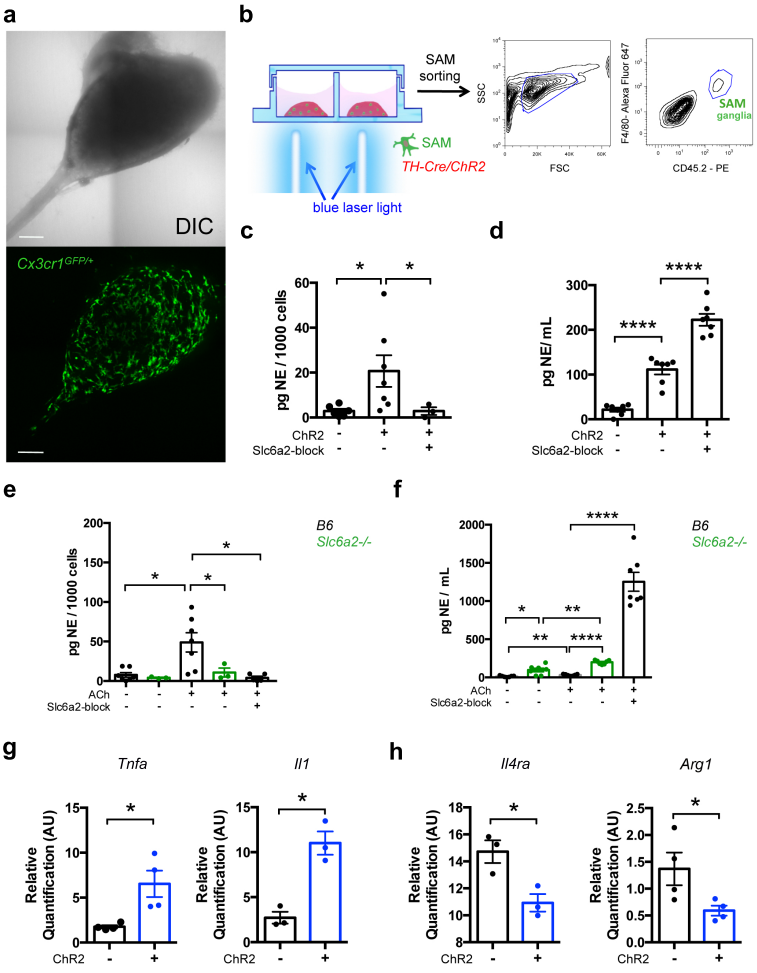

Figure 3.3. SAMs import and metabolize NE via Slc6a2 and MAOa, respectively, to regulate extracellular NE availability.

(a) Representative images of *ex vivo* SCG explant cultures. The area of the sympathetic ganglia is represented using reflected light differential interference contrast (DIC) channel in the upper panel, and the *Cx3cr1*$^{GFP/+}$ cells from the same explant culture are shown in the lower panel (GFP channel). Images are representative of 20 similar experiments. **(b)** Schematic representation (left) of optogenetic activation of sympathetic SCG explant culture followed by CD45.2-PE, F4/80-Alexa Fluor 647-double-positive cell sorting (right). **(c)** NE content in CD45.2-PE, F4/80-Alexa Fluor 647-double-positive cells isolated from SCG explant cultures from *TH-Cre; LSL-ChR2-YFP* and *LSL-ChR2-YFP* mice after optogenetic activation. Each data point represents tissues pooled from 6 mice. n = 3-7 experiments, *P $<$ 0.05. The following number of cells were used in NE assays: 189 ± 30 from *TH-Cre; LSL-ChR2-YFP* SCG (n = 7), 126 ± 21 from *LSL-ChR2-YFP* SCG (n = 6), and 159 ± 19 from *TH-Cre; LSL-ChR2-YFP* SCG stimulated with Slc6a2-blocker (n = 3). **(d)** *Ex vivo* NE release upon optogenetic stimulation of SCG explants isolated from *TH-Cre; LSL-ChR2-YFP* and *LSL-ChR2-YFP* mice. Each data point represents medium collected from one explant culture. n = 7 per group, ****P $<$ 0.0001. **(e)** NE content in CD45.2, F4/80-double-positive cells isolated from SCG of either *B6* or *Slc6a2-/-* mice and then incubated with ACh, an ACh and Slc6a2-blocker, or culture medium. Each data point represents tissues pooled from 6 mice. n = 3-7 experiments, *P $<$ 0.05. The following number of cells were used in NE assays: 364 ± 128 from *B6* SCG (n = 7), 238 ± 55 from *Slc6a2-/-* SCG (n = 3), 216 ± 58 from *B6* SCG incubated with ACh (n = 7), 201 ± 63 from *Slc6a2-/-* SCG incubated with ACh (n = 3), 196 ± 18 from *B6* SCG incubated with ACh and Slc6a2-blocker (n = 5).

(f) *Ex vivo*NE release from SCG of either B6 or Slc6a2-/- mice after incubation with ACh, an ACh and Slc6a2-blocker, an ACh and MAOa-blocker or culture medium. Each data point represents medium collected from one explant culture. n = 7 per group, ****P $<$ 0.0001, **P $<$ 0.01. **(g)** Expression of mRNA by qRT-PCR and relative to Gapdh for pro-inflammatory genes (Tnfa and Il1) in CD45.2, F4/80-double-positive cells isolated from SCG explant cultures from *TH-Cre; LSL-ChR2-YFP* (blue) and *LSL-ChR2-YFP* (black) mice. Prior to cell sorting, SCG explants were optogenetically stimulated. n = 3-4 experiments, *P $<$ 0.05 (for Tnfa, n = 4, P = 0.0467; for Il1, n = 3, P = 0.011). **(h)** Expression of mRNA by qRT-PCR and relative to Gapdh for anti-inflammatory genes (Il4ra and Arg1) in CD45.2, F4/80-double-positive cells isolated from SCG explant cultures from *TH-Cre; LSL-ChR2-YFP* (blue) and *LSL-ChR2-YFP* (black) mice. Prior to cell sorting, SCG explants were optogenetically stimulated. n = 3-4 experiments, *P $<$ 0.05 (for Il4ra, n = 3, P = 0.0257; for Arg1, n = 4, P = 0.0497). Data in textbfc-h were analyzed by two-tailed unpaired Student's t-test and are shown as average ± SEM.

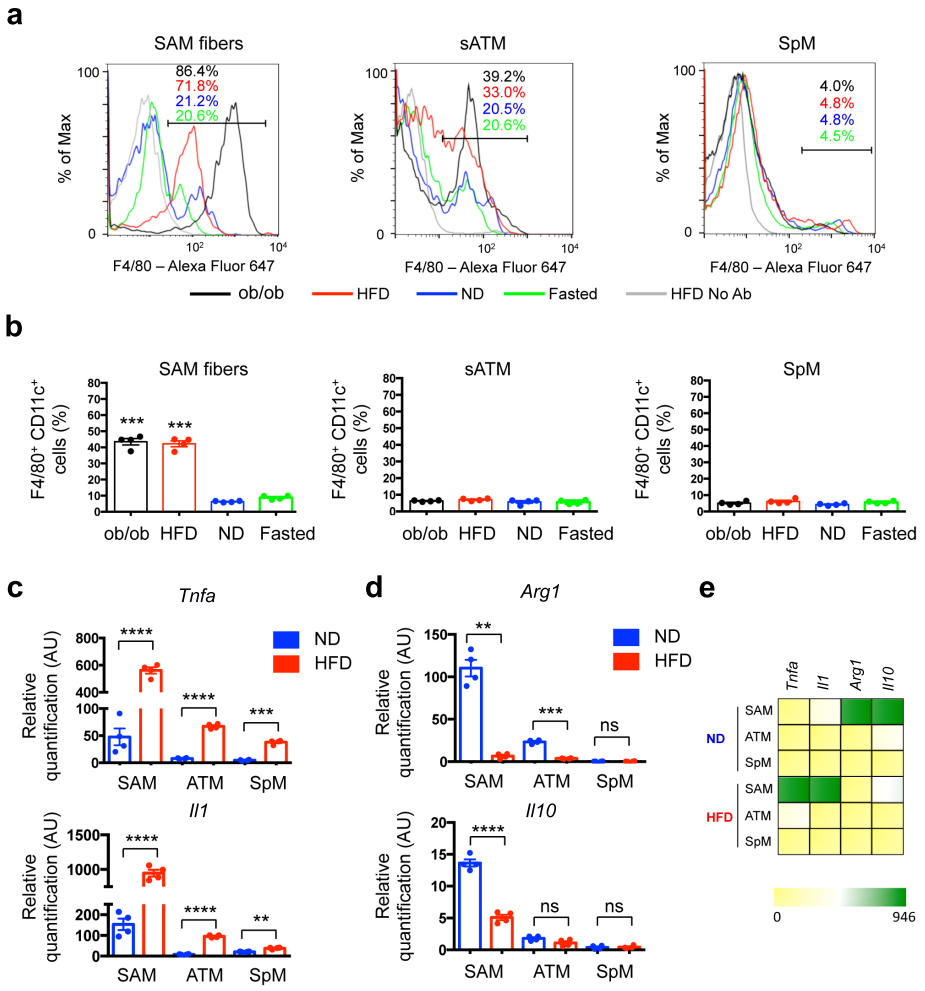

Figure 3.4. Obesity-induced accumulation of SAMs.

(a) Representative histograms showing percentages of F4/80-Alexa Fluor 647-positive cells in sympathetic nerve fibers (left panel), subcutaneous adipose tissue (middle panel) and spleen (right panel) in mice that were genetically obese (*ob/ob*; black), obese due to high fat diet (red), fed normal diet (blue) or food-deprived for 24 hours (green). CD45.2-PE-positive cells were gated. Histograms are representative of 4 independent experiments. **(b)** Percentages of F4/80-Alexa Fluor 647- and CD11c-FITC-double-positive cells in sympathetic nerve fibers (left panel), subcutaneous adipose tissue (middle panel) and spleen (right panel) in mice that were genetically obese (ob/ob; black), obese due to high fat diet (red), fed normal diet (blue) or food-deprived for 24 hours (green). CD45.2-PE-positive cells were gated. n = 4 experiments per group, ***P $<$ 0.001. **(c)** Expression of mRNA determined by qRT-PCR and relative to Gapdh for pro-inflammatory genes (Tnfa and Il1) in CD45.2-PE, F4/80-Alexa Fluor 647-double-positive cells in sympathetic nerve fibers (SAM), subcutaneous adipose tissue (ATM) and spleen (SpM) isolated from mice that were fed either normal (blue) or high fat (red) diet. n = 4 experiments per group, ****P $<$ 0.0001, ***P $<$ 0.001, **P $<$ 0.01. Each data point represents tissues pooled from 10 mice.

(d) Expression of mRNA determined by qRT-PCR and relative to Gapdh for anti-inflammatory genes (Arg1 and Il10) in CD45.2-PE, F4/80-Alexa Fluor 647-double-positive cells in sympathetic nerve fibers (SAM), subcutaneous adipose tissue (ATM) and spleen (SpM) isolated from mice that were fed either normal (blue) or high fat (red) diet. n = 4 experiments per group, ****P $<$ 0.0001, **P $<$ 0.01. Each data point represents tissues pooled from 10 mice. **(e)** Heat map for pro- and anti-inflammatory genes determined by the qRT-PCR analyses in **c**, **d**. Data in **b** were analyzed by one-way ANOVA followed by Bonferroni multiple comparison test with ND as a control group. Data in **c**, **d** were analyzed by two-tailed unpaired Student's t-test. Data are shown as average ± SEM.

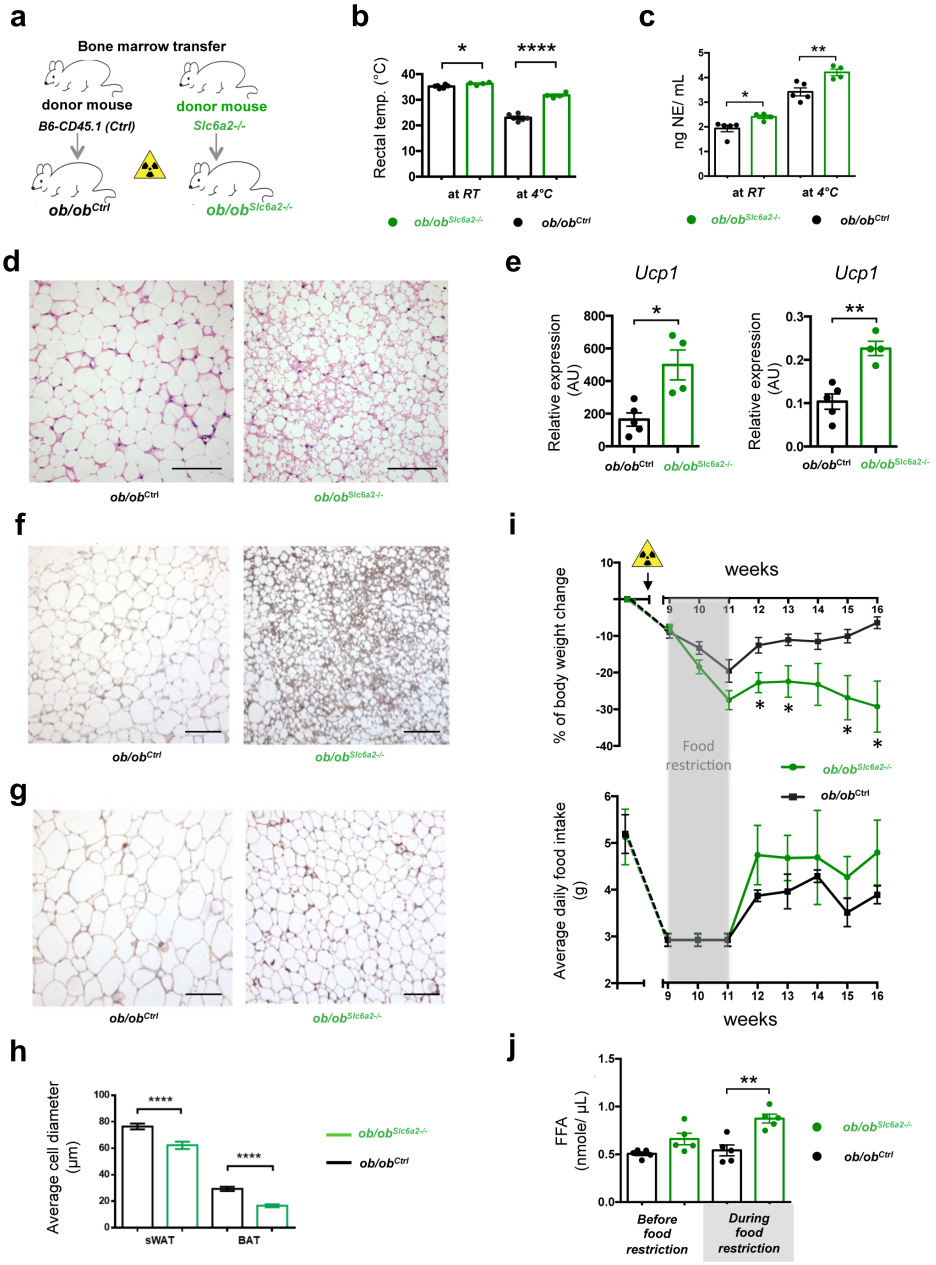

Figure 3.5. Loss of function of Slc6a2 in SAMs rescues thermogenic capacities of ob/ob mice. **(a)** Schematic representation of bone marrow transplant from either *Slc6a2-/-* or control *B6-CD45.1* mice into genetically obese *ob/ob* mice ($ob/ob^{Slc6a2\text{-}/\text{-}}$ and ob/ob^{Ctrl} chimeras, respectively). **(b)** Rectal temperature of ob/ob^{Ctrl} (black) and $ob/ob^{Slc6a2\text{-}/\text{-}}$ (green) chimeras was measured at RT and after 2 hours of cold challenge. Each data point represents one mouse. n = 4 mice for $ob/ob^{Slc6a2\text{-}/\text{-}}$, n = 6 mice for ob/ob^{Ctrl}, *P = 0.025, ****P < 0.0001. **(c)** Serum NE levels of the ob/ob^{Ctrl} (black) and $ob/ob^{Slc6a2\text{-}/\text{-}}$ (green) chimeras were measured at RT and after 2 hours of cold exposure. Each data point represents one mouse. n = 4 mice per group for $ob/ob^{Slc6a2\text{-}/\text{-}}$, n = 5 mice per group for ob/ob^{Ctrl}, *P = 0.022, **P = 0.0072.

(d) Optical micrographs of BAT removed from ob/ob chimeras following 2 hours of cold challenge and stained with H and E. Left panel represents BAT from ob/ob^{Ctrl} and right panel shows BAT from the $ob/ob^{Slc6a2\text{-}/\text{-}}$ chimeras. Images are representative of fat organs collected from 4 mice (ob/ob^{Ctrl}) or 6 mice ($ob/ob^{Slc6a2\text{-}/\text{-}}$). **(e)** Expression of mRNA for Ucp1 determined by qRT-PCR and relative to Gapdh in BAT (left panel) and sWAT (right panel) dissected after 2 hours of cold challenge. Ob/ob^{Ctrl} chimeras are represented in black and $ob/ob^{Slc6a2\text{-}/\text{-}}$ chimeras are shown in green. Each data point represents one mouse. n = 4 mice for $ob/ob^{Slc6a2\text{-}/\text{-}}$, n = 5 mice for ob/ob^{Ctrl}, *P = 0.0269; **P = 0.0015. **(f)** Optical micrographs of BAT from ob/ob^{Ctrl} (left) and $ob/ob^{Slc6a2\text{-}/\text{-}}$ (right) chimeras following 2 hours of cold challenge and stained with anti-UCP1 antibody. Images are representative of fat organs collected from 4 mice (ob/ob^{Ctrl}) or 6 mice ($ob/ob^{Slc6a2\text{-}/\text{-}}$). **(g)** Optical micrographs of sWAT from ob/ob^{Ctrl} (left) and $ob/ob^{Slc6a2\text{-}/\text{-}}$ (right chimeras following 2 hours of cold challenge and stained with anti-UCP1 antibody. Images are representative of fat organs collected from 4 mice (ob/ob^{Ctrl}) or 6 mice ($ob/ob^{Slc6a2\text{-}/\text{-}}$). **(h)** Average adipocyte diameter quantified from optical micrographs of sWAT and BAT from *ob/ob* chimeras following 2 hours of cold challenge. Measurements are representative of 4 independent micrographs (4 $ob/ob^{Slc6a2\text{-}/\text{-}}$ mice) or 6 micrographs (6 ob/ob^{Ctrl} mice). 18-34 measurements were obtained per micrograph. n = 169 for ob/ob^{Ctrl} sWAT, n = 120 for $ob/ob^{Slc6a2\text{-}/\text{-}}$ sWAT, n = 180 for ob/ob^{Ctrl} BAT, n = 120 for $ob/ob^{Slc6a2\text{-}/\text{-}}$ BAT, ****P < 0.0001. **(i)** Body weight change (upper panel) and daily food intake (lower panel) of ob/ob^{Ctrl}(n = 4 mice) and $ob/ob^{Slc6a2\text{-}/\text{-}}$ (n = 6 mice) chimeras monitored for 7 weeks following 2 weeks of food intake normalization (grey shade) that started 9 weeks after bone marrow transplant. Yellow triangle indicates when irradiation was performed. *P < 0.05. **(j)** Blood plasma non-esterified (free) fatty acid concentration in control ob/ob^{Ctrl} and $ob/ob^{Slc6a2\text{-}/\text{-}}$ chimeras measured 8 weeks after bone marrow transplant and during a 3 gr/day regimen. n = 5 mice per group, **P = 0.0022. Data in panels **b, c, e, h, j** were analyzed by two-tailed unpaired Student's t-test and in panel **i** by multiple t-tests – Student's t-test per row with correction for multiple comparisons using the Holm-Sidak method. Data are shown as average ± SEM. Scale bars in **d, f** and **g**, 100 μm.

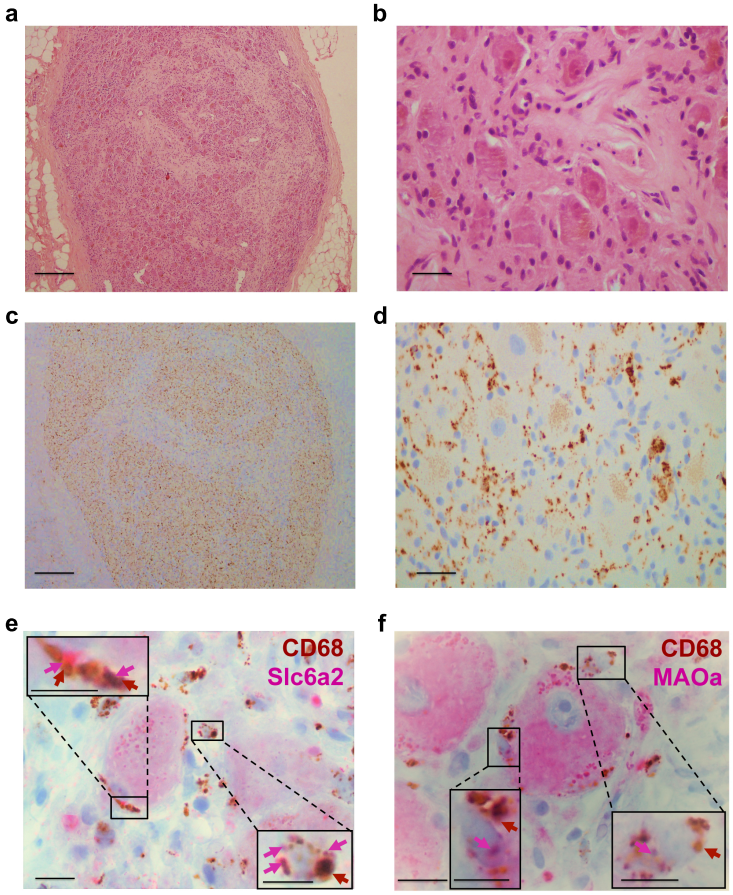

Figure 3.6. SAMs in the human Sympathetic Nervous System.

(a,b) Optical micrographs of human ganglia from the thoracolumbar region stained with H and E. **(b)** Higher magnification of the micrograph in panel **a**. **(c,d)** Optical micrographs of human ganglia from the thoracolumbar region stained with an antibody against CD68. **(d)** Higher magnification of the micrograph in panel **c**. **(e)** Optical micrographs of human ganglia from the thoracolumbar region stained with an antibody against CD68 and Slc6a2. Red arrows, CD68- and Slc6a2- double positive regions. **(f)** Optical micrographs of human ganglia from the thoracolumbar region stained with an antibody against CD68 and MAOa. Red arrows, CD68- and MAOa- double positive regions. Boxed regions in panels **e** and **f** represent higher magnification of the main micrographs. Scale bars for **a** and **b**, 1 mm, for **c** and **d** , 100 μm, for **e** and **f** , 50 μm, for boxed regions 25 μm. Images in **a-f** are representative of 9 different human samples.

3.3 DISCUSSION

Unlike most other neurons, which exclusively release neurotransmitter at a terminal synapse, SNS neurons also release NE via varicosities that distribute along the axons, which can extend for tens of centimeters within the body (Stjärne, 1989). SAMs could serve to prevent NE spillover into the blood stream or neighboring tissues when the SNS activity is driven. Indeed, we demonstrate that when SNS neurons are optogenetically driven, SAMs uptake even more NE, and also become more polarized. In this regard, NE can be regarded as a noxious stimulus, which has to be locally delivered in a controlled manner to a target tissue. Chronic and excessive systemic NE in serum, such as in chronic stress conditions or medullary adrenal tumors, leads to hypertension and cardiopathy due to a direct action in the cardiovascular tissues (Schroeder and Jordan, 2012).

The activated polarization state of SAMs is consistent with a model in which SAMs have a role in tissue protection, for being alert and scavenging an endogenous neurotransmitter that, if spilled in excess from varicosities, could potentially be harmful. Tissue-protective immune cells have been documented in the brain and other non-neuronal systems (Filiano et al., 2016; Galle-Treger et al., 2016; Ibiza et al., 2016; Kipnis, 2016; Louveau et al., 2015; Rosas-Ballina et al., 2011). For instance, muscularis resident macrophages in the gut induce rapid tissue-protective responses to potentially pathogenic insults via the β2-AR signaling (Gabanyi et al., 2016). This and our study indicate specialization of macrophage populations to fulfill tissue-specific tasks in response to neuronal cues. Divergent gene expression landscapes across resident-macrophage populations isolated from different tissues likely support the idea of local macrophage adaptations (Gautier et al., 2012; Gosselin et al., 2014; Okabe and Medzhitov, 2014). In this study we use transcriptional data to molecularly position SAMs within other macrophage populations. Our results support the idea that macrophages associated with the SNS may have specialized molecular programs. Exploring these programs might give more insights into mechanisms underlying the communication between macrophages and the sympathetic neurons in general.

Although SAMs express genes in common with macrophages from the brain and reside in proximity to nerve cells, the pseudopodia in SAMs are morphologically distinct from the finely branching ramifications of resting microglia (Crotti and Ransohoff, 2016; Prinz and Priller, 2014). Moreover the gene expression signatures reveal that SAMs have conserved features of macrophages at the molecular level but are also distinct from microglia. In this regard, SAMs could have origin in the bone marrow, based on the high expression of CD45 and macrophage markers, as well as our bone marrow chimera studies. The latter require the use of irradiation that may generate recruitment artifacts due to tissue/nerve inflammation. However, if given enough time for irradiation-induced inflammation to subside (2 months) recruited brain macrophages dissipate, as seen by the residual amount of $Cx3cr1^{GFP/+}$ brain macrophages in our chimeras (0.06%). SAMs persisted at levels that greatly surmounted the background of irradiation-induced recruitment of macrophages and were nearly identical to those in non-irradiated mice. Future tracing studies are necessary to determine the origin of SAMs — whether microglia lineages could also exist outside the brain or whether SAMs derive from other lineages.

Independently of the embryological origin of these cells, no reports exist on NE uptake by microglia

and we verified that machinery for NE uptake is not expressed in these cells. In this regard, only one study has reported that NE can trigger microglia to uptake and degrade amyloid, but not NE itself (Kong et al., 2010). Neurotransmitter uptake has been mostly studied in astroglia, which are Cx3cr1-negative (Kettenmann and Ransom, 2005). We show that several astroglial markers are lowly expressed in SAMs. Thus it is open to discussion whether SAMs are a hybrid peripheral cell type that unites some of the features of macrophages and glia. A less parsimonious model would be that SAMs are in the same lineage as satellite glial cells (SGC), which are derived from the neural crest of the embryo (Jessen and Mirsky, 2005). Alternatively, genes that are shared between glial cells and SAMs are due to their proximity to neuron-derived signals. This would be analogous to the observation that microglia, astrocytes and neurons share certain genes that are specific to the CNS (Butovsky et al., 2014; Gosselin et al., 2014). SGC cells have long been described in classical histology literature and are often coined as the peripheral glia. SGC have been mostly studied in sensory dorsal root ganglia (DRG) and share several astroglial markers (Hanani, 2005). However, fundamental knowledge on the biology and function of autonomic SGCs is still lacking and the existence of SGCs that uptake and degrade NE has never been reported before (Hanani, 2010). Our study may have filled up this gap in the literature, and more importantly, we validate a cellular and molecular mechanism that is alternative, or complementary to the existence of NE-producing macrophages in WAT (Nguyen et al., 2011).

Elevation of NE in adipose tissue promotes lipolysis and fat mass reduction, which would be beneficial for diseases such as obesity. We demonstrated that SAMs contribute to obesity, by accumulating in the SNS in two mouse models of obesity. Furthermore, we demonstrated that loss of function of Slc6a2 in SAMs rescues brown adipose tissue and adaptive thermogenesis in obese ob/ob mice, which leads to sustained weight loss and lipid mobilization after a brief normalization of food intake.

It remains to be seen whether the recently documented macrophages in BAT, which aid SNS axon maintenance, uptake NE using the same mechanism as SAMs (Wolf et al., 2017). Overall, our results put forward SAMs as a potential new target for obesity, for instance, by targeted delivery of existent Slc6a2 inhibitors to SAMs.

3.4 EXPERIMENTAL PROCEDURES

Antibodies, stain reagents and drugs

The antibodies were obtained from the following vendors: anti-F4/80-Alexa Fluor 647 (BioLegend, cat No. 123122, clone BM8), anti-human CD68 (Dako, cat No. M 0876, clone PG-M1), anti-human Norepinephrine Transporter (Mab Technologies, cat No. NET17-1, clone 3-6C1 sc H10), anti-Monoamine Oxidase A (Abcam, cat No. ab126751, clone GR155892-5), anti-TH (Pel-Freez Biologicals, cat No. P40101-150, lot 16736), anti-GFP (Abcam, cat No. ab13970, lot GR279236-1), anti-TH (Aves Lab, cat No. TYH, lot TH1205), anti-GFP (Invitrogen, cat No. A11120, lot 1563696), anti-GFP (Abcam, cat No. ab6556, lot: GR292567-1), Goat anti-Chicken IgY (H+L) Secondary Antibody, Alexa Fluor 488 (Molecular Probes/ Thermo Fisher Scientific, cat No. A-11039, lot 1759025), Goat anti-Rabbit IgG (H+L) Cross-Adsorbed Secondary Antibody, Alexa Fluor 594 (Molecular Probes/ Thermo Fisher Scientific, cat No. A-11012, lot 1704538), anti-Ly6c-eFluor 405 (eBioscience, cat No. 48-5932-82, clone HK1.4, lot 4306743), anti-CD11c-PE (BD Pharmingen, cat No. 553802, clone HL3, lot 47030), anti-CD45.2-PE (Biolegend, cat No. 109808, clone 104.2), anti-CD45.2-FITC (obtained from Dr. Shoji Kimura from Memorial Sloan-Kettering Cancer Center, New York, NY; clone 104.2), anti-CD11b-FITC (ATCC No. TIB-128, clone M1/70), anti-MHCII-Bio (clone M5/114, ATCC No. TIB-120), SAv-APC/Cy7 (Biolegend, cat No. 405208, lot B215107), anti-Ki67-Alexa488 (BD Biosciences, cat No. 558616, clone B56, lot 7138687), anti IgG-Alexa488, Isotype Control (BD Biosciences, cat No. 557782, lot 7102576), anti-Siglec-f-BV421 (BD Biosciences, cat No. 562681, lot 7047598), anti-CD68 (Bio-Rad, cat No. MCA1957GA, clone FA-11), Goat anti-Rat IgG (H+L) Cross-Adsorbed Secondary Antibody, Alexa Fluor 594 (Invitrogen, cat No. A-11007), Goat Anti-Chicken IgY H and L, Alexa Fluor 647 (Abcam, cat No. ab150171), Goat Anti-Rabbit IgG H and L, Alexa Fluor 488, (Abcam, cat No. ab150077), Goat anti-Mouse IgG (H+L), Alexa Fluor 488 (Sigma, cat No. SAB4600387), Anti-Mouse IgG (whole molecule), Cy3 (Sigma, cat No. C0992), anti-Rabbit to UCP1 (Abcam, cat No. ab10983, lot GR249119-8), anti-mouse NET (Mab Technologies, cat No. NET05-2, clone 2-3 B2 sc D7). Sytox Blue dead cell stain (Molecular Probes/ Thermo Fisher Scientific, cat No. S34857, lot 1851462) was used to exclude dead cells. HCS LipidTOX Deep Red Neutral Lipid Stain (Molecular Probes/ Thermo Fisher Scientific, cat No. H34477) and HCS LipidTOX Red Neutral Lipid Stain (Molecular Probes/ Thermo Fisher Scientific, cat No. H34476) were used to stain lipids. Acetylcholine chloride, Nisoxetine hydrochloride, Clorgyline and Norepienphrine were purchased from Sigma-Aldrich.

Mice

Cx3cr1$^{GFP/+}$ (Cx3cr1tm1Litt/LittJ; Stock No: 008451), *TH-Cre* (Stock No: 008601), *GFP-L10* mice (Stock No: 024750), *LysM-Cre* mice (Stock No: 004781), *LSL-ChR2-YFP* mice (Stock No: 012-569, Daou et al., 2013), *LSL-tdTomato* (Stock No: 007909), and *ob/ob* (Stock No: 000632) mice were purchased from the Jackson Laboratory (JAX). *Slc6a2-/-* mice were kindly provided by Maureen Hahn from the University of Vanderbilt. *B6* (*C57BL/B6J*) and *B6-CD45.1* were purchased from Charles River, bred and maintained at Instituto Gulbenkian de Ciência. Both males and females were used in this study. Mice were 4-10 weeks old (for details see Life Sciences Reporting Summary). Animal procedures were approved by the ethics committee of Instituto Gulbenkian de Ciência.

Immunofluorescence and confocal microscopy

Tissues were dissected and fixed in 4% Paraformaldehyde for 2 hours (at room temperature (RT), with agitation). For images in Figure 2 j and k we employed frozen sections and the fixation step was followed by cryoprotection in 30% sucrose (Alfa Aesar). 16µm sections were obtained in a Leica Cryostat CM3050S. Both frozen sections and the whole mount tissues were incubated in a blocking/ permeabilization solution (3% Bovine serum albumin, 2% Goat serum, 0.1% Tween and 0.1% Sodium azide in 1xPBS) for 1 hour at RT, with (whole mouns) or without (frozen sections) agitation. Incubations with primary antibodies were performed overnight at 4°C with (whole mount) or without (frozen sections) agitation.The following dilutions of primary antibodies were used: anti-GFP (1:500), anti-TH (1:1000), anti-Slc6a2 (1:500), anti-MAOa (1:100). Incubation with secondary antibodies was performed for 1-2 hours at RT, with or without (in case of frozen sections) agitation. Z-series stacks were acquired on a Leica TCS SP5 confocal Inverted microscope. Analysis and quantification of images were performed in FIJI.

In vivo 2-photon microscopy

Mice 2 months old were kept anesthetized with 2% isofluorane. During surgery, body temperature was maintained at 37°C with a warming pad. After application of local anesthetics (lidocaine), a sagittal incision of the skin was made above the supra-pelvic flank to expose the subcutaneous inguinal fat pad. An imaging chamber was custom built to minimize fat movement. Warm imaging solution (in mM: 130 NaCl, 3 KCl, 2.5 CaCl2, 0.6 6H2O,MgCl2, 10 HEPES without Na, 1.2 NaHCO3, 10 glucose, pH 7.45 with NaOH) (37°C) mixed with a fat dye (LipidTOX) was applied to label adipocytes, maintain tissue integrity, and to allow the use of immersion objective. Imaging experiments were performed under a two-photon laser-scanning microscope (Ultima, Prairie Instruments Inc.). Live images were acquired at 8–12 frames per second, at depths below the surface ranging from 100 to 250 mm, using an Olympus 20x 1.0 N.A. water immersion objective, with a laser tuned to 810-940 nm wavelength, and emission filters 525/50 nm and 595/50 nm for green and red fluorescence, respectively. Laser power was adjusted to be 20–25 mW at the focal plane (maximally 35 mW), depending on the imaging depth and level of expression of GFP and LipidTOX spread. Analysis and quantification of images were performed in FIJI.

Electron microscopy

Fresh tissue was perfused with 2% paraformaldehyde (Electron Microscopy Services (EMS)), 0.2% glutaraldehyde (EMS) in 0.1M phosphate buffer (PB) (pH 7.4). After perfusion, fibers were isolated and immersion fixed for 2 hours at room temperature (RT) in the same fixative. For quenching free-aldehydes auto-fluorescence, nerves were washed with 0.15% glycine (VWR), in PB for 10 minutes at RT.

Correlative Light-Electron microscopy

After fixation, the fibers were stabilized with 0.1% tannic acid (EMS) and embed in 2% agarose (Omnipur) before cryoprotection in 30% sucrose (Alfa Aesar) ON at 4°C. Embed samples were placed in optimal cutting temperature (OCT) compound (Sakura) and plunge freeze in liquid nitrogen. 10µm sections were obtained in a Leica Cryostat CM3050S and placed in cover-glasses coated with 2% (3-Aminopropyl)triethoxysilane (Sigma Aldrich) in acetone. The light microscopy imaging was performed in a Leica SP5 Live microscope after mounting the sections with PB. For electron microscopy processing, samples were washed 10 times with PB and post-fixed in 1% osmium tetroxide (EMS) with 1% potassium hexacyanoferrate (Sigma Aldrich) in PB for 30 minutes, on

ice. Dehydration was done in a graded ethanol series of 30%, 50%, 75%, 90% and 100%, for 10 minutes each. EPON resin (EMS) was used for embedding. 70nm serial sections were obtained in a Leica UC7 and stained with 1% uranyl acetate and lead citrate for 5 minutes each. Electron microscopy images were acquired on a Hitachi H-7650 operating at 100kV.

Single cell suspension

Tissues were dissected from 10 mice. Spleen, brain, visceral fat and subcutaneous fat were excised and digested for 30 minutes with collagenase (Sigma) at 37°C with shaking. Sympathetic nerve fibers were isolated from subcutaneous adipose tissues and digested for 30 minutes with Hyaluronidase (Sigma) at 37°C with shaking, washed and further digested with collagenase for 15 minutes. SCG were dissected and digested with collagenase for 10 minutes, washed and further digested with trypsin (Biowest) for 30 minutes at 37°C with shaking. Cell suspensions were filtered through a 70 μm sieve and centrifuged at 450 xg for 5 minutes.

Flow cytometry

Flow cytometry data were acquired on a LSR Fortessa X-20 SORP (Becton-Dickinson), FACScalibur (Becton-Dickinson) or Cyan-ADP (Beckman Coulter) and analyzed using FlowJo software package (Tree Star). Macrophages were sorted as live CD45, F4/80-double positive using a FACS Aria IIu High Speed cell sorter (Becton Dickinson) or MoFlo High-Speed Cell Sorter produced by Dako Cytomation (now owned by Beckman Coulter).

Bone marrow chimeras

B6-CD45.1 mice (8-10 weeks), *B6 (C57BL/6J)* mice (8-10 weeks) or *ob/ob* (8-10 weeks) mice were lethally irradiated (900 rad, 3.42 minutes, 137Cs source) (Gammacell 2000) and reconstituted with bone marrow cells from either *Cx3cr1*$^{GFP/+}$ mice (6 weeks), *Slc6a2-/-* mice (6-8 weeks), *B6* mice (6-8 weeks) or *B6-CD45.1* mice (6-8 weeks). *B6-CD45.1* mice and *B6* mice were reconstituted with 5 x 10^6 total bone marrow cells and *ob/ob* mice were reconstituted with 3 x 10^7 total bone marrow cells. Chimerism was assessed 8 weeks after by flow cytometry.

Low-input RNAseq library preparation

Sequencing libraries were prepared according to the Smart-seq2 method (Picelli et al., 2013) with some modifications. 1715 ± 115 cells from nerve fibers, 1534 ± 85 cells from superior cervical ganglia and 5000 cells from other tissues (visceral fat, subcutaneous fat, spleen and brain) were isolated as live CD45+F4/80+ in Trizol (Thermo Fisher) and were used as starting material. RNA was extracted with the Direct-zol MicroPrep kit (Zymo Research) with on-column DNAseI treatment. 10 μL of purified RNA was mixed with 5.5 μL of SMARTScribe 5X First-Strand Buffer (Clontech), 1 μL polyT-RT primer (2.5 μM, 5'-AAGCAGTGGTATCAACGCAGAGTAC(T30)VN-3'), 0.5 μL SUPERase-IN (Ambion), 4 μL dNTP mix (10 mM, Invitrogen), 0.5 μL DTT (20 mM, Clontech) and 2 μL Betaine solution (5 M, Sigma), incubated 50°C 3 min. 3.9 μL of first strand mix, containing 0.2 μL 1% Tween-20, 0.32 μL MgCl2 (500 mM), 0.88 μL Betaine solution (5 M, Sigma), 0.5 μL SUPERase-IN (Ambion) and 2 μL SMARTScribe Reverse Transcriptase (100 U/μL, Clontech) was added and incubated one cycle 25°C 3 min., 42°C 60 min. 1.62 μL template switch (TS) reaction mix containing 0.8 μL biotin-TS oligo (10 μM, Biotin-5'-AAGCAGTGGTATCAACGCAGAGTACATrGrG+G-3'), 0.5 μL SMARTScribe Reverse Transcriptase (100 U/μL Clontech) and 0.32 μL SMARTScribe 5X First-Strand Buffer (Clontech) was added, then incubated

at 50°C 2 min., 42°C 80 min., 70°C 10 min. 14.8 µL second strand synthesis, pre-amplification mix containing 1 µL pre-amp oligo (10 µM, 5'AAGCAGTGGTATCAACGCAGAGT-3'), 8.8 µL KAPA HiFi Fidelity Buffer (5X, KAPA Biosystems), 3.5 µL dNTP mix (10 mM, Invitrogen) and 1.5 µL KAPA HiFi HotStart DNA Polymerase (1U/µL, KAPA Biosystems), was added, then amplified by PCR: 95°C 3 min., 8 cycles 98°C 20 seconds, 67°C 15 sec and 72°C 6 min, final extension 72°C 5 min. The synthesized dsDNA was purified using Sera-Mag Speedbeads (Thermo Fisher Scientific) with final 8.4% PEG8000, 1.1M NaCl, then eluted with 13 µL UltraPure water (Invitrogen). The product was quantified by Qubit dsDNA High Sensitivity Assay Kit (Invitrogen) and libraries were prepared using the Nextera DNA Sample Preparation kit (Illumina). Tagmentation mix containing 11 µL 2X Tagment DNA Buffer and 1 µL Tagment DNA Enzyme was added to 10 µL purified DNA, then incubated at 55°C 15 min. 6 µL Nextera Resuspension Buffer (Illumina) was added and incubated at room temperature for 5 min. Tagmented DNA was purified using Sera-Mag Speedbeads (Thermo Fisher Scientific) with final 7.8% PEG8000, 0.98M NaCl, then eluted with 25 µL UltraPure water (Invitrogen). Final enrichment amplification was performed with Nextera primers, adding 1 µL Index 1 primers (100 µM, N7xx), 1 µL Index 2 primers (100 µM, N5xx) and 27 µL NEBNext High-Fidelity 2X PCR Master Mix (New England BioLabs), then amplified by PCR: 72°C 5 min., 98°C 30 sec., 8-13 cycles 98°C 10 seconds, 63°C 30 sec., and 72°C 1 min. Libraries were size selected, quantified Qubit dsDNA HS Assay Kit (Thermo Fisher Scientific), pooled and sequenced on a NextSeq 500 (Illumina) for 76 cycles at a depth of 25 to 30 million single end reads per sample. To normalize for genomic DNA contamination, which occurred in some samples due to incomplete DNA removal during RNA isolation, the average intronic noise per base pair in all intronic regions per gene was calculated. The exonic reads were then normalized by subtracting the background noise per base pair for the complete length of the exonic regions. Genes without introns were not normalized, as these genes are the minority of genes and are typically short. Fastq files from sequencing experiments were mapped to the mouse mm10 genome using default parameters for STAR (Dobin et al., 2013). Mapped data were analyzed with HOMER (Heinz et al., 2010), custom R, and Perl scripts.

Superior cervical ganglia explant cultures

SCG were removed from 4-6 weeks old mice under a stereomicroscope and placed in Dulbecco's Modified Eagle's medium (DMEM, Invitrogen, Carlsbad, CA, U.S.A.). Ganglia were cleaned from the surrounding tissue capsule and transferred into 8-well Tissue Culture Chambers (Sarstedt, Nümbrecht, Germany) that were previously coated with poly-D-lysine (Sigma/Aldrich, Steinheim, Germany) in accordance to the manufacturer's instructions. Ganglia were then covered with 5 µl of Matrigel (BD Bioscience, San Jose, CA, U.S.A.) and incubated for 7 min at 37°C. DMEM without phenol red (Invitrogen) supplemented with 10% fetal bovine serum (Invitrogen), 2 mM L-Glutamine (Biowest, Nuaillé, France) and nerve growth factor (Sigma/Aldrich) were subsequently added. 12 SCG explants cultures were prepared per condition. SCG ganglia were cultured for minimum 24 hours prior to further manipulation. Stimulation protocol in Fig. 3.3 was performed for 2 hours with the following concentrations of drugs: 10 mM Acetylcholine chloride, 100 nM Nisoxetine hydrochloride, and 100 µM Clorgyline. NE measurements after optogenetic stimulation ex vivo. Depolarization of sympathetic neurons in *TH-Cre; LSL-ChR2-YFP* explant cultures were performed on a Yokogawa CSU-X Spinning Disk confocal using the 488 nm laser line and pointing at the region of interest (ROI) for 200 µs. Stimulation was repeated 7 times using 40% of laser intensity. NE in the SCG explant culture medium and sorted CD45,F4/80-double positive cells was determined with NE ELISA kit (Labor Diagnostika Nord GmbH, Nordhorn, Germany, cat No. BA E-5200). The same procedure was performed for *LSL-ChR2-YFP* control mice. NE measurements in macrophages from sWAT. CD45.2-PE, F4/80-Alexa Fluor 647 – double positive cells from sWAT were sorted as live and incubated with 2 µM Norepinephrine for 2 hours

using the same culture conditions as for SCG explant cultures. Afterwards cells were washed twice with 1xPBS and NE content was measured with NE ELISA kit (Labor Diagnostika Nord GmbH, Nordhorn, Germany, cat No. BA E-5200).

Quantitative PCR

Total RNA from sorted cells was isolated using RNeasy Plus Micro Kit (Qiagen, cat No. 50974034). Total RNA from adipose tissues was isolated with PureLink RNA Mini Kit (Ambion, Life Technologies, cat No. 12183025). cDNA was reverse transcribed using SuperScript II (Invitrogen) and random primers (Invitrogen). Quantitative PCR was performed using SYBR Green (Applied Biosystems) in ABI QuantStudio 7 (Applied Biosystems). GAPDH housekeeping gene was used to normalize samples.

The primers used are listed below:

Lpl-forward, 5'-CAGCTGGGCCTAACTT TGAG-3';

Lpl-reverse, 5'-CCTCTCTGCAATCACACGAA-3';

Pnpla2-forward, 5'-CACTTTAGCTCCAAGGATGA-3';

Pnpla2-reverse, 5'-TGGTTCAGTAG GCCATTCCT-3';

Gfap-forward, 5'-CCAGCTTCGAGCCAAGGA-3';

Gfap- reverse, 5'-GAAGCTCCGCCTGGTAGACA-3';

Gap43-forward, 5'-AGCC AAGGAGGAGCCTAAAC-3';

Gap43-reverse, 5'-CTGTCGGGCACTTTCCTTAG-3';

Ucp1-forward, 5'-GTGAAGGTCAGAATGCAAGC-3';

Ucp1-reverse, 5'-AGGGCCCCCTTCATGAGGTC-3';

Slc6a2-forward, 5'-CAGGCACCT CCATTCTGTTT-3';

Slc6a2-reverse, 5'-GCGGCTTGAAGTTGATGATG CTG-3';

Maoa-forward, 5'-GCCCAGTA TCACAGGCCAC 3';

Maoa-reverse, 5'-GTCCCACATAAGCTCCACCA-3';

Chrm1-forward, 5'-CA GTCCCAACATCACCGTCTT-3';

Chrm1-reverse, 5'-GAGAACGAAGGAAACCAACCAC-3';

Chrm2-forward, 5'-TGTCTCCCAGTCTAGTGCAAGG-3';

Chrm2-reverse, 5'-CATTCTGA CCTGACGATCCAAC-3';

Chrm4-forward, 5'-GCCTTCATCC TCACCTGGAC-3';

Chrm4-reverse, 5'-AGTGGCATTGCAGAGTGCAT-3';

Chrm5-forward, 5'-CCA TGGACTGTGGGAAGTCA-3';

Chrm5-reverse, 5'-CAGCGTCC CATGAGGATGTA-3';

Chrna2-forward, 5'-CTCCCATCCT GCTTTCCAG-3';

Chrna2-reverse, 5'-GTTTGAACAGGCGGTCCTC-3';

Chrna3-forward, 5'-GCGAACAGGTCACAGTTTATG-3';

Chrna3-reverse, 5'-GCATTTT TCTCTGGGTTTTCA-3';

Chrna5-forward, 5'-CGCTCTTCT TCCACACACAA-3';

Chrna5-reverse, 5'-TAGGTCCACCGTCTTTCTCG-3';

Chrna6-forward, 5'-CTTTGTCACGCTGTCCAT-3';

Chrna6-reverse, 5'- GCCTCCT TTGTCTTGTCC-3';

Chrna7-forward, 5'-ACAGTACTTC GCCAGCACCA-3';

Chrna7-reverse, 5'-AAACCATGCACACCAATTCA-3';

Chrna9-forward, 5'-ACAAGGCCACCAACTCCA-3';

Chrna9-reverse, 5'-ACCAACCCACTCCTCCTCTT-3';

Chrna10-forward, 5'-TCTGACCTCACAACCCACAA-3';

Chrna10-reverse, 5'-TCC TGTCTCAGCCTCCATGT-3';

Chrnb2-forward, 5'-GGGCAGGCA CACTATTCTTC-3';

Chrnb2-reverse, 5'-TCCAATCCTCCCTCACACTC-3';

Chrnb3-forward, 5'-CTCCTCAGACATT GGTTCCAAGG-3';

Chrnb3-reverse, 5'-AATGAGG TCAACCATGGT-3';

Chrnb4-forward, 5'-TCTGGTTGCCTGACATCGTG-3';

Chrnb4-reverse, 5'- GGGTTCACAAAGTACATGGA-3';

Adrb2-forward, 5'- GGTTATCGTCCTGGCCATCGTGTTTG-3';

Adrb2-reverse, 5'-TGGTTCGTGAAGAAGTCACAGCAAGTCTC-3';

Th-forward, 5'-GGTATACGCCACGCTGAAGG-3';

Th-reverse, 5'- TAGCCACAGTACCGTTCCAGA-3';

Tnfa-forward, 5'- ATGAG CACAGA AAGCATGATC-3';

Tnfa-reverse, 5'-TACAGGCTTGTCACTCGAATT-3';

Il10- forward, 5'-GCTCTTACTGACTGGCATGAG-3';

Il10-reverse, 5'-CGCAG CTCTAG GAGCATGTG-3';

Il1-forward, 5'- GAAGAAGAGCCCATCCT CTG-3';

Il1-reverse, 5'- TCATCTCGGAGCCTGTAGTG-3';

Il4ra-forward, 5'-TGACCTCACAGGAACCCAGGC-3';

Il4ra-reverse, 5'-GAACAGGC AAAACAACGGGAT-3';

Gapdh-forward, 5'-AACTTTGGCATTGTGGAAGG-3';

Gapdh-reverse, 5'-ACACATTGGGGGTAGGAACA-3'.

Functional studies

We measured body rectal temperature with an electronic thermometer (Precision) when the animals were housed both at RT and at 4°C with ND food and water ad libitum. Free fatty acids were measured in blood plasma using Free Fatty Acid Quantitation Kit (Sigma-Aldrich, cat No. MAK044-1KT). Serum NE levels were determined with NE ELISA kit (Labor Diagnostika Nord GmbH, Nordhorn, Germany, cat No. BA E-5200).

High-fat diet challenge

High-fat diet challenge. When *B6* mice reached 8 weeks we replaced ND with HFD (Ssniff, Spezialdiäten GmbH, Soest, Germany). Analyses in Fig. 4 were performed when mice gained 40% increase in body weight, after 3 months of HFD.

Intracellular stain with Ki67

Intracellular stain with Ki67. Cells were surface stained for 30 min. Subsequently, cells were washed and fixed with fixation/permeabilization buffer (eBiosciences) and then permeabilized with permeabilization buffer (eBiosciences). Following this process cells were intracellularly stained with anti-Ki67 or isotype control.

Histopathological and immunohistochemical analysis

The human and mouse tissues were fixed in buffered formalin and the inclusion in paraffin was done according to the standard technical procedures. Histochemical and immunohistochemical studies were performed on formalin-fixed paraffin-embedded tissue sections. Sections were 2 microns (human ganglia) or 3-6 microns (mouse tissues) thick (for H and E) and 4 microns thick (for the immunohistochemical study). The following markers were used for immunohistochemistry– aminoethylcarbazole (AEC) and 3,3'-diaminobenzidine (DAB), accordingly to the usual technical procedure for the marker. For the immunohistochemical studies sections underwent antigenic recovery prior to incubation with primary antibodies – anti-CD68 (Dako; clone PG-M1; dilution 1/150) anti-human Slc6a2 (Mab Techonolgies, clone 3-6C1 sc H10; dilution 1/1000), anti-MAOa (Abcam, clone GR155892-5, dilution 1/50), anti-UCP1 (Abcam, dilution 1/500). Human tissues were analyzed under an optical microscope (Nikon Eclipse 50i) and iconography microscopic images captured using a coupled digital camera (DS Camera Control Unit DS-L2). Mouse tissues were analyzed using Leica DM LB2 microscope and images were captured with Leica DFC 250 camera.

Statistics

Statistical analyses were performed using GraphPad Prism software (San Diego, CA) using unpaired Student's t-test (two-tailed) when two groups were being compared or one-way ANOVA test when several groups were being compared. One way-ANOVA was followed by Tukey's mulitiple comparison test, except for the data in Fig. 4b and Supplementary Fig. 8a where it was followed by Bonferroni multiple comparison test with one group indicated as a control group. A $P < 0.05$ was considered statistically significant. Data were represented as mean ± SEM. Sample size was predetermined based on previous studies. Data displayed normal variance.

Data availability

The RNA-seq data sets are available at GEO accession code GSE103847.

3.5 REFERENCES

Aderem, A., and Underhill, D.M. (1999). Mechanisms of phagocytosis in macrophages. Annu. Rev. Immunol. 17, 593–623.

Amano, S.U., Cohen, J.L., Vangala, P., Tencerova, M., Nicoloro, S.M., Yawe, J.C., Shen, Y., Czech, M.P., and Aouadi, M. (2014). Local Proliferation of Macrophages Contributes to Obesity-Associated Adipose Tissue Inflammation. Cell Metab. 19, 162–171.

Anlauf, E., and Derouiche, A. (2013). Glutamine Synthetase as an Astrocytic Marker: Its Cell Type and Vesicle Localization. Front. Endocrinol. 4.

Bignami, A., Eng, L.F., Dahl, D., and Uyeda, C.T. (1972). Localization of the glial fibrillary acidic protein in astrocytes by immunofluorescence. Brain Res. 43, 429–435.

Butovsky, O., Jedrychowski, M.P., Moore, C.S., Cialic, R., Lanser, A.J., Gabriely, G., Koeglsperger, T., Dake, B., Wu, P.M., Doykan, C.E., et al. (2014). Identification of a unique TGF-[beta]-dependent molecular and functional signature in microglia. Nat. Neurosci. 17, 131–143.

Buttgereit, A., Lelios, I., Yu, X., Vrohlings, M., Krakoski, N.R., Gautier, E.L., Nishinakamura, R., Becher, B., and Greter, M. (2016). Sall1 is a transcriptional regulator defining microglia identity and function. Nat. Immunol. 17, 1397–1406.

Chaudhry, F.A., Lehre, K.P., van Lookeren Campagne, M., Ottersen, O.P., Danbolt, N.C., and Storm-Mathisen, J. (1995). Glutamate transporters in glial plasma membranes: highly differentiated localizations revealed by quantitative ultrastructural immunocytochemistry. Neuron 15, 711–720.

Clausen, B.E., Burkhardt, C., Reith, W., Renkawitz, R., and Förster, I. (1999). Conditional gene targeting in macrophages and granulocytes using LysMcre mice. Transgenic Res. 8, 265–277.

Crotti, A., and Ransohoff, R.M. (2016). Microglial Physiology and Pathophysiology: Insights from Genome-wide Transcriptional Profiling. Immunity 44, 505–515.

Dobin, A., Davis, C.A., Schlesinger, F., Drenkow, J., Zaleski, C., Jha, S., Batut, P., Chaisson, M., and Gingeras, T.R. (2013). STAR: ultrafast universal RNA-seq aligner. Bioinformatics 29, 15–21.

Filiano, A.J., Xu, Y., Tustison, N.J., Marsh, R.L., Baker, W., Smirnov, I., Overall, C.C., Gadani, S.P., Turner, S.D., Weng, Z., et al. (2016). Unexpected role of interferon-γ in regulating neuronal connectivity and social behaviour. Nature 535, 425–429.

Fischer, K., Ruiz, H.H., Jhun, K., Finan, B., Oberlin, D.J., van der Heide, V., Kalinovich, A.V., Petrovic, N., Wolf, Y., Clemmensen, C., et al. (2017). Alternatively activated macrophages do not synthesize catecholamines

or contribute to adipose tissue adaptive thermogenesis. Nat. Med. advance online publication.

Gabanyi, I., Muller, P.A., Feighery, L., Oliveira, T.Y., Costa-Pinto, F.A., and Mucida, D. (2016). Neuro-immune Interactions Drive Tissue Programming in Intestinal Macrophages. Cell 164, 378–391.

Galle-Treger, L., Suzuki, Y., Patel, N., Sankaranarayanan, I., Aron, J.L., Maazi, H., Chen, L., and Akbari, O. (2016). Nicotinic acetylcholine receptor agonist attenuates ILC2-dependent airway hyperreactivity. Nat. Commun. 7.

Gautier, E.L., Shay, T., Miller, J., Greter, M., Jakubzick, C., Ivanov, S., Helft, J., Chow, A., Elpek, K.G., Gordonov, S., et al. (2012). Gene-expression profiles and transcriptional regulatory pathways that underlie the identity and diversity of mouse tissue macrophages. Nat. Immunol. 13, 1118–1128.

Gosselin, D., Link, V., Romanoski, C.E., Fonseca, G.J., Eichenfield, D.Z., Spann, N.J., Stender, J.D., Chun, H.B., Garner, H., Geissmann, F., et al. (2014). Environment drives selection and function of enhancers controlling tissue-specific macrophage identities. Cell 159, 1327–1340.

Gosselin, D., Skola, D., Coufal, N.G., Holtman, I.R., Schlachetzki, J.C.M., Sajti, E., Jaeger, B.N., O'Connor, C., Fitzpatrick, C., Pasillas, M.P., et al. (2017). An environment-dependent transcriptional network specifies human microglia identity. Science 356.

Hanani, M. (2005). Satellite glial cells in sensory ganglia: from form to function. Brain Res. Brain Res. Rev. 48, 457–476.

Hanani, M. (2010). Satellite glial cells in sympathetic and parasympathetic ganglia: in search of function. Brain Res. Rev. 64, 304–327.

Heinz, S., Benner, C., Spann, N., Bertolino, E., Lin, Y.C., Laslo, P., Cheng, J.X., Murre, C., Singh, H., and Glass, C.K. (2010). Simple combinations of lineage-determining transcription factors prime cis-regulatory elements required for macrophage and B cell identities. Mol. Cell 38, 576–589.

Ibiza, S., García-Cassani, B., Ribeiro, H., Carvalho, T., Almeida, L., Marques, R., Misic, A.M., Bartow-McKenney, C., Larson, D.M., Pavan, W.J., et al. (2016). Glial-cell-derived neuroregulators control type 3 innate lymphoid cells and gut defence. Nature 535, 440–443.

Jessen, K.R., and Mirsky, R. (2005). The origin and development of glial cells in peripheral nerves. Nat. Rev. Neurosci. 6, 671–682.

Kipnis, J. (2016). Multifaceted interactions between adaptive immunity and the central nervous system. Science 353, 766–771.

Kong, Y., Ruan, L., Qian, L., Liu, X., and Le, Y. (2010). Norepinephrine promotes microglia to uptake

and degrade amyloid beta peptide through upregulation of mouse formyl peptide receptor 2 and induction of insulin-degrading enzyme. J. Neurosci. Off. J. Soc. Neurosci. 30, 11848–11857.

Louveau, A., Smirnov, I., Keyes, T.J., Eccles, J.D., Rouhani, S.J., Peske, J.D., Derecki, N.C., Castle, D., Mandell, J.W., Kevin, S.L., et al. (2015). Structural and functional features of central nervous system lymphatics. Nature 523, 337–341.

Ludwin, S.K., Kosek, J.C., and Eng, L.F. (1976). The topographical distribution of S-100 and GFA proteins in the adult rat brain: an immunohistochemical study using horseradish peroxidase-labelled antibodies. J. Comp. Neurol. 165, 197–207.

Mathis, D. (2013). Immunological Goings-on in Visceral Adipose Tissue. Cell Metab. 17, 851–859.

Mearow, K.M., Mill, J.F., and Vitkovic, L. (1989). The ontogeny and localization of glutamine synthetase gene expression in rat brain. Brain Res. Mol. Brain Res. 6, 223–232.

Merad, M., Manz, M.G., Karsunky, H., Wagers, A., Peters, W., Charo, I., Weissman, I.L., Cyster, J.G., and Engleman, E.G. (2002). Langerhans cells renew in the skin throughout life under steady-state conditions. Nat. Immunol. 3, 1135–1141.

Nguyen, K.D., Qiu, Y., Cui, X., Goh, Y.P.S., Mwangi, J., David, T., Mukundan, L., Brombacher, F., Locksley, R.M., and Chawla, A. (2011). Alternatively activated macrophages produce catecholamines to sustain adaptive thermogenesis. Nature 480, 104–108.

Okabe, Y., and Medzhitov, R. (2014). Tissue-specific signals control reversible program of localization and functional polarization of macrophages. Cell 157, 832–844.

Picelli, S., Björklund, Å.K., Faridani, O.R., Sagasser, S., Winberg, G., and Sandberg, R. (2013). Smart-seq2 for sensitive full-length transcriptome profiling in single cells. Nat. Methods 10, 1096–1098.

Prinz, M., and Priller, J. (2014). Microglia and brain macrophages in the molecular age: from origin to neuropsychiatric disease. Nat. Rev. Neurosci. 15, 300–312.

Raff, M.C., Mirsky, R., Fields, K.L., Lisak, R.P., Dorfman, S.H., Silberberg, D.H., Gregson, N.A., Leibowitz, S., and Kennedy, M.C. (1978). Galactocerebroside is a specific cell-surface antigenic marker for oligodendrocytes in culture. Nature 274, 813–816.

Regan, M.R., Huang, Y.H., Kim, Y.S., Dykes-Hoberg, M.I., Jin, L., Watkins, A.M., Bergles, D.E., and Rothstein, J.D. (2007). Variations in promoter activity reveal a differential expression and physiology of glutamate transporters by glia in the developing and mature CNS. J. Neurosci. Off. J. Soc. Neurosci. 27, 6607–6619.

Reitman, M.L. (2017). How Does Fat Transition from White to Beige? Cell Metab. 26, 14–16.

Rosas-Ballina, M., Olofsson, P.S., Ochani, M., Valdés-Ferrer, S.I., Levine, Y.A., Reardon, C., Tusche, M.W., Pavlov, V.A., Andersson, U., Chavan, S., et al. (2011). Acetylcholine-Synthesizing T Cells Relay Neural Signals in a Vagus Nerve Circuit. Science 334, 98–101.

Rusnakova, V., Honsa, P., Dzamba, D., Ståhlberg, A., Kubista, M., and Anderova, M. (2013). Heterogeneity of astrocytes: from development to injury - single cell gene expression. PloS One 8, e69734.

Schroeder, C., and Jordan, J. (2012). Norepinephrine transporter function and human cardiovascular disease. Am. J. Physiol. Heart Circ. Physiol. 303, H1273-1282.

Sensenbrenner, M., Lucas, M., and Deloulme, J.C. (1997). Expression of two neuronal markers, growth-associated protein 43 and neuron-specific enolase, in rat glial cells. J. Mol. Med. Berl. Ger. 75, 653–663.

Shirey-Rice, J.K., Klar, R., Fentress, H.M., Redmon, S.N., Sabb, T.R., Krueger, J.J., Wallace, N.M., Appalsamy, M., Finney, C., Lonce, S., et al. (2013). Norepinephrine transporter variant A457P knock-in mice display key features of human postural orthostatic tachycardia syndrome. Dis. Model. Mech. 6, 1001–1011.

Spadaro, O., Camell, C.D., Bosurgi, L., Nguyen, K.Y., Youm, Y.-H., Rothlin, C.V., and Dixit, V.D. (2017). IGF1 Shapes Macrophage Activation in Response to Immunometabolic Challenge. Cell Rep. 19, 225–234.

Stjärne, L. (1989). Basic mechanisms and local modulation of nerve impulse-induced secretion of neurotransmitters from individual sympathetic nerve varicosities. Rev. Physiol. Biochem. Pharmacol. 112, 1–137.

Wentworth, J.M., Naselli, G., Brown, W.A., Doyle, L., Phipson, B., Smyth, G.K., Wabitsch, M., O'Brien, P.E., and Harrison, L.C. (2010). Pro-inflammatory CD11c+CD206+ adipose tissue macrophages are associated with insulin resistance in human obesity. Diabetes 59, 1648–1656.

Wolf, Y., Boura-Halfon, S., Cortese, N., Haimon, Z., Sar Shalom, H., Kuperman, Y., Kalchenko, V., Brandis, A., David, E., Segal-Hayoun, Y., et al. (2017). Brown-adipose-tissue macrophages control tissue innervation and homeostatic energy expenditure. Nat. Immunol. 18, 665–674.

Zeng, W., Pirzgalska, R.M., Pereira, M.M.A., Kubasova, N., Barateiro, A., Seixas, E., Lu, Y.-H., Kozlova, A., Voss, H., Martins, G.G., et al. (2015). Sympathetic Neuro-adipose Connections Mediate Leptin-Driven Lipolysis. Cell 163, 84–94.

(2013). Neuroglia (Oxford, New York: Oxford University Press).

3.6 SUPPLEMENTARY FIGURES

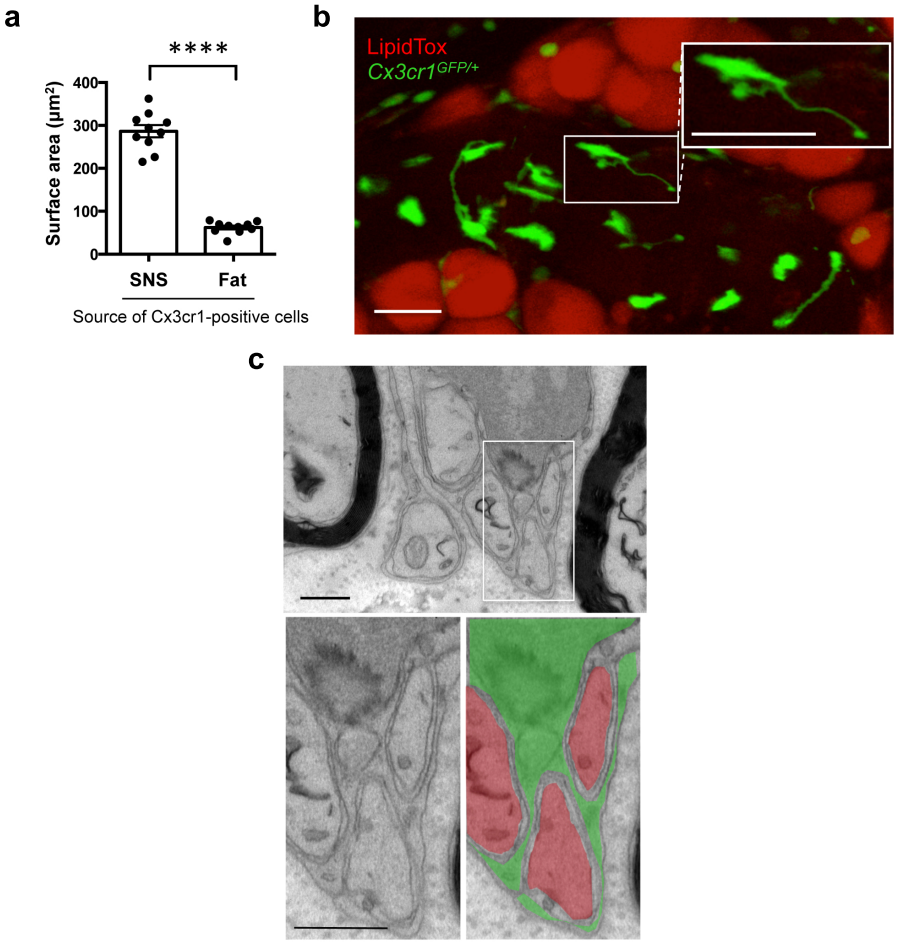

Figure 3.S1. Sympathetic neuron-associated *Cx3cr1*$^{GFP/+}$ cells differ in morphology from *Cx3cr1*$^{GFP/+}$ cells in the parenchyma of adipose tissue and wrap around non-myelinated neurons in adipose tissue.

(a) Surface area of *Cx3cr1*$^{GFP/+}$ cells associated with the nerve fibers (SNS) and fat was quantified from 3 independent experiments. 3-4 measurements were taken per one multi-photon image. n = 10 per group, ****P $<$ 0.0001. **(b)** Intra-vital multi-photon visualization of a neuro-adipose connection in the inguinal fat pad of a live *Cx3cr1*$^{GFP/+}$ mouse; LipidTOX (red) labels adipocytes. Images are representative of 3 similar experiments. Boxed region represents higher magnification of the same micrograph. Scale bar, 50 µm.**(c)** Upper panel: electron microscopy image of a sympathetic fiber dissected from subcutaneous adipose tissue with lower panels being higher magnification of the same micrograph. Lower right panel: electron micrograph with false color-coding highlighting cells wrapping around the neurons (green) and sympathetic neurons (red). Scale bars, 500 nm. Data in panel **a** were analyzed by two-tailed Student's t-test.

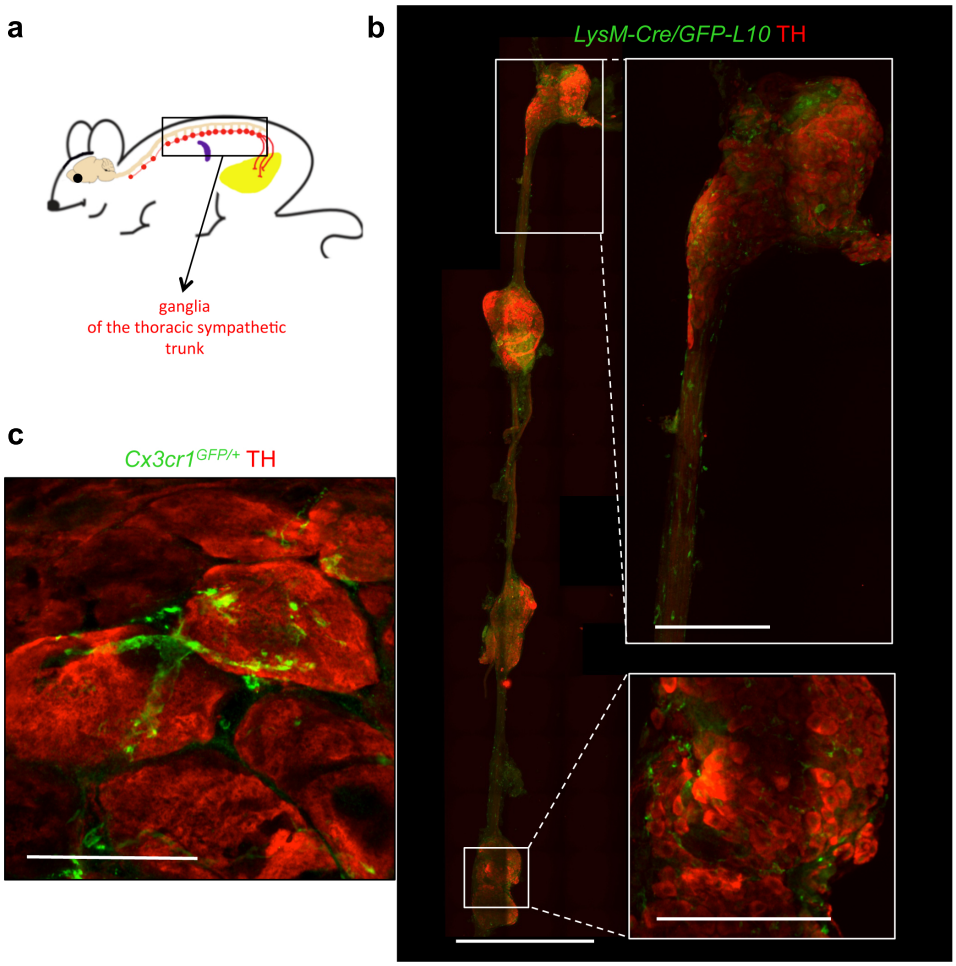

Figure 3.S2. Sympathetic neuron-associated *Cx3cr1*$^{GFP/+}$ cells are present in different compartments of the SNS.

(a) Schematic representation of the sympathetic thoracic chain ganglia. **(b)** Confocal images from sympathetic thoracic chain isolated from *LysM-Cre*$^{GFP\text{-}L10}$ mice and stained using anti-TH (red) and anti-GFP (green) antibodies. Images are representative of 3 similar experiments. Scale bar, 0.5 mm. Boxed regions represent higher magnification of the same micrograph - scale bars, 125 μm **(c)** Confocal images from sympathetic chain isolated from *Cx3cr1*$^{GFP/+}$ mice and stained using anti-TH (red) and anti-GFP (green) antibodies. Images are representative of 3 similar experiments. Scale bar, 25 μm.

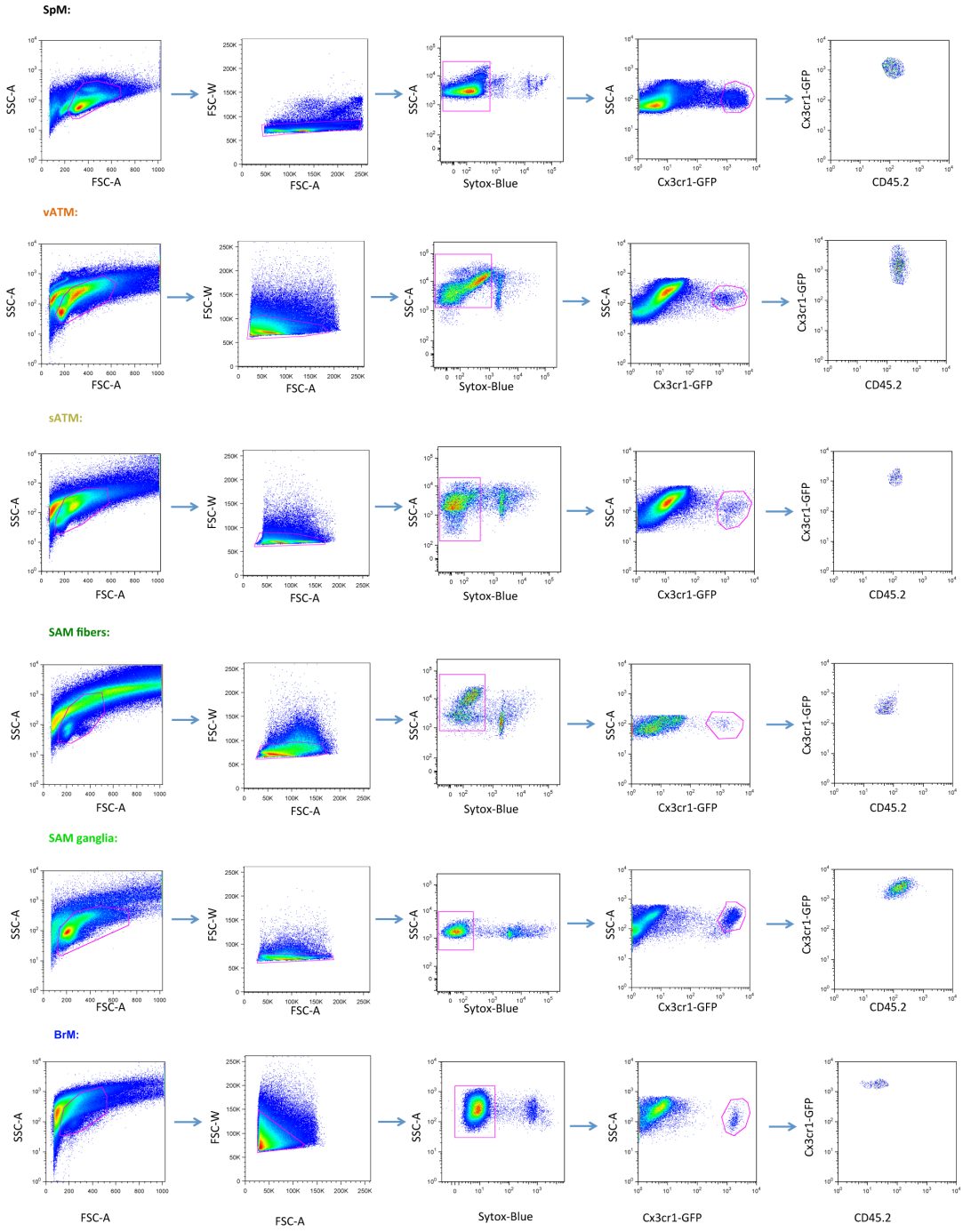

Figure 3.S3. Sympathetic-associated *Cx3cr1*$^{GFP/+}$ cells are CD45$^{Medium/High}$.
Representative flow cytometry plots showing gating strategies used to indicate CD45.2 expression by *Cx3cr1*$^{GFP/+}$ cells from: spleen (SpM), visceral adipose tissue (vATM), subcutaneous adipose tissue (sATM), nerve fibers from subcutaneous adipose tissue (SAM fibers), superior cervical ganglia (SAM ganglia), brain (BrM). Data are representative of 3 experiments.

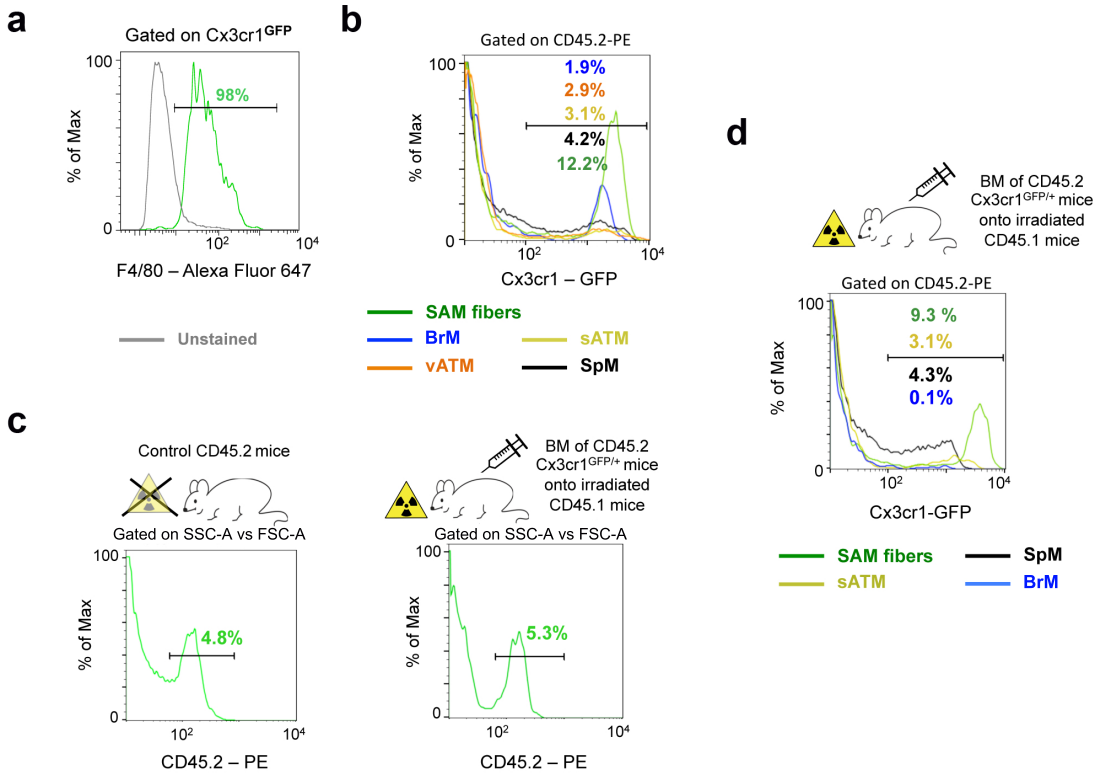

Figure 3.S4. Sympathetic neuron-associated *Cx3cr1*$^{GFP/+}$ cells are macrophages and repopulate after bone marrow irradiation.

(a) Representative flow cytometry histogram for F4/80–Alexa Fluor 647 expression by Cx3cr1-positive cells in the nerve fibers in subcutaneous fat from *Cx3cr1*$^{GFP/+}$ mice. Cells were gated on *Cx3cr1*$^{GFP/+}$ population. Histograms are representative of 5 independent experiments. **(b)** Percentages of *Cx3cr1*$^{GFP/+}$ cells in the following tissues: spleen (SpM; black), visceral adipose tissue (vATM; orange), subcutaneous adipose tissue (sATM; yellow), sympathetic nerve fibers (SAM fibers; green) and brain (BrM; blue). Cells were gated on CD45.2-PE-positive population. Histograms are representative of 5 independent experiments. **(c-d)** Bone marrow chimeras of *Cx3cr1*$^{GFP/+}$ donors onto irradiated *B6-CD45.1* host mice. **(c)** Percentages of CD45.2-PE-positive cells in sympathetic nerve fibers are shown in non-irradiated control *B6-CD45.2* (left panel) and irradiated *B6-CD45.1* chimeric mice that were reconstituted with bone marrow from *B6-CD45.2* mice (right panel). Histograms are representative of 3 experiments. **(d)** Percentages of *Cx3cr1*$^{GFP/+}$ cells in sympathetic nerve fibers (green), adipose tissue (yellow), spleen (black) and brain (blue) in irradiated *B6-CD45.1* mice that were reconstituted with bone marrow from *Cx3cr1*$^{GFP/+}$ mice. Cells were gated on CD45.2-PE-positive population. Histograms are representative of 3 experiments.

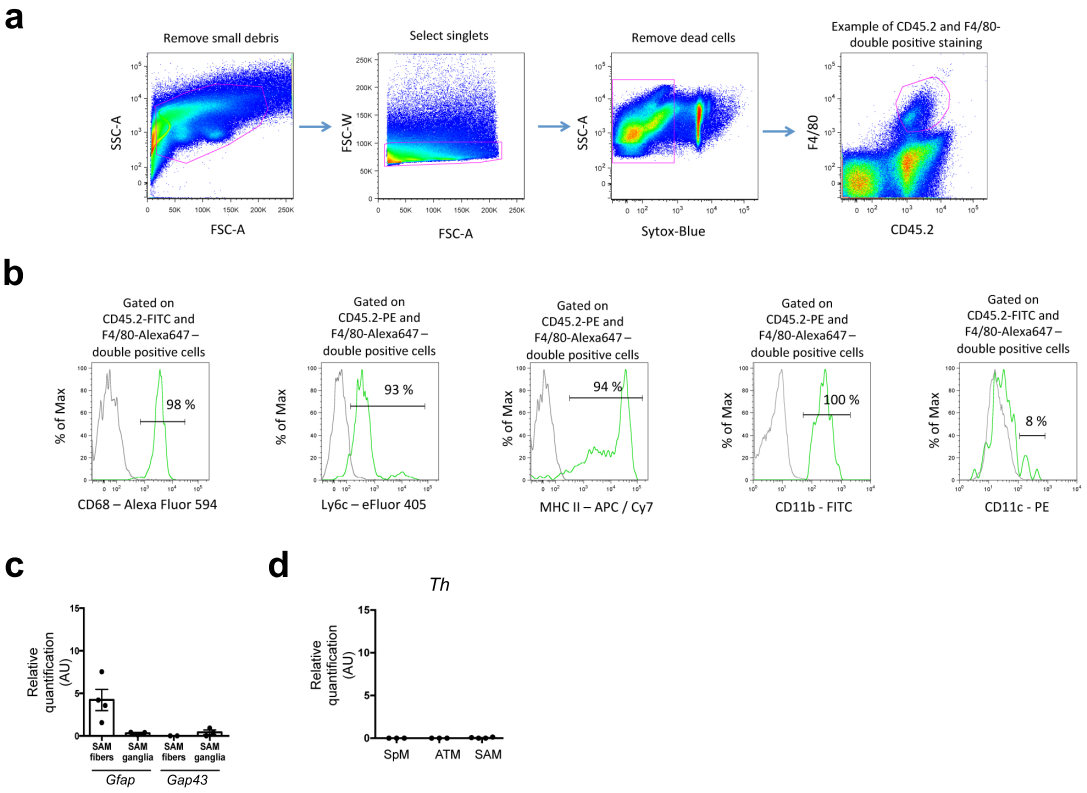

Figure 3.S5. Gating strategy for identification of macrophages. Myeloid and glial marker expression by macrophages. Absence of machinery for NE biosynthesis in SAMs.

(a) Flow cytometry gating scheme for identification of CD45.2, F4/80-double positive macrophage populations. Dot plots represent gating strategy for macrophages in subcutaneous adipose tissue. **(b)** Representative flow cytometry histograms for CD68, Ly6c, MHC II, CD11b and CD11c expression in SAMs. Cells were gated on CD45.2, F4/80-double positive population. Histograms are representative of 3 experiments. **(c)** CD45.2, F4/80- double positive macrophages were isolated from sympathetic nerve fibers (SAM fibers) and superior cervical ganglia (SAM ganglia). Expression of mRNA for Gfap and Gap43 was determined by qRT-PCR and is presented relative to Gapdh expression. n = 4 experiments for SAM fibers (Gfap), n = 3 experiments for SAM ganglia (Gfap and Gap43), n = 2 experiments SAM fibers (Gap43). **(d)** CD45.2, F4/80- double positive macrophages were isolated from spleen (SpM), adipose tissue (ATM), and sympathetic nerve fibers (SAM). Expression of mRNA for TH was determined by qRT-PCR and is presented relative to Gapdh expression. Tissues were pooled from 10 mice. n = 3 experiments for SpM and ATM and n = 4 experiments for SAM. Data were analyzed in panel **c** by two-tailed Student's t-test and panel **d** by one-way ANOVA followed by Tukey's multiple comparison test. Data are shown as average ± SEM.

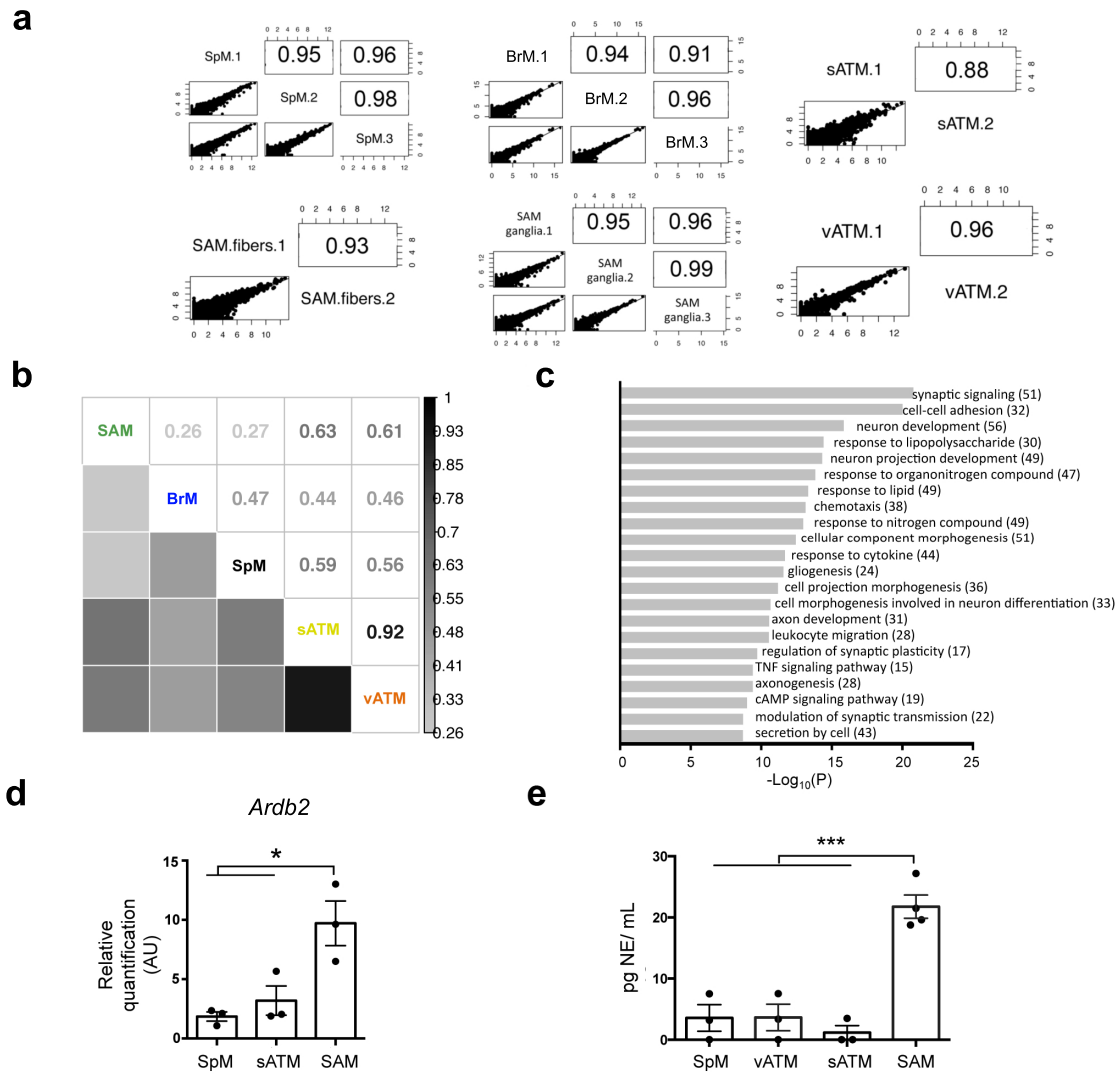

Figure 3.S6. Identity of SAMs can be reliably probed with low-input RNA-seq.

(a) Scatterplots illustrating relative gene expression of transcripts from independent experiments. The following numbers of CD45.2, F4/80- double positive cells were used to generate the datasets: 1715 ± 115 cells from nerve fibers (SAM fibers, n = 2 experiments), 1534 ± 85 cells from superior cervical ganglia (SAM ganglia, n = 3 experiments) and 5000 cells from other tissues - visceral fat (vATM, n = 2 experiments), subcutaneous fat (sATM, n = 2 experiments), spleen (SpM, n = 3 experiments) and brain (BrM, n = 3 experiments). Represented values are Reads Per Kilobase of transcript per Million mapped reads (RPKM), determined by low input RNA-seq. **(b)** Pearson correlation of transcripts is represented by Pearson coefficient of RPKM values differing in expression by at least 4-fold in at least one of the indicated subsets, determined by low-input RNA-seq. n = 2-3 experiments as indicated above. **(c)** Annotated gene ontology biological processes assigned to genes upregulated in SAMs relative to sATMs, determined by RNA-seq. Results are representative of 2 experiments. **(d)** CD45.2, F4/80- double positive macrophages were isolated from spleen (SpM), adipose tissue (ATM), and sympathetic nerve fibers (SAM). Expression of mRNA for Adrb2 was determined by qRT-PCR and is presented relative to Gapdh expression. Tissues were pooled from 10 mice. n = 3 experiments per group, *P $<$ 0.05.

(e) NE content in sorted CD45.2, F4/80- double positive cells measured by NE ELISA. Number of cells used in NE assays were as follows: 858 ± 258 for SAMs (n = 4 experiments), 1000 cells for sATM, vATM and SpM (n = 3 experiments). ***P $<$ 0.001. The same data is presented in Fig. 3.2 i as pg of NE per 1000 cells. Data in panels **d,e** were analyzed by one-way ANOVA followed by Tukey's multiple comparison test and are shown as average ± SEM.

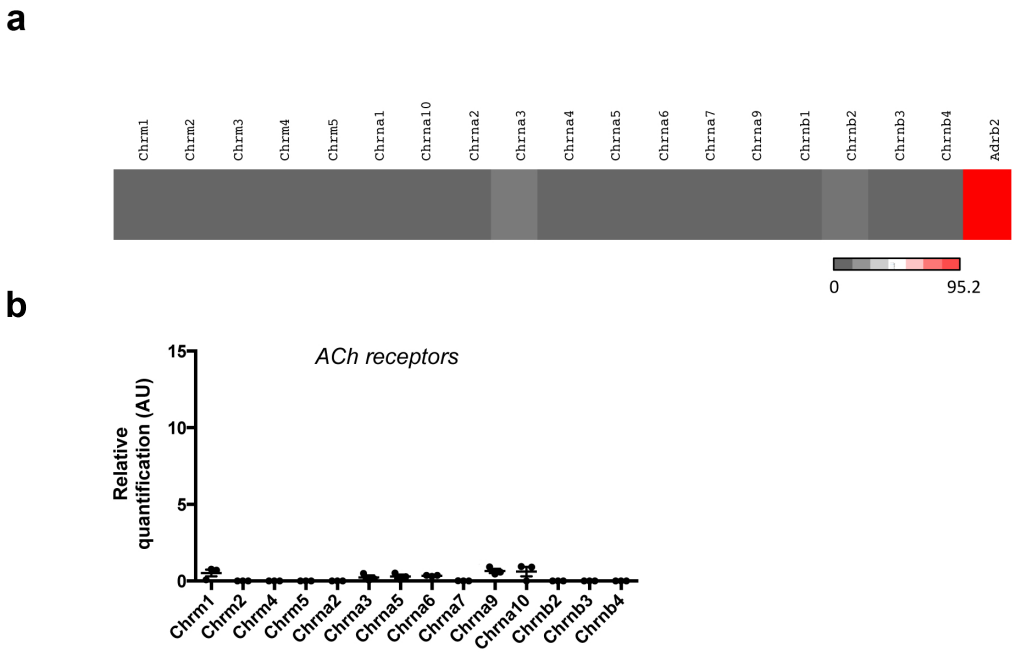

Figure 3.S7. Lack of acetylcholine receptor expression in SAMs.

(a-b) Macrophages were isolated from sympathetic ganglia and sorted as live CD45.2, F4/80- double positive cells. **(a)** Heat map of genes for nicotinic and muscarinic ACh receptors determined by low-input RNA-seq. Adrb2 expression is shown as a positive control. Values are RPKM and are representative of 3 experiments. **(b)** Expression of mRNA for nicotinic and muscarinic ACh receptors determined by qRT-PCR presented relative to Gapdh expression. Each data point represents 20 pooled ganglia. n = 3 experiments per group. Data are shown as average ± SEM.

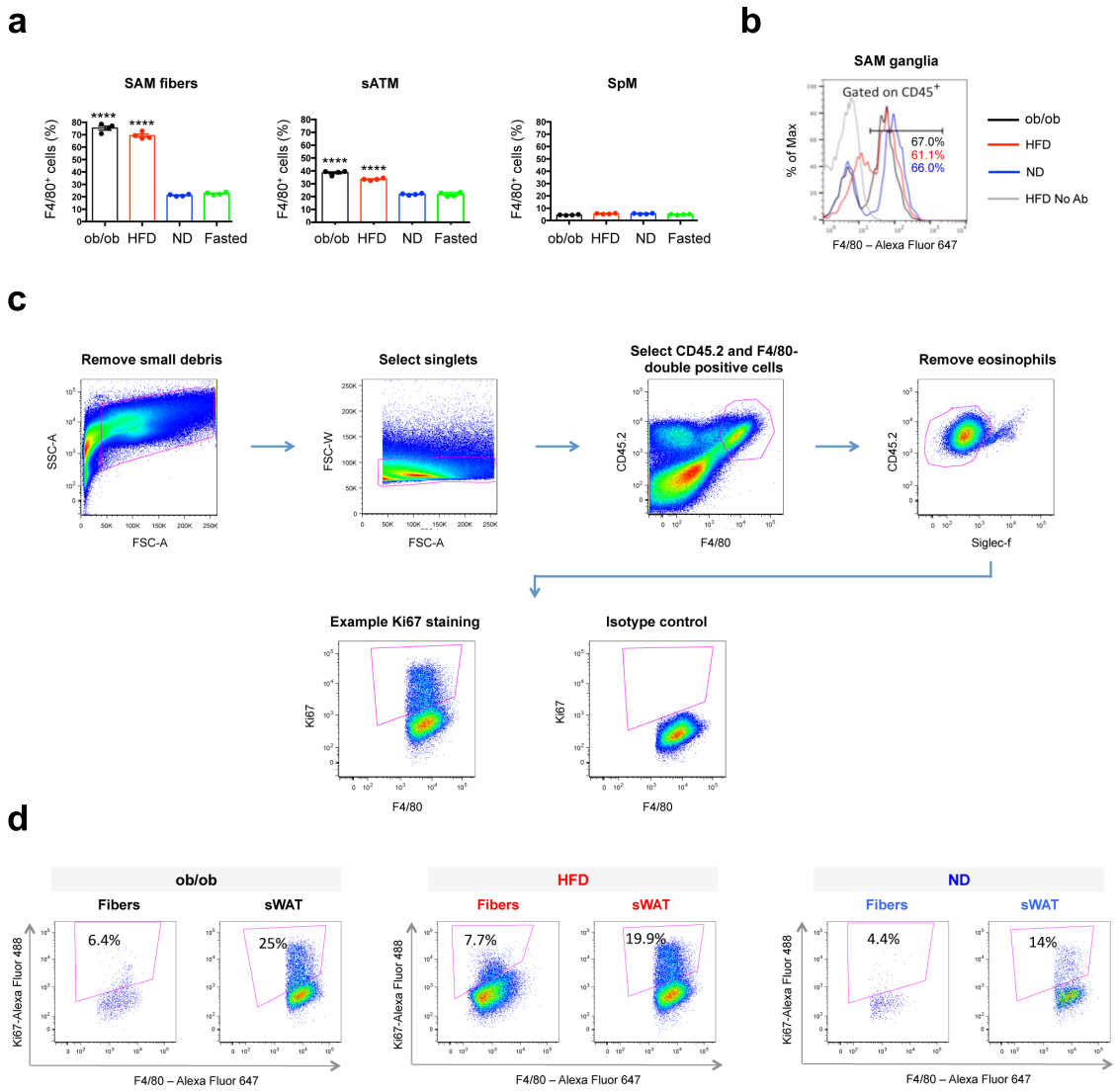

Figure 3.S8. Obesity recruits macrophages to sympathetic nerve fibers but not to superior cervical ganglia. Obesity induces proliferation of macrophages in subcutaneous white adipose tissue but not in sympathetic nerve fibers.

(a) Percentages of totals cells that are F4/80-positive in sympathetic nerve fibers (left panel), subcutaneous adipose tissue (middle panel) and spleen (right panel) in mice that were genetically obese (*ob/ob*; black), obese due to high fat diet (HFD; red), fed normal diet (ND; blue) or food-deprived for 24 hours (Fasted; green). Cells were gated on CD45.2-positive population. n = 4 experiments per group, ****P $<$ 0.0001. **(b)** Representative histograms showing percentages of total cells that were F4/80-positive in superior cervical ganglia of mice that were genetically obese (*ob/ob*; black), obese due to high fat diet (HFD; red), or fed normal diet (ND; blue). Cells were gated on CD45.2-positive population. Histograms are representative of 4 independent experiments. **(c)** Representative gating scheme for identification of macrophages expressing Ki67 proliferation marker in the subcutaneous adipose tissue. **(d)** Percentages of Ki67-positive cells in sympathetic nerve fibers and subcutaneous adipose tissue (sWAT) in mice that were genetically obese (*ob/ob*; black), obese due to high fat diet (HFD; red) or fed normal diet (ND; blue). Results are representative of 2 experiments. Data in panel **a** were analyzed by one-way ANOVA followed by Bonferroni multiple comparison test with ND as a control group and are shown as average ± SEM.

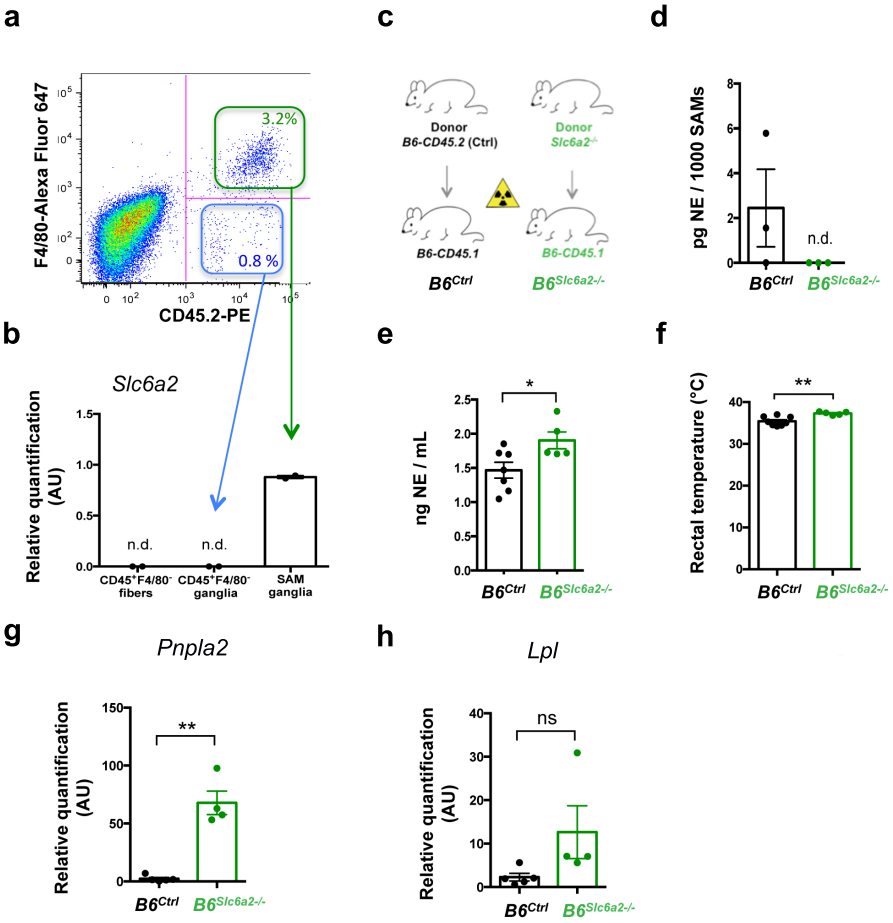

Figure 3.S9. Absence of Slc6a2 in CD45.2-positive, F4/80-negative cells from superior cervical ganglia and Slc6a2 depletion in macrophages using bone marrow transplantation from Slc6a2-/- mice.

(a) Representative flow cytometry plots showing percentages of CD45.2, F4/80 – double positive cells (green box) and CD45.2-positive, F4/80- negative cells (blue box) in SCG. Data are representative of 5 similar experiments. **(b)** Expression of mRNA for Slc6a2 in CD45.2-PE-positive and F4/80-negative cells from nerve fibers and SCG, and CD45.2, F4/80– double positive cells from SCG. n = 2 experiments. n.d. – not determined.**(c-h)** *B6-CD45.1* mice received bone marrow transplant from either *Slc6a2-/-* mice ($B6^{Slc6a2-/-}$ chimeras) or control *B6* mice ($B6^{Ctrl}$). **(c)** Schematic representation of the bone marrow transplant experiment. **(d)** NE content in CD45.2, F4/80– double positive cells sorted from SCG was assayed with NE ELISA. ∼249 cells from $B6^{Slc6a2-/-}$ chimeras and ∼353 cells from $B6^{Ctrl}$ were used per assay. n = 3 assays per group. n.d.-not determined. **(e)** Serum NE levels measured 8 weeks after BM transfer. Each data point represents one mouse. n = 5 mice for $B6^{Slc6a2-/-}$ chimeras, n = 7 mice for $B6^{Ctrl}$ chimeras, *P = 0.029. **(f)** Rectal temperature was measured 8 weeks after BM transfer at RT. Each data point represents one mouse. n = 5 mice for $B6^{Slc6a2-/-}$ chimeras, n = 7 mice for $B6^{Ctrl}$ chimeras, **P = 0.0016. **(g-h)** Expression of mRNA for **(g)** Pnpla2 and **(h)** Lpl in WAT after 6 hours of cold exposure (4°C) determined by qRT-PCR relative to Gapdh expression. Each data point represents one mouse. n = 4 mice for $B6^{Slc6a2-/-}$ and n = 5 mice for $B6^{Ctrl}$ chimeras, **P = 0.0071. Data were analyzed by two-tailed Student's t-test and are shown as average ± SEM.

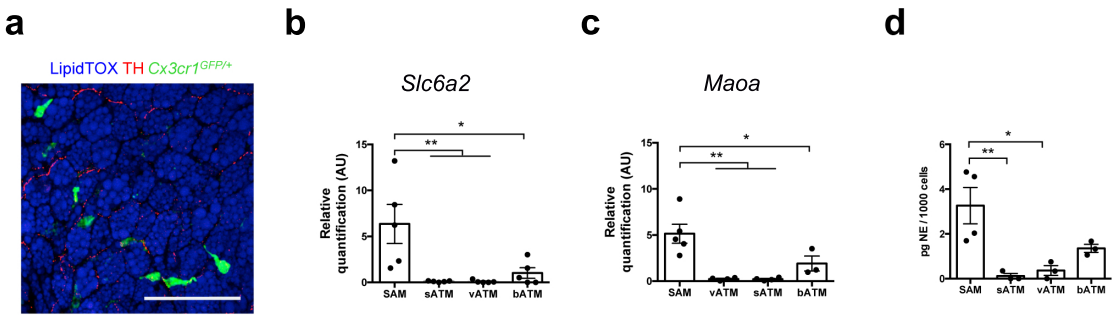

Figure 3.S10. Macrophages in brown adipose tissue have intermediate phenotype between ATMs and SAMs.

(a) Confocal image of BAT isolated from $Cx3cr1^{GFP/+}$ mice and stained using lipid stain LipidTOX (blue), anti-TH (red) and anti-GFP (green) antibodies. Micrograph is representative of 2 experiments. Scale bar, 100 μm. **(b)** Expression of mRNA for Slc6a2 determined by qRT-PCR relative to Gapdh expression. Each data point represents tissues pooled from 10 mice. n = 5 experiments for SAM, vATM, sATM and bATM, **P < 0.01, *P < 0.05. **(c)** Expression of mRNA for Maoa determined by qRT-PCR relative to Gapdh expression. Each data point represents tissues pooled from 10 mice. n = 5 experiments for SAM, n = 4 experiments for vATM, sATM and n = 3 experiments for bATM, **P < 0.01, *P < 0.05. **(d)** NE content in sorted CD45.2, F4/80– double positive cells measured by NE ELISA. Number of cells used in NE assays were as follows: 858 ± 258 for SAMs (n = 4 experiments), 1000 cells for sATM and vATM (n = 3 experiments), 1494 ± 172 for bATM (n = 3 experiments). *P < 0.05, **P < 0.01. Data were analyzed by one-way ANOVA followed by Tukey's multiple comparison test and are shown as average ± SEM. Data for SAM, sATM and vATM in panels **b-d** are also shown in Figure 3.2 **g,h** and **i**.

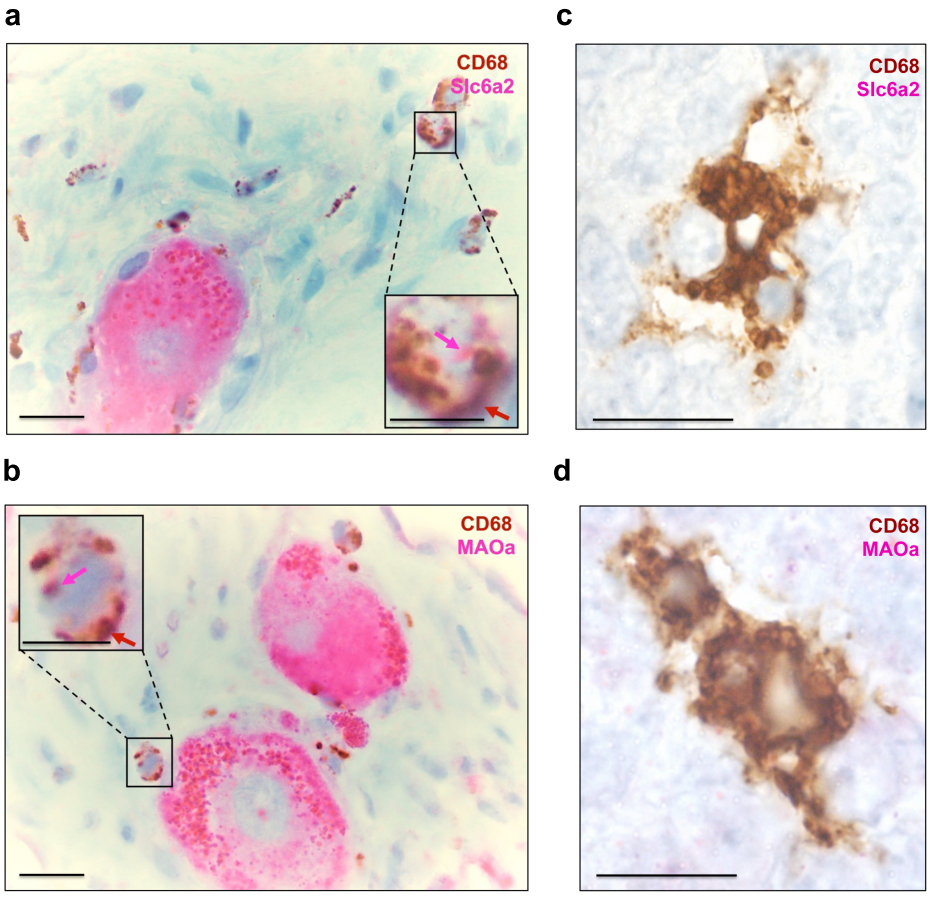

Figure 3.S11. Macrophages in human sympathetic ganglia, but not in the gut-associated lymphoid tissue, express Slc6a2 and MAOa.

(a) Optical micrograph of human ganglia from the thoracolumbar region stained with an antibody against CD68 and Slc6a2. Red arrows indicate CD68- and Slc6a2- double positive regions. **(b)** Optical micrograph of human ganglia from the thoracolumbar region stained with an antibody against CD68 and MAOa. Red arrows indicate CD68- and MAOa- double positive regions. **(c)** Optical micrograph of human gut-associated lymphoid tissue (GALT) stained with an antibody against CD68 and Slc6a2. **(d)** Optical micrograph of human GALT stained with an antibody against CD68 and MAOa. Micrographs in panels **c** and **d** serve as negative controls. Scale bars for **a** and **b**, 50 μm, for **c** and **d**, 25 μm, for boxed regions, 20 μm. Images in panels **a-d** are representative of 9 different human samples (n = 9).

4 | FINAL REMARKS

Roksana M Pirzgalska[1]

[1]Obesity Laboratory, Instituto Gulbenkian de Ciencia, Oeiras, 2780-156, Portugal

Our work has provided novel insight into the neural and immune regulation of adipose tissue (AT). In this section, I will discuss the relevance of our findings at the level of both basic and clinical research.

Starting with the neuronal-centric component of the work, we showed that the white AT (WAT) is targeted by sympathetic axons (Zeng et al., 2015). It was previously known that brown AT (BAT) was regulated by leptin-mediated sympathetic signalling (Bachman et al., 2002; Landsberg et al., 1984). Our observations extend this concept to WAT. We have provided evidence that sympathetic activity is responsible for the leptin-induced lipolysis in WAT. Although the sympathetic activation in the BAT is mediated by the central nervous system (CNS), the pathways regulating this process in the WAT are still unknown (Fenselau et al., 2017; Gautron et al., 2015). In this context, we can envisage two non-mutually exclusive scenarios. The first is that the same CNS centres that modulate sympathetic nervous system (SNS) activity in BAT play a similar role in the WAT. The second is that the yet unknown peripheral leptin sensors mediate the leptin-driven activation of WAT innervation. Future studies aiming to clarify this aspect will be particularly welcome additions to the literature.

A clinically important question is whether the activation of the sympathetic nerve bundles in WAT can drive the "beige-ing" of white adipocytes. As previously discussed, beige fat has anti-obesity and anti-diabetic potential, and its formation can be induced by adrenergic agonists (Bachman et al., 2002; Dempersmier et al., 2015; Giralt and Villarroya, 2013). Thus, sympathetic output to the AT may promote the transition of white adipocytes to beige ones (Bachman et al., 2002; Dempersmier et al., 2015; Giralt and Villarroya, 2013). Consistent with this, leptin has been suggested to increase the formation of beige fat (Dodd et al., 2015) and our results indicate that leptin increases the SNS outflow to the inguinal WAT. Future studies employing local stimulation of neurons, such as optogenetics, will likely uncover

whether the activation of the SNS in WAT could drive the "beige-ing" of WAT.

Whereas optogenetic activation of the peripheral nervous system is feasible in the context of basic research, optogenetic intervention in humans is far more challenging. In this regard, pharmacological approaches specific to the nerve fibres in the AT would be of clinical significance. Currently, available medications do not differentiate between various segments of the SNS. Such medications, therefore, affect overall SNS activity, which represents a great risk for all target organs regulated by sympathetic outputs (Grassi et al., 1995, 2004; Troisi et al., 1991). A more in-depth molecular characterization of the neuronal fibres in the AT may lead to the identification of druggable molecular targets which are specific to the neurons in AT. Such targets would allow the pharmacological modulation of AT neurons without affecting the sympathetic innervation of muscles, kidney or heart.

To identify molecular targets specific to the AT neurons we can again envisage a basic research-centric approach. This approach would take advantage of the sympathetic neuronal cell bodies (ganglia) projecting to the AT. Ganglia are bigger and easier to dissect, thus do not require tissue pooling from a very high number of animals. To this end, previous studies employing neural tracing methods in syberian hamsters have revealed that sympathetic neurons innervating the subcutaneous inguinal fat pads localize to the 13^{th} thoracic ganglia (Youngstrom and Bartness, 1995). Therefore, an important next step will be to explore whether the same ganglia project to the murine AT. Currently, available methods can map the output pathways of genetically marked neurons (Lo and Anderson, 2011). Knowing which sympathetic regions extend to the AT (and other internal organs), may expedite the discovery of the AT-specific molecular targets. If the specificity of such targets would also be conserved in the human SNS, that would represent a clinically-relevant breakthrough.

Our work also brought additional insight on the immunological regulation of the AT during obesity. Whereas it has been well established that obesity drives inflammation in the peripheral tissues (Schenk et al., 2008) and in the CNS (Thaler et al., 2012), we show that obesity also triggers local inflammatory responses in the AT sympathetic fibres. We observed that obesity-induced inflammation of the AT preferentially affected the sympathetic nerve fibres targeting the fat and was closely associated with accumulation of sympathetic-neuron associated macrophages (SAMs). In addition to the increased numbers of AT macrophages (ATMs) and SAMs in the AT of obese mice, obesity also drove the up-regulation of their pro-inflammatory profiles. These observations put forward two pressing questions: **1)** what are the factors that shape the inflammatory profiles of these cells, and **2)** would the targeting of the inflammatory pathways in SAMs and ATMs ameliorate the obesity-linked inflammation. The answer to both questions could lead to a better clinical management of AT inflammation in obese patients. Regarding the first question, one possibility to explore is that the combination of lipid overload and AT hypoxia directly alters the metabolic programmes of ATMs and SAMs. Such alteration would lead to increased levels of pro-inflammatory cytokines in these cells (Hosogai et al., 2007; Olefsky and Glass, 2010). Another possibility is that the constant stimulation of sympathetic neurons in fat (to regulate the adipose mass), directly activates the inflammatory pathways in SAMs. These cells would, in turn, communicate

with ATMs and activate their respective pro-inflammatory profile. This relay hypothesis is supported by evidence suggesting that activated sympathetic neurons release not only norepinephrine (NE), but also adenosine triphosphate (ATP) (Kennedy et al., 1996). ATP is a potent activator of the NLRP3 inflammasome complex in macrophages (Jo et al., 2016). Accordingly, our data indicate that optogenetic stimulation of noradrenergic neurons up-regulates the expression of pro-inflammatory cytokines (such as TNF-α and IL-1) in SAMs. A more in-depth molecular characterization of the inflammatory profiles of ATMs and SAMs in obesity will be an important aspect in the potential identification of clinically-relevant targets. In this regard, testing if the modulation of inflammatory pathways in ATMs or SAMs can ultimately ameliorate AT inflammation (and possibly obesity) will be an exciting next step.

Our observations also put forward the hypothesis that SAMs can directly modulate SNS activity in the AT of obese individuals. The relationship between macrophages and the neurotransmitter NE has been a topic of debate. A study from 2011 suggested that anti-inflammatory ATMs produce NE upon stimulation with low temperatures and this response was shown to facilitate thermogenesis and browning of the AT (Nguyen et al., 2011). Several years later, however, other groups reported that ATMs do not express the biosynthetic machinery for the NE production, thus contradicted the former model (Fischer et al., 2017; Reitman, 2017; Spadaro et al., 2017). Our study shed some additional light on the possible mechanisms that link macrophages in the AT to the neurotransmitter NE. Our results indicate that SAMs, which reside in direct contact with sympathetic neurons in WAT, may possess the machinery for NE uptake and catabolism via the expression of the Norepinephrine Transporter (SLC6A2) and the Monoamine Oxidase-A (MAO-A), respectively. Therefore, it is possible that the decreased SNS outflow to the AT during obesity may be mediated by SAMs activity. Supporting such hypothesis, we showed that bone marrow transfer from SLC6A2-KO mice into genetically obese *ob/ob* mice improved thermogenic capacities and fat oxidation. In addition, macrophage-mediated NE degradation was also noted to be responsible for the compromised lipolysis during ageing (Camell et al., 2017), thus confirming a model in which chronic low-grade inflammation drives the accumulation of macrophages in the AT and correlates with reduced availability of NE. However, whether the reduced sympathetic output to the AT observed during ageing and obesity is caused by the SAM-linked catabolism of NE or other alternative mechanisms remain to be elucidated.

It is possible that other, NE-independent, molecular pathways regulate SAMs activity in the context of obesity. In this regard, identifying the key genetic signatures of the AT resident macrophages across different fat depots and how they change during obesity will be an important challenge. In fact, the establishment of the transcriptional program of tissue-resident macrophages across different cellular contexts is an active area of research (Gautier and Yvan-Charvet, 2014; Gautier et al., 2012; Gosselin et al., 2014, 2017). Exploring these programs might shed additional light on how ATMs are regulated during obesity and whether specific molecular pathways are common to macrophages from different fat depots.

Another open question is whether targeting the macrophages in BAT could ameliorate some of the obesity-related pathologies. The richly innervated BAT was recently reported to be inhabited by a

specialized population of macrophages (Pirzgalska et al., 2017; Wolf et al., 2017). Our data support that these macrophages express the machinery for NE degradation. Moreover, BAT macrophages have been shown to play an essential role in the maintenance of the sympathetic innervation of the adipose organ (Wolf et al., 2017). Deletion of the nuclear transcription regulator methyl-CpG-binding protein 2 (*Mecp2*) in these cells resulted in compromised innervation of the BAT and obesity (Wolf et al., 2017). Determining which molecular programs in BAT macrophages are affected by obesity will be the likely next step in verifying new targets with clinical potential.

Our studies focus mostly on the neuro-immune regulation of the AT during obesity, yet, we still do not have a clear idea of the function of SAMs in healthy individuals. Our RNA-seq analyses point out to several biological processes that are enriched in SAMs when compared to ATMs. These include synaptic signalling, cell-cell adhesion, and neuron development, thus suggesting possible roles in local neuronal maintenance. It is possible that the function of SAMs at steady state is different from their role during obesity. An obvious paradigm here would be microglial cells. Under normal conditions, microglial cells fulfil tissue-protective tasks, whereas prolonged exposure to high-fat diets drives them to orchestrate brain inflammation (Gao et al., 2014; Graeber, 2010; Paolicelli et al., 2011). Future studies exploring the molecular programs enriched in SAMs, and their potential similarity with those of microglial cells, will be important in the clarification of the role of these cells in healthy AT.

Collectively, our observations have contributed to a better understanding of the neuro-immune axis in the AT, particularly on its regulation in the context of obesity. Our work has opened the door to exciting new questions on AT biology. Answering such questions will, most likely, require a multidisciplinary approach. A firm understanding of the fundamental aspects of organismal homeostasis is a cornerstone of evidence-based medicine. It is my expectation that expanding on the observations reported in this thesis from a mainly basic research perspective, may one day lead to the improved clinical management of obese patients.

4.1 REFERENCES

Bachman, E.S., Dhillon, H., Zhang, C.-Y., Cinti, S., Bianco, A.C., Kobilka, B.K., and Lowell, B.B. (2002). betaAR signaling required for diet-induced thermogenesis and obesity resistance. Science 297, 843–845.

Camell, C.D., Sander, J., Spadaro, O., Lee, A., Nguyen, K.Y., Wing, A., Goldberg, E.L., Youm, Y.-H., Brown, C.W., Elsworth, J., et al. (2017). Inflammasome-driven catecholamine catabolism in macrophages blunts lipolysis during ageing. Nature 550, 119–123.

Dempersmier, J., Sambeat, A., Gulyaeva, O., Paul, S.M., Hudak, C.S.S., Raposo, H.F., Kwan, H.-Y., Kang, C., Wong, R.H.F., and Sul, H.S. (2015). Cold-inducible Zfp516 activates UCP1 transcription to promote browning of white fat and development of brown fat. Mol. Cell 57, 235–246.

Dodd, G.T., Decherf, S., Loh, K., Simonds, S.E., Wiede, F., Balland, E., Merry, T.L., Münzberg, H., Zhang, Z.-Y., Kahn, B.B., et al. (2015). Leptin and insulin act on POMC neurons to promote the browning of white fat. Cell 160, 88–104.

Fenselau, H., Campbell, J.N., Verstegen, A.M.J., Madara, J.C., Xu, J., Shah, B.P., Resch, J.M., Yang, Z., Mandelblat-Cerf, Y., Livneh, Y., et al. (2017). A rapidly acting glutamatergic ARC-PVH satiety circuit postsynaptically regulated by a-MSH. Nat. Neurosci. 20, 42.

Fischer, K., Ruiz, H.H., Jhun, K., Finan, B., Oberlin, D.J., van der Heide, V., Kalinovich, A.V., Petrovic, N., Wolf, Y., Clemmensen, C., et al. (2017). Alternatively activated macrophages do not synthesize catecholamines or contribute to adipose tissue adaptive thermogenesis. Nat. Med. 23, 623–630.

Gao, Y., Ottaway, N., Schriever, S.C., Legutko, B., García-Cáceres, C., de la Fuente, E., Mergen, C., Bour, S., Thaler, J.P., Seeley, R.J., et al. (2014). Hormones and diet, but not body weight, control hypothalamic microglial activity. Glia 62, 17–25.

Gautier, E.L., and Yvan-Charvet, L. (2014). Understanding macrophage diversity at the ontogenic and transcriptomic levels. Immunol. Rev. 262, 85–95.

Gautier, E.L., Shay, T., Miller, J., Greter, M., Jakubzick, C., Ivanov, S., Helft, J., Chow, A., Elpek, K.G., Gordonov, S., et al. (2012). Gene expression profiles and transcriptional regulatory pathways underlying mouse tissue macrophage identity and diversity. Nat. Immunol. 13, 1118–1128.

Gautron, L., Elmquist, J.K., and Williams, K.W. (2015). Neural Control of Energy Balance: Translating Circuits to Therapies. Cell 161, 133–145.

Giralt, M., and Villarroya, F. (2013). White, brown, beige/brite: different adipose cells for different functions? Endocrinology 154, 2992–3000.

Gosselin, D., Link, V., Romanoski, C.E., Fonseca, G.J., Eichenfield, D.Z., Spann, N.J., Stender, J.D., Chun, H.B., Garner, H., Geissmann, F., et al. (2014). Environment drives selection and function of enhancers controlling tissue-specific macrophage identities. Cell 159, 1327–1340.

Gosselin, D., Skola, D., Coufal, N.G., Holtman, I.R., Schlachetzki, J.C.M., Sajti, E., Jaeger, B.N., O'Connor, C., Fitzpatrick, C., Pasillas, M.P., et al. (2017). An environment-dependent transcriptional network specifies human microglia identity. Science 356.

Graeber, M.B. (2010). Changing face of microglia. Science 330, 783–788.

Grassi, G., Seravalle, G., Cattaneo, B.M., Bolla, G.B., Lanfranchi, A., Colombo, M., Giannattasio, C., Brunani, A., Cavagnini, F., and Mancia, G. (1995). Sympathetic activation in obese normotensive subjects. Hypertens. Dallas Tex 1979 25, 560–563.

Grassi, G., Dell'Oro, R., Facchini, A., Quarti Trevano, F., Bolla, G.B., and Mancia, G. (2004). Effect of central and peripheral body fat distribution on sympathetic and baroreflex function in obese normotensives. J. Hypertens. 22, 2363–2369.

Hosogai, N., Fukuhara, A., Oshima, K., Miyata, Y., Tanaka, S., Segawa, K., Furukawa, S., Tochino, Y., Komuro, R., Matsuda, M., et al. (2007). Adipose tissue hypoxia in obesity and its impact on adipocytokine dysregulation. Diabetes 56, 901–911.

Jo, E.-K., Kim, J.K., Shin, D.-M., and Sasakawa, C. (2016). Molecular mechanisms regulating NLRP3 inflammasome activation. Cell. Mol. Immunol. 13, 148–159.

Kennedy, C., McLaren, G.J., Westfall, T.D., and Sneddon, P. (1996). ATP as a co-transmitter with noradrenaline in sympathetic nerves-function and fate. Ciba Found. Symp. 198, 223-235; discussion 235-238.

Landsberg, L., Saville, M.E., and Young, J.B. (1984). Sympathoadrenal system and regulation of thermogenesis. Am. J. Physiol. 247, E181-189.

Lo, L., and Anderson, D.J. (2011). A Cre-Dependent, Anterograde Transsynaptic Viral Tracer for Mapping Output Pathways of Genetically Marked Neurons. Neuron 72, 938–950.

Nguyen, K.D., Qiu, Y., Cui, X., Goh, Y.P.S., Mwangi, J., David, T., Mukundan, L., Brombacher, F., Locksley, R.M., and Chawla, A. (2011). Alternatively activated macrophages produce catecholamines to sustain adaptive thermogenesis. Nature 480, 104–108.

Olefsky, J.M., and Glass, C.K. (2010). Macrophages, inflammation, and insulin resistance. Annu. Rev. Physiol. 72, 219–246.

Paolicelli, R.C., Bolasco, G., Pagani, F., Maggi, L., Scianni, M., Panzanelli, P., Giustetto, M., Ferreira, T.A.,

Guiducci, E., Dumas, L., et al. (2011). Synaptic pruning by microglia is necessary for normal brain development. Science 333, 1456–1458.

Pirzgalska, R.M., Seixas, E., Seidman, J.S., Link, V.M., Sánchez, N.M., Mahú, I., Mendes, R., Gres, V., Kubasova, N., Morris, I., et al. (2017). Sympathetic neuron-associated macrophages contribute to obesity by importing and metabolizing norepinephrine. Nat. Med. 23, 1309–1318.

Reitman, M.L. (2017). How Does Fat Transition from White to Beige? Cell Metab. 26, 14–16.

Schenk, S., Saberi, M., and Olefsky, J.M. (2008). Insulin sensitivity: modulation by nutrients and inflammation. J. Clin. Invest. 118, 2992–3002.

Spadaro, O., Camell, C.D., Bosurgi, L., Nguyen, K.Y., Youm, Y.-H., Rothlin, C.V., and Dixit, V.D. (2017). IGF1 Shapes Macrophage Activation in Response to Immunometabolic Challenge. Cell Rep. 19, 225–234.

Thaler, J.P., Yi, C.-X., Schur, E.A., Guyenet, S.J., Hwang, B.H., Dietrich, M.O., Zhao, X., Sarruf, D.A., Izgur, V., Maravilla, K.R., et al. (2012). Obesity is associated with hypothalamic injury in rodents and humans. J. Clin. Invest. 122, 153–162.

Troisi, R.J., Weiss, S.T., Parker, D.R., Sparrow, D., Young, J.B., and Landsberg, L. (1991). Relation of obesity and diet to sympathetic nervous system activity. Hypertension 17, 669–677.

Wolf, Y., Boura-Halfon, S., Cortese, N., Haimon, Z., Sar Shalom, H., Kuperman, Y., Kalchenko, V., Brandis, A., David, E., Segal-Hayoun, Y., et al. (2017). Brown-adipose-tissue macrophages control tissue innervation and homeostatic energy expenditure. Nat. Immunol. 18, 665–674.

Youngstrom, T.G., and Bartness, T.J. (1995). Catecholaminergic innervation of white adipose tissue in Siberian hamsters. Am. J. Physiol. 268, R744-751.

Zeng, W., Pirzgalska, R.M., Pereira, M.M.A., Kubasova, N., Barateiro, A., Seixas, E., Lu, Y.-H., Kozlova, A., Voss, H., Martins, G.G., et al. (2015). Sympathetic Neuro-adipose Connections Mediate Leptin-Driven Lipolysis. Cell 163, 84–94.

5 | APPENDIX

Original versions of the peer-reviewed articles

Article

Cell

Sympathetic Neuro-adipose Connections Mediate Leptin-Driven Lipolysis

Graphical Abstract

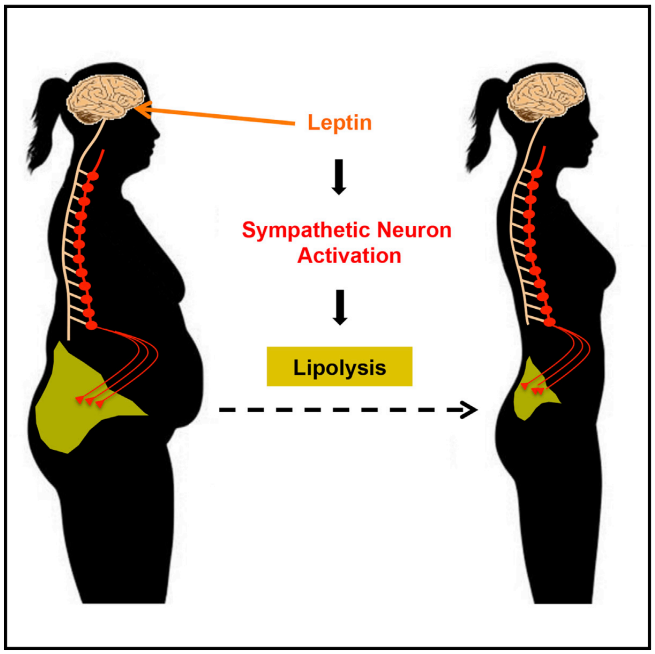

Authors

Wenwen Zeng, Roksana M. Pirzgalska, Mafalda M.A. Pereira, ..., Gabriel G. Martins, Jeffrey M. Friedman, Ana I. Domingos

Correspondence

dominan@igc.gulbenkian.pt

In Brief

The lipolytic effect of leptin is mediated by sympathetic neurons that innervate adipocytes, forming neuro-adipose junctions that directly mediate fat breakdown. Anti-obesity strategies targeting the sympathetic neurons in fat have the potential to circumvent central leptin resistance.

Highlights

- The neuro-adipose junction in white adipose tissue is visualized in vivo
- Adipocyte-projecting neurons can completely envelop an adipocyte
- Leptin stimulates lipolysis via sympathetic neurons in fat
- Optogenetic activation of sympathetic fibers in fat drives lipolysis and fat mass reduction

Zeng et al., 2015, Cell *163*, 84–94
September 24, 2015 ©2015 Elsevier Inc.
http://dx.doi.org/10.1016/j.cell.2015.08.055

Cell

Article

Sympathetic Neuro-adipose Connections Mediate Leptin-Driven Lipolysis

Wenwen Zeng,[2,3,7] Roksana M. Pirzgalska,[1,7] Mafalda M.A. Pereira,[1] Nadiya Kubasova,[1] Andreia Barateiro,[1,6] Elsa Seixas,[1] Yi-Hsueh Lu,[2] Albina Kozlova,[2] Henning Voss,[5] Gabriel G. Martins,[4] Jeffrey M. Friedman,[2,3,8] and Ana I. Domingos[1,8,*]

[1]Obesity Laboratory, Instituto Gulbenkian de Ciência, Oeiras 2780-156, Portugal
[2]Laboratory of Molecular Genetics, The Rockefeller University, New York, NY 10021, USA
[3]Howard Hughes Medical Institute, The Rockefeller University, New York, NY 10021, USA
[4]Advanced Microscopy Unit, Instituto Gulbenkian de Ciência, Oeiras 2780-156, Portugal
[5]Department of Radiology, Weill Cornell Medical College, New York, NY 10021, USA
[6]Research Institute for Medicines (iMed.ULisboa), Faculty of Pharmacy, Universidade de Lisboa, Avenue Professor Gama Pinto, Lisbon 1649-003, Portugal
[7]Co-first author
[8]Co-senior author
*Correspondence: dominan@igc.gulbenkian.pt
http://dx.doi.org/10.1016/j.cell.2015.08.055

SUMMARY

Leptin is a hormone produced by the adipose tissue that acts in the brain, stimulating white fat breakdown. We find that the lipolytic effect of leptin is mediated through the action of sympathetic nerve fibers that innervate the adipose tissue. Using intravital two-photon microscopy, we observe that sympathetic nerve fibers establish neuro-adipose junctions, directly "enveloping" adipocytes. Local optogenetic stimulation of sympathetic inputs induces a local lipolytic response and depletion of white adipose mass. Conversely, genetic ablation of sympathetic inputs onto fat pads blocks leptin-stimulated phosphorylation of hormone-sensitive lipase and consequent lipolysis, as do knockouts of dopamine β-hydroxylase, an enzyme required for catecholamine synthesis. Thus, neuro-adipose junctions are necessary and sufficient for the induction of lipolysis in white adipose tissue and are an efferent effector of leptin action. Direct activation of sympathetic inputs to adipose tissues may represent an alternative approach to induce fat loss, circumventing central leptin resistance.

INTRODUCTION

White adipose tissues (WATs) serve as a storage depot for energy-rich triglycerides. In times of privation, this lipid storage can be released as part of an adaptive response to the energy shortage. Lipolysis, the process of hydrolyzing stored triglycerides in adipocytes, is regulated by several G-protein-coupled receptors, including adrenergic receptors, all of which activate protein kinase A (PKA) and elevate the intracellular levels of cyclic adenosine monophosphate (cAMP) (Brasaemle, 2007). PKA also phosphorylates several key target proteins, including lipid-droplet-associated protein perilipin, hormone-sensitive lipase (HSL), and a set of esterases that collectively promote the hydrolysis of triglycerides into free fatty acids (FFAs) and glycerol, which are then released into plasma to meet the energy demands of other tissues (Brasaemle, 2007). HSL is a canonical target of PKA in adipocytes, and this enzyme catalyzes the conversion of diacylglycerol to monoacyl glycerol (Brasaemle, 2007).

Adipose tissue mass is homeostatically controlled by an endocrine loop in which leptin acts on neural circuits in the hypothalamus and elsewhere in brain to regulate food intake and peripheral metabolism (Friedman and Halaas, 1998). In wild-type (WT) and leptin-deficient *ob* animals, leptin treatment reduces food intake and leads to a rapid depletion of fat mass (Halaas et al., 1995, 1997; Montez et al., 2005). Of note, the depletion of fat mass after leptin treatment is distinct from that observed after food restriction in a number of respects: leptin treatment spares lean body mass and also potently stimulates glucose metabolism, while starvation results in a loss of lean body mass and causes insulin resistance (Newman and Brodows, 1983; Koffler and Kisch, 1996; Awad et al., 2009; Elia et al., 1999). In addition, leptin-deficient *ob/ob* mice pair-fed to leptin-treated *ob* mice lose only half the weight of those treated with leptin, further implicating a mechanism beyond a reduced food intake (Rafael and Herling, 2000). Because leptin has been shown to increase the sympathetic efferent signal to brown adipose tissues (BAT) (Scarpace and Matheny, 1998; Rezai-Zadeh and Münzberg, 2013), it has been suggested that leptin also activates sympathetic efferents to WAT to increase lipolysis in WAT. However, this has not been directly shown, and the nature of the effector mechanism underlying leptin-stimulated lipolysis in WAT has not been defined. In particular, it has not been established whether the increased lipolysis in WAT in response to leptin is due to a circulating hormone (or hormones) such as norepinephrine (NE) and/or another mediator that is released either centrally or peripherally (adrenal gland or macrophages), or specific efferent neural inputs to WAT, which mediates central leptin action. However, the effect of leptin on energy balance does not

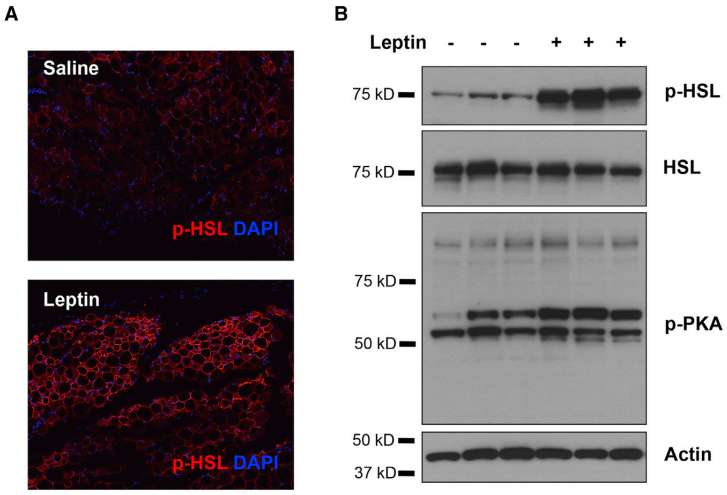

Figure 1. Leptin Stimulates HSL Phosphorylation in WAT

(A) Immunostaining of p-HSL (red) in paraffin sections of epididymal fat of C57Bl6/J mice that were peripherally administrated with 500 ng/hr recombinant leptin for 2 days.

(B) p-HSL and phosphorylated PKA substrates in total protein extracts of epididymal fats were examined by immunoblot analysis.

require the presence of intact adrenals, suggesting that this organ is unlikely to be the source of the lipolytic signal (Arvaniti et al., 1998).

While numerous previous studies have shown dense neural innervation of BAT, both functionally and anatomically, the innervation of WAT has been difficult to visualize. Thus, it has been suggested that neural inputs to WAT are either very sparse or difficult to be distinguished from en passant axons with terminals on other cell types, such as those in vasculature (Bartness et al., 2005; Bartness and Song, 2007; Youngstrom and Bartness, 1995; Giordano et al., 1996). Indeed, some reports have suggested that the only innervation of WAT is perivascular and that white adipocytes themselves are not directly innervated (Giordano et al., 2005). This controversy has heightened the uncertainty as to the relative roles of sympathetic neural activity to regulate WAT metabolism. Alternatively, macrophages in adipose tissue account for about 10% of the stromal vascular fraction (SVF); hence, local catecholamines produced by these cells could also contribute to lipolysis in WAT in vivo (Weisberg et al., 2003; Nguyen et al., 2011). Thus, the dramatic decrease of adipose tissue mass observed after leptin treatment could, in principle, be mediated by catecholamines or other mediators that are either locally produced or produced by neurons.

In this study, we use anatomic, optogenetic, biochemical, and genetic approaches to show that the catecholamines released at heretofore-unidentified neuro-adipose junctions mediates the lipolytic effect of leptin, thus establishing the effector mechanism underlying the depletion of fat mass by leptin and, potentially, other stimuli. Our data demonstrate that the local sympathetic activity in WAT is necessary and sufficient for the lipolytic effect of leptin. In addition, genetic evidence shows that the β-adrenergic, but not α-adrenergic, receptors partially constitute a signaling pathway that accounts for the lipolytic effect of leptin. Moreover, the effect of pre-synaptic manipulations, such as neural gain of function or loss of function, is more profound than that of post-synaptic manipulations, thus suggesting direct activation of sympathetic inputs to adipose tissues as a strategy for the induction of fat loss.

RESULTS

Phosphorylation of HSL in WAT as a Lipolysis Marker for Leptin Action

To directly assess the cellular effect of leptin on lipolysis in white adipocytes and provide a marker for leptin action, we searched for biochemical responses in white adipocytes that were specifically activated by leptin treatment. We used a battery of phospho-specific antibodies and found that the phosphorylation of HSL was robustly increased in adipose tissue in response to leptin treatment. Note that our ability to define a biochemical effect of leptin is dependent on the quality of the antibodies, and we found that the anti-pHSL antibody was extremely robust. As shown, peripheral administration of leptin led to a significant increase of phosphorylated HSL (p-HSL) in WAT that could be visualized by immunohistochemistry (Figure 1A) and quantified by immunoblot analysis (Figure 1B). We set out to investigate whether the effect of leptin to increase HSL phosphorylation was mediated by neural efferent outputs onto WAT.

Axonal Bundles Project to WAT and Form Sympathetic Neuro-adipose Junctions

We first used tomography methods to determine whether fat pads were innervated. By coupling optical projection tomography (OPT) to a fat-clearing method that renders whole organs transparent, we were able to macroscopically visualize and document the nerve bundles that innervate the inguinal fat pad (Figure 2A; Experimental Procedures; Supplemental Experimental Procedures for details) (Gualda et al., 2013; Quintana and Sharpe, 2011). A full series of projections of the whole organ are acquired from multiple angles, typically 800–1,600 angles, and from this series of projections, a stack of axial slices can be visualized through back-projection reconstruction (Figure 2B).

From an OPT series of coronal optical sections of inguinal fat organ, we performed a 3D reconstruction, which enabled the visualization of thick axon bundles targeting the fat pad (Figures 2C and 2D). Axon bundles can be identified based on the gray threshold level and morphological features that distinguish them from the vasculature (Figure 2E). These structures within the fat were then segmented using semi-automated software (see Experimental Procedures).

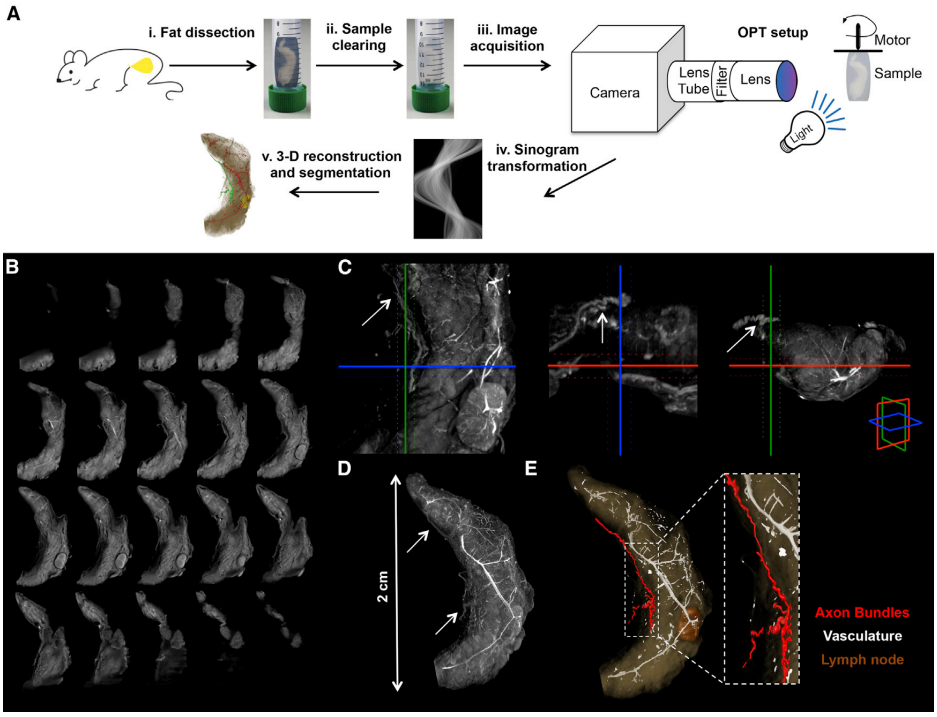

Figure 2. Neural Projections in Fat Detected with OPT

(A) Schematic representation of the OPT method applied to the subcutaneous inguinal fat. (i) Tissue dissection. (ii) Sample clearing. (iii) Image acquisition. (iv) Sinogram transformation. (v) 3D reconstruction and segmentation.

(B) OPT series of coronal sections of inguinal fat organ after 3D reconstruction.

(C) Orthogonal 400-μm OPT slabs of inguinal fat in coronal, axial, and sagittal views. Axon bundles were identified based on the gray threshold level (arrows).

(D) 3D reconstruction in maximal intensity projection of the OPT coronal sections.

(E) Surface view of segmented structures within inguinal fat.

The neural bundles were micro-dissected from the subcutaneous fat pads and subjected to immunostaining for tyrosine hydroxylase (TH), a marker of sympathetic neurons, and β3-tubulin (Tub-3), a general marker for the peripheral nervous system (PNS) (Figure 3A). We found that, overall, ~50% of the Tub-3-positive neurons also expressed TH, thus establishing the presence of both catecholaminergic and non-catecholaminergic axons innervating subcutaneous fat pads (Figure 3A). Then, we used multiphoton microscopy on the intact inguinal WAT of a living mouse to visualize sympathetic neuro-adipose connections (Figures 3B and 3C; Experimental Procedures). We labeled adipocytes with LipidTOX, a lipophylic dye, and sympathetic axons by crossing TH Cre-recombinase mice (*TH-Cre*) with a Tdtomato-reporter line (*Rosa26-LSL-Tdtomato*) (Figure 3C). We observed that Tdtomato-positive axons in fat pads made dense contacts with adipocytes through bouton-like structures that had the anatomic appearance of neuro-adipocyte junctions, resembling synapses (Figure 3C). We quantified these from eight independent two-photon micrographs and determined that 8% ± 4.6% of adipocytes are in direct contact with sympathetic nerves.

Optogenetic Stimulation of Sympathetic Inputs to WAT Leads to Catecholamine Release, HSL Phosphorylation, and Fat Mass Depletion

We assessed the function of the catecholaminergic fibers by crossing the *TH-Cre* mice to a channelrhodopsin (ChR2) reporter line, *Rosa26-LSL-ChR2-YFP*. ChR2-YFP (yellow fluorescent protein) showed a complete co-localization with the endogenous TH, as determined by immunostaining of YFP and TH (Figure 4A). ChR2-YFP-expressing axons that projected onto subcutaneous WAT were then optogenetically activated using a subcutaneously implanted optical fiber targeting the right inguinal fat depot (see Experimental Procedures for surgical details).

While optogenetic tools have been widely used in the CNS, it has not been used as frequently to probe the function of peripheral cells, including sympathetic neurons. We began by validating the use of optogenetic stimulation of sympathetic neurons in primary cultures of superior cervical ganglia (SCG) of *TH-Cre* X *Rosa26-LSL-ChR2-YFP* mice; SCG can be dissected with less difficulty compared to other sympathetic ganglia (see Supplemental Experimental Procedures for culture details). We found

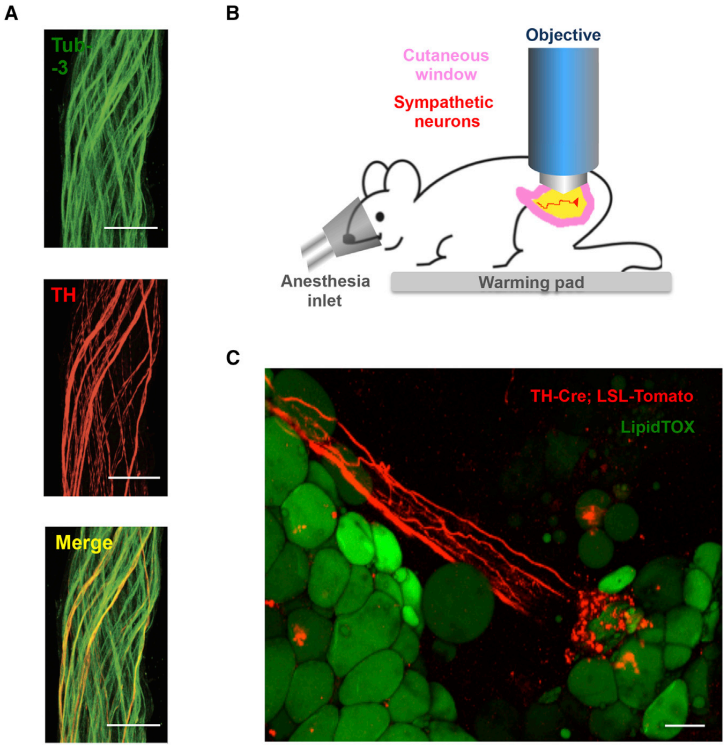

Figure 3. Catecholaminergic Neurons Innervating Adipocytes Integrate Nerve Bundles of Mixed Molecular Identity

(A) Partial co-localization of TH (red), an SNS marker, and Tub-3 (green), a general PNS marker, shown by immunohistochemistry of nerve bundles dissected from the inguinal fat pads of WT mice. Scale bars, 50 μm.

(B) Schematic representation of the two-photon intra-vital imaging of neurons in the inguinal fat pad.

(C) Intra-vital two-photon microscopy visualization of a neuro-adipose connection in the inguinal fat pad of a live *TH-Cre; LSLS-Tomato* mouse; LipidTOX (green) labels adipocytes. Scale bar, 100 μm.

that optogenetic stimulation of cultured sympathetic neurons increased expression of c-Fos, a marker for neuronal activity, in TH-positive cells and significantly stimulated NE release ex vivo, as assayed with ELISA (Figures 4B and 4C). NE release of ChR2-positive neurons was significantly higher relative to that of ChR2-negative cells (749.6 ± 170.1 pg/ml versus 4.8 ± 1.7 pg/ml, $p < 0.05$) (Figures 4B and 4C; see Experimental Procedures for culture and stimulation details).

Next, we stimulated ChR2-YFP-expressing axons in vivo unilaterally by placing optical fibers subcutaneously, aiming at inguinal fat pads located in the supra-pelvic flank of *TH-Cre* X *Rosa26-LSL-ChR2-YFP* mice (see Experimental Procedures for stimulation details). Activation of the ChR2-positive axons in subcutaneous WAT led to a significant increase of NE in the stimulated fat pad, relative to the contralateral un-stimulated control side (2.7 ± 0.5 versus 1.1 ± 0.2, $p < 0.05$; Figure 4D). We also observed a significant increase of HSL phosphorylation of fat on the side ipsilateral to the optical fiber, compared to the contralateral un-stimulated side (Figure 4E). These data show that local activation of catecholaminergic inputs to fat could locally mimic the biochemical effect of leptin (Figures 4D and 4E). Then, we tested whether a more prolonged (4-week) optogenetic stimulation of ChR2-positive neurons in WAT could deplete fat mass (Figure 4F). The optical stimulation protocol was set to deliver light for every other second at 20 Hz, and the volume of subcutaneous WAT was determined using MRI with 3D reconstruction (Figures 4F and 4G; see Experimental Procedures for details). After chronic activation, the size of the optogenetically stimulated ipsilateral fat pads of *TH-Cre*; *Rosa26-LSL-ChR2-YFP* mice was 23% ± 3.4% that of the contralateral control side, representing a statistically and biologically significant decrease in fat mass (Figures 4F and 4G, $p < 0.0001$). This effect depended on ChR2 expression, as the fat pad volume of stimulated fat pads in ChR2-negative mice was unchanged (86% ± 4.3% of the size of the contralateral control fat pad), ruling out a potential nonspecific effect of laser stimulation (Figure 4G; see Experimental Procedures for details). Together, the results provide anatomical and functional evidence that there are synapse-like sympathetic inputs onto white adipocytes and that their activation is sufficient to promote local NE release, HSL phosphorylation, and a reduction in the mass of an adipose tissue depot.

Local Sympathetic Inputs Are Required for Leptin-Stimulated HSL Lipolysis in WAT

Similarly to optogenetic stimulation of sympathetic innervation in white fat, leptin treatment led to an increase in NE levels in the subcutaneous adipose organ. NE levels in WATs dissected from leptin-treated animals were significantly higher than those in controls (78.7 ± 16.8 pg NE/μg of protein versus 30.7 ± 4.1 pg NE/μg of protein, $p < 0.05$; Figure 5A). Interestingly, leptin treatment did not affect serum NE levels (Figure 5B), indicating that leptin locally increases NE release in white fat, but not systemically.

Next, we evaluated whether sympathetic activation is necessary for leptin-stimulated lipolysis by disrupting the neural inputs in WAT, using a pharmacologic blockade or local genetic ablation. First, we observed that administration of hexamethonium, a non-depolarizing anti-cholinergic ganglion blocker, significantly decreased the leptin-stimulated phosphorylation of HSL

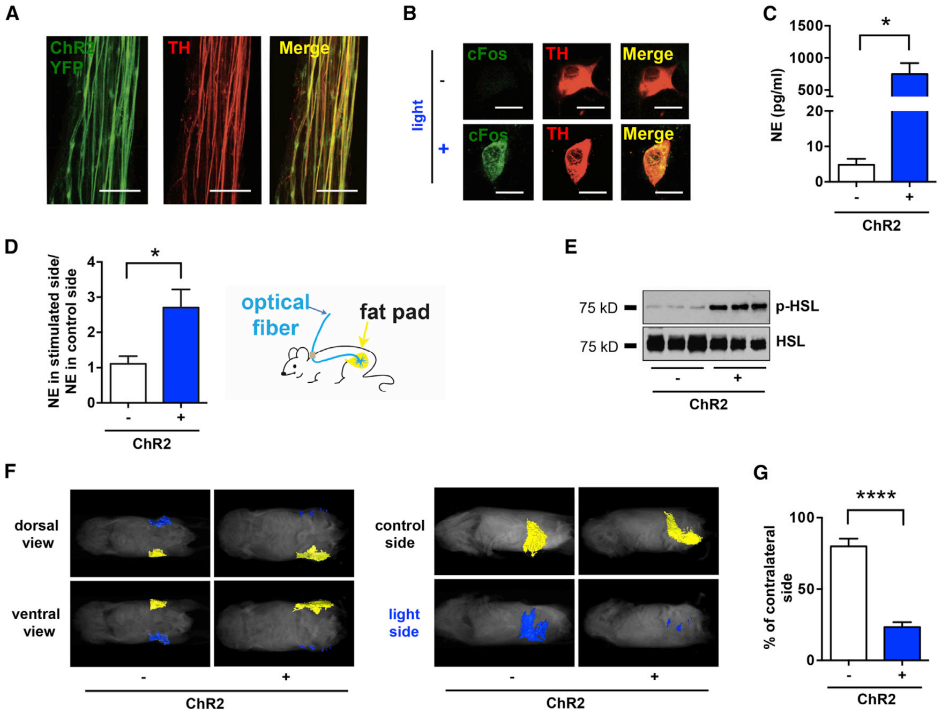

Figure 4. Optogenetic Stimulation of SNS Neurons in Fat Is Sufficient to Drive Lipolysis

(A) Complete co-localization of YFP (green) and TH (red) shown by immunohistochemistry of nerve bundles dissected from the inguinal fat pads of *TH-Cre; LSLS-ChR2-YFP*. Scale bars, 50 μm.

(B) c-Fos (green) induction in cultured SNS neurons after optogenetic activation. Scale bars, 10 μm.

(C) Ex vivo NE release upon optogenetic stimulation of sympathetic SCG explants isolated from *TH-Cre; LSL-ChR2-YFP* mice and *LSL-ChR2-YFP* control mice (*$p < 0.05$; n = 3–6). Results are shown as mean ± SEM.

(D) In vivo NE release in subcutaneous fat upon optogenetic stimulation of sympathetic neurons in WATs of *TH-Cre; LSL-ChR2-YFP* and *LSL-ChR2-YFP* control mice that were subcutaneously implanted with optical fibers targeting the inguinal fat pad (*$p < 0.05$; n = 8). Results are shown as mean ± SEM.

(E) Immunoblot analysis of p-HSL in total protein extracts of subcutaneous fats of *TH-Cre; LSL-ChR2-YFP* and *LSL-ChR2-YFP* control mice that were subcutaneously implanted with optical fibers targeting the inguinal fat pad and optogenetically stimulated for 2 weeks (details are given in Experimental Procedures).

(F) MRI-guided visualization of fat in *TH-Cre; LSL-ChR2-YFP* and *LSL-ChR2-YFP* control mice that were optogenetically stimulated for 4 weeks (yellow indicates control inguinal fat pat, blue indicates light-stimulated fat pad; details are given in Experimental Procedures).

(G) Quantification of fat reduction in stimulated side versus the contralateral control side (****$p < 0.0001$; n = 6). Results are shown as mean ± SEM.

See also Movies S1 and S2.

in adipose tissue (Figure 5C). However, as the action of hexamethonium is systemic and is not cell type specific, affecting all ganglionic transmission, we took a complementary approach by introducing a local neural crush injury to the fibers innervating epididymal fat pads. Because of the anatomy of the fat pad, nerve fibers in the distal portion of the tissues can be efficiently eliminated by a surgical crush of the perivascular axons running parallel to the main vessels (see Experimental Procedures). We carried out physical denervation with a forcep crushing the fibers 2 mm from the distal tip for 30 s. Leptin was delivered 3 days post-surgery through osmotic pump for 2 days. Consistent with the effect of hexamethonium, after a crush injury to the local nerve, leptin treatment failed to increase HSL phosphorylation on the denervated side compared to the intact contralateral control (Figure 5D). This showed that local neural activation to WAT is required for the biochemical changes associated with leptin treatment.

To confirm that leptin-mediated lipolysis is the result of activation of sympathetic neural outputs to fat, we ablated these neurons by crossing the *TH-Cre* line with the diphtheria toxin receptor (DTR) mice, *Rosa26-LSL-DTR*, and injected diphtheria toxin (DT) locally in subcutaneous inguinal WAT (Buch et al., 2005). Local treatment with DT eliminated only those sympathetic axons in the regions of the injection site, without effects on other local neuronal populations as shown by the sparing TH-negative Tub-3-positive axons at the site of injection (Figure 5E, $p < 0.001$; see Supplemental Experimental Procedures for details). These injections were administered peripherally at

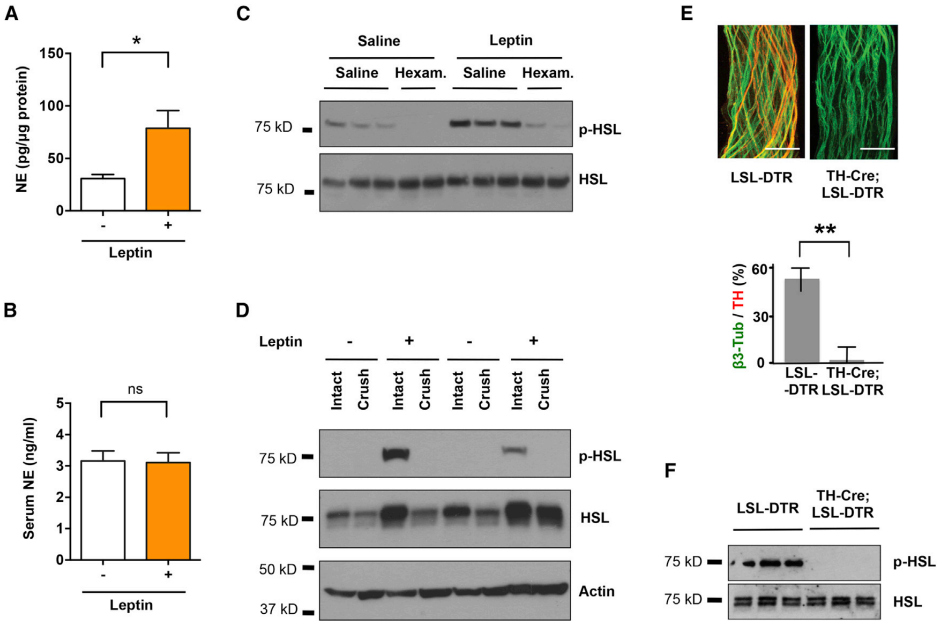

Figure 5. Sympathetic Neurons Are Locally Required for Leptin-Induced Lipolysis

(A and B) C57BL6/J mice were peripherally administrated with 500 ng/hr recombinant leptin or saline for 2 days. (A) NE content in subcutaneous fat pads (*$p < 0.05$; n = 5) and (B) NE serum levels were measured by NE ELISA (n = 4). Results are shown as mean ± SEM. ns, not significant.

(C and D) C57BL6/J mice were peripherally administrated with 500 ng/hr recombinant leptin (C) in combination with 500 µg/hr ganglionic blocker hexamethonium (Hexam.) or (D) at 3 days after local crush injury of nerves in fat pads. p-HSL in total protein extracts of epididymal fats were examined by immunoblot analysis.

(E) Fat pads in *TH-Cre; LSL-DTR* mice were locally treated with DT. Tissue-specific ablation of SNS axons confirmed by immunostaining for Tub-3 and TH (**$p < 0.001$; n = 6). Results are shown as mean ± SEM.

(F) Immunoblot analysis of p-HSL in total protein extracts of subcutaneous fats of *TH-Cre; LSL-DTR* and control mice injected with DT following leptin treatment (500 ng/hr).

See also Figure S1.

low doses (10 ng/g) to ensure that the effect was local and to also spare TH-positive neurons in CNS (Figure S1; Domingos et al., 2013). Genetic ablation of sympathetic input to adipose tissue completely blocked the effect of leptin on HSL phosphorylation on the ipsilateral compared to the contralateral untreated side (Figure 5F). Together, these results demonstrate that activation of sympathetic neurons in fat is necessary for leptin to stimulate HSL phosporylation in adipose tissue.

β-Adrenergic Signaling Influences Leptin-Stimulated Lipolysis in WAT

Consistent with a sympathetic mechanism for the leptin-mediated stimulation of lipolysis, systemic administration of the β-adrenergic agonist isoproterenol resulted in the rapid induction of p-HSL. As previously reported, isoproterenol also increased FFA release from WAT in vitro and in vivo (Figure S2). Therefore, we set out to test whether β-adrenergic signaling was required for leptin-stimulated lipolysis.

We first examined the lipolytic response to leptin in mice with a knockout (KO) of dopamine β-hydroxylase (*DBH*), a key enzyme in the synthesis of NE and epinephrine from dopamine (Figure 6). After peripheral administration of leptin, there was a dramatic increase of HSL phosphorylation in WAT in the WT or $DBH^{+/+}$ animals but a markedly diminished response in the $DBH^{-/-}$ littermates (Figure 6A). Consistent with this, the total fat composition dramatically decreased in the WT mice treated with leptin, while there was only a slight change of fat mass in mice with the *DBH* deletion ($p < 0.05$; Figure 6B). Also consistent with a diminished lipolytic effect of leptin, there was also a lower amount of weight loss in the $DBH^{-/-}$ mice (Figure 6C). After 2 days of leptin treatment, the body weight of WT mice decreased more than 6%, while the weight loss of $DBH^{-/-}$ was less than 2% ($p < 0.05$). The data suggest that catecholamines contribute to more than 50% of leptin's effect on body weight. Altogether, the results confirm that catecholamines are required for the leptin-stimulated lipolysis and HSL phosphorylation in WAT.

To test whether the action of leptin to drive lipolysis is mediated through β-adrenergic signaling, we crossed the β1/β2 double-KO to β3 KO to generate animals with a deletion of all three β-adrenergic receptors (Figure 7). Animals with a deletion of all three isoforms of the β-adrenergic receptors showed

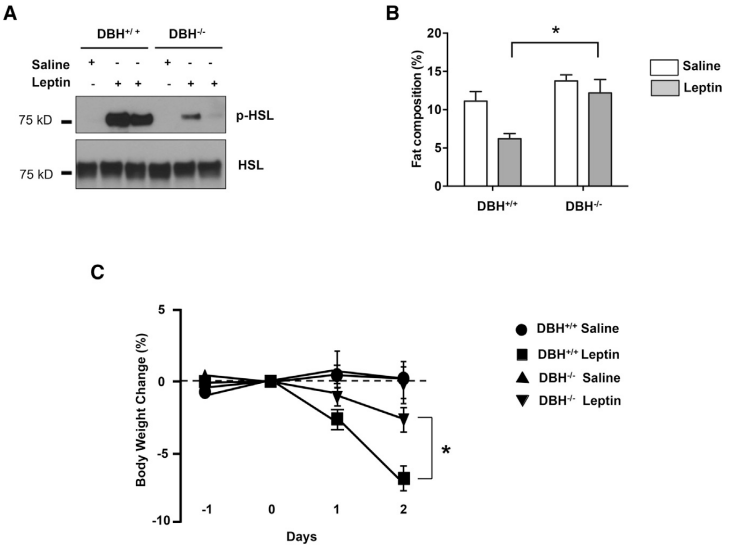

Figure 6. Norepinephrine Deficiency Impairs Leptin-Induced Lipolysis

(A) Immunoblot analysis of p-HSL in total protein extracts of fat pads of dopamine β-monoxygenase mutant and control littermates ($DBH^{-/-}$ and $DBH^{+/+}$, respectively) mice that were treated with 500 ng/hr recombinant leptin.

(B) Whole-body fat composition (*p < 0.05). Results are shown as mean ± SEM (n = 4–5).

(C) Body weight change after leptin treatment (*p < 0.05). Results are shown as mean ± SEM (n = 5).

significantly decreased HSL phosphorylation after leptin treatment in comparison to the double-KO controls (Figure 7A). However, this decrease was not as marked as that seen in individual depots after local ablation of sympathetic fibers using DT (Figure 5F). While leptin treatment significantly decreased total fat mass in $\beta1^{-/-}\beta2^{-/-}$ mice, this effect was significantly reduced in $\beta1^{-/-}\beta2^{-/-}\beta3^{-/-}$ triple-KO mice (Figure 7B; paired ANOVA post hoc test, $p < 0.01$, comparing $\beta1^{-/-}\beta2^{-/-}\beta3^{-/-}$ with $\beta1^{-/-}\beta2^{-/-}\beta3^{+/+}$ mice after leptin treatment). In contrast, α-adrenergic receptors appeared to play only a minor role in the leptin-stimulated loss of fat mass, because the α-adrenergic blockers phentolamine (5 mg/kg, intraperitoneally [i.p.]) and phenoxybenzamine (10 mg/kg i.p.) failed to diminish the catabolic responses to leptin treatment in $\beta1^{-/-}\beta2^{-/-}\beta3^{+/+}$ control mice or $\beta1^{-/-}\beta2^{-/-}\beta3^{-/-}$ mice (Figure 7C). There was also a small suppression of body weight loss in response to leptin in the $\beta1^{-/-}\beta2^{-/-}\beta3^{-/-}$ mice (Figure 7D). These results showed that the β-adrenergic receptors are only partially necessary for leptin-mediated lipolysis of WAT but that the magnitude of the effect of a loss of β-adrenergic signaling is not as great as that observed by interfering with local neural outputs, thus suggesting that there could also be other neural mediators or interacting receptors on adipocytes (Figure 5).

DISCUSSION

Leptin is known to stimulate lipolysis and reduce fat mass, though the physiologic mechanisms responsible for this have not been fully delineated. In this study, we present data using functional, anatomic, biochemical, and genetic approaches to show that leptin increases lipolysis via the actions of sympathetic neuronal efferents to adipose tissue. These data also provide molecular, cellular, and anatomic evidence confirming the existence of neuronal projections onto adipocytes, which have been the subject of conjecture but which have not been directly visualized.

The existence of neuro-adipose junctions in WAT had been inferred based on the fact that a pseudorabies retrograde-tracing virus can visualize a set of neural projections in the brain (Bartness and Song, 2007). In addition, immunohistochemistry, and immunofluorescence have been used to visualize contacts between sympathetic neurons and adipocytes in sliced tissue (Giordano et al., 1996, 2005; Thompson, 1986). However, these methods, which require tissue slicing and fixation, do not distinguish en passant neurons from those that directly project onto adipocytes. The visualization of adipocyte-projecting neurons that can completely envelop an adipocyte has not been accomplished so far. We were able to directly visualize neural termini onto adipocytes using intra-vital multiphoton microscopy, which allows deep penetrance onto the live intact tissue, allowing us to visualize deeper structures without the perturbations associated with classical histological methods, which, in past studies, may have compromised the integrity of the neuro-adipose termini (Helmchen and Denk, 2005).

Confocal or multiphoton microscopy methods are suitable for histological analysis at a microscopic spatial scale, but do not give a 3D perspective of the organization of the organ as a whole. At a macroscopic spatial scale, methods such as MRI or computed tomography (CT) allow for measurement of whole-body fat distribution. However, all of these methods lack the spatial resolution that is required for visualizing structures such as nerve bundles. OPT is a technique with physical principles similar to those of X-ray CT/gamma radiation, which uses visible light instead of radiation (Gualda et al., 2013). Scattering of light passing through tissues is minimized by clearing lipids from the whole organ (Quintana and Sharpe, 2011). Unlike most currently available methods, OPT coupled to tissue clearing allows imaging of whole-mount samples with a spatial scale in the order of centimeters.

It has been previously shown that electrical stimulation of WAT nerve bundles can drive lipolysis (Correll, 1963). However, as shown here, nerve bundles in WAT have mixed molecular identity, making it difficult to ascertain the identity of the neurons responsible for this effect. To address this limitation, we used

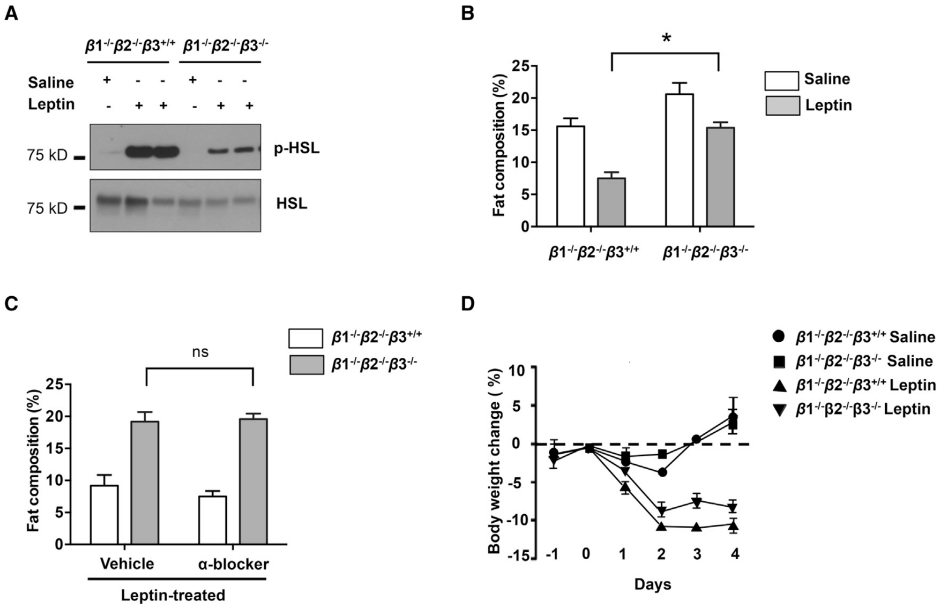

Figure 7. Deficiency of All β-Adrenergic Receptors Influences Leptin-Induced Lipolysis

(A) Immunoblot analysis of p-HSL in total protein extracts of fat pads of $\beta1^{-/-}\beta2^{-/-}\beta3^{+/+}$ and $\beta1^{-/-}\beta2^{-/-}\beta3^{-/-}$ mice that were treated with 500 ng/hr recombinant leptin.

(B) Whole-body fat composition (*$p < 0.05$, $n = 4–5$). Results are shown as mean ± SEM.

(C) α-Adrenergic receptors had a minor function in leptin-induced lipolysis (*$p > 0.05$, $n = 4–5$). Results are shown as mean ± SEM. ns, not significant.

(D) Whole-body fat composition of mice peripherally treated with recombinant leptin and α-blockers (phentolamine, 5 mg/kg, i.p.; and phenoxybenzamine, 10 mg/kg, i.p.) was measured ($n = 4–5$). Results are shown as mean ± SEM.

See also Figure S2.

optogenetics, which allows for cell-specific stimulation of neurons (Domingos et al., 2011, 2013). In the present study, we used optogenetics to specifically activate sympathetic neurons in *TH-Cre* mice. Another advantage of this approach is that it enables the specific activation of axonal projections and does not require stimulation of neuronal cell bodies (Petreanu et al., 2007; Vrontou et al., 2013). This feature is particularly convenient for autonomic neurons, given the deep localization of their cell bodies along the anterior face of the spinal cord and the intrinsic difficulty of implanting optical fibers in this location. Previous studies using neural tracing have revealed that sympathetic neurons innervating the subcutaneous inguinal fat pads localize to the 13th thoracic ganglia, which localizes at the dorsal edge of the diaphragm muscle, in the transition between the thorax and the abdomen (Youngstrom and Bartness, 1995). This anatomical location is particularly inaccessible and unsuitable for chronic implants of optical fibers or equivalent devices. However, as we show here, subcutaneous implant of optical fibers for stimulation of nerve terminals is feasible and effective. We used this approach to show that optogenetic gain of function of the catecholaminergic signaling to the neuro-adipose junction can lead to the phosphorylation of HSL and lipolysis of WAT. Similarly, previous loss-of-function experiments that assessed the effect of sympathetic input on lipolysis also did not allow analysis of the effect of specific cells in the way that optogenetics can. Thus, the use of mechanical denervation does not distinguish between neurons that directly innervate adipocytes versus those that are passing through. We have not yet profiled the non-TH nerve fibers, but it is reasonable to expect that some might be parasympathetic, nociceptive, sensory fibers and/or en passant axons. The function of these fibers could be assessed similarly to those that we report, using optogenetics, to activate other populations, including cholinergic neurons, by studying choline acetyltransferase (ChAT)-Cre mice and/or neurons expressing other molecular markers. Chemical ablation with capsaicin also has limitations, as this treatment is not specific to sympathetic neurons and affects all transient-receptor-potencial-vaniloid (TRPV)-expressing fibers (Holzer, 1991). Chemical ablation with 6-hydroxydopamine is likely to affect dopaminergic as well as enteric neurons, creating secondary systemic effects (Ding et al., 2004).

To avoid these limitations and gain local control over sympathetic neural activity, we used additional molecular genetic tools that combine tissue specificity with a localized effect. We show that ablation of the sympathetic neurons by DTR expression in TH-positive neurons followed by local DT injection in WAT abolishes the effect of leptin on HSL phosphorylation. We also noted

that the loss of function due to post-synaptic manipulations (i.e., the triple β-adrenergic receptor KO in Figure 7) has a lesser effect on the size of adipose tissue depots than that seen after pre-synaptic manipulations such as a loss of *DBH* or pharmacologic or mechanical ablation of neural input to fat (Figure 6). This suggests that leptin-induced production of NE from sympathetic neurons could act through additional receptors that are not one of the three β-adrenergic receptors that we tested, which have been suggested by others (Tavernier et al., 2005). Alternatively, sympathetic neurons may co-release other neurotransmitters or neuropeptides that signal through non-adrenergic receptors. This could account for the residual leptin-induced weight loss seen in $DBH^{-/-}$, although this effect is not significant when compared to controls. Thus, an in-depth knowledge of the underlying sympathetic neural circuits could provide strategies to pharmacologically activate specific sympathetic neuronal population, thus circumventing leptin resistance, as potential treatment of obesity.

A canonical effect of leptin is to increase sympathetic signaling to BAT, thus promoting thermogenesis (Bachman et al., 2002; Landsberg et al., 1984). However the role of autonomic stimulation of white fat has been less well studied. We now show that the sympathetic activity is also responsible for the leptin-stimulated lipolysis in WAT. While leptin has been assumed to increase lipolysis via activation of sympathetic efferent fibers, this has not been directly shown. Adrenergic agonists have been shown to induce the formation of beige (brite) fat, and these data suggest that sympathetic innervation may also stimulate this phenotypic change in adipose tissue (Bachman et al., 2002; Giralt and Villarroya, 2013; Dempersmier et al., 2015). Consistent with this, leptin has also been suggested to increase the formation of beige fat (Dodd et al., 2015).

Because brown adipocytes have relatively smaller fat storages compared to white adipocytes, while having higher metabolic demand, the continuous thermogenic response of BAT might require the supply of FFA from WAT mobilized in other parts of the body. Therefore, it is reasonable to speculate that the coordinated sympathetic actions in BAT and WAT in response to leptin could help maximize the hormone's effect on energy expenditure and fat metabolism. Future studies delineating the neural circuits connecting the central action of leptin with the peripheral activation of sympathetic system will be necessary to test this hypothesis. Particularly, it would be of great importance to develop technologies that would allow whole-body visualization and mapping of peripheral neuronal circuits using some of the approaches presented here.

In summary, we provide direct evidence that the sympathetic neuro-adipose junction is both necessary and sufficient for leptin to drive lipolysis in WAT.

EXPERIMENTAL PROCEDURES

Antibodies and Drugs

The antibodies were obtained from the following vendors: HSL (Cell Signaling Technology), phospho-HSL (Cell Signaling Technology), phospho-PKA substrate (Cell Signaling Technology), TH (Pel-Freez Biologicals), and actin (Sigma). Hexamethonium chloride, phentolamine, and phenoxybenzamine were from Sigma-Aldrich. DT was purchased from Merck Millipore. Recombinant mouse leptin was obtained from Amylin Pharmaceuticals.

Mice

DBH KO mice were kindly provided by Steve Thomas at the University of Pennsylvania. $Adr\beta1^{-/-}2^{-/-}$ and $Adr\beta3^{-/-}$ were kindly provided by Bruce Spiegelman at Harvard Medical School. *TH-Cre*, Rosa26-LSL-ChR2-YFP (Stock No. 012-569; Daou et al., 2013), Rosa26-LSL-DTR, and C57BL/B6J mice at 6–10 weeks old were purchased from The Jackson Laboratory. Animal procedures were approved by the ethics committee of Instituto Gulbenkian de Ciência and the Institutional Animal Care and Use Committee of Rockefeller University.

OPT

Six-week-old C57BL/6 mice were sacrificed with carbon dioxide. The inguinal fat pads were dissected from the mice with Dumont #5 Forceps, fixed in 4% paraformaldehyde (PFA; Sigma-Aldrich) for 3 hr at room temperature (RT) and subjected to the OPT clearing protocol as described in the Supplemental Experimental Procedures. Images of the whole fat tissue were acquired using a 1× lens mounted on an Infinitube tube lens and projected into a Hamamatsu FlashLT sCMOS camera. A total of 1,600 images were acquired for a full rotation (0.25° steps). The series of projections were then pre-processed for back-projection using FIJI in order to remove hot pixels and re-align the axis of rotation in relation to the camera chip, and finally the back-projection reconstruction was conducted using the Skyscan's NRecon software (Schindelin et al., 2012). The stack of slices was further processed with FIJI to increase contrast and saved to posterior analysis with the software Amira V5.3. Using this software, 3D reconstructions and image segmentation were performed to identify and reconstruct individual parts of the fat organs. Detailed instructions for setting up an OPT system can be found at https://sites.google.com/site/openspinmicroscopy/home/opt.

In Vivo Two-Photon Microscopy

Two-month-old mice were kept anesthetized with 2% isofluorane. During surgery, body temperature was maintained at 37°C with a warming pad. After application of local anesthetics (lidocaine), a sagittal incision of the skin was made above the supra-pelvic flank to expose the subcutaneous inguinal fat pad. An imaging chamber was custom built to minimize fat movement. Warm imaging solution (in millimolar: 130 NaCl, 3 KCl, 2.5 $CaCl_2$, 0.6 $MgCl_2 \cdot 6H_2O$, 10 HEPES without Na, 1.2 $NaHCO_3$, 10 glucose (pH 7.45), with NaOH) (37°C) mixed with a fat dye (LipidTOX) was applied to label adipocytes, maintain tissue integrity, and allow the use of immersion objective. Imaging experiments were performed under a two-photon laser-scanning microscope (Ultima, Prairie Instruments). Live images were acquired at 8–12 frames per second, at depths below the surface ranging from 100 to 250 mm, using an Olympus 20× 0.8 N.A. water immersion objective, with a laser tuned to 860–940 nm wavelength, and emission filters 525/50 nm and 595/50 nm for green and red fluorescence, respectively. Laser power was adjusted to be 20–25 mW at the focal plane (maximally, 35 mW), depending on the imaging depth and level of expression of dtTomato and LipidTOX spread. tdTomato fluorescence was used to identify TH-positive fibers until photobleaching occurred.

Leptin Treatment and Lipolysis Analysis

To examine the effect of leptin treatment on lipolysis, leptin (delivery rate of 500 ng/hr) or saline was delivered through osmotic pumps (Alzet) subcutaneously for 2 days. Body weight was recorded daily. Body fat composition was measured using the EchoMRI body analyzer at end point before subcutaneous or epididymal adipose tissues were collected. HSL phosphorylation was detected by immunohistochemistry of paraffin sections at 6-μm thickness and/or western blot of subcutaneous or epididymal adipose tissues. NE levels in serum and subcutaneous fat pads were determined with an NE ELISA kit (Labor Diagnostika Nord GmbH). Tissues were homogenized and sonicated in homogenization buffer (1 N HCl, 1 mM EDTA), and cellular debris was pelleted by centrifugation at 13,000 rpm for 15 min at 4°C. All tissue samples were normalized to total tissue protein concentration.

Mechanical Denervation

The nerve bundle 2 mm distal from the tip of the epididymal fat was physically crushed for 30 s and then released using a forcep. Leptin was administrated through osmotic pump 3 days after nerve crush. HSL phosphorylation was detected 2 days upon leptin treatment.

Hexamethonium Chloride, Isopreterenol, and α-Blocker Treatment

Hexamethonium chloride (500 μg/hr) was administrated during leptin treatment through a separate osmotic pump, and the α-blockers phentolamine (5 mg/kg, intraperitoneally [i.p.]) and phenoxybenzamine (10 mg/kg; i.p.) were administrated twice a day during the course of leptin treatment (500 ng/hr). Isopreterenol (250 μg per mouse) was delivered in saline through jugular vein injection. Blood was drawn through tail bleeding, and plasma FFA was measured using a NETO kit (Wako Pure Chemicals Industries). For FFA release upon isopreterenol treatment in vitro, adipose tissue explants were dissected and cultured in Hank's medium and stimulated with isopreterenol at 10 μg/ml for 3 hr. FFA was measured in the medium.

NE Measurements after Optogenetic Stimulation Ex Vivo

SCG were removed from 28- to 30-day-old *TH-Cre* X *Rosa26-LSL-ChR2-YFP* mice under a stereomicroscope and placed in DMEM (Invitrogen). Ganglia were cleaned from the surrounding tissue capsule and transferred into eight-well tissue culture chambers (Sarstedt) that were previously coated with poly-D-lysine (Sigma-Aldrich) in accordance to the manufacturer's instructions. Ganglia were then covered with 5 μl Matrigel (BD Biosciences) and incubated for 7 min at 37°C. DMEM without phenol red (Invitrogen) supplemented with 10% fetal bovine serum (Invitrogen), 2 mM L-glutamine (Biowest), and nerve growth factor (Sigma-Aldrich) was subsequently added. SCG ganglia were cultured for a minimum of 24 hr prior to further manipulation. Depolarization of sympathetic neurons in explant cultures was performed on a Yokogawa CSU-X1 Spinning Disk confocal system using the 488-nm laser line and pointing at the region of interest (ROI) for 200 μs. Stimulation was repeated five times using 40% of laser intensity. NE in the SCG explant culture medium was determined with an NE ELISA kit (Labor Diagnostika Nord GmbH). The same procedure was performed for *LSL-ChR2-YFP* control mice.

Surgeries and Optogenetic Stimulation

General anesthesia was induced and maintained with isofluorane. After application of local anesthetics (lidocaine), a sagittal incision of the skin was made above the neck and supra-pelvic flank. A hemostat was inserted into the incision and, by opening and closing the jaws of the hemostat, spread the subcutaneous tissue to create a longitudinal pocket for the optical fiber. The pocket was made long enough to allow about 4–6 cm of fiber (Thorlabs FT200). The tip of the fiber targeted the anatomical location of the inguinal fat pad. The other end of the fiber, the ferrule-connector end, was secured along the skin via sutures and dermal staples. Appropriate local analgesic was used post-surgically. Optogenetical stimulations were performed 48 hr after surgical procedures.

The stimulation session in Figure 4D lasted 4–6 hr and was performed via a 1-s 20-Hz pulse of blue laser every other second, originating from a 473-nm solid laser source (OEM-BL-473-00100-CWM-SD-05). The laser source had an output power of 100 mW. Ferrule-coupled optical fibers of 200-μm diameter (Thorlabs; FT200EMT-CANNULA-TS1031629) were connected to ferrule patch cords (Thorlabs; FT200EMT-FC/PC-ferrule) with mating sleeves (Thorlabs; ADAF1), and the later to the laser source via FC/PC adaptor.

NE in subcutaneous fad pads was determined with an NE ELISA kit (Labor Diagnostika Nord GmbH) as described earlier.

Stimulation protocol in Figure 4E took place every day for 2 weeks and solely during the rodent rest period. Longer sessions, as in Figure 4F, had a duration of 4 weeks. Stimulation sessions lasted 4–6 hr and were performed as described earlier.

MRI Fat Measurements and Fat Pad Segmentation

Mice were subjected to optogenetic stimulation as stated earlier, perfused with 4% PFA/PBS, post-fixed over 2–3 days, and embedded in Fomblin Oil (Sigma-Aldrich) for scanning. Imaging was performed on a 7.0 T 70/30 Bruker Biospec small-animal MRI system with a 12-cm diameter 450 mT/m amplitude and 4,500 T/m/s slew rate actively shielded gradient subsystems with integrated shim capability. A linear coil with 7-cm diameter and a length sufficient to cover the whole body of the animal was used for excitation and reception of the magnetic resonance signal. Two image sets were acquired, one with fat suppression and one without. Axial images, covering the whole animal in 75 0.4-mm-thick slices without gap, were acquired in an interleaved way by using a RARE (rapid acquisition with relaxation enhancement) pulse sequence with RARE factor 2. Four averages with a flip angle of 90°—echo time (TE) = 10 ms, repetition time (TR) = 2,468 ms, field of view = 10 × 3 cm, and matrix size = 256 × 128 (acquisition matrix size = 256 × 96), resulting in a spatial resolution of 0.391 × 0.234 × 0.4 mm—were acquired. The fat suppression, added to the second scan, consists of a 90° Gaussian pulse with 2.6067-ms duration and 1051.1-Hz bandwidth. Data were converted into .tif files by FIJI software. The subcutaneous inguinal fat distribution was determined with semi-automated Amira V5.3 software segmentation of scanned images. Amira V5.3 software segmentation relies on the automated grouping of pixels with the same index of intensity in the grayscale. An automatic segmentation based on the gray threshold levels, which decomposes the image domain into subsets, allowed us to define the right and the left inguinal fat depots, which were further saved as unique fields. Volumes of the right and the left subcutaneous fat pads were defined as the number of voxels multiplied by the size of a single voxel. The size of stimulated fat pads was determined, and the effect of optogenetic stimulation of neurons on fat mass was calculated in the same animal relative to non-stimulated contralateral side.

Statistical Methods

Statistics were performed in GraphPad Prism and involved the computation of means and SEM, which accompany each figure legend. Student's t tests and ANOVAs were used where appropriate, and p values are indicated in text.

SUPPLEMENTAL INFORMATION

Supplemental Information includes Supplemental Experimental Procedures, two figures, and two movies and can be found with this article online at http://dx.doi.org/10.1016/j.cell.2015.08.055.

AUTHOR CONTRIBUTIONS

Two-photon microscopy and optogenetics were performed by A.I.D. and R.M.P., and related rodent husbandry was performed by N.K. and E.S. OPT was performed by R.M.P., M.M.A.P., and G.G.M.; MRI scans were conducted by H.V.; Amira segmentation of MRI data was performed by R.M.P. and M.M.A.P.; cell cultures and neuronal explants were developed by A.B. and R.M.P. Biochemical analyses and measurement of whole body fat composition and body weights were performed by W.Z., N.K., E.S., Y.H.L., and A.K.; A.I.D. and J.M.F. wrote the manuscript.

ACKNOWLEDGMENTS

This work was supported by the Fundação para a Ciência e Tecnologia (FCT), the European Molecular Biology Organization (EMBO), and the JPB Foundation. The FCT supported A.I.D., R.M.P., M.M.A.P., N.K., G.G.M., A.B., and E.S. The JPB Foundation supported the work of W.Z., Y.H.L., and A.K. J.M.F. is a Howard Hughes Medical Institute (HHMI) investigator.

Received: May 6, 2015
Revised: July 17, 2015
Accepted: August 6, 2015
Published: September 24, 2015

REFERENCES

Arvaniti, K., Deshaies, Y., and Richard, D. (1998). Effect of leptin on energy balance does not require the presence of intact adrenals. Am. J. Physiol. *275*, R105–R111.

Awad, S., Constantin-Teodosiu, D., Macdonald, I.A., and Lobo, D.N. (2009). Short-term starvation and mitochondrial dysfunction - a possible mechanism leading to postoperative insulin resistance. Clin. Nutr. *28*, 497–509.

Bachman, E.S., Dhillon, H., Zhang, C.Y., Cinti, S., Bianco, A.C., Kobilka, B.K., and Lowell, B.B. (2002). betaAR signaling required for diet-induced thermogenesis and obesity resistance. Science *297*, 843–845.

Bartness, T.J., and Song, C.K. (2007). Thematic review series: adipocyte biology. Sympathetic and sensory innervation of white adipose tissue. J. Lipid Res. *48*, 1655–1672.

Bartness, T.J., Kay Song, C., Shi, H., Bowers, R.R., and Foster, M.T. (2005). Brain-adipose tissue cross talk. Proc. Nutr. Soc. *64*, 53–64.

Brasaemle, D.L. (2007). Thematic review series: adipocyte biology. The perilipin family of structural lipid droplet proteins: stabilization of lipid droplets and control of lipolysis. J. Lipid Res. *48*, 2547–2559.

Buch, T., Heppner, F.L., Tertilt, C., Heinen, T.J., Kremer, M., Wunderlich, F.T., Jung, S., and Waisman, A. (2005). A Cre-inducible diphtheria toxin receptor mediates cell lineage ablation after toxin administration. Nat. Methods *2*, 419–426.

Correll, J.W. (1963). Adipose tissue: ability to respond to nerve stimulation in vitro. Science *140*, 387–388.

Daou, I., Tuttle, A.H., Longo, G., Wieskopf, J.S., Bonin, R.P., Ase, A.R., Wood, J.N., De Koninck, Y., Ribeiro-da-Silva, A., Mogil, J.S., and Séguéla, P. (2013). Remote optogenetic activation and sensitization of pain pathways in freely moving mice. J. Neurosci. *33*, 18631–18640.

Dempersmier, J., Sambeat, A., Gulyaeva, O., Paul, S.M., Hudak, C.S., Raposo, H.F., Kwan, H.Y., Kang, C., Wong, R.H., and Sul, H.S. (2015). Cold-inducible Zfp516 activates UCP1 transcription to promote browning of white fat and development of brown fat. Mol. Cell *57*, 235–246.

Ding, Y.M., Jaumotte, J.D., Signore, A.P., and Zigmond, M.J. (2004). Effects of 6-hydroxydopamine on primary cultures of substantia nigra: specific damage to dopamine neurons and the impact of glial cell line-derived neurotrophic factor. J. Neurochem. *89*, 776–787.

Dodd, G.T., Decherf, S., Loh, K., Simonds, S.E., Wiede, F., Balland, E., Merry, T.L., Münzberg, H., Zhang, Z.Y., Kahn, B.B., et al. (2015). Leptin and insulin act on POMC neurons to promote the browning of white fat. Cell *160*, 88–104.

Domingos, A.I., Vaynshteyn, J., Voss, H.U., Ren, X., Gradinaru, V., Zang, F., Deisseroth, K., de Araujo, I.E., and Friedman, J. (2011). Leptin regulates the reward value of nutrient. Nat. Neurosci. *14*, 1562–1568.

Domingos, A.I., Sordillo, A., Dietrich, M.O., Liu, Z.W., Tellez, L.A., Vaynshteyn, J., Ferreira, J.G., Ekstrand, M.I., Horvath, T.L., de Araujo, I.E., and Friedman, J.M. (2013). Hypothalamic melanin concentrating hormone neurons communicate the nutrient value of sugar. eLife *2*, e01462.

Elia, M., Stubbs, R.J., and Henry, C.J. (1999). Differences in fat, carbohydrate, and protein metabolism between lean and obese subjects undergoing total starvation. Obes. Res. *7*, 597–604.

Friedman, J.M., and Halaas, J.L. (1998). Leptin and the regulation of body weight in mammals. Nature *395*, 763–770.

Giordano, A., Morroni, M., Santone, G., Marchesi, G.F., and Cinti, S. (1996). Tyrosine hydroxylase, neuropeptide Y, substance P, calcitonin gene-related peptide and vasoactive intestinal peptide in nerves of rat periovarian adipose tissue: an immunohistochemical and ultrastructural investigation. J. Neurocytol. *25*, 125–136.

Giordano, A., Frontini, A., Murano, I., Tonello, C., Marino, M.A., Carruba, M.O., Nisoli, E., and Cinti, S. (2005). Regional-dependent increase of sympathetic innervation in rat white adipose tissue during prolonged fasting. J. Histochem. Cytochem. *53*, 679–687.

Giralt, M., and Villarroya, F. (2013). White, brown, beige/brite: different adipose cells for different functions? Endocrinology *154*, 2992–3000.

Gualda, E.J., Vale, T., Almada, P., Feijó, J.A., Martins, G.G., and Moreno, N. (2013). OpenSpinMicroscopy: an open-source integrated microscopy platform. Nat. Methods *10*, 599–600.

Halaas, J.L., Gajiwala, K.S., Maffei, M., Cohen, S.L., Chait, B.T., Rabinowitz, D., Lallone, R.L., Burley, S.K., and Friedman, J.M. (1995). Weight-reducing effects of the plasma protein encoded by the obese gene. Science *269*, 543–546.

Halaas, J.L., Boozer, C., Blair-West, J., Fidahusein, N., Denton, D.A., and Friedman, J.M. (1997). Physiological response to long-term peripheral and central leptin infusion in lean and obese mice. Proc. Natl. Acad. Sci. USA *94*, 8878–8883.

Helmchen, F., and Denk, W. (2005). Deep tissue two-photon microscopy. Nat. Methods *2*, 932–940.

Holzer, P. (1991). Capsaicin: cellular targets, mechanisms of action, and selectivity for thin sensory neurons. Pharmacol. Rev. *43*, 143–201.

Koffler, M., and Kisch, E.S. (1996). Starvation diet and very-low-calorie diets may induce insulin resistance and overt diabetes mellitus. J. Diabetes Complications *10*, 109–112.

Landsberg, L., Saville, M.E., and Young, J.B. (1984). Sympathoadrenal system and regulation of thermogenesis. Am. J. Physiol. *247*, E181–E189.

Montez, J.M., Soukas, A., Asilmaz, E., Fayzikhodjaeva, G., Fantuzzi, G., and Friedman, J.M. (2005). Acute leptin deficiency, leptin resistance, and the physiologic response to leptin withdrawal. Proc. Natl. Acad. Sci. USA *102*, 2537–2542.

Newman, W.P., and Brodows, R.G. (1983). Insulin action during acute starvation: evidence for selective insulin resistance in normal man. Metabolism *32*, 590–596.

Nguyen, K.D., Qiu, Y., Cui, X., Goh, Y.P., Mwangi, J., David, T., Mukundan, L., Brombacher, F., Locksley, R.M., and Chawla, A. (2011). Alternatively activated macrophages produce catecholamines to sustain adaptive thermogenesis. Nature *480*, 104–108.

Petreanu, L., Huber, D., Sobczyk, A., and Svoboda, K. (2007). Channelrhodopsin-2-assisted circuit mapping of long-range callosal projections. Nat. Neurosci. *10*, 663–668.

Quintana, L., and Sharpe, J. (2011). Optical projection tomography of vertebrate embryo development. Cold Spring Harb. Protoc. *2011*, 586–594.

Rafael, J., and Herling, A.W. (2000). Leptin effect in ob/ob mice under thermoneutral conditions depends not necessarily on central satiation. Am. J. Physiol. Regul. Integr. Comp. Physiol. *278*, R790–R795.

Rezai-Zadeh, K., and Münzberg, H. (2013). Integration of sensory information via central thermoregulatory leptin targets. Physiol. Behav. *121*, 49–55.

Scarpace, P.J., and Matheny, M. (1998). Leptin induction of UCP1 gene expression is dependent on sympathetic innervation. Am. J. Physiol. *275*, E259–E264.

Schindelin, J., Arganda-Carreras, I., Frise, E., Kaynig, V., Longair, M., Pietzsch, T., Preibisch, S., Rueden, C., Saalfeld, S., Schmid, B., et al. (2012). Fiji: an open-source platform for biological-image analysis. Nat. Methods *9*, 676–682.

Tavernier, G., Jimenez, M., Giacobino, J.P., Hulo, N., Lafontan, M., Muzzin, P., and Langin, D. (2005). Norepinephrine induces lipolysis in beta1/beta2/beta3-adrenoceptor knockout mice. Mol. Pharmacol. *68*, 793–799.

Thompson, G.E. (1986). Vascular and lipolytic responses of the inguinal fat pad of the sheep to adrenergic stimulation, and the effects of denervation and autotransplantation. Q. J. Exp. Physiol. *71*, 559–567.

Vrontou, S., Wong, A.M., Rau, K.K., Koerber, H.R., and Anderson, D.J. (2013). Genetic identification of C fibres that detect massage-like stroking of hairy skin in vivo. Nature *493*, 669–673.

Weisberg, S.P., McCann, D., Desai, M., Rosenbaum, M., Leibel, R.L., and Ferrante, A.W., Jr. (2003). Obesity is associated with macrophage accumulation in adipose tissue. J. Clin. Invest. *112*, 1796–1808.

Youngstrom, T.G., and Bartness, T.J. (1995). Catecholaminergic innervation of white adipose tissue in Siberian hamsters. Am. J. Physiol. *268*, R744–R751.

nature medicine

Sympathetic neuron–associated macrophages contribute to obesity by importing and metabolizing norepinephrine

Roksana M Pirzgalska[1,11], Elsa Seixas[1,11], Jason S Seidman[2], Verena M Link[2,3], Noelia Martínez Sánchez[1], Inês Mahú[1], Raquel Mendes[1], Vitka Gres[1], Nadiya Kubasova[1], Imogen Morris[1], Bernardo A Arús[1,4], Chelsea M Larabee[1], Miguel Vasques[1,5], Francisco Tortosa[6], Ana L Sousa[7], Sathyavathy Anandan[1], Erin Tranfield[7], Maureen K Hahn[8], Matteo Iannacone[9], Nathanael J Spann[2], Christopher K Glass[2] & Ana I Domingos[1,10]

The cellular mechanism(s) linking macrophages to norepinephrine (NE)-mediated regulation of thermogenesis have been a topic of debate. Here we identify sympathetic neuron–associated macrophages (SAMs) as a population of cells that mediate clearance of NE via expression of solute carrier family 6 member 2 (SLC6A2), an NE transporter, and monoamine oxidase A (MAOA), a degradation enzyme. Optogenetic activation of the sympathetic nervous system (SNS) upregulates NE uptake by SAMs and shifts the SAM profile to a more proinflammatory state. NE uptake by SAMs is prevented by genetic deletion of *Slc6a2* or inhibition of the encoded transporter. We also observed an increased proportion of SAMs in the SNS of two mouse models of obesity. Genetic ablation of *Slc6a2* in SAMs increases brown adipose tissue (BAT) content, causes browning of white fat, increases thermogenesis, and leads to substantial and sustained weight loss in obese mice. We further show that this pathway is conserved, as human sympathetic ganglia also contain SAMs expressing the analogous molecular machinery for NE clearance, which thus constitutes a potential target for obesity treatment.

Sympathetic innervation of adipose tissue promotes lipolysis and fat mass reduction via NE signaling[1]. In obesity, chronic local inflammation underlies adipose tissue dysfunction, and macrophages have been shown to play a central role[1,2]. The mechanism that links macrophages in white adipose tissue (WAT) to NE remains controversial. Some groups have reported that anti-inflammatory adipose tissue macrophages (ATMs) in the WAT produce NE to sustain thermogenesis and browning. In direct contradiction, other groups have reported that ATMs do not express a key enzyme required for NE production and that genetic deletion of this enzyme in mouse macrophages has no effect on thermogenesis and body weight[3–6].

Here we identify a previously undescribed population of SAMs that import and degrade NE via specific proteins that are absent from ATMs. We found by transcriptional profiling of isolated SAMs that neural- and adrenergic-related genes are differentially expressed in these cells relative to other macrophage populations. SAMs accumulate intracellular NE despite lacking enzymes for NE biosynthesis. Using optogenetics, we demonstrate that SNS activity increases NE content and the proinflammatory state of SAMs. We functionally demonstrate that SAMs import and degrade NE via NE transporter (SLC6A2) and degradation enzyme (MAOA), respectively. We further demonstrate that SAM-mediated clearance of extracellular NE contributes to obesity, as inhibiting NE import by SAMs ameliorates obesity, thermogenesis, and browning in mutant obese (*ob*/*ob*) mice and mice fed a high-fat diet (HFD). Finally, we demonstrate human relevance for this mechanism, as we found that SAMs are also present in human sympathetic ganglia and express similar molecular machinery as that observed in mice. Thus, the identification of SAMs represents a new contribution to the ongoing controversy surrounding the role of macrophages in thermogenesis and obesity while identifying an unforeseen immunological player in noradrenergic homeostasis with therapeutic potential for obesity.

RESULTS

Specialized morphology and activation of SNS *Cx3cr1*-expressing cells

Our initial aim was to visualize the *in vivo* morphology of ATMs using two-photon and confocal microscopy in *Cx3cr1*$^{GFP/+}$ mice, in which macrophages are labeled with GFP. ATMs in fat parenchyma had a regular circular shape (**Fig. 1a**), whereas those located on sympathetic

[1]The Howard Hughes Medical Institute (HHMI) and Obesity Laboratory, Instituto Gulbenkian de Ciência, Oeiras, Portugal. [2]Department of Cellular and Molecular Medicine, University of California, San Diego, La Jolla, California, USA. [3]Faculty of Biology, Department II, Ludwig-Maximilians Universität München, Planegg-Martinsried, Germany. [4]Departamento de Bioquímica, Instituto de Ciências Básicas da Saúde, Universidade Federal do Rio Grande do Sul, Porto Alegre, Brazil. [5]Department of Endocrinology, Curry Cabral Hospital, Centro Hospitalar de Lisboa Central, Lisbon, Portugal. [6]Department of Pathology, Centro Hospitalar Lisboa Norte, Hospital de Santa Maria, EPE, Lisbon, Portugal. [7]Electron Microscopy Unit, Instituto Gulbenkian de Ciência, Oeiras, Portugal. [8]Vanderbilt Kennedy Center for Research on Human Development, Vanderbilt University School of Medicine, Nashville, Tennessee, USA. [9]Division of Immunology, Transplantation and Infectious Diseases, Istituto di Ricovero e Cura a Carattere Scientifico (IRCCS) San Raffaele Scientific Institute, Milan, Italy. [10]The Howard Hughes Medical Institute (HHMI), New York, New York, USA. [11]These authors contributed equally to this work. Correspondence should be addressed to A.I.D. (dominan@igc.gulbenkian.pt).

Received 6 May; accepted 12 September; published online 9 October 2017; doi:10.1038/nm.4422

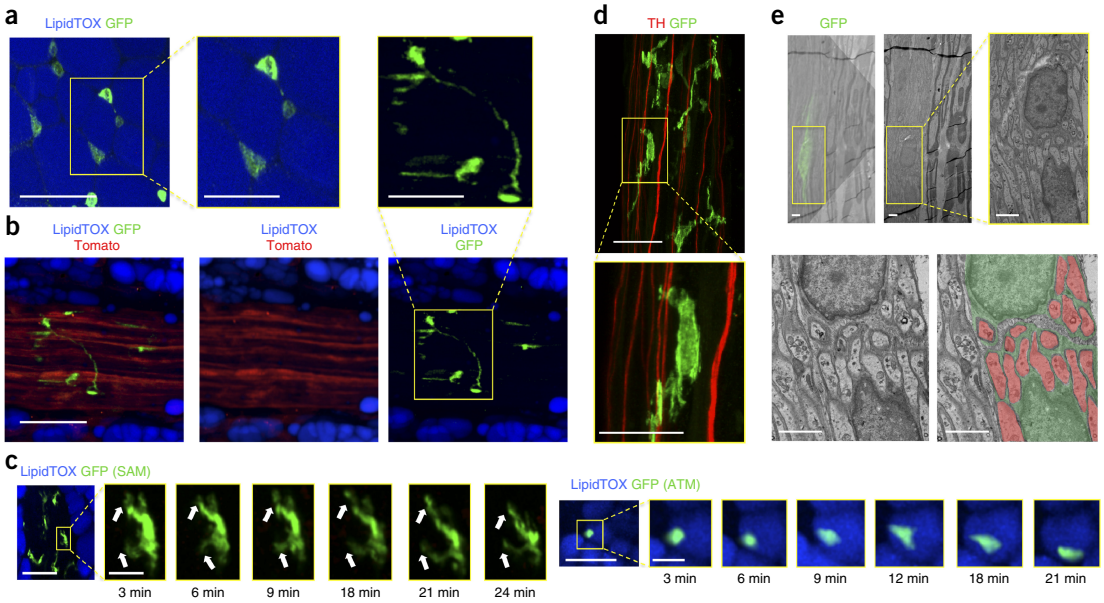

Figure 1 Sympathetic neuron–associated *Cx3cr1*-GFP$^+$ cells exhibit differentiated morphology for specific association with SNS neurons. (**a**) Confocal images of WAT isolated from a *Cx3cr1*$^{GFP/+}$ mouse and stained using lipid stain LipidTOX (blue) and anti-GFP antibody (green). Images are representative of five similar experiments. (**b**) Confocal images of sympathetic nerve fibers in subcutaneous adipose tissue isolated from a cross of *TH-cre*; *LSL-Tomato* (red) and *Cx3cr1*$^{GFP/+}$ (green) mice. Adipocytes were stained using lipid stain LipidTOX (blue). Images are representative of three similar experiments. Scale bars in **a** and **b**, 50 µm. The boxed regions in the main micrographs in **a** and **b** are shown at higher magnification; scale bars, 25 µm. (**c**) Intravital multiphoton visualization of a neural–adipose connection in the inguinal fat pad of a live *Cx3cr1*$^{GFP/+}$ mouse; LipidTOX (blue) labels adipocytes. Images depict the morphological features and cell dynamics of *Cx3cr1*-GFP$^+$ cells associated with sympathetic nerve fibers (left) and *Cx3cr1*-GFP$^+$ cells in the parenchyma of subcutaneous fat (right). Images are representative of three similar experiments. Scale bars, 50 µm. Boxed regions in the main micrographs are shown at higher magnification at the indicated time points; scale bars, 10 µm. White arrows indicate dendritiform processes over time. (**d**) Confocal images of sympathetic nerve fibers isolated from the inguinal fat pad of a *Cx3cr1*$^{GFP/+}$ mouse and stained using anti-TH (red) and anti-GFP (green) antibodies. Images are representative of five similar experiments. Scale bar, 50 µm. The boxed region in the main micrograph is shown at higher magnification below; scale bar, 25 µm. (**e**) Correlative confocal and transmission electron microscopy of nerve fibers isolated from the subcutaneous fat pad of a *Cx3cr1*$^{GFP/+}$ mouse. Shown are an overlay of the GFP fluorescence (green) with the electron micrograph of the same section (upper left; the lower left image is a higher-magnification view of the boxed region), the electron micrograph alone (upper middle; the yellow boxed region is shown at higher magnification to the right), and the electron micrograph from the lower left with false coloring highlighting *Cx3cr1*-GFP$^+$ cells (green) and sympathetic nerves (red) (lower right). Images are representative of two similar experiments. Scale bars, 2 µm.

nerve bundles exhibited profuse pseudopodia that extended over a greater surface area (**Fig. 1b** and **Supplementary Fig. 1a**,**b**). Furthermore, we observed that sympathetic neuron–associated *Cx3cr1*-GFP$^+$ cells displayed dynamic extensions and retractions of dendritiform processes over time (**Fig. 1c** and **Supplementary Video 1**). In contrast, ATMs surrounding adipocytes displayed minimal temporal plasticity or displacement (**Fig. 1c** and **Supplementary Video 2**). Using correlative light–electron microscopy on WAT-derived nerve bundles, we confirmed that *Cx3cr1*-GFP$^+$ cells extended thin pseudopodial processes that enveloped nonmyelinated SNS axons (**Fig. 1d**,**e** and **Supplementary Fig. 1c**).

We then investigated whether sympathetic neuron–associated *Cx3cr1*-GFP$^+$ cells were present in other SNS compartments, such as paravertebral sympathetic ganglia. Through imaging superior cervical ganglia (SCGs) and thoracic chains, we visualized *Cx3cr1*-GFP$^+$ cells that were morphologically similar to those within WAT-derived SNS bundles (**Supplementary Fig. 2**). Owing to the established *ex vivo* explant potential of SCGs, we used them along with WAT-derived SNS nerve bundles as model systems for subsequent functional and molecular analyses.

SNS *Cx3cr1*-expressing SAMs exhibit hematopoietic characteristics

Because nearly all *Cx3cr1*-GFP$^+$ cells isolated from sympathetic fibers expressed the immune marker CD45 (**Supplementary Fig. 3**) and macrophage marker F4/80 (**Supplementary Fig. 4a**), we designated these cells SAMs. Because of the specialized morphology and location of SAMs, we next explored how these cells compared to other tissue macrophages and brain microglia. We sorted F4/80$^+$CD45$^+$ cells from the following tissues: sympathetic ganglia (SAM ganglia), sympathetic nerve fibers from inguinal fat (SAM fibers), neighboring subcutaneous fat (sATM), visceral fat (vATM), spleen (SpM), and brain (microglia) (**Fig. 2a**; gating details in **Supplementary Fig. 3**). The relative abundance of CD45^{high}*Cx3cr1*-GFP$^+$ cells was nearly four times higher within nerve fibers (SAMs) than in subcutaneous WAT (sWAT) (sATMs; **Supplementary Fig. 4b**).

CD45 is highly expressed in hematopoietic cells but expressed at low levels in microglia. Flow cytometric analysis revealed that SAMs are CD45^{medium} or CD45^{high} (**Supplementary Fig. 3**), suggesting a hematopoietic origin for these cells. To test this hypothesis, we generated chimeras through transplantation of bone marrow from

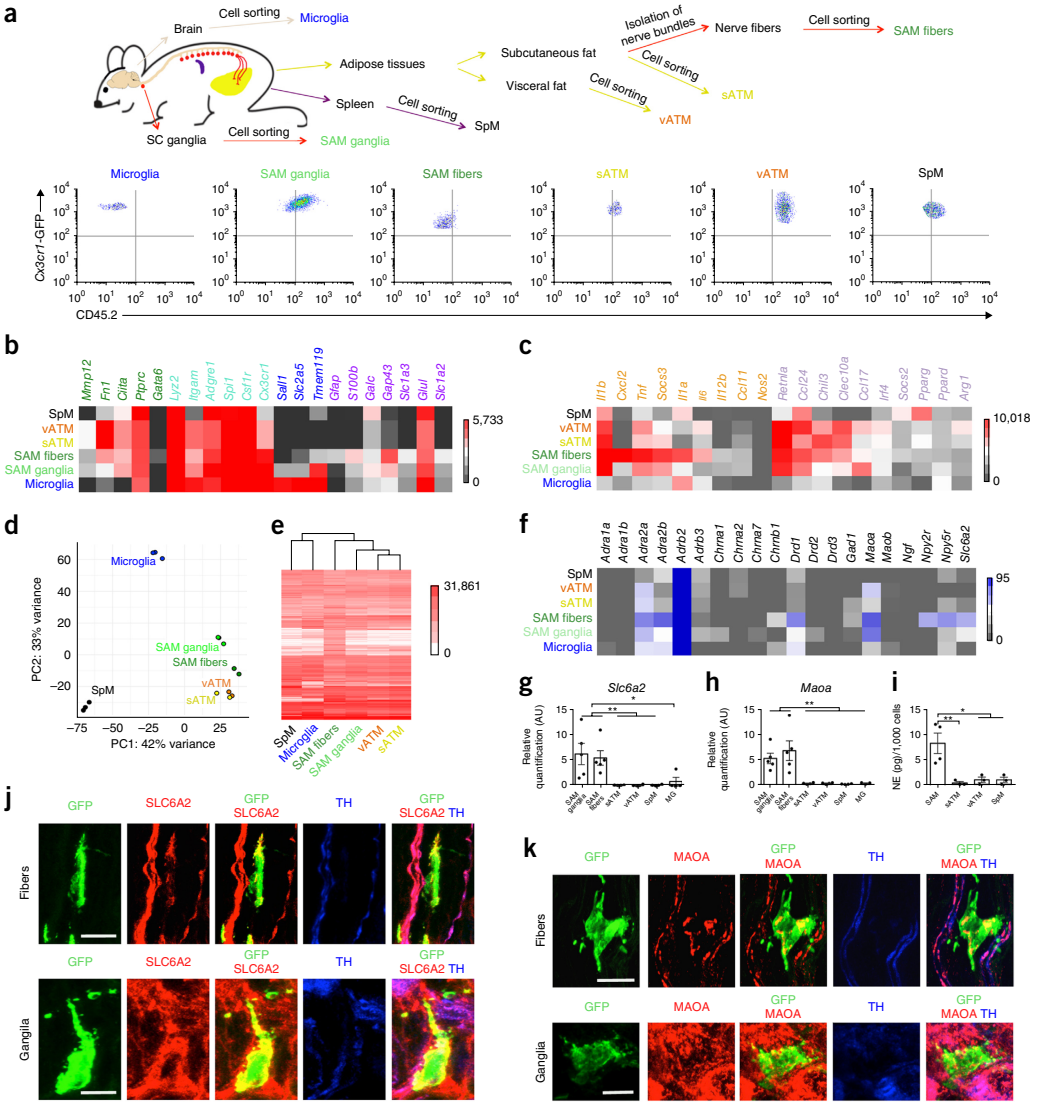

Figure 2 SAMs highly express macrophage-associated markers and possess the machinery for uptake and degradation of norepinephrine. (**a**) Top, schematic representation of tissue dissections and processing of macrophages isolated from the following tissues: brain, spleen, visceral fat, subcutaneous fat, sympathetic nerve fibers from subcutaneous fat, and superior cervical ganglia (SC ganglia). Bottom, representative flow cytometry dot plots indicating the CD45.2 status of macrophages from each tissue analyzed. (**b**) Heat map showing expression of genes associated with macrophage (green and cyan), microglial (blue and cyan), and glial (purple) profiles as determined by low-input RNA-seq. Values are in reads per kilobase of transcript per million mapped reads (RPKM). (**c**) Heat map showing expression of proinflammatory (orange) and anti-inflammatory (purple) genes as determined by low-input RNA-seq. Values are in RPKM. (**d**) PCA based on the top 500 genes with the most variable expression across SAM fibers (green), SAM ganglia (light green), vATM (orange), sATM (yellow), SpM (black), and microglia (blue). Each dot represents an independent experiment. (**e**) Heat map of transcript levels (RPKM values) based on the 5,000 genes most highly expressed by SAM fibers as determined by low-input RNA-seq. (**f**) Heat map showing expression of genes encoding neurotransmitter receptors, transporters, and catalytic enzymes. RPKM values were determined by low-input RNA-seq. Values in **b**–**f** represent three (SpM, microglia, and SAM ganglia) or two (vATM, sATM, and SAM fibers) independent experiments. (**g**) Expression of mRNA for *Slc6a2* as determined by qRT–PCR presented with normalization to *Gapdh* expression. Each data point represents tissues pooled from ten mice. $n = 5$ experiments for SAM fibers and SAM ganglia and $n = 4$ experiments for SpM, vATM, sATM, and microglia (MG). (**h**) Expression of mRNA for *Maoa* as determined by qRT–PCR with normalization to *Gapdh* expression. Each data point represents tissues pooled from ten mice. $n = 5$ experiments for SAM fibers and SAM ganglia, $n = 4$ experiments for SpM, vATM, and sATM, and $n = 3$ experiments for microglia. (**i**) NE content in sorted CD45.2 (PE)$^+$F4/80 (Alexa Fluor 647)$^+$ cells measured by NE ELISA. The numbers of cells used in NE assays were as follows: 858 ± 258 for SAMs ($n = 4$ experiments) and 1,000 cells for sATMs, vATMs, and SpMs ($n = 3$ experiments). (**j**,**k**) Confocal images of sympathetic nerve fibers (top) and SCG (bottom) isolated from *Cx3cr1*$^{GFP/+}$ mice and stained using anti-GFP (green) and anti-TH (blue) antibodies together with anti-SLC6A2 (**j**) or anti-MAOA (**k**) antibody (red). Images are representative of two experiments. Scale bars, 10 µm. Data in **g**–**i** were analyzed by one-way ANOVA followed by Tukey's multiple-comparisons test. Data are shown as average ± s.e.m. $^*P < 0.05$, $^{**}P < 0.01$.

CD45.2 *Cx3cr1*$^{GFP/+}$ donors into irradiated CD45.1 recipient mice and observed complete repopulation of CD45$^+$ cells derived from the CD45.2 *Cx3cr1*$^{GFP/+}$ donors (**Supplementary Fig. 4c**). Eight weeks following transplantation, we established that CD45.2$^+$*Cx3cr1*-GFP$^+$ SAMs repopulated sympathetic nerve bundles in WAT, whereas microglial repopulation in the brain did not occur (**Supplementary Fig. 4d**). This suggests that SAMs in sympathetic fibers have an origin similar to that of other hematopoietic macrophages rather than being from a microglial lineage.

SAM expression profile is more macrophage- than glial-like

Considering the association of SAMs with neurons, we asked how the gene expression profile of SAMs compared to those of other tissue-resident macrophages and microglia (**Fig. 2**). We sorted macrophages from various tissues as described above (F4/80$^+$CD45$^+$ cells designated as SAM ganglia, SAM fibers, sATMs, vATMs, SpMs, and microglia; **Fig. 2a** and **Supplementary Fig. 3**) and profiled gene expression by low-input RNA-seq (**Fig. 2b–f**). As expected, SAMs highly expressed markers common to both microglia and macrophages, such as *Adgre1*, *Csf1r*, and *Cx3cr1* (**Fig. 2b**). SAMs expressed macrophage-associated genes whose expression was excluded from microglia, such as *Fn1* and *Ciita* (**Fig. 2b**)[7]. Flow cytometric analysis showed that additional macrophage-specific markers whose expression was excluded from microglia (CD68, Ly6C, major histocompatibility complex II (MHCII), and CD11b) were also highly expressed in SAMs (**Supplementary Fig. 5a**,**b**). SAMs did not robustly express microglial- or glial-specific genes relative to macrophage-specific genes (**Fig. 2b** and **Supplementary Fig. 5c**)[8–17]. Expression of the *Sall1* gene, encoding a key microglial lineage-determining transcription factor, was strikingly absent from SAMs[18] (**Fig. 2b**).

Principal-component analysis (PCA) of the RNA-seq data showed tight clustering across replicates, indicating low contamination and high reproducibility (**Fig. 2d**). The absence of tyrosine hydroxylase (*Th*) expression in SAMs (**Supplementary Fig. 5d**) further excluded the possibility of contaminating cargo from neighboring cells, as *Th* was highly expressed in adjacent SNS neurons (**Fig. 1b**,**d**). PCA indicated that SAMs from fibers and ganglia were closely related, but both were distant from microglia and other macrophages (**Fig. 2d**). This was confirmed by phylogenetic analysis (**Fig. 2e**).

We hypothesized that the increased motility of SAMs (**Fig. 1c**) could indicate an activated, proinflammatory state. Therefore, we measured expression of a constellation of pro- and anti-inflammatory markers in SAMs by RNA-seq (**Fig. 2c**). Relative to other macrophage populations, SAMs highly expressed genes associated with macrophage activation, including *Cxcl2*, *Tnf*, *Socs3*, and *Il1a* (**Fig. 2c**), suggesting a constitutively proinflammatory steady state.

SAMs are phylogenetically distinct from other macrophages

Consistent with the PCA results (**Fig. 2d**), Pearson correlation analyses of transcript levels indicated differential expression patterns across SAMs, sATMs, vATMs, SpMs, and microglia (**Supplementary Fig. 6a**,**b**). Adipose tissue macrophages (sATMs and vATMs) showed similar expression landscapes ($R = 0.92$) that were distant from those of SAMs in fibers ($R = 0.63$ for sATMs and $R = 0.61$ for vATMs; **Supplementary Fig. 6b**). The expression landscapes of microglia and spleen macrophages were least correlated with other groups (**Supplementary Fig. 6b**).

Gene ontology analyses identified several biological processes associated with genes whose expression was enriched in SAMs relative to surrounding sATMs (**Supplementary Fig. 6c**). SAMs preferentially expressed genes involved in synaptic signaling, cell–cell adhesion, and neuron development (**Supplementary Fig. 6c**), suggesting that these cells fulfill an intrinsic role in local neuronal maintenance. Taken together, these data demonstrate divergent gene expression patterns in SAMs and ATMs, constituting within-tissue macrophage specialization.

SAMs import and degrade but do not synthesize NE

We next examined specific transcripts corresponding to the genes with divergent macrophage expression. The aforementioned populations of macrophages were sorted (**Fig. 2a** and **Supplementary Fig. 3**) for transcriptome analysis via low-input RNA-seq. Considering the gene ontology results (**Supplementary Fig. 6c**) and spatial proximity of SAMs to nerves (**Fig. 1**), we hypothesized that there would be differential expression of neurotransmitter receptors, transporters, or catalytic enzymes among these macrophage populations (**Fig. 2f**). In agreement with the Immunological Genome Project (ImmGen) database, we detected abundant expression of the *Adrb2* gene encoding β2 adrenergic receptor in all macrophage populations (**Fig. 2f**), which was confirmed by qRT–PCR (**Supplementary Fig. 6d**).

However, SAMs were the only population that expressed *Slc6a2*, the gene encoding the NE transporter (**Fig. 2f**). Similarly, *Maoa* was highly expressed in SAMs relative to the other macrophage types (**Fig. 2f**). Both results were validated by qRT–PCR (**Fig. 2g**,**h** and **Supplementary Table 1**). As SLC6A2 imports and MAOA degrades NE, we also tested for the presence of NE and detected it through enzyme-linked immunosorbent assay (ELISA) in sorted SAMs (**Fig. 2i** and **Supplementary Fig. 6e**). In agreement with our results, neither *Slc6a2* nor *Maoa* was substantially expressed in any macrophage population listed in the ImmGen database. Furthermore, we validated SLC6A2 and MAOA protein expression by immunofluorescence in SNS nerve fibers and SCG cryosections from *Cx3cr1*$^{GFP/+}$ mice (**Fig. 2j**,**k**). Representative photomicrographs show that GFP-expressing SAMs were double positive for membrane-bound SLC6A2 (**Fig. 2j**) and mitochondria-bound MAOA (**Fig. 2k**).

As SAMs, but not the other macrophage types assessed, possess the molecular machinery for import (**Fig. 2f**,**g**,**j**) and degradation (**Fig. 2f**,**h**,**k**) of NE, as well as considerably more NE than other macrophages (**Fig. 2i** and **Supplementary Fig. 6e**), we tested the possibility that SAMs synthesize NE. Through qRT–PCR of sorted SAMs, we did not detect expression of *Th*, which encodes an enzyme necessary for NE biosynthesis (**Supplementary Fig. 5d**). Taken together, these results indicate that SAMs have the molecular machinery for importing and degrading NE but not for biosynthesis of it.

To explore the responsiveness of SAMs to NE, we optogenetically stimulated sympathetic neurons in SCG cultures from mice produced by crossing *Th-cre* mice with *loxP*-STOP-*loxP* (LSL)-*ChR2-YFP* mice[1], which allowed us to visualize sympathetic neuron–macrophage interactions *ex vivo* (**Fig. 3a**,**b**). After optogenetic stimulation, we measured the NE content of sorted CD45$^+$F4/80$^+$ cells. SAMs from channelrhodopsin-2 (ChR2)$^+$ cultures exhibited significantly higher NE levels (**Fig. 3c**) that were proportional to NE availability in the culture medium (**Fig. 3d**). NE release by ChR2$^+$ neurons was significantly higher than that from ChR2$^-$ neurons (**Fig. 3d**). Uptake of NE by SAMs was prevented by pharmacological blockade of SLC6A2 using the pharmacological inhibitor nisoxetine, despite the significant increase of NE in the culture medium (**Fig. 3c**,**d**).

To validate our optogenetic findings with a physiologically relevant stimulus, we activated SNS explants with acetylcholine (ACh), which is presynaptically released from spinal cord neurons to innervate SCGs.

ACh-treated CD45$^+$F4/80$^+$ cells sorted from SCG explants contained significantly higher levels of NE than vehicle-treated controls (**Fig. 3e**). We validated that blockade of the NE importer SLC6A2 by nisoxetine prevented NE accumulation in SAMs (**Fig. 3e**). Co-incubation with ACh and nisoxetine further abolished NE uptake (**Fig. 3e**), despite the substantial increase in extracellular NE levels in the culture medium (**Fig. 3f**). These results, along with the negligible expression levels of *Chrna1* (*AChR*) in SAMs (**Supplementary Fig. 7a**; also validated by qRT–PCR in **Supplementary Fig. 7b**), exclude a role for acetylcholine receptors (AChRs) in mediating NE import.

Next, we assessed the effect of blocking MAOA on NE content in CD45$^+$F4/80$^+$ cells (**Fig. 3e**). Treatment with the MAOA inhibitor

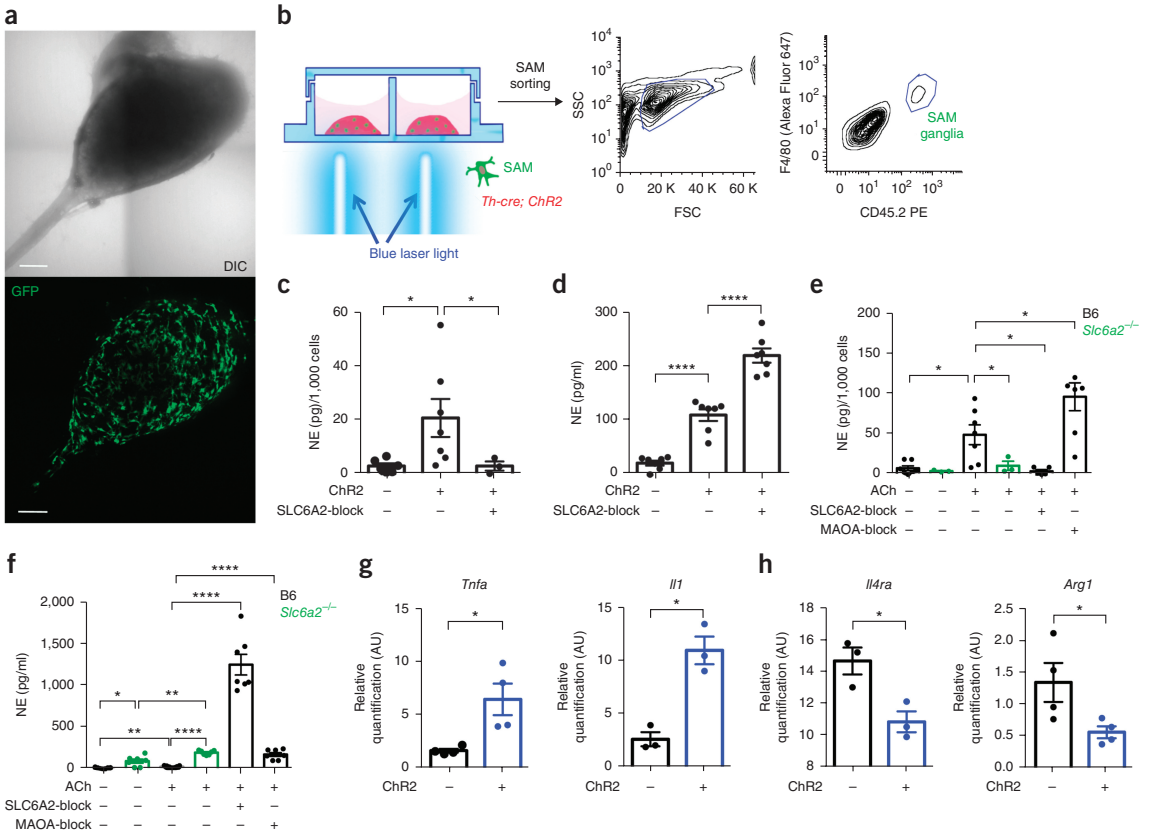

Figure 3 SAMs import and metabolize norepinephrine via SLC6A2 and MAOA, respectively, to regulate extracellular norepinephrine availability. (**a**) Representative images of *ex vivo* SCG explant cultures. Top, the area of the sympathetic ganglia is represented using the reflected-light differential interference contrast (DIC) channel. Bottom, *Cx3cr1*-GFP$^+$ cells in the same explant culture (GFP channel). Images are representative of 20 similar experiments. Scale bar, 100 µm. (**b**) Schematic representation of optogenetic activation of sympathetic SCG explant culture (left) followed by CD45.2 (PE)$^+$F4/80 (Alexa Fluor 647)$^+$ cell sorting (right). FSC, forward scatter; SSC, side scatter. (**c**) NE content in CD45.2$^+$F4/80$^+$ cells isolated from SCG explant cultures from *Th-cre*; LSL-*ChR2-YFP* and LSL-*ChR2-YFP* mice after optogenetic activation. Each data point represents tissues pooled from six mice. n = 3–7 experiments. The following numbers of cells were used in NE assays (run in duplicate): 189 ± 30 from *Th-cre*; LSL-*ChR2-YFP* SCG (n = 7), 126 ± 21 from LSL-*ChR2-YFP* SCG (n = 6), and 159 ± 19 from *Th-cre*; LSL-*ChR2-YFP* SCG stimulated with SLC6A2 blocker (n = 3). (**d**) *Ex vivo* NE release upon optogenetic stimulation of SCG explants isolated from *Th-cre*; LSL-*ChR2-YFP* and LSL-*ChR2-YFP* mice. Each data point represents medium collected from one explant culture. n = 7 per group. (**e**) NE content in CD45.2$^+$F4/80$^+$ cells isolated from the SCG of either B6 or *Slc6a2*$^{-/-}$ mice and then incubated with ACh, ACh and SLC6A2 blocker, ACh and MAOA blocker, or culture medium. Each data point represents tissues pooled from six mice. n = 3–7 experiments. The following numbers of cells were used in NE assays (run in duplicate): 364 ± 128 from B6 SCG (n = 7), 238 ± 55 from *Slc6a2*$^{-/-}$ SCG (n = 3), 216 ± 58 from B6 SCG incubated with ACh (n = 7), 201 ± 63 from *Slc6a2*$^{-/-}$ SCG incubated with ACh (n = 3), 196 ± 18 from B6 SCG incubated with ACh and SLC6A2 blocker (n = 5), and 133 ± 11 from B6 SCG incubated with ACh and MAOA blocker (n = 7). (**f**) *Ex vivo* NE release from the SCG of either B6 or *Slc6a2*$^{-/-}$ mice after incubation with ACh, ACh and SLC6A2 blocker, ACh and MAOA blocker, or culture medium. Each data point represents medium collected from one explant culture. n = 7 per group. (**g**) Expression of mRNA as determined by qRT–PCR relative to *Gapdh* expression for proinflammatory genes (*Tnfa* and *Il1*) in CD45.2$^+$F4/80$^+$ cells isolated from SCG explant cultures from *Th-cre*; LSL-*ChR2-YFP* (blue) and LSL-*ChR2-YFP* (black) mice. Prior to cell sorting, SCG explants were optogenetically stimulated. n = 3–4 experiments (for *Tnfa*, n = 4, P = 0.0467; for *Il1*, n = 3, P = 0.011). (**h**) Expression of mRNA as determined by qRT–PCR relative to *Gapdh* expression for anti-inflammatory genes (*Il4ra* and *Arg1*) in CD45.2$^+$F4/80$^+$ cells isolated from SCG explant cultures from *Th-cre*; LSL-*ChR2-YFP* (blue) and LSL-*ChR2-YFP* (black) mice. Prior to cell sorting, SCG explants were optogenetically stimulated. n = 3–4 experiments (for *Il4ra*, n = 3, P = 0.0257; for *Arg1*, n = 4, P = 0.0497). Data in **c**–**h** were analyzed by two-tailed unpaired Student's t-test and are shown as average ± s.e.m. *P < 0.05, **P < 0.01, ****P < 0.0001.

clorgyline was sufficient to nearly double intracellular NE levels in SAMs (**Fig. 3e**). In agreement with this finding, clorgyline increased NE levels in the medium (**Fig. 3f**), to which neuronal MAOA expression may also contribute. Genetic ablation of *Slc6a2* (in SCG cultures isolated from *Slc6a2*$^{-/-}$ mice) prevented NE uptake by SAMs regardless of NE availability in the culture medium (**Fig. 3e,f**). Finally, ATMs cultured *in vitro* with NE did not accumulate intracellular NE (**Supplementary Fig. 7c**), further demonstrating the specificity of NE uptake by SAMs. Altogether, our results indicate that *Slc6a2* is required for NE accumulation in SAMs.

We further probed whether the availability of NE, which can be manipulated *in vivo* by optogenetic activation of SNS neurons, changes the inflammatory profile of SAMs. We found that optogenetic stimulation of SCG explants correlated with an increase in proinflammatory gene expression, as measured by changes in expression of *Tnf* (*Tnfa*) and *Il1a* (*Il1*) (**Fig. 3g**), and a decrease in the expression of anti-inflammatory genes, as measured by changes in expression of *Il4r* (*Il4ra*) and *Arg1* (**Fig. 3h**).

SAMs are recruited and activated in obesity

We next used two mouse models to characterize the effect of obesity on tissue-specific functions of SAMs. In total, we employed four experimental groups: HFD, *Lep* (*Leptin*)-deficient (*ob*/*ob*), normal diet (ND), and 24-h-fasted ND mice. Flow cytometric analysis demonstrated that both obesity models (HFD and *ob*/*ob*) exhibited significantly higher percentages of SAMs than lean mice (ND) (**Fig. 4a** and **Supplementary Fig. 8a**). Furthermore, the acute metabolic challenge of fasting did not result in upregulation of SAMs, suggesting an obesity-specific causation of elevated macrophage content in sympathetic fibers (**Fig. 4a** and **Supplementary Fig. 8a**). Within the F4/80^{+}

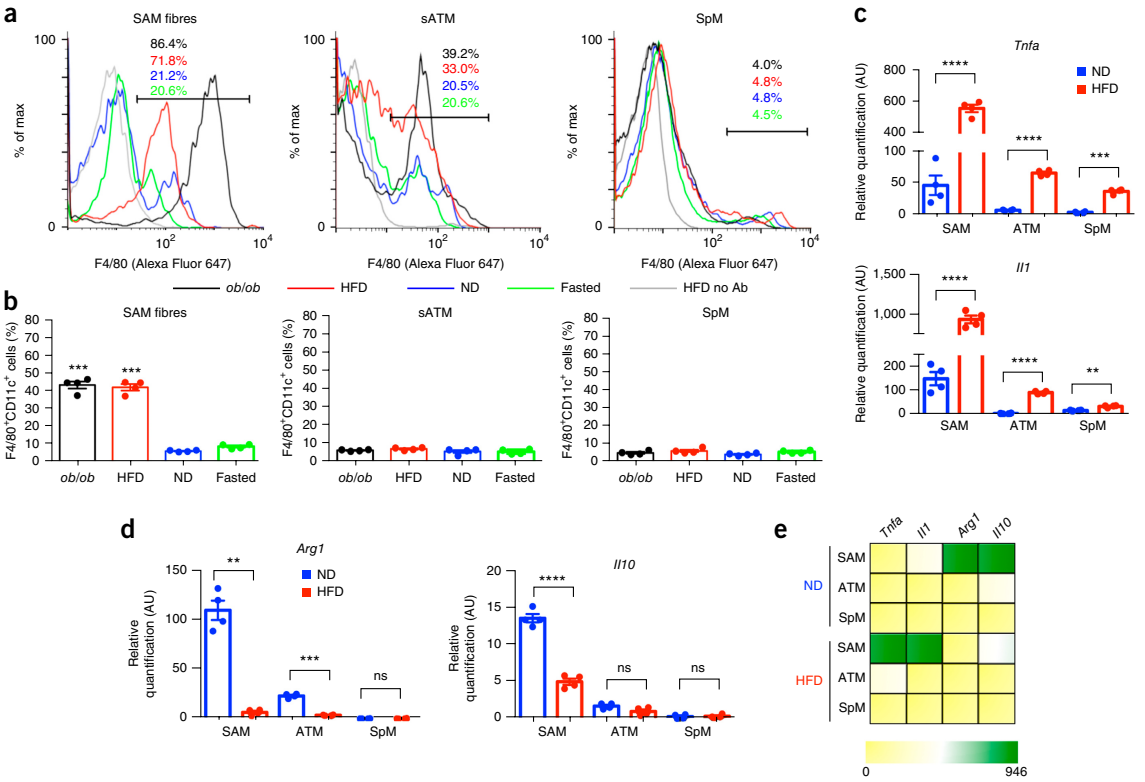

Figure 4 Obesity-induced accumulation of SAMs. (**a**) Representative histograms showing percentages of F4/80 (Alexa Fluor 647)$^{+}$ cells in sympathetic nerve fibers (left), subcutaneous adipose tissue (middle), and spleen (right) in mice that were genetically obese (*ob*/*ob*; black), obese due to HFD (red), ND fed (blue), or fasted for 24 h (green). CD45.2 (PE)$^{+}$ cells were gated. Histograms are representative of four independent experiments. HFD no Ab, cells without antibody staining harvested from mice fed a HFD. Black lines indicate the region defining F4/80^{+} cells. (**b**) Percentages of F4/80 (Alexa Fluor 647)$^{+}$CD11c (FITC)$^{+}$ cells in sympathetic nerve fibers (left), subcutaneous adipose tissue (middle), and spleen (right) in mice that were genetically obese (*ob*/*ob*; black), obese due to HFD (red), ND fed (blue), or fasted for 24 h (green). CD45.2 (PE)$^{+}$ cells were gated. $n = 4$ experiments per group. Each data point represents one experiment. (**c**) Expression of mRNA as determined by qRT–PCR relative to *Gapdh* expression for proinflammatory genes (*Tnfa* and *Il1*) in CD45.2^{+}F4/80^{+} cells in sympathetic nerve fibers (SAMs), subcutaneous adipose tissue (ATMs), and spleen (SpMs) isolated from mice that were fed either ND (blue) or HFD (red). $n = 4$ experiments per group. Each data point represents tissues pooled from ten mice. (**d**) Expression of mRNA as determined by qRT–PCR relative to *Gapdh* expression for anti-inflammatory genes (*Arg1* and *Il10*) in CD45.2^{+}F4/80^{+} cells including SAMs, ATMs, and SpMs isolated from mice that were fed either ND (blue) or HFD (red). $n = 4$ experiments per group. Each data point represents tissues pooled from ten mice. (**e**) Heat map showing the expression of pro- and anti-inflammatory genes as determined by the qRT–PCR analyses in **c** and **d**. Data in **b** were analyzed by one-way ANOVA followed by Bonferroni multiple-comparisons test with ND as the control group. Data in **c** and **d** were analyzed by two-tailed unpaired Student's *t*-test. Data are shown as average ± s.e.m. $^{**}P < 0.01$, $^{***}P < 0.001$, $^{****}P < 0.0001$; ns, not significant.

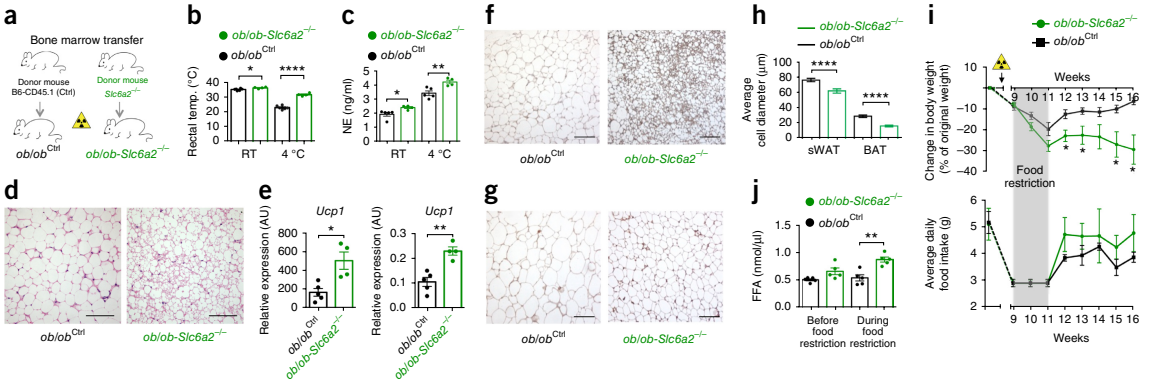

Figure 5 Loss of *Slc6a2* function in SAMs rescues the thermogenic capacity of *ob*/*ob* mice. (**a**) Schematic representation of bone marrow transplant from either *Slc6a2*$^{-/-}$ or control B6 (CD45.1) mice into genetically obese *ob*/*ob* mice (*ob*/*ob-Slc6a2*$^{-/-}$ and *ob*/*ob*^{Ctrl} chimeras, respectively). (**b**) Rectal temperature of *ob*/*ob*^{Ctrl} (black) and *ob*/*ob-Slc6a2*$^{-/-}$ (green) chimeras was measured at room temperature (RT) and after 2 h of cold challenge (4 °C). Each data point represents one mouse. $n = 4$ *ob*/*ob-Slc6a2*$^{-/-}$ mice and $n = 6$ *ob*/*ob*^{Ctrl} mice. $^{*}P = 0.025$, $^{****}P < 0.0001$. (**c**) Serum levels of NE in *ob*/*ob*^{Ctrl} (black) and *ob*/*ob-Slc6a2*$^{-/-}$ (green) chimeras were measured at room temperature and after 2 h of cold exposure (4 °C). Each data point represents one mouse. $n = 4$ mice per group for *ob*/*ob-Slc6a2*$^{-/-}$ mice and $n = 5$ mice per group for *ob*/*ob*^{Ctrl} mice. $^{*}P = 0.022$, $^{**}P = 0.0072$. (**d**) Optical micrographs of BAT removed from *ob*/*ob* chimeras following 2 h of cold challenge (4 °C) and stained with H&E. Left, BAT from an *ob*/*ob*^{Ctrl} chimera. Right, BAT from an *ob*/*ob-Slc6a2*$^{-/-}$ chimera. Images are representative of fat organs collected from four *ob*/*ob*^{Ctrl} and six *ob*/*ob-Slc6a2*$^{-/-}$ mice. (**e**) Expression of mRNA for *Ucp1* as determined by qRT–PCR relative to *Gapdh* expression in BAT (left) and sWAT (right) dissected after 2 h of cold challenge (4 °C). Each data point represents one mouse. $n = 4$ *ob*/*ob-Slc6a2*$^{-/-}$ mice (green) and $n = 5$ *ob*/*ob*^{Ctrl} mice (black). $^{*}P = 0.0269$, $^{**}P = 0.0015$. (**f**) Optical micrographs of BAT dissected from *ob*/*ob*^{Ctrl} (left) and *ob*/*ob-Slc6a2*$^{-/-}$ (right) chimeras following 2 h of cold challenge (4 °C) and stained with anti-UCP1 antibody. Images are representative of fat organs collected from four *ob*/*ob*^{Ctrl} and six *ob*/*ob-Slc6a2*$^{-/-}$ mice. (**g**) Optical micrographs of sWAT dissected from *ob*/*ob*^{Ctrl} (left) and *ob*/*ob-Slc6a2*$^{-/-}$ mice (right) following 2 h of cold challenge (4 °C) and stained with anti-UCP1 antibody. Images are representative of fat organs collected from four *ob*/*ob*^{Ctrl} and six *ob*/*ob-Slc6a2*$^{-/-}$ mice. (**h**) Average adipocyte diameter quantified from optical micrographs of sWAT and BAT from *ob*/*ob* chimeras following 2 h of cold challenge (4 °C). Measurements are representative of four (*ob*/*ob-Slc6a2*$^{-/-}$) and six (*ob*/*ob*^{Ctrl}) independent micrographs. 18–34 measurements were obtained per micrograph. $n = 169$ cells for *ob*/*ob*^{Ctrl} sWAT, $n = 120$ cells for *ob*/*ob-Slc6a2*$^{-/-}$ sWAT, $n = 180$ cells for *ob*/*ob*^{Ctrl} BAT, $n = 120$ cells for *ob*/*ob-Slc6a2*$^{-/-}$ BAT. $^{****}P < 0.0001$. (**i**) Body weight change (top) and daily food intake (bottom) of *ob*/*ob*^{Ctrl} ($n = 4$ mice) and *ob*/*ob-Slc6a2*$^{-/-}$ ($n = 6$ mice) chimeras monitored for 7 weeks following 2 weeks of food intake normalization (0.06 g of food per 1 g of body weight per day; gray shading) that started 9 weeks after bone marrow transplant. The yellow triangle indicates when irradiation was performed. $^{*}P < 0.05$. (**j**) Blood plasma nonesterified (free) fatty acid (FFA) concentration in *ob*/*ob*^{Ctrl} and *ob*/*ob-Slc6a2*$^{-/-}$ chimeras measured 8 weeks after bone marrow transplant before and while mice were under a regimen of 0.06 g of food per 1 g of body weight per day. $n = 5$ mice per group. $^{**}P = 0.0022$. Data in **b**, **c**, **e**, **h**, and **j** were analyzed by two-tailed unpaired Student's *t*-test and in **i** by multiple *t*-tests (one Student's *t*-test per row with correction for multiple comparisons using the Holm–Sidak method). Data are shown as average ± s.e.m. Scale bars in **d**, **f**, and **g**, 100 µm.

SAM fraction from HFD and *ob*/*ob* mice, we noted a high frequency of CD11c^{+} cells (**Fig. 4b**), which are hallmarks of inflammation and insulin resistance in human obesity[19]. In contrast to SAM accumulation in SNS nerve fibers dissected from WAT, SAMs did not accumulate in SCG, which innervates neck structures such as salivary glands (**Supplementary Fig. 8b**).

The differential distribution of macrophages under conditions of obesity suggests that cytokine levels are also sensitive to obesity. Comparison of the anti- and proinflammatory gene profiles of SAMs, ATMs, and SpMs (**Fig. 4c–e**) revealed that obesity correlated with higher levels of proinflammatory genes (i.e., *Tnfa* or *Il1*; **Fig. 4c**,**e**) and lower levels of anti-inflammatory genes (i.e., *Arg1* or *Il10*; **Fig. 4d**,**e**).

To determine whether local proliferation contributes to SAM accumulation, we measured the proliferation marker Ki-67 in SAMs by flow cytometry (**Supplementary Fig. 8c**,**d**). We observed that obesity (in the HFD and *ob*/*ob* models) did not substantially increase Ki-67^{+} SAM percentage, whereas (in accordance with previous reports[20]) obesity increased Ki-67^{+} ATMs from sWAT (**Supplementary Fig. 8d**).

Slc6a2 deletion in SAMs rescues obesity

We probed how ablating *Slc6a2* in SAMs affects obesity-associated pathology. We considered a Cre–*loxP* approach, but the established macrophage Cre lines (*Cx3cr1-cre*[21,22] and *LyzM-cre*[23]) would not allow for specificity of ablation to SAMs. We thus took advantage of the cell-type specificity of *Slc6a2* expression, which is high in SAMs but negligible in other macrophage and hematopoietic cell populations (**Fig. 2b**,**g** and ImmGen[24]). We validated that there was not another population of hematopoietic origin expressing *Slc6a2* aside from SAMs; a rare population of CD45^{+}F4/80^{-} cells was present in SCG (**Supplementary Fig. 9a**) but did not express SLC6A2 (**Supplementary Fig. 9b**). SAM-specific genetic ablation of *Slc6a2* was achieved through bone marrow transfer from *Slc6a2*$^{-/-}$ mice[25] into genetically obese *ob*/*ob* recipients (*ob*/*ob-Slc6a2*$^{-/-}$; **Fig. 5a**). Control chimeras consisted of *ob*/*ob* mice (*ob*/*ob*^{Ctrl}) that received a bone marrow transfer from B6 CD45.1 mice. Chimeras recovered for 9 weeks following transplant to allow irradiation-induced inflammation to subside.

As cold temperature is a robust driver of SNS activity, we challenged mice for 2 h at 4 °C and observed that *ob*/*ob-Slc6a2*$^{-/-}$ chimeras displayed superior capacity for maintaining body temperature as compared to control *ob*/*ob*^{Ctrl} chimeras (**Fig. 5b**). These thermogenic effects were accompanied by significant upregulation of NE levels in serum (**Fig. 5c**), rescue of BAT morphology (**Fig. 5d**), and browning of white fat, as measured by *Ucp1* mRNA and uncoupling protein 1 (UCP1) levels (**Fig. 5e–g**).

Transplant of bone marrow from *Slc6a2*$^{-/-}$ mice into *ob*/*ob* mice prevented obesity-induced hypertrophy of both BAT and WAT adipocytes (**Fig. 5h**) but did not affect total body weight (**Fig. 5i**). Because food-restriction challenge drives SNS activity and mobilizes lipid stores from adipose tissue, we normalized the daily food intake of the *ob*/*ob* chimeras for 2 weeks (**Fig. 5i**,**j**). After a dieting challenge, *ob*/*ob*-*Slc6a2*$^{-/-}$ mice lost nearly 30% of their body weight relative to their original body weight, after which their body weight was stable for up to 16 weeks, even after they were given *ad libitum* access to food (**Fig. 5i**). We also found that *ob*/*ob*-*Slc6a2*$^{-/-}$ mice exhibited higher lipid mobilization during food restriction relative to controls (**Fig. 5j**).

We analyzed wild-type B6 chimeras reconstituted with bone marrow from *Slc6a2*$^{-/-}$ mice relative to CD45.1 controls (B6-*Slc6a2*$^{-/-}$ and B6^{Ctrl} chimeras, respectively) (**Supplementary Fig. 9c**). SAMs from B6-*Slc6a2*$^{-/-}$ chimeras did not accumulate NE (**Supplementary Fig. 9d**). In accordance with the results from *ob*/*ob* chimeras (**Fig. 5**), B6-*Slc6a2*$^{-/-}$ chimeras also exhibited increased serum levels of NE, thermogenesis, and lipolysis, as well as marked weight loss, relative to control mice (**Supplementary Fig. 9e–i**). Upon challenge with HFD, we observed weight-gain prevention in B6-*Slc6a2*$^{-/-}$ but not B6^{Ctrl} mice (**Supplementary Fig. 9g**). These results indicate a notable anti-obesity effect of SAM-specific *Slc6a2* ablation.

SAMs are in BAT and act as a NE sink

In light of the enhanced thermogenic capacity of *ob*/*ob*-*Slc6a2*$^{-/-}$ chimeras, we questioned whether SAMs are present in BAT (**Supplementary Fig. 10**). BAT did contain *Cx3cr1*-GFP^{+} cells (in accordance with a previous report[19]) that exhibited a morphology intermediate to those of SAMs (multiple pseudopodia) and ATMs (round) (**Supplementary Fig. 10a** as compared to **Fig. 1c**). Some of these cells appeared to make close contacts with thin TH^{+} axons (**Supplementary Fig. 10a**). Because TH^{+} nerve fibers in BAT are too delicate for dissection, we sorted macrophages from whole BAT for qRT–PCR analysis. *Slc6a2* and *Maoa* were expressed in BAT macrophages, although at lower levels than in SAMs isolated from dissected SNS nerve bundles in sWAT or SCG (**Supplementary Fig. 10b**,**c**). We also detected the presence of NE in BAT macrophages, although at lower levels than SAMs (**Supplementary Fig. 10d**). The lower levels of *Slc6a2*, *Maoa*, and NE content may reflect a dilution of BAT SAMs by BAT ATMs, as mixed (as opposed to isolated) populations were analyzed.

Finally, we used *LyzM-cre*; *Csf1r*-LSL-*DTR* mice with conditional expression of diphtheria toxin receptor (DTR) on macrophages to test whether macrophages serve as a sink for NE. After validating ablation of macrophages (**Supplementary Fig. 11a**,**b**), we observed a significant increase of NE in sWAT of *LyzM-cre*; *Csf1r*-LSL-*DTR* mice relative to *Csf1r*-LSL-*DTR* controls (**Supplementary Fig. 11c**). Note that, owing to constant hematopoietic input, it is practically impossible to completely deplete macrophages. This limitation notwithstanding, these results are consistent with a model in which macrophages act as a sink for NE.

Human sympathetic ganglia also contain NE-degrading SAMs

Finally, we asked whether SAMs exist in humans. We obtained nine human excisional biopsies of SNS or thoracolumbar ganglia that were collected during sympathectomy and/or gangliotomy. We stained tissue sections with H&E (**Fig. 6a**,**b**) or an antibody against CD68, a human macrophage marker, and identified the presence of macrophages in SNS tissues (**Fig. 6c**,**d** and **Supplementary Fig. 12**).

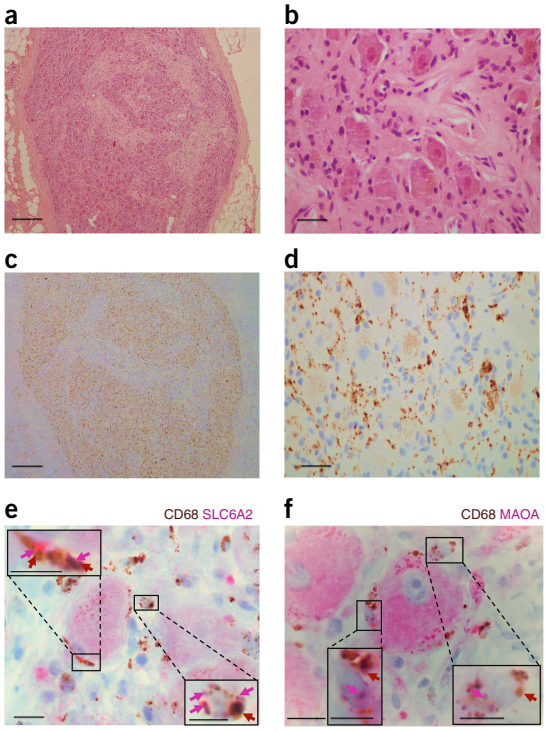

Figure 6 SAMs in the human sympathetic nervous system. (**a**,**b**) Optical micrograph of human ganglia from the thoracolumbar region stained with H&E (**a**) and a higher-magnification image (**b**). (**c**,**d**) Optical micrograph of human ganglia from the thoracolumbar region stained with an antibody against CD68 (**c**) and a higher-magnification image (**d**). (**e**) Optical micrograph of human ganglia from the thoracolumbar region stained with antibodies against CD68 and SLC6A2. Red arrows indicate CD68^{+}SLC6A2^{+} regions. Pink arrows indicate SLC6A2^{+} regions. (**f**) Optical micrographs of human ganglia from the thoracolumbar region stained with antibodies against CD68 and MAOA. Red arrows indicate CD68^{+}MAOA^{+} regions. Pink arrows indicate MAOA^{+} regions. Boxed regions in **e** and **f** represent higher-magnification images of the main micrographs. Scale bars: 1 mm (**a**,**c**), 100 µm (**b**,**d**), and 50 µm (**e**,**f**); for boxed regions, 25 µm. Images in **a**–**f** are representative of nine different human samples.

We next determined whether SAMs in human sympathetic ganglia also contain the machinery for uptake and degradation of NE (**Fig. 6e**,**f** and **Supplementary Fig. 12**). The CD68 macrophage marker colocalized with staining for SLC6A2 (**Fig. 6e** and **Supplementary Fig. 12a**) and MAOA (**Fig. 6f** and **Supplementary Fig. 12b**). Both SLC6A2^{+} and MAOA^{+} neurons existed, but the background levels were low relative to control human gut-associated lymphoid tissue (GALT) samples that also contained CD68^{+} macrophages (**Supplementary Fig. 12c**,**d**).

DISCUSSION

SAMs are a previously undescribed population of SNS-resident macrophages that import and degrade NE. To fulfill their function, SAMs express a dedicated molecular machinery that is, as best we can tell, absent from neighboring macrophages and other known macrophage populations (shown by our data and the ImmGen database). In SAMs, NE is imported by SLC6A2 and degraded by MAOA. This is a specialized

molecular mechanism for NE uptake with a role that is not fulfilled by the canonical phagocytic mechanisms generally present in macrophages[26].

Unlike most other neurons, which exclusively release neurotransmitter at a terminal synapse, SNS neurons also release NE via varicosities distributed along axons that can extend for tens of centimeters[27]. SAMs possibly serve to prevent NE spillover into the bloodstream or neighboring tissues when SNS activity is high. Indeed, we demonstrate that, when SNS neurons are optogenetically activated, SAMs import increased levels of NE and become more polarized toward a proinflammatory phenotype. In this regard, NE can be considered a noxious stimulus that must be locally delivered in a controlled manner to a target tissue. Chronic and excessive systemic NE in serum, such as the levels present under chronic stress conditions or in medullary adrenal tumors, leads to hypertension and cardiopathy due to direct action in cardiovascular tissues[28].

The activated polarization state of SAMs is consistent with a model in which these cells play a tissue-protective role by acting as a sentinel and scavenger of surplus levels of an endogenous neurotransmitter (i.e., NE) that, if released in excess from varicosities, could potentially be harmful. Tissue-protective immune cells have been documented in the brain and other, non-neuronal systems[29–34]. For instance, muscularis-resident macrophages in the gut induce rapid tissue-protective responses to potentially pathogenic insults via β2 adrenergic receptor signaling[35]. This mechanism and our study indicate specialization of macrophage populations for fulfillment of tissue-specific tasks in response to neuronal cues. Divergent gene expression landscapes across populations of resident macrophages isolated from different tissues support the idea of local macrophage adaptations[22,36,37]. In this study, we use transcriptional data to molecularly characterize SAMs alongside other macrophage populations. Our results suggest that macrophages associated with the SNS have specialized molecular programs, whose exploration might give further insight into mechanisms underlying SNS macrophage–neuron communication.

Although SAMs express common microglial genes and reside in proximity to nerve cells, SAM pseudopodia are morphologically distinct from the finely branching ramifications of resting microglia[38,39]. Moreover, SAMs are seemingly of hematopoietic origin, as suggested by our bone marrow chimera studies and their high expression of CD45 and macrophage markers. Future tracing studies are necessary to definitively determine SAM origin. To our knowledge, no reports exist on NE uptake by microglia, and we verified that the machinery for NE uptake is not expressed in these cells. In this regard, only one study has reported that NE can trigger microglia to import and degrade amyloid but not NE itself[40]. Neurotransmitter uptake has primarily been studied in astroglia, which are CX3CR1$^-$ (ref. 41).

Chimeric models require irradiation that generates inflammation. However, if given adequate recovery time (8 weeks), recruited macrophages dissipate from the brain, as represented in our chimeras by minimal residual *Cx3cr1*-GFP$^+$ microglia (0.06%). SAMs persist at levels that greatly surpass background irradiation-induced macrophage recruitment, and regenerated SAMs are seemingly identical to those in non-irradiated mice.

We show low expression of several astroglial markers in SAMs, raising the possibility of a hybrid peripheral cell type that unites some of the features of macrophages and glia. Alternatively, genes expressed in common by glial cells and SAMs may be attributable to the proximity of SAMs to neuron-derived signals, analogous to the observation that microglia, astrocytes, and neurons share the expression of certain central nervous system–specific genes[7,42]. An alternative model is that SAMs share the lineage of satellite glial cells (SGCs), which are derived from embryonic neural crest[11] and also express canonical astroglial markers[43]. However, SGC import or degradation of NE has not been reported[44].

Our study may fill a gap in the literature by demonstrating a cellular and molecular mechanism alternative to the proposed existence of NE-producing macrophages in WAT[3]. In this regard, our findings are consistent with other reports[4–6], as we did not detect the NE biosynthetic machinery in SAMs nor in ATMs. The identification of SAMs sheds new light on this recent controversy by documenting how a particular population of macrophages can contain NE in the absence of its biosynthesis. We also document that BAT macrophages contain similar molecular machinery to that in SAMs for NE uptake, extending and validating the findings of our colleagues[21]. SAMs may play a tissue-protective role through regulation of regional NE levels by serving as a local sink that prevents the dangerous effects of chronically increased levels of systemic NE.

In sharp contrast to the anti-inflammatory state of intestinal nerve–associated *Cx3cr1*-GFP$^+$ macrophages[35], SAMs exhibit a proinflammatory profile at steady state. This could be due to the constitutive presence of a danger signal—namely, NE. Whether this polarization is caused by NE import or by adrenergic signaling remains to be established. In this regard, polarization of enteric-associated macrophages has been linked to activation of β2 adrenergic receptor, which is also expressed in SAMs[35]. Regardless, our core message is relevant: SAMs are proinflammatory and act as a NE sink, and blocking NE uptake has an antiobesity effect. Our results support a model whereby SAMs pathologically accumulate in the SNS nerves of obese subjects in an organ-specific manner, thus explaining why we detect SAM accumulation in the WAT-associated SNS but not in SCG, which innervates salivary glands and other neck structures. The NE-scavenging role of SAMs may have become evolutionarily maladaptive, as in the past obesity was not a common physiological stress to which humans had to adapt. In modern times, the prevalence of overnutrition has created a need for increased lipolysis-inducing NE signaling to maintain fat stores, which is obstructed by the 'original' function of SAMs to limit NE levels.

Reduced NE availability in the adipose tissue is linked to blunted lipolysis and obesity. Very recently, our colleagues have shown that ATMs degrade NE during aging[45]. Whether this observation is also associated with the accumulation of SAMs in fat, as we observed in the two mouse models of obesity, remains to be established.

Our results demonstrate that SAM-specific *Slc6a2* ablation rescues BAT and adaptive thermogenesis in obese *ob*/*ob* mice, which in turn leads to sustained weight loss and lipid mobilization. We determine that blocking NE import into SAMs mitigates the recidivism of obesity that is typical after dieting. Overall, our results identify SAMs as a potential new molecular and cellular target for obesity therapy.

METHODS

Methods, including statements of data availability and any associated accession codes and references, are available in the online version of the paper.

Note: Any Supplementary Information and Source Data files are available in the online version of the paper.

ACKNOWLEDGMENTS

We would like to thank the Unit for Imaging and Cytometry at the Instituto Gulbenkian de Ciência (IGC) for assistance with flow cytometry, cell sorting, and multiphoton microscopy. We also want to thank the Antibody Service at the IGC

for the antibodies produced in house and the Histopathology facility at the IGC for tissue processing and histological assessment. This work was supported by the Fundação para a Ciência e Tecnologia (FCT), the European Molecular Biology Organization (EMBO), the Human Frontier Science Program (HFSP), Maratona da Saúde, and the US National Institutes of Health (NIH). R.M.P. was supported by FCT (SFRH/BD/88454/2012), J.S.S. was supported by the American Heart Association (16PRE30980030) and a training grant (T32DK007541), B.A.A. was supported by Conselho Nacional de Desenvolvimento Científico e Tecnológico (CNPq), and N.M.-S. was supported by Xunta de Galicia (ED481B 2016/168-0). We thank M. Aouadi for helpful discussions.

AUTHOR CONTRIBUTIONS

A.I.D. conceptualized the study. R.M.P. performed two-photon and confocal microscopy. E.S. and R.M.P. performed flow cytometry. J.S.S. and R.M.P. performed low-input RNA-seq. V.M.L., J.S.S., and R.M.P. analyzed the RNA-seq data. M.I., A.L.S., S.A., and E.T. performed electron microscopy. E.S., R.M.P., N.M.S., I. Mahú, B.A.A., and C.M.L. performed functional tests. N.K., I. Morris, R.M., and V.G. performed related mouse husbandry and genotyping. F.T. and M.V. processed human ganglia. M.K.H. provided the *Slc6a2*$^{-/-}$ mice. N.J.S. developed the low-input RNA-seq protocols. A.I.D., C.K.G., and R.M.P. wrote the original draft of the manuscript. A.I.D., C.K.G., R.M.P., and C.M.L. reviewed and edited the final version of the manuscript.

COMPETING FINANCIAL INTRESTS

The authors declare no competing financial interests.

1. Zeng, W. *et al.* Sympathetic neuro-adipose connections mediate leptin-driven lipolysis. *Cell* **163**, 84–94 (2015).
2. Mathis, D. Immunological goings-on in visceral adipose tissue. *Cell Metab.* **17**, 851–859 (2013).
3. Nguyen, K.D. *et al.* Alternatively activated macrophages produce catecholamines to sustain adaptive thermogenesis. *Nature* **480**, 104–108 (2011).
4. Fischer, K. *et al.* Alternatively activated macrophages do not synthesize catecholamines or contribute to adipose tissue adaptive thermogenesis. *Nat. Med.* **23**, 623–630 (2017).
5. Spadaro, O. *et al.* IGF1 shapes macrophage activation in response to immunometabolic challenge. *Cell Rep.* **19**, 225–234 (2017).
6. Reitman, M.L. How does fat transition from white to beige? *Cell Metab.* **26**, 14–16 (2017).
7. Gosselin, D. *et al.* Environment drives selection and function of enhancers controlling tissue-specific macrophage identities. *Cell* **159**, 1327–1340 (2014).
8. Anlauf, E. & Derouiche, A. Glutamine synthetase as an astrocytic marker: its cell type and vesicle localization. *Front. Endocrinol. (Lausanne)* **4**, 144 (2013).
9. Bignami, A., Eng, L.F., Dahl, D. & Uyeda, C.T. Localization of the glial fibrillary acidic protein in astrocytes by immunofluorescence. *Brain Res.* **43**, 429–435 (1972).
10. Chaudhry, F.A. *et al.* Glutamate transporters in glial plasma membranes: highly differentiated localizations revealed by quantitative ultrastructural immunocytochemistry. *Neuron* **15**, 711–720 (1995).
11. Jessen, K.R. & Mirsky, R. The origin and development of glial cells in peripheral nerves. *Nat. Rev. Neurosci.* **6**, 671–682 (2005).
12. Ludwin, S.K., Kosek, J.C. & Eng, L.F. The topographical distribution of S-100 and GFA proteins in the adult rat brain: an immunohistochemical study using horseradish peroxidase–labelled antibodies. *J. Comp. Neurol.* **165**, 197–207 (1976).
13. Mearow, K.M., Mill, J.F. & Vitkovic, L. The ontogeny and localization of glutamine synthetase gene expression in rat brain. *Brain Res. Mol. Brain Res.* **6**, 223–232 (1989).
14. Raff, M.C. *et al.* Galactocerebroside is a specific cell-surface antigenic marker for oligodendrocytes in culture. *Nature* **274**, 813–816 (1978).
15. Regan, M.R. *et al.* Variations in promoter activity reveal a differential expression and physiology of glutamate transporters by glia in the developing and mature CNS. *J. Neurosci.* **27**, 6607–6619 (2007).
16. Rusnakova, V. *et al.* Heterogeneity of astrocytes: from development to injury—single cell gene expression. *PLoS One* **8**, e69734 (2013).
17. Sensenbrenner, M., Lucas, M. & Deloulme, J.C. Expression of two neuronal markers, growth-associated protein 43 and neuron-specific enolase, in rat glial cells. *J. Mol. Med. (Berl.)* **75**, 653–663 (1997).
18. Buttgereit, A. *et al.* Sall1 is a transcriptional regulator defining microglia identity and function. *Nat. Immunol.* **17**, 1397–1406 (2016).
19. Wentworth, J.M. *et al.* Pro-inflammatory CD11c^{+}CD206^{+} adipose tissue macrophages are associated with insulin resistance in human obesity. *Diabetes* **59**, 1648–1656 (2010).
20. Amano, S.U. *et al.* Local proliferation of macrophages contributes to obesity-associated adipose tissue inflammation. *Cell Metab.* **19**, 162–171 (2014).
21. Wolf, Y. *et al.* Brown-adipose-tissue macrophages control tissue innervation and homeostatic energy expenditure. *Nat. Immunol.* **18**, 665–674 (2017).
22. Gosselin, D. *et al.* An environment-dependent transcriptional network specifies human microglia identity. *Science* **356**, eaal3222 (2017).
23. Clausen, B.E., Burkhardt, C., Reith, W., Renkawitz, R. & Förster, I. Conditional gene targeting in macrophages and granulocytes using LysMcre mice. *Transgenic Res.* **8**, 265–277 (1999).
24. Merad, M. *et al.* Langerhans cells renew in the skin throughout life under steady-state conditions. *Nat. Immunol.* **3**, 1135–1141 (2002).
25. Shirey-Rice, J.K. *et al.* Norepinephrine transporter variant A457P knock-in mice display key features of human postural orthostatic tachycardia syndrome. *Dis. Model. Mech.* **6**, 1001–1011 (2013).
26. Aderem, A. & Underhill, D.M. Mechanisms of phagocytosis in macrophages. *Annu. Rev. Immunol.* **17**, 593–623 (1999).
27. Stjärne, L. Basic mechanisms and local modulation of nerve impulse–induced secretion of neurotransmitters from individual sympathetic nerve varicosities. *Rev. Physiol. Biochem. Pharmacol.* **112**, 1–137 (1989).
28. Schroeder, C. & Jordan, J. Norepinephrine transporter function and human cardiovascular disease. *Am. J. Physiol. Heart Circ. Physiol.* **303**, H1273–H1282 (2012).
29. Filiano, A.J. *et al.* Unexpected role of interferon-γ in regulating neuronal connectivity and social behaviour. *Nature* **535**, 425–429 (2016).
30. Galle-Treger, L. *et al.* Nicotinic acetylcholine receptor agonist attenuates ILC2-dependent airway hyperreactivity. *Nat. Commun.* **7**, 13202 (2016).
31. Ibiza, S. *et al.* Glial-cell-derived neuroregulators control type 3 innate lymphoid cells and gut defence. *Nature* **535**, 440–443 (2016).
32. Kipnis, J. Multifaceted interactions between adaptive immunity and the central nervous system. *Science* **353**, 766–771 (2016).
33. Louveau, A. *et al.* Structural and functional features of central nervous system lymphatic vessels. *Nature* **523**, 337–341 (2015).
34. Rosas-Ballina, M. *et al.* Acetylcholine-synthesizing T cells relay neural signals in a vagus nerve circuit. *Science* **334**, 98–101 (2011).
35. Gabanyi, I. *et al.* Neuro-immune interactions drive tissue programming in intestinal macrophages. *Cell* **164**, 378–391 (2016).
36. Gautier, E.L. *et al.* Gene-expression profiles and transcriptional regulatory pathways that underlie the identity and diversity of mouse tissue macrophages. *Nat. Immunol.* **13**, 1118–1128 (2012).
37. Okabe, Y. & Medzhitov, R. Tissue-specific signals control reversible program of localization and functional polarization of macrophages. *Cell* **157**, 832–844 (2014).
38. Crotti, A. & Ransohoff, R.M. Microglial physiology and pathophysiology: insights from genome-wide transcriptional profiling. *Immunity* **44**, 505–515 (2016).
39. Prinz, M. & Priller, J. Microglia and brain macrophages in the molecular age: from origin to neuropsychiatric disease. *Nat. Rev. Neurosci.* **15**, 300–312 (2014).
40. Kong, Y., Ruan, L., Qian, L., Liu, X. & Le, Y. Norepinephrine promotes microglia to uptake and degrade amyloid β peptide through upregulation of mouse formyl peptide receptor 2 and induction of insulin-degrading enzyme. *J. Neurosci.* **30**, 11848–11857 (2010).
41. Kettenmann, H. & Ransom, B.R. *Neuroglia* (Oxford University Press, 2013).
42. Butovsky, O. *et al.* Identification of a unique TGF-β-dependent molecular and functional signature in microglia. *Nat. Neurosci.* **17**, 131–143 (2014).
43. Hanani, M. Satellite glial cells in sensory ganglia: from form to function. *Brain Res. Brain Res. Rev.* **48**, 457–476 (2005).
44. Hanani, M. Satellite glial cells in sympathetic and parasympathetic ganglia: in search of function. *Brain Res. Rev.* **64**, 304–327 (2010).
45. Camell, C.D. *et al.* Inflammasome-driven catecholamine catabolism in macrophages blunts lipolysis during ageing. *Nature* http://dx.doi.org/10.1038/nature24022 (2017).

ONLINE METHODS

General experimental approaches. No samples, mice, or data points were excluded from the reported analyses. Samples were not randomized to experimental groups. Analyses were not performed in a blinded fashion. More detailed information can be found in the **Life Sciences Reporting Summary**.

Antibodies, stain reagents, and drugs. Antibodies were obtained from the following vendors: anti-F4/80–Alexa Fluor 647 (BioLegend, catalog no. 123122, clone BM8), anti–human CD68 (Dako, catalog no. M 0876, clone PG-M1), anti–human NE transporter (NET) (MAb Technologies, catalog no. NET17-1, clone 3-6C1 sc H10), anti-MAOA (Abcam, catalog no. ab126751, clone GR155892-5), anti-TH (Pel-Freez Biologicals, catalog no. P40101-150, lot 16736), anti-GFP (Abcam, catalog no. ab13970, lot GR279236-1), anti-TH (Aves Lab, catalog no. TYH, lot TH1205), anti-GFP (Invitrogen, catalog no. A11120, lot 1563696), anti-GFP (Abcam, catalog no. ab6556, lot GR292567-1), goat anti–chicken IgY (H+L) secondary antibody, Alexa Fluor 488 (Molecular Probes/Thermo Fisher Scientific, catalog no. A-11039, lot 1759025), goat anti–rabbit IgG (H+L) cross-adsorbed secondary antibody, Alexa Fluor 594 (Molecular Probes/Thermo Fisher Scientific, catalog no. A-11012, lot 1704538), anti-Ly6c–eFluor 405 (eBioscience, catalog no. 48-5932-82, clone HK1.4, lot 4306743), anti-CD11c-PE (BD Pharmingen, catalog no. 553802, clone HL3, lot 47030), anti-CD45.2-PE (BioLegend, catalog no. 109808, clone 104.2), anti-CD45.2-FITC (obtained from S. Kimura (Memorial Sloan Kettering Cancer Center); clone 104.2), anti-CD11b-FITC (ATCC, catalog no. TIB-128, clone M1/70), anti-MHCII-Bio (clone M5/114, ATCC, catalog no. TIB-120), SAv-APC/Cy7 (BioLegend, catalog no. 405208, lot B215107), anti-Ki-67-Alexa488 (BD Biosciences, catalog no. 558616, clone B56, lot 7138687), IgG-Alexa488, isotype control (BD Biosciences, catalog no. 557782, lot 7102576), anti-Siglec-F-BV421 (BD Biosciences, catalog no. 562681, lot 7047598), anti-CD68 (Bio-Rad, catalog no. MCA1957GA, clone FA-11), goat anti–rat IgG (H+L) cross-adsorbed secondary antibody, Alexa Fluor 594 (Invitrogen, catalog no. A-11007), goat anti–chicken IgY (H+L), Alexa Fluor 647 (Abcam, catalog no. ab150171), goat anti–rabbit IgG (H+L), Alexa Fluor 488, (Abcam, catalog no. ab150077), goat anti–mouse IgG (H+L), Alexa Fluor 488 (Sigma, catalog no. SAB4600387), anti–mouse IgG (whole molecule), Cy3 (Sigma, catalog no. C0992), rabbit anti-UCP1 (Abcam, catalog no. ab10983, lot GR249119-8), mouse anti-NET (MAb Technologies, catalog no. NET05-2, clone 2-3 B2 sc D7). SYTOX Blue dead cell stain (Molecular Probes/Thermo Fisher Scientific, catalog no. S34857, lot 1851462) was used to exclude dead cells. HCS LipidTOX Deep Red Neutral Lipid Stain (Molecular Probes/Thermo Fisher Scientific, catalog no. H34477) and HCS LipidTOX Red Neutral Lipid Stain (Molecular Probes/Thermo Fisher Scientific, catalog no. H34476) were used to stain lipids.

Acetylcholine chloride, nisoxetine hydrochloride, clorgyline, and NE were purchased from Sigma-Aldrich.

Mice. *Cx3cr1*$^{GFP/+}$ mice (*Cx3cr1*^{tm1Litt}/LittJ; stock no. 008451), *Th-cre* mice (stock no. 008601), *GFP-L10* mice (stock no. 024750), *LysM-cre* mice (stock no. 004781), LSL-*ChR2-YFP* mice (stock no. 012-569), LSL-*tdTomato* mice (stock no. 007909), *ob*/*ob* mice (stock no. 000632), and *Csf1r*-LSL-*DTR* mice (stock no. 024046) were purchased from the Jackson Laboratory (JAX). *NET*$^{P/P}$ (*Slc6a2*$^{-/-}$) mice were kindly provided by M. Hahn (Vanderbilt University). B6 (C57BL/B6J) and B6-CD45.1 mice were purchased from Charles River and were bred and maintained at Instituto Gulbenkian de Ciência. Both males and females were used in this study. Mice were 4–10 weeks old (for details, see the **Life Sciences Reporting Summary**). Animal procedures were approved by the ethics committee of Instituto Gulbenkian de Ciência.

Immunofluorescence and confocal microscopy. Tissues were dissected and fixed in 4% paraformaldehyde for 2 h (at room temperature (RT), with agitation). For images in **Figure 2j**,**k**, we employed frozen sections and the fixation step was followed by cryoprotection in 30% sucrose (Alfa Aesar). 16-µm sections were obtained in a Leica Cryostat CM3050 S. Both frozen sections and whole-mount tissues were incubated in a blocking and permeabilization solution (3% BSA, 2% goat serum, 0.1% Tween, and 0.1% sodium azide in 1× PBS) for 1 h at RT with (whole mounts) or without (frozen sections) agitation. Incubations with primary antibodies were performed overnight at 4 °C with (whole mounts) or without (frozen sections) agitation. The following dilutions of primary antibodies were used: anti-GFP (1:500), anti-TH (1:1,000), anti-SLC6A2 (1:500), anti-MAOA (1:100). Incubation with secondary antibodies was performed for 1–2 h at RT, with or without (in the case of frozen sections) agitation. *Z*-series stacks were acquired on a Leica TCS SP5 confocal inverted microscope. Analysis and quantification of images were performed in Fiji.

***In vivo* two-photon microscopy.** Mice aged 2 months were kept anesthetized with 2% isoflurane. During surgery, body temperature was maintained at 37 °C with a warming pad. After application of local anesthetics (lidocaine), a sagittal incision of the skin was made above the suprapelvic flank to expose the subcutaneous inguinal fat pad. An imaging chamber was custom-built to minimize fat movement. Warm imaging solution (in mM: 130 NaCl, 3 KCl, 2.5 $CaCl_2$, 0.6 $MgCl_2.6H_2O$, 10 HEPES without sodium, 1.2 $NaHCO_3$, 10 glucose, pH 7.45 with NaOH) (37 °C) mixed with a fat dye (LipidTOX) was applied to label adipocytes, maintain tissue integrity, and allow the use of an immersion objective. Imaging experiments were performed under a two-photon laser-scanning microscope (Ultima, Prairie Instruments). Live images were acquired at 8–12 frames per second at depths below the surface ranging from 100–250 mm, using an Olympus 20× 1.0 N.A. water-immersion objective with a laser tuned to a wavelength of 810–940 nm and emission filters at 525/50 nm and 595/50 nm for green and red fluorescence, respectively. Laser power was adjusted to be 20–25 mW at the focal plane (maximally 35 mW), depending on the imaging depth and levels of GFP expression and LipidTOX spread. Analysis and quantification of images were performed in Fiji.

Electron microscopy. Fresh tissue was perfused with 2% paraformaldehyde (Electron Microscopy Services (EMS)) and 0.2% glutaraldehyde (EMS) in 0.1 M phosphate buffer (PB; pH 7.4). After perfusion, fibers were isolated and immersion fixed for 2 h at RT in the same fixative. For quenching of autofluorescence from free aldehydes, nerves were washed with 0.15% glycine (VWR) in PB for 10 min at RT.

Correlative light–electron microscopy. After fixation, fibers were stabilized with 0.1% tannic acid (EMS) and embedded in 2% agarose (Omnipur) before cryoprotection in 30% sucrose (Alfa Aesar) overnight at 4 °C. Embedded samples were placed in optimal cutting temperature (OCT) compound (Sakura) and plunge frozen in liquid nitrogen. 10-µm sections were obtained in a Leica Cryostat CM3050 S and placed on cover glasses coated with 2% (3-aminopropyl) triethoxysilane (Sigma-Aldrich) in acetone. Light microscopy imaging was performed in a Leica SP5 Live microscope after mounting the sections with PB. For electron microscopy processing, samples were washed ten times with PB and post-fixed in 1% osmium tetroxide (EMS) with 1% potassium hexacyanoferrate (Sigma-Aldrich) in PB for 30 min on ice. Dehydration was done in a graded ethanol series of 30%, 50%, 75%, 90%, and 100% ethanol for 10 min each. EPON resin (EMS) was used for embedding. 70-nm serial sections were obtained in a Leica EM UC7 and stained with 1% uranyl acetate and lead citrate for 5 min each. Electron microscopy images were acquired on a Hitachi H-7650 operating at 100 kV.

Single-cell suspension. Tissues were dissected from ten mice. Spleen, brain, visceral fat, and subcutaneous fat were excised and digested for 30 min with collagenase (Sigma) at 37 °C with shaking. Sympathetic nerve fibers were isolated from subcutaneous adipose tissues and digested for 30 min with hyaluronidase (Sigma) at 37 °C with shaking, washed, and further digested with collagenase for 15 min. SCGs were dissected and digested with collagenase for 10 min, washed, and further digested with trypsin (Biowest) for 30 min at 37 °C with shaking. Cell suspensions were filtered through a 70-µm sieve and centrifuged at 450*g* for 5 min.

Flow cytometry. Flow cytometry data were acquired on an LSR Fortessa X-20 SORP (Becton-Dickinson), FACSCalibur (Becton-Dickinson), or CyAn ADP (Beckman Coulter) and analyzed using the FlowJo software package (Tree Star). Macrophages were sorted as live CD45 and F4/80 double-positive cells using a FACSAria IIu high-speed cell sorter (Becton Dickinson) or MoFlo High-Speed Cell Sorter produced by Dako Cytomation (now owned by Beckman Coulter).

Bone marrow chimeras. B6-CD45.1 mice (aged 8–10 weeks), B6 (C57BL/6J) mice (aged 8–10 weeks), and *ob*/*ob* mice (aged 8–10 weeks) were lethally irradiated (900 rad, 3.42 min, ^{137}Cs source) (Gammacell 2000) and reconstituted with bone marrow cells from *Cx3cr1*$^{GFP/+}$ mice (aged 6 weeks), *Slc6a2*$^{-/-}$ mice (aged 6–8 weeks), B6 mice (aged 6–8 weeks), or B6-CD45.1 mice (aged 6–8 weeks). B6-CD45.1 mice and B6 mice were reconstituted with 5×10^6 total bone marrow cells, and *ob*/*ob* mice were reconstituted with 3×10^7 total bone marrow cells. Chimerism was assessed 8 weeks after reconstitution using flow cytometry.

Low-input RNA-seq library preparation. Sequencing libraries were prepared according to the Smart-seq2 method[46] with some modifications. 1,715 ± 115 cells from nerve fibers, 1,534 ± 85 cells from superior cervical ganglia, and 5,000 cells from other tissues (visceral fat, subcutaneous fat, spleen, and brain) were isolated as live CD45$^+$F4/80$^+$ cells in TRIzol (Thermo Fisher) and were used as starting material. RNA was extracted with the Direct-zol MicroPrep kit (Zymo Research) with on-column DNase I treatment. 10 µl of purified RNA was mixed with 5.5 µl of SMARTScribe 5× First-Strand Buffer (Clontech), 1 µl of poly(T) primer for reverse transcription (2.5 µM; 5′-AAGCAGTGGTATCAACGCAGA GTAC(T_{30})VN-3′), 0.5 µl of SUPERase IN (Ambion), 4 µl of dNTP mix (10 mM; Invitrogen), 0.5 µl of dithiothreitol (DTT) (20 mM; Clontech), and 2 µl of betaine solution (5 M; Sigma), and samples were incubated at 50 °C for 3 min. 3.9 µl of first-strand mix, containing 0.2 µl of 1% Tween-20, 0.32 µl of $MgCl_2$ (500 mM), 0.88 µl of betaine solution (5 M; Sigma), 0.5 µl of SUPERase IN (Ambion), and 2 µl of SMARTScribe Reverse Transcriptase (100 U/µl; Clontech), was added, and samples were incubated with one step at 25 °C for 3 min and one step at 42 °C for 60 min. 1.62 µl of template-switch (TS) reaction mix containing 0.8 µl of biotin-TS oligonucleotide (10 µM; biotin-5′-AAGCAGT GGTATCAACGCAGAGTACATrGrG+G-3′), 0.5 µl of SMARTScribe Reverse Transcriptase (100 U/µl; Clontech), and 0.32 µl of SMARTScribe 5× First-Strand Buffer (Clontech) was added, and samples were then incubated at 50 °C for 2 min, 42 °C for 80 min, and 70 °C for 10 min. 14.8 µl of second-strand synthesis, preamplification mix containing 1 µl of preamplification oligonucleotide (10 µM; 5′-AAGCAGTGGTATCAACGCAGAGT-3′), 8.8 µl of KAPA HiFi Fidelity Buffer (5×; KAPA Biosystems), 3.5 µl of dNTP mix (10 mM; Invitrogen), and 1.5 µl of KAPA HiFi HotStart DNA Polymerase (1U/µl; KAPA Biosystems) was added, and samples were amplified by PCR: 95 °C for 3 min, 8 cycles at 98 °C for 20 s, 67 °C for 15 s, and 72 °C for 6 min, and a final extension step at 72 °C for 5 min. The synthesized double-stranded DNA (dsDNA) was purified using Sera-Mag SpeedBeads (Thermo Fisher Scientific) with final concentrations of 8.4% PEG 8000 and 1.1 M NaCl and then was eluted with 13 µl of UltraPure water (Invitrogen). The product was quantified by Qubit dsDNA High Sensitivity Assay Kit (Invitrogen), and libraries were prepared using the Nextera DNA Sample Preparation Kit (Illumina). Tagmentation mix containing 11 µl of 2× Tagment DNA Buffer and 1 µl of Tagment DNA Enzyme was added to 10 µl of purified DNA, and samples were then incubated at 55 °C for 15 min. 6 µl of Nextera Resuspension Buffer (Illumina) was added, and samples were incubated at RT for 5 min. Tagmented DNA was purified using Sera-Mag SpeedBeads (Thermo Fisher Scientific) with final concentrations of 7.8% PEG 8000 and 0.98 M NaCl and then eluted with 25 µl of UltraPure water (Invitrogen). Final enrichment amplification was performed with Nextera primers, adding 1 µl of Index 1 primers (100 µM; N7xx), 1 µl of Index 2 primers (100 µM; N5xx) and 27 µl of NEBNext High-Fidelity 2× PCR Master Mix (New England BioLabs) and then amplifying samples by PCR: 72 °C for 5 min, 98 °C for 30 s, and 8–13 cycles of 98 °C for 10 s, 63 °C for 30 s, and 72 °C for 1 min. Libraries were size selected, quantified by Qubit dsDNA HS Assay Kit (Thermo Fisher Scientific), and pooled and sequenced on a NextSeq 500 (Illumina) for 76 cycles at a depth of 25 to 30 million single-end reads per sample. To normalize for genomic DNA contamination, which occurred in some samples due to incomplete DNA removal during RNA isolation, the average intronic noise per base pair in all intronic regions per gene was calculated. The exonic reads were then normalized by subtracting the background noise per base pair for the complete length of the exonic regions. Genes without introns were not normalized, as these genes are the minority of genes and are typically short (code available at https://github.com/vlink/DNA_contamination/).

Fastq files from sequencing experiments were mapped to the mouse mm10 genome using default parameters for STAR[47]. Mapped data were analyzed with HOMER[48] and custom R and Perl scripts.

Superior cervical ganglion explant cultures. SCGs were removed from mice aged 4–6 weeks under a stereomicroscope and placed in DMEM (Invitrogen, Carlsbad, CA, USA). Ganglia were cleaned from the surrounding tissue capsule and transferred into eight-well tissue culture chambers (Sarstedt, Nümbrecht, Germany) that were previously coated with poly-D-lysine (Sigma-Aldrich, Steinheim, Germany) in accordance with the manufacturer's instructions. Ganglia were then covered with 5 µl of Matrigel (BD Bioscience, San Jose, CA, USA) and incubated for 7 min at 37 °C. DMEM without phenol red (Invitrogen) supplemented with 10% FBS (Invitrogen), 2 mM L-glutamine (Biowest, Nuaillé, France), and nerve growth factor (Sigma-Aldrich) was subsequently added. 12 SCG explant cultures were prepared per condition. SCGs were cultured for a minimum of 24 h before further manipulation. The stimulation protocol in **Figure 3** was performed for 2 h with the following concentrations of drugs: 10 mM acetylcholine chloride, 100 nM nisoxetine hydrochloride, and 100 µM clorgyline.

NE measurements after optogenetic stimulation *ex vivo*. Depolarization of sympathetic neurons in *Th-cre*; LSL-*ChR2-YFP* explant cultures was performed on a Yokogawa CSU-X Spinning Disk confocal microscope using the 488-nm laser line pointing at the region of interest (ROI) for 200 µs. Stimulation was repeated seven times using 40% laser intensity. NE content in the SCG explant culture medium and in sorted CD45$^+$F4/80$^+$ cells was determined by NE ELISA kit (Labor Diagnostika Nord, Nordhorn, Germany, catalog no. BA E-5200). The same procedure was performed for LSL-*ChR2-YFP* control mice.

NE measurements in macrophages from sWAT. CD45.2 (PE)$^+$F4/80 (Alexa Fluor 647)$^+$ cells from sWAT were sorted as live cells and incubated with 2 µM NE for 2 h using the same culture conditions as those used for SCG explant cultures. Afterwards, cells were washed twice with 1× PBS, and NE content was measured by NE ELISA kit (Labor Diagnostika Nord, Nordhorn, Germany, catalog no. BA E-5200).

qPCR. Total RNA from sorted cells was isolated using the RNeasy Plus Micro Kit (Qiagen, catalog no. 50974034). Total RNA from adipose tissues was isolated with the PureLink RNA Mini Kit (Ambion, Life Technologies, catalog no. 12183025). cDNA was reverse transcribed using SuperScript II (Invitrogen) and random primers (Invitrogen). qPCR was performed using SYBR Green (Applied Biosystems) in ABI QuantStudio 7 (Applied Biosystems). The *Gapdh* housekeeping gene was used to normalize samples. We used the following formula to calculate relative expression levels: $RQ = 2^{-\Delta Ct} \times 100 = 2^{-(Ct\ gene\ of\ interest - Ct\ Gapdh)} \times 100$.

The primers used were as follows: *Lpl*-forward, 5′-CAGCTGGGCCTAACTT TGAG-3′; *Lpl*-reverse, 5′-CCTCTCTGCAATCACACGAA-3′; *Pnpla2*-forward, 5′-CACTTTAGCTCCAAGGATGA-3′; *Pnpla2*-reverse, 5′-TGGTTCAG TAG GCCATTCCT-3′; *Gfap*-forward, 5′-CCAGCTTCGAGCCAAGGA-3′; *Gfap*-reverse, 5′-GAAGCTCCGCCTGGTAGACA-3′; *Gap43*-forward, 5′-AGCC AAGGAGGAGCCTAAAC-3′; *Gap43*-reverse, 5′-CTGTCGGGCA CTTTCC TTAG-3′; *Ucp1*-forward, 5′-GTGAAGGTCAGAATGCAAGC-3′; *Ucp1*-reverse, 5′-AGGGCCCCCTTCATGAGGTC-3′; *Slc6a2*-forward, 5′-CAGGCACCT CCATTCTGTTT-3′; *Slc6a2*-reverse, 5′-GCGGCTTGAAGTTGATGATG CTG-3′; *Maoa*-forward, 5′-GCCCAGTA TCACAGGCCAC 3′; *Maoa*-reverse, 5′-GTCCCACATAAGCTCCACCA-3′; *Chrm1*-forward, 5′-CA GTCCCAACAT CACCGTCTT-3′; *Chrm1*-reverse, 5′-GAGAACGAAGGAAACCAACCAC-3′; *Chrm2*-forward, 5′-TGTCTCCCAGTCTAGTGCAAGG-3′; *Chrm2*-reverse, 5′-CATTCTGA CCTGACGATCCAAC-3′; *Chrm4*-forward, 5′-GCCTTCATCC TCACCTGGAC-3′; *Chrm4*-reverse, 5′-AGTGGCATTGCAGAGTGCAT-3′; *Chrm5*-forward, 5′-CCA TGGACTGTGGGAAGTCA-3′; Chrm5-reverse, 5′-CAGCGTCC CATGAGGATGTA-3′; *Chrna2*-forward, 5′-CTCCCATCCT GCTTTCCAG-3′; *Chrna2*-reverse, 5′-GTTTGAACAGGCGGTCCTC-3′; *Chrna3*-forward, 5′-GCGAACAGGTCACAGTTTATG-3′; *Chrna3*-reverse, 5′-GCATTTT TCTCTGGGTTTTCA-3′; *Chrna5*-forward, 5′-CGCTCTTCT TCCACACACAA-3′; *Chrna5*-reverse, 5′-TAGGTCCACCGTCTTTCTCG-3′; *Chrna6*-forward, 5′-CTTTGTCACGCTGTCCAT-3′; *Chrna6*-reverse, 5′-GCCTCCT TTGTCTTGTCC-3′; *Chrna7*-forward, 5′-ACAGTACTTC GCCAGCACCA-3′; *Chrna7*-reverse, 5′-AAACCATGCACACCAATTCA-3′; *Chrna9*-forward, 5′-ACAAGGCCACCAACTCCA-3′; *Chrna9*-reverse, 5′-ACCAACCCACTCCTCCTCTT-3′; *Chrna10*-forward, 5′-TCTGACCTCA

CAACCCACAA-3′; *Chrna10*-reverse, 5′-TCC TGTCTCAGCCTCCATGT-3′; *Chrnb2*-forward, 5′-GGGCAGGCA CACTATTCTTC-3′; *Chrnb2*-reverse, 5′-TCCAATCCTCCCTCACACTC-3′; *Chrnb3*-forward, 5′-CTCCTCAGACATT GGTTCCAAGG-3′; *Chrnb3*-reverse, 5′-AATGAGG TCAACCATGGT-3′; *Chrnb4*-forward, 5′-TCTGGTTGCCTGACATCGTG-3′; *Chrnb4*-reverse, 5′-GGGTTCACAAAGTACATGGA-3′;*Adrb2*-forward, 5′- GGTTATCGTCCTGG CCATCGTGTTTG-3′; *Adrb2*-reverse, 5′-TGGTTCGTGAAGAAGTCACAGC AAGTCTC-3′; *Th*-forward, 5′-GGTATACGCCACGCTGAAGG-3′; *Th*-reverse, 5′- TAGCCACAGTACCGTTCCAGA-3′; *Tnfa*-forward, 5′- ATGAG CACAGA AAGCATGATC-3′; *Tnfa*-reverse, 5′-TACAGGCTTGTCACTCGAATT-3′; *Il10*-forward, 5′-GCTCTTACTGACTGGCATGAG-3′; *Il10*-reverse, 5′-CGCAG CTCTAG GAGCATGTG-3′; *Il1*-forward, 5′- GAAGAAGAGCCCATCCT CTG-3′; *Il1*-reverse, 5′- TCATCTCGGAGCCTGTAGTG-3′; *Il4ra*-forward, 5′-TGACCTCACAGGAACCCAGGC-3′; *Il4ra*-reverse, 5′-GAACAGGC AAAACAACGGGAT-3′; *Gapdh*-forward, 5′-AACTTTGGCATTGTGGA AGG-3′; *Gapdh*-reverse, 5′-ACACATTGGGGGTAGGAACA-3′.

Functional studies. We measured rectal temperature with an electronic thermometer (Precision) when the mice were housed both at RT and at 4 °C with ND food and water *ad libitum*.

Free fatty acids were measured in blood plasma using the Free Fatty Acid Quantitation Kit (Sigma-Aldrich, catalog no. MAK044-1KT).

Serum levels of NE were determined by NE ELISA kit (Labor Diagnostika Nord, Nordhorn, Germany, catalog no. BA E-5200).

High-fat diet challenge. When B6 mice reached 8 weeks of age, we replaced ND with HFD (Ssniff, Spezialdiäten, Soest, Germany, catalog no. D12492). Analyses in **Figure 4** were performed when mice achieved a 40% increase in body weight after 3 months of a HFD.

Intracellular staining for Ki-67. Cells were surface-stained for 30 min. Subsequently, cells were washed and fixed with fixation and permeabilization buffer (eBioscience) and then permeabilized with permeabilization buffer (eBioscience). Following this process, cells were intracellularly stained with anti-Ki-67 or isotype control.

Histopathological and immunohistochemical analyses. Human and mouse tissues were fixed in buffered formalin, and inclusion in paraffin was done according to standard technical procedures. Histochemical and immunohistochemical studies were performed on formalin-fixed and paraffin-embedded (FFPE) tissue sections. Sections were 2 µm (human ganglia) or 3–6 µm (mouse tissues) thick for H&E or were 4 µm thick for immunohistochemical studies. The following markers were used for immunohistochemistry: aminoethylcarbazole (AEC) and 3,3′-diaminobenzidine (DAB) according to the usual technical procedure for the marker. For the immunohistochemical studies, sections underwent antigenic recovery before incubation with primary antibodies: anti-CD68 (Dako, clone PG-M1; dilution 1:150) anti–human SLC6A2 (MAb Technologies, clone 3-6C1 sc H10; dilution 1:1,000), anti-MAOA (Abcam, clone GR155892-5; dilution 1:50), and anti-UCP1 (Abcam; dilution 1:500). Human tissues were analyzed under an optical microscope (Nikon Eclipse 50i), and iconography microscopic images were captured using a coupled digital camera (DS Camera Control Unit DS-L2). Mouse tissues were analyzed using a Leica DM LB2 microscope, and images were captured with a Leica DFC 250 camera.

Diphtheria toxin–mediated macrophage depletion. We used *LysM-cre*; LSL-*Csf1r-DTR* mice for this experiment and LSL-*Csf1r-DTR* mice as controls. Animals received injections of diphtheria toxin (DT) from *Corynebacterium diphtheria* (Calbiochem) once daily for four consecutive days. The first dose was 500 ng of DT in PBS per 20 g of body weight followed by three doses of 250 ng of DT in PBS per 20 g of body weight. Depletion was assessed by flow cytometry 12 h after the fourth injection. NE levels in adipose tissues were assayed by NE ELISA kit (Labor Diagnostika Nord, Nordhorn, Germany, catalog no. BA E-5200). Protein concentration was determined by the Bradford method.

Statistics. Statistical analyses were performed with GraphPad Prism software (San Diego, CA) using unpaired Student's *t*-test (two-tailed) when two groups were being compared or one-way ANOVA when several groups were being compared. One-way ANOVA was followed by Tukey's multiple-comparisons test, except for the data in **Figure 4b** and **Supplementary Figure 8a**, where it was followed by Bonferroni multiple-comparisons test with one group indicated as a control group. $P < 0.05$ was considered statistically significant. Data are represented as mean ± s.e.m. Sample size was predetermined based on previous studies (for more information, see the **Life Sciences Reporting Summary**). Data displayed normal variance.

Data availability. The RNA-seq data sets are available at GSE103847. The data that support the findings herein presented are available from the corresponding author upon reasonable request. A **Life Sciences Reporting Summary** is available.

46. Picelli, S. *et al.* Smart-seq2 for sensitive full-length transcriptome profiling in single cells. *Nat. Methods* **10**, 1096–1098 (2013).
47. Dobin, A. *et al.* STAR: ultrafast universal RNA-seq aligner. *Bioinformatics* **29**, 15–21 (2013).
48. Heinz, S. *et al.* Simple combinations of lineage-determining transcription factors prime *cis*-regulatory elements required for macrophage and B cell identities. *Mol. Cell* **38**, 576–589 (2010).

2018

Neuro-immune interactions in obesity.

Roksana Maria Pirzgalska